Towards closed-loop control in photopolymer-based additive manufacturing

TOWARDS CLOSED-LOOP CONTROL IN PHOTOPOLYMER-BASED ADDITIVE MANUFACTURING

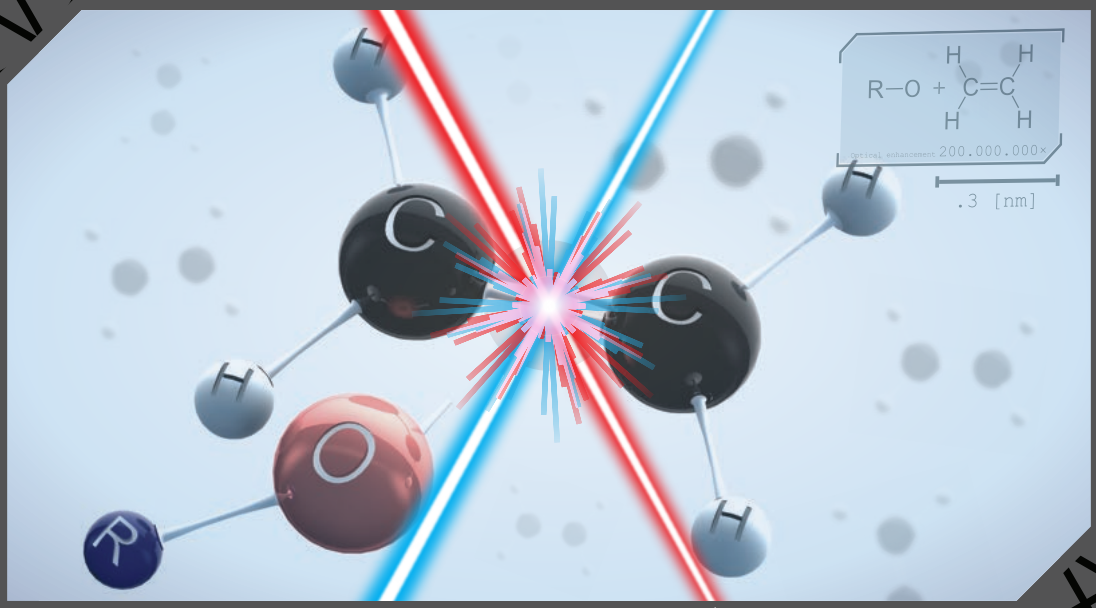

PHOTO-POLYMERIZATION

UV LASER ACTUATOR

IR LASER SENSOR

CLOSED-LOOP CONTROLLER

THOMAS HAFKAMP

Towards closed-loop control in photopolymer-based additive manufacturing

T.M. Hafkamp

September 22, 2020

The research presented in this thesis was financially supported by TNO and carried out as part of the TNO-TU/e-HTSC AMSYSTEMS project on Additive Manufacturing of Ceramics.

A catalogue record is available from the Eindhoven University of Technology Library.
ISBN: 978-90-386-5129-3

Printed by: Print Service Ede

Towards closed-loop control in photopolymer-based additive manufacturing

PROEFSCHRIFT

ter verkrijging van de graad van doctor aan de Technische Universiteit Eindhoven, op gezag van de rector magnificus prof.dr.ir. F.P.T. Baaijens, voor een commissie aangewezen door het College voor Promoties, in het openbaar te verdedigen op maandag 26 oktober 2020 om 13:30 uur

door

Thomas Martijn Hafkamp

geboren te Rheden

Dit proefschrift is goedgekeurd door de promotoren en de samenstelling van de promotiecommissie is als volgt:

voorzitter:	prof.dr. H. Nijmeijer
1^{e} promotor:	dr.ir. L.F.P. Etman
2^{e} promotor:	dr.ir. A.G. de Jager
leden:	prof.dr. I. Gibson (Universiteit Twente)
	prof.dr.ir. M. Steinbuch
	prof.dr.ir. P.D. Anderson
	prof.dr.ir. A. van Keulen (Technische Universiteit Delft)
adviseur:	ir. G.E. van Baars (TNO Optomechatronics)

Het onderzoek dat in dit proefschrift wordt beschreven is uitgevoerd in overeenstemming met de TU/e Gedragscode Wetenschapsbeoefening.

Summary

Additive Manufacturing (AM) embodies a distinct approach to manufacturing that may revolutionize the industry. Rather than subtracting material from the workpiece, AM machines typically build products from the bottom up by adding material in a layer-by-layer fashion. In particular cases, this additive approach alleviates the traditional manufacturing restrictions on product geometry and facilitates enhanced product functionality and performance.

Vat photopolymerization, also known as Stereolithography, is a class of AM techniques that stands out due to small feature sizes and high build speeds. This AM technique solidifies layers of photocurable resin with UV light according to the part's cross-sectional geometry. By mixing the photopolymer resin with sinterable powder, vat photopolymerization can be used as the shape forming step in an indirect production method for ceramic or metallic parts.

Although vat photopolymerization is a promising AM technology, manufacturing near-net shape parts from high-performance ceramic materials is challenging. To meet the high tech industry's needs, AM equipment has to scale up to larger product sizes and has to consistently build parts of high quality by becoming robust to uncertainty in the machine, the material, and the process. These challenges motivate a mechatronic systems engineering approach towards AM equipment development. This thesis takes the mechatronic systems stand-of-view, and investigates novel methods to improve the print quality and robustness of AM technology. In particular, closed-loop control system architectures are developed for future integration into vat photopolymerization equipment.

The thesis starts with proposing a classification scheme for AM control strategies based on the systems engineering V-model that facilitates the identification of control strategies. The AM process is decomposed along the spatial and temporal dimension in analogy to the V-model. Rather than targeting the indispensable low-level machine control systems, this work further focuses on real-time control schemes that close the loop on the actual material transformation process, i.e., UV curing.

The thesis then continues with a thorough review of the state of the art in process modelling, sensing, actuation, and control in the context of vat photopolymerization. Both major process functions are addressed: material deposition through recoating

on the one hand and material transformation through UV curing on the other. In both process functions, multiple methods are identified to fulfill them, leading to a set of potential AM system architectures. The aim of this thesis is to identify potential control strategies that are compatible with these architectures and to analyze their feasibility and potential performance improvements.

The main conclusion of the feasibility study is that real-time control of UV curing is only feasible for mask-projection-based photopolymerization systems and that feasibility is governed by limited sampling rates. This conclusion is drawn based on a comparison of time scales related to physical phenomena in vat photopolymerization, sampling rates of relevant sensors, and response times of several actuator topologies. Particularly, future machine integration of real-time control strategies poses challenging requirements on the sensing aspect. For example, it is desired to measure many voxels spanning a large range at high sampling rates, i.e., at high spatio-temporal resolution. Another challenge is the lack of availability of machine-implementable sensors that can measure the photopolymer cure state.

As a first step towards experimentally demonstrating the feasibility of feedback-controlled vat photopolymerization, the challenging sensing requirements are relaxed and the scope is reduced to a single voxel. An experimental setup is developed in which the degree of conversion is measured in situ by an infrared spectrometer at a low rate. Experimental data obtained from this proof-of-principle setup is used to develop a control-oriented process model and identify its parameters. A material perturbation is applied by adding an inhibitor and the case with and without feedback control were compared. The results show that the closed-loop controller successfully compensates for the material perturbation and reaches the setpoint conversion value, in contrast to the open-loop controller.

As a second step in the effort to better meet the challenging AM process requirements, an optical degree of conversion measuring instrument is designed, realized, and tested. The instrument's measuring principle is based on a molecular absorption photometer in the near-infrared wavelength range and aims to provide a simpler, cost-effective, and high-speed alternative to general-purpose instruments for chemical analysis. Ultimately, the instrument's use is demonstrated as a photopolymer characterization device for future implementation into AM equipment.

Contents

Chapter 1

Introduction

Some say that a fourth industrial revolution is imminent in which the manufacturing industry is transforming from machine-dominant to highly-interconnected, digital production lines [1, 2]. This revolution, also known as Industry 4.0, may have a profound impact on the economy and society as a whole [1], as it may improve industrial performance through end-to-end engineering, horizontal, and vertical integration [3]. One could associate the onset of this revolution with the birth of 3D printing technologies in the early 1980's [4]. In these years, as with many technological innovations, several researchers worked independently on a similar idea [2, 4]. The idea was to build up 3D objects by successively adding layers of material according to their 2D cross-sections. The term "3D Printing" was coined for this build process, since material layers can be added through 2D printing techniques that are extended to the third dimension [2]. Today, Additive Manufacturing (AM) is the standardized term [5] for this process and a wide variety of derived technologies have emerged [2].

AM offers unique capabilities compared to traditional manufacturing technologies, including more design freedom, "complexity for free," and customizable material properties [2, 6]. These capabilities make that AM plays a prominent role in the Industry 4.0 revolution, along with at least two other reasons.

Firstly, AM accelerates the product development cycle, because system or part representations can be created quickly in a process called rapid prototyping. The capability to rapidly create a tangible prototype revolutionizes the design review process [4], since the physical part can be touched, analyzed, and evaluated by all stakeholders. From a scientific and engineering perspective, AM not only provides the ability to evaluate the part's geometry, but also makes it possible to rapidly validate models and theories through experimental evaluation of the part's physical properties.

Secondly, AM is developing from a Rapid Prototyping technology for mock-ups to a Direct Digital Manufacturing technology for end-use parts [2]. As AM

technology is reaching a higher level of maturity, parts are now being manufactured for final use, directly from a digital CAD description. Although many other (subtractive) manufacturing technologies are by definition digital since they are Computer Numerical Controlled (CNC), determining the machining program can be involved for a CNC machine in comparison to the build program for an AM machine. Hence, AM is becoming a feasible option for producing complex and unique geometries while digitally archiving information throughout the life cycle, despite the comparatively inferior accuracy, quality, speed and material properties that are frequently attributed to AM [2].

1.1 The birth of 3D printing

Although multiple researchers worked on similar 3D printing concepts at the same time, it is Charles W. Hull who is regarded as the inventor of the first commercial rapid prototyping technology [2,4]. In the 1980's, Hull developed a concept to build 3D objects by successively curing photopolymer layers with ultraviolet (UV) light and named the technology Stereolithography [4,7]. Today, Stereolithography belongs to a broader family of technologies known as vat photopolymerization (VP) [2]. Hull patented Stereolithography in 1986 [8] and founded the company 3D Systems in California to commercialize the technology [4]. 3D Systems then introduced the SLA-1 in 1987, which was the first commercially 3D printer. Figure 1.1 shows a photograph of the SLA-1 and a related block diagram that was adopted from the original patent [8].

The basic 3D printer functions have not changed since the introduction of the SLA-1 and are basically the same among all present-day AM technologies, whether they are photopolymer-based or not. Their primary function is to transform the feedstock's geometry and material properties into a solid stack of layers to create a finished part [10, 11]. This primary function is fulfilled by several subfunctions that are allocated to components represented by the blocks in Figure 1.1. The digital or electronic subfunctions include slicing the input geometry, generating the numerical control program, and controlling the build process by means of computers. The physical subfunctions include supplying and arranging material and energy in 3D space according to the numerical control program. These subfunctions are generally fulfilled by an energy source, such as a laser, and one or more motion stages, such as galvanometer mirror scanners and z-stages that act as an elevator for the build platform. Auxiliary subfunctions include storing the feedstock, supporting the previously processed material, and conditioning the build chamber environment through gas flows or thermal actuators.

Despite their functional commonality, a wide variety of AM technologies have emerged from the fundamental principles to transform materials and the conceptual choice to pattern the material, the energy, or both. To facilitate the classification of this variety of AM technologies, seven AM process categories were defined in the ISO/ASTM standard 52900:2015 [5], i.e., binder jetting, directed energy deposition,

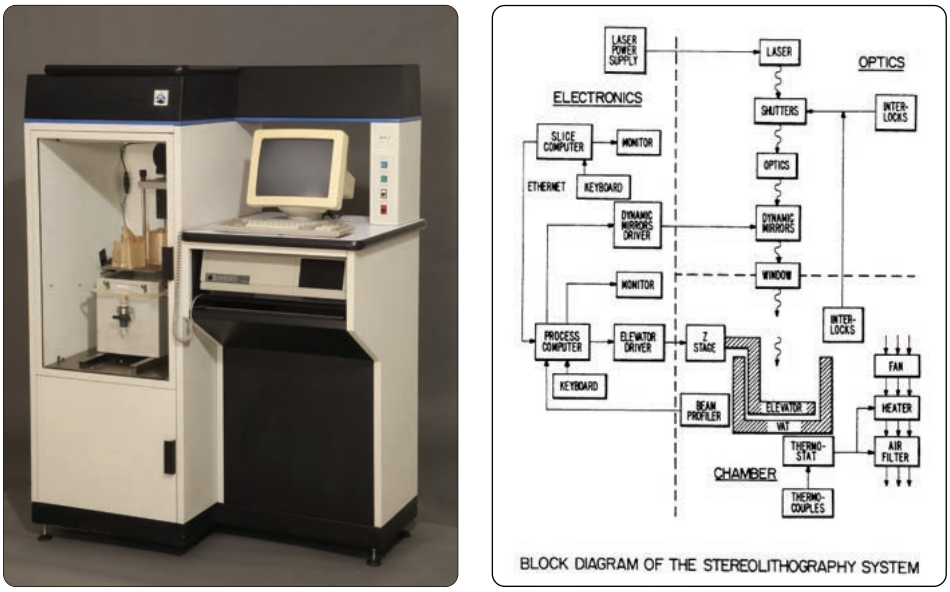

Figure 1.1: The 3D Systems SLA-1 was the first commercially available 3D printer from 1987 [4]. At the time of writing it is a museum piece (photograph on the left) [9] and the original patent has expired (block diagram on the right) [8].

material extrusion, material jetting, powder bed fusion, sheet lamination, and vat photopolymerization. The reader is referred to standard text books on AM [2, 12] for a general overview of these process categories. This thesis considers the VP process category, in which the optical energy or light is patterned in space during UV curing to create the cross-sections, whereas the material is deposited evenly to form thin layers during recoating.

1.2 The mechatronic system design challenge

Since its invention in the early 1980's, the VP process category in itself has developed to a wealth of variations in system architectures. At the time of writing, dozens of AM equipment manufacturers offer a wide variety of photopolymerization-based AM machines. These machines have build volumes ranging from under 1-liter desktop sizes or even smartphone sizes [12] to over 1000-liter industrial sizes that allow for manufacturing complete car bumpers or dashboards [13]. Machines operating at the bottom of this size range employ two-photon polymerization, which is a microfabrication technology in which the typical photopolymer feature resolutions have been reduced from the order of 100 [μm] to 100 [nm] [14]. Interestingly, the photopolymerization working principle can be applied at such widely separated

length scales.

No matter the machine size, the successful development of VP technology requires a transdisciplinary systems engineering approach [15], addressing technical challenges from different viewpoints [14] and following a systematic development process as exemplified by the classical V-model [16]. To prove this point, note that VP involves major contributions from chemistry, laser physics, applied mathematics, computer software, CAD modelling, viscous fluid dynamics, materials science, optics, as well as electrical, mechanical and control systems engineering [4]. Clearly, VP exhibits a highly multidisciplinary character and presents an interesting mechatronic system design challenge [17].

Figure 1.2 gives an idea of the many combinations that arise from just six high-level design choices, even though not all options are compatible. Evidently, the machine designer has quite some options to configure a photopolymer-based AM machine. In traditional AM machines, the recoating and photopolymerization steps were executed in alternating consecutive steps. Hence, the choices concerning the type of light engine and the type of recoater were independent as they were used at separate times in the build process. Recently, significantly higher build speeds have been achieved by continuously moving the build platform while concurrently supplying (recoating) and solidifying (curing) the resin. The translational version of this continuous process is known as continuous liquid interface production (CLIP) [18, 19], while the rotational version is known as tomographic volumetric AM [20, 21]. Next to building at significantly higher speeds, a few modern VP systems use robotic build plate handlers to automate the production line and pave the way to Industry 4.0.

1.3 Towards zero-defect AM: the need for control

For AM to evolve to an Industry 4.0-ready manufacturing technology, the overall performance of the manufacturing processes need to evolve as well. The performance of any manufacturing process can be quantified in terms of its productivity, quality, reliability and associated costs [10, 22]. From the machine operator's perspective, one just wants to press "Ctrl-(3D)P" and shortly wait for the 3D printer to produce an end-use part that is always right the first time and has zero defects. However, 3D printing has not reached such a level of performance yet, let alone approached the performance found in 2D printing.

To reach this level of performance and realize AM's potential, there is a high-priority need for research on process modelling, sensing, and control [23]. In other words, there is a need for a mechatronic approach towards AM equipment development as AM machine architectures have hardly changed since the first-generation prototypes [24]. Decades of advancements in mechatronic systems [17] have already contributed significantly to the current state of the art in AM equipment. Likewise, feedback control systems have been instrumental in attaining the precision required for well-coordinated motion between the machine axes and tools, and have

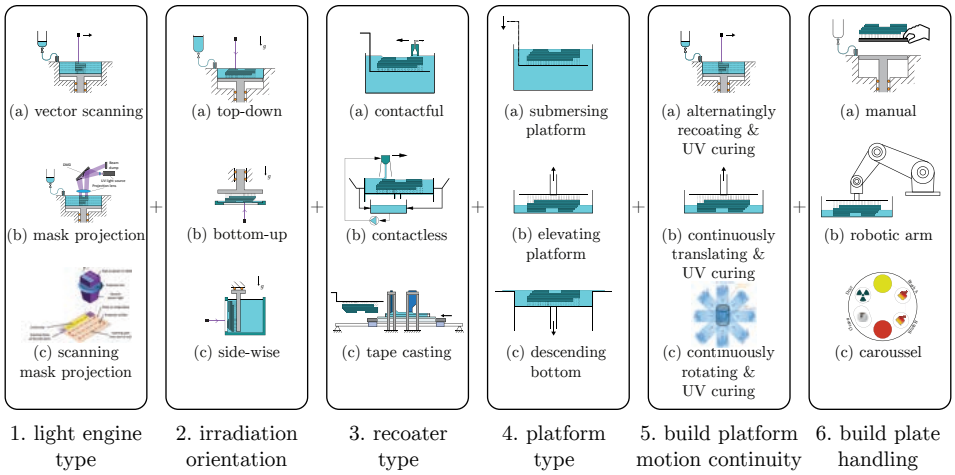

Figure 1.2: A "machine configurator" for photopolymer-based AM equipment. Just six high-level design choices already reveal the wealth of possible variations in system architectures encountered among AM equipment manufacturers.

always been present in manufacturing systems in several forms [10]. However, both academia and industry have hardly investigated the potential of closing feedback loops in AM at higher levels than such low-level machine control.

In an attempt to address the above-mentioned research needs, the Netherlands Organisation for applied scientific research (TNO) formulated a research program in collaboration with the High Tech Systems Center (HTSC) of Eindhoven University of Technology (TU/e). The research program focused on AM equipment engineering challenges for ceramic vat photopolymerization and consisted of three related PhD research projects, one of which resulted in the present thesis. The three projects shared the goal of developing novel AM equipment concepts aimed at closed-loop control on the process and product level. To this end, one project studied computational methods to model the build-up of mechanical properties during photopolymerization [25], another focused on computational modelling of resin flow during recoating [26], and the present work focused on the integration of control solutions into AM equipment. In addition, three one-year Professional Doctorate in Engineering Degree (PDEng) design projects were carried out regarding the machine control [27], sensing [28], and recoating systems [29] of a prototype machine developed by TNO.

The integration of closed-loop control solutions is facilitated by the increasing amount of data that is being generated and stored during the complete AM product life cycle. This data as a whole can be considered as part of a "digital thread" that spans from the initial product's design phase to its operation in the field [30–33]. Figure 1.3 visualizes various aspects of the digital thread during an AM part's life

cycle and a closely related concept known as a "digital twin" [30]. This concept aims to update the same models that were used to design and build the product with data obtained from the physical object during its operation in the field. More relevantly, in-situ process measurements could be compared to the digital reference and fed back to the models that were used initially to create the machine instructions and now to correct them during the build.

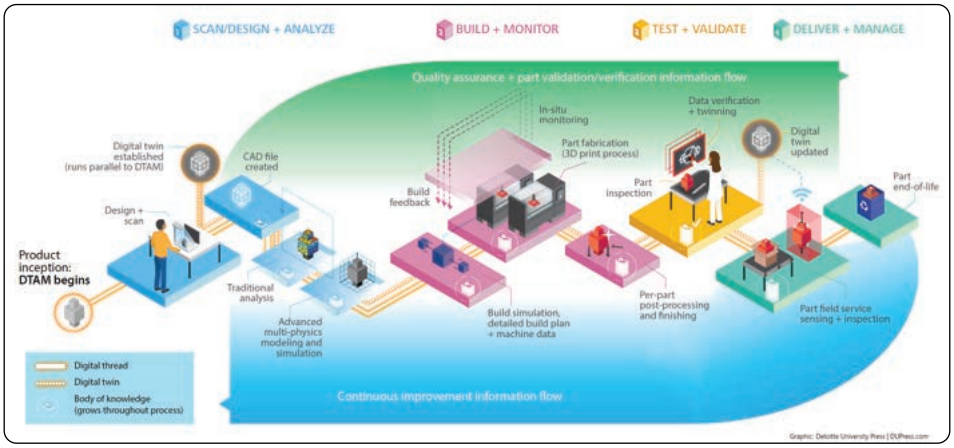

Figure 1.3: The concepts of a digital thread and a digital twin applied to an AM product's life cycle. Note the feedback loop in the build phase by virtue of in-situ monitoring. Image adopted from [30].

1.4 The AM control problem

At the highest abstraction level, any AM process can be modelled as a generic manufacturing system whose primary inputs are the *desired* digital object's geometry and properties, and whose primary outputs are the actually *realized* physical geometry and properties [10]. The secondary inputs and parameters are the boundary conditions of the working environment and the machine and material characteristics. The secondary outputs encompass any relevant data that is acquired during the build and stored in the digital thread, whose input-output relationships are determined by several interconnected subsystems. Figure 1.4 shows these subsystems in a hierarchy representing photopolymer-based AM systems on several levels.

Multiple hierarchical control architectures have already been proposed in the literature for mechatronic systems [17,34], the process industry [35], and automated manufacturing systems in general [36]. For instance, the ISA-95 "automation pyramid" is a widely accepted hierarchical model that was standardized by the International Society of Automation (ISA) [37]. The top of this pyramid concerns business plan-

ning, scheduling, operations management, and logistics, which are implemented in Enterprise Resource Planning (ERP) and Manufacturing Execution Systems (MES). These top levels govern the intermediate levels concerned with monitoring and supervisory control, which in turn govern the low-level controllers that measure and manipulate physical machines and processes through sensors and actuators [36].

Ultimately, each controller collaborates through the control hierarchy towards the common goal of producing a desired output, i.e., the 3D object, having maximum product quality, minimum error, and reduced sensitivity to disturbances and uncertainties. Nonetheless, most AM process controllers still lack the feedback loops required to control part quality through corrective actions [17, 23, 38–46]. Therefore, this thesis aims to make advancements towards closed-loop control in photopolymer-based AM. To this end, the control system development cycle was followed from beginning to end. Although the opinions are divided on the exact development steps and their sequence [35, 47–49], the cycle can be summarized as follows:

0. Design the system & equipment around a particular AM process (the plant);
1. Study the system and process from the perspective of control;
2. Formulate the control objectives and specify the desired performance;
3. Model the system and uncertainties (disturbances, noise, model mismatch);
4. Analyze the model, determine its properties;
5. Decide on the measured and manipulated variables (sensors and actuators);
6. Devise a control strategy: select the control structure and type of controller;
7. Design the controller;
8. Evaluate the (closed-loop) controlled system in a virtual or pilot plant;
9. Choose hard-/software, implement in real plant;
10. Test/validate control system, tune on-line.

Following a holistic mechatronic approach implies that one should look at the combined controller and plant design, i.e., taking control into account while designing the plant (the machine). However, designing a completely new machine from scratch was not within the scope of this thesis, but developing control systems for existing machines was, while keeping in mind their compatibility with existing AM equipment architectures. In other words, step 0 in the development cycle was only partially followed.

Upon study of the system, the scope was further reduced to the build step as visualized in Figure 1.4. Although the post-processing steps can have a significant impact on the final product [2, 7, 50], the focus was on the actual AM build process as internal defects that materialize during the build step are likely to turn out uncorrectable afterwards. The control objectives are formulated as avoiding such defects altogether and maximizing product quality. However, the desired performance is not specified so straightforwardly, as quality is the culmination of each and every subprocess. Nevertheless, the following performance targets are specified for each subprocess in the build step.

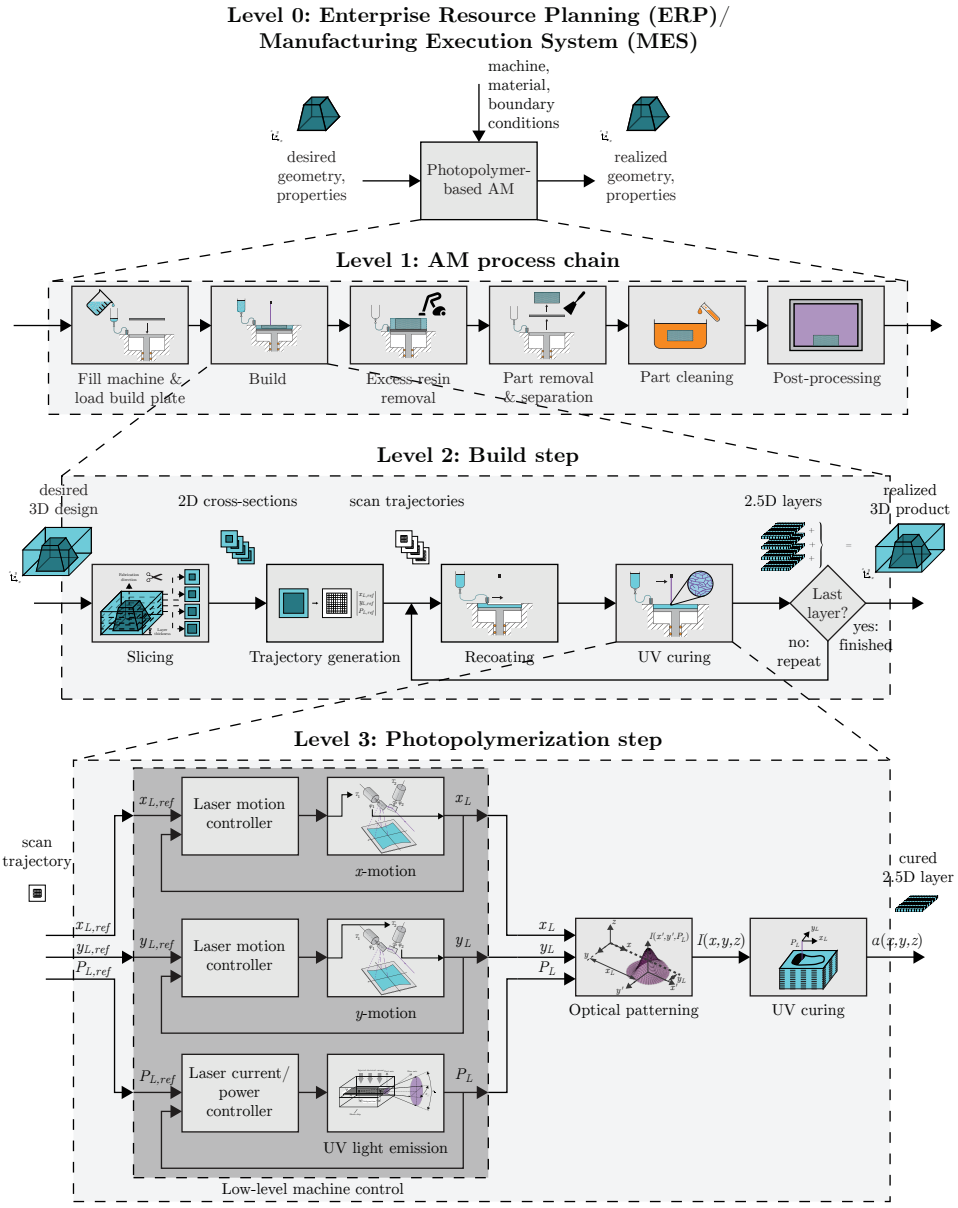

Figure 1.4: System hierarchy that illustrates the photopolymer-based AM control problem and the current state of the art in the field.

Firstly, slicing the input geometry should have minimal impact on final product quality, despite the discretization errors common to all layer-based AM processes [2]. Secondly, generating the process trajectories should be done according to a proper build strategy and storing them in the numerical control program should not introduce significant errors, despite the limited resolution of digital masks and scan trajectories [50]. Thirdly, recoating should produce an evenly spread layer of desired thickness, despite abrupt changes in resin flow regimes while traversing the build area [51]. Finally, UV curing should produce a sufficiently and homogeneously cured layer, despite the physically imposed UV light attenuation with layer depth.

If these performance targets can be met consistently and repeatedly, final product quality may be obtained on the *full product scale* through the build-up of many "2.5D" layers. To this end, the desired properties on the *individual layer scale* should follow from the translation of *layer* properties to *product* properties through processing-structure-property relationships [2]. Once these relationships have been established, final product quality may be obtained through tight control of individual-layer fabrication. Therefore, the main hypothesis of this thesis is that both recoating and UV curing may benefit from closed-loop control on the individual-layer scale as opposed to present-day open-loop control. Although both process steps are addressed in this thesis, the focus is primarily on UV curing. Note that a few specific machine functions are already controlled in closed loop, as seen in the bottom of Figure 1.4. The hypothesis is that performance can be gained by controlling the actual *process outputs* in closed loop rather than the *process inputs* alone.

1.5 Research objectives and contributions

Having outlined the AM control problem at hand, the main research objective of this thesis is defined as follows.

Main objective: *Investigate closed-loop control system architectures for photopolymer-based AM and assess their potential to improve final product quality.*

To this end, a mechatronic systems engineering approach is followed for both the recoating and the photopolymerization step. This approach generally entails investigating process modelling, sensing, actuation, and control for both major process steps. Specifically, the following research objectives are derived from the main objective.

(i) Formulate a hierarchical classification scheme for AM control strategies that allows for the positioning of control system development efforts in the AM research field. (Chapter 2)

(ii) Analyze trade-offs between recoating methods to aid the system designer in selecting a suitable recoating method in line with control system design considerations. (Chapter 3)

(iii) Identify potential in-situ real-time control schemes for photopolymerization and analyze their feasibility. (Chapter 4)

(iv) Demonstrate the feasibility of in-situ real-time feedback control of photopolymer conversion through proof-of-principle experiments. (Chapter 5)

(v) Develop and realize a measuring instrument for the degree of photopolymer conversion for future implementation into AM machines. (Chapter 6)

Each chapter in this thesis contributes to these research objectives, is self-contained, and is based on either a journal article or a conference paper (except for Chapter 6) as indicated below.

Chapter 2 proposes an AM control classification scheme titled "The AM V-model", which is based on existing hierarchical control schemes and specific examples from AM literature in its broad sense. This classification scheme is inspired by the well-known systems engineering V-model, where the verification and validation between the two legs of the V represent closed-loop AM control strategies. The proposed scheme constitutes a spatial and temporal decomposition into seven hierarchical levels and is applicable to both recoating and photopolymerization. Chapter 2 is based on:

> T. Hafkamp, G. van Baars, B. de Jager, and P. Etman, "A Classification Scheme for AM Control Strategies: the AM V-model," in *Proceedings of the 2018 ASPE and euspen Summer Topical Meeting - Advancing Precision in Additive Manufacturing*, vol. 69, pp. 161–166, 2018 [52].

Chapter 3 conducts a trade-off study between a multitude of recoating methods in VP by comparing their adherence to several process requirements and design considerations from a control systems perspective. The chapter provides a comprehensive overview of existing actuation methods, sensing methods, and control strategies for recoating. The actuation methods are compared with each other in terms of their characteristics and capabilities. Chapter 3 is based on:

> T. Hafkamp, G. van Baars, B. de Jager, and P. Etman, "A Trade-off Analysis of Recoating Methods for Vat Photopolymerization of Ceramics," in *Proceedings Solid Freeform Fabrication Symposium*, pp. 687–711, 2017 [53].

Chapter 4 provides a thorough literature review of the state of the art in process modelling, sensing, actuation, and control in the context of photopolymerization. The chapter presents the process models in terms of the physical

phenomena that manifest themselves during UV curing and discusses the potential use of these models for control applications. Several actuation methods are identified to provide the UV light field that is required to initiate this curing reaction. Similarly, monitoring and characterization techniques are evaluated for potential applicability as in-line metrology. The chapter finally reviews the only three feedback control strategies that were published at the time, and evaluates the feasibility of novel in-situ real-time control strategies by comparing actuator response times, sensor sampling times, and physical time scales. Chapter 4 is based on:

> T. Hafkamp, G. van Baars, B. de Jager, and P. Etman, "A feasibility study on process monitoring and control in vat photopolymerization of ceramics," *Mechatronics*, vol. 56, pp. 220–241, Dec. 2018 [54].

Chapter 5 takes a first step towards experimentally demonstrating the feasibility previously established in Chapter 4. To this end, an experimental setup is developed that is based on an existing spectroscopic measuring instrument. The instrument is used to acquire in-situ measurement data of the degree of cure, compare the data with the desired process trajectory, and compute a corrective action for a UV-LED-based light source by means of a proportional-integral feedback controller. The chapter describes how this measurement data is used to develop a control-oriented process model and identify its parameters. Moreover, it describes the design of proof-of-principle experiments in order to show the benefits of feedback control by comparing open- and closed-loop controlled cases in the presence of material perturbations. Chapter 5 is based on:

> T. Hafkamp, G. van Baars, B. de Jager, and P. Etman, "Real-time feedback controlled conversion in vat photopolymerization of ceramics: A proof of principle," *Additive Manufacturing*, vol. 30, 100775, 2019 [55].

Chapter 6 takes a second step towards future AM machine implementation by developing a novel measuring instrument for the degree of conversion. The measuring instrument uses an optical measuring principle derived from the instrument used in Chapter 5, but operates in a different wavelength range. This chapter discusses the requirements and design considerations that have led to the final instrument design and demonstrates the realized instrument's use as an in-situ photopolymer characterization device.

Chapter 7 finally provides a discussion on the collective results of the preceding contributory chapters, draws conclusions regarding the central problem statement of the thesis, and provides directions for future research.

1.6 Overview of the thesis

Figure 1.5 provides a graphical overview of the present thesis and puts the individual chapters in their respective mechatronic research contexts. The figure indicates the focus of each chapter in terms of process modelling, sensing, actuation, and control, for both recoating and photopolymerization.

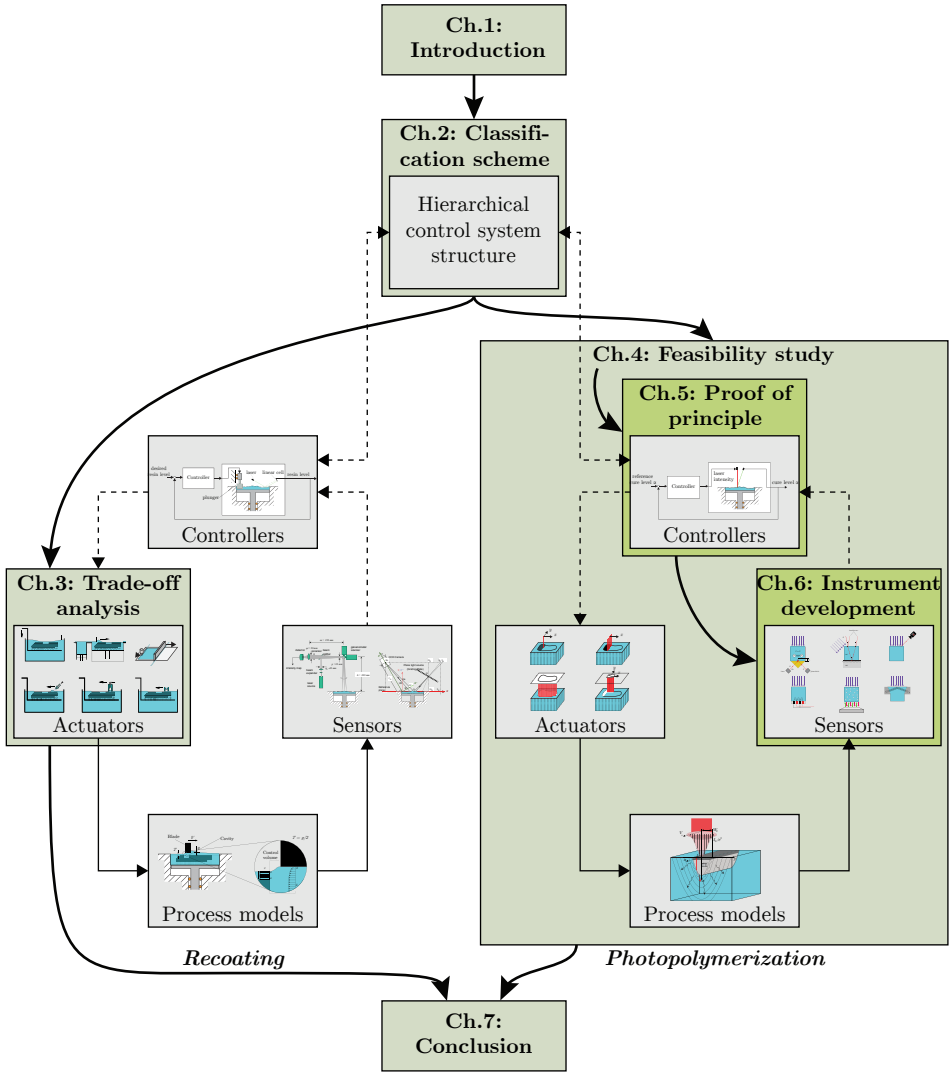

Figure 1.5: Graphical overview of the present thesis that puts the chapters in their respective mechatronic contexts.

References

[1] E. Oztemel and S. Gursev, "Literature review of Industry 4.0 and related technologies," *Journal of Intelligent Manufacturing*, vol. 31, pp. 127–182, Jan. 2020.

[2] I. Gibson, D. Rosen, and B. Stucker, *Additive Manufacturing Technologies*. New York, NY: Springer, 2nd ed., 2015.

[3] L. S. Dalenogare, G. B. Benitez, N. F. Ayala, and A. G. Frank, "The expected contribution of Industry 4.0 technologies for industrial performance," *International Journal of Production Economics*, vol. 204, pp. 383–394, Oct. 2018.

[4] P. Jacobs, *Rapid Prototyping & Manufacturing: Fundamentals of Stereolithography*. Dearborn, MI: Society of Manufacturing Engineers, 1992.

[5] C. K. Chua, C. H. Wong, and W. Y. Yeong, *Standards, quality control, and measurement sciences in 3D printing and additive manufacturing*. London; San Diego, CA: Academic Press, an imprint of Elsevier, 2017.

[6] W. Gao, Y. Zhang, D. Ramanujan, K. Ramani, Y. Chen, C. B. Williams, C. C. Wang, Y. C. Shin, S. Zhang, and P. D. Zavattieri, "The status, challenges, and future of additive manufacturing in engineering," *Computer-Aided Design*, vol. 69, pp. 65–89, Dec. 2015.

[7] P. J. Bartolo, ed., *Stereolithography*. New York, NY: Springer US, 1st ed., 2011.

[8] C. W. Hull, "Apparatus for production of three-dimensional objects by stereolithography," Mar. 1986. US4575330.

[9] The Henry Ford Museum, "First Commercially Successful Stereolithography Machine, Model SLA-1, 1987." Accessed on: May 19, 2020. [Online]. Available: https://www.thehenryford.org/collections-and-research/digital-collections/artifact/242212/.

[10] D. Hardt, "Modeling and control of manufacturing processes: Getting more involved," *Journal of Dynamic Systems, Measurement, and Control*, vol. 115, pp. 291–300, June 1993.

[11] C. B. Williams, F. Mistree, and D. W. Rosen, "A functional classification framework for the conceptual design of additive manufacturing technologies," *Journal of Mechanical Design*, vol. 133, no. 12, p. 121002, 2011.

[12] J. Zhang and Y.-G. Jung, *Additive Manufacturing: Materials, Processes, Quantifications and Applications*. Butterworth-Heinemann, May 2018.

[13] S. Sōmiya, ed., *Handbook of advanced ceramics: materials, applications, processing, and properties*. Amsterdam; Boston: Academic Press, imprint of Elsevier, 2nd ed., 2013.

[14] T. Baldacchini, ed., *Three-dimensional microfabrication using two-photon polymerization: fundamentals, technology, and applications*. Micro & nano technologies series, Amsterdam; Boston: Elsevier/William Andrew, 2016.

[15] P. Witherell, Y. Lu, and A. Jones, "Additive Manufacturing: A Transdisciplinary Experience," in *Transdisciplinary Perspectives on Complex Systems* (F.-J. Kahlen, S. Flumerfelt, and A. Alves, eds.), pp. 145–175, Springer International Publishing, 2017.

[16] A. Kossiakoff, ed., *Systems engineering: principles and practice*. No. 67 in Wiley series in systems engineering and management, Hoboken, N.J: Wiley-Interscience, 2nd ed., 2011.

[17] K. Barton, D. Bristow, D. Hoelzle, and S. Mishra, "Mechatronics advances for the next generation of AM process control," *Mechatronics*, vol. 64, p. 102281, Dec. 2019.

[18] J. R. Tumbleston, D. Shirvanyants, N. Ermoshkin, R. Janusziewicz, A. R. Johnson, D. Kelly, K. Chen, R. Pinschmidt, J. P. Rolland, A. Ermoshkin, E. T. Samulski, and J. M. DeSimone, "Continuous liquid interface production of 3D objects," *Science*, vol. 347, pp. 1349–1352, Mar. 2015.

[19] D. A. Walker, J. L. Hedrick, and C. A. Mirkin, "Rapid, large-volume, thermally controlled 3D printing using a mobile liquid interface," *Science*, vol. 366, pp. 360–364, Oct. 2019.

[20] B. E. Kelly, I. Bhattacharya, H. Heidari, M. Shusteff, C. M. Spadaccini, and H. K. Taylor, "Volumetric additive manufacturing via tomographic reconstruction," *Science*, vol. 363, pp. 1075–1079, Mar. 2019.

[21] D. Loterie, P. Delrot, and C. Moser, "High-resolution tomographic volumetric additive manufacturing," *Nature Communications*, vol. 11, pp. 1–6, Feb. 2020.

[22] R. H. Chenhall, "Reliance on manufacturing performance measures, total quality management and organizational performance," *Management Accounting Research*, vol. 8, pp. 187–206, June 1997.

[23] Y. Huang, M. C. Leu, J. Mazumder, and A. Donmez, "Additive manufacturing: Current state, future potential, gaps and needs, and recommendations," *Journal of Manufacturing Science and Engineering*, vol. 137, no. 1, p. 014001, 2015.

[24] D. Fornea and H. Van Laere, "Living tomorrow. 3D printing — a tool to empower the European economy. Opinion of the European Economic and

Social Committee CCMI/131," *Official Journal of the European Union*, pp. C 332/36 – C 332/44, Oct. 2015. 2015/C 332/05.

[25] S. Westbeek, J. A. W. van Dommelen, J. J. C. Remmers, and M. G. D. Geers, "Multiphysical modeling of the photopolymerization process for additive manufacturing of ceramics," *European Journal of Mechanics - A/Solids*, vol. 71, pp. 210–223, Sept. 2018.

[26] A. Kozhevnikov, R. P. Kunnen, G. E. van Baars, and H. J. Clercx, "Investigation of the fluid flow during the recoating process in additive manufacturing," *Rapid Prototyping Journal*, vol. ahead-of-print, Jan. 2019.

[27] T. Verdonschot, *Development of the machine control architecture for an additive manufacturing system: improvement of the Lepus Next Gen for the AMSYSTEMS Center*. PDEng thesis, Eindhoven University of Technology, Eindhoven, Oct. 2018.

[28] R. Smits, *Integrated sensing for additive manufacturing of ceramic components*. PDEng thesis, Eindhoven University of Technology, Eindhoven, Mar. 2019.

[29] J. Senden, *Design of a recoater concept for additive manufacturing of ceramics*. PDEng thesis, Eindhoven University of Technology, Eindhoven, Oct. 2018.

[30] M. Cotteleer, S. Trouton, and E. Dobner, "3D opportunity and the digital thread: Additive manufacturing ties it all together," tech. rep., Deloitte University Press, Westlake, TX, 2016.

[31] A. R. Nassar and E. W. Reutzel, "A Proposed Digital Thread for Additive Manufacturing," in *Solid Freeform Fabrication Symposium Proceedings*, pp. 19–43, 2015.

[32] D. B. Kim, P. Witherell, R. Lipman, and S. C. Feng, "Streamlining the additive manufacturing digital spectrum: A systems approach," *Additive Manufacturing*, vol. 5, pp. 20–30, Jan. 2015.

[33] D. Mies, W. Marsden, and S. Warde, "Overview of Additive Manufacturing Informatics: "A Digital Thread"," *Integrating Materials and Manufacturing Innovation*, vol. 5, Dec. 2016.

[34] R. Isermann, *Mechatronic systems: fundamentals*. London: Springer, 2005.

[35] D. E. Seborg, T. F. Edgar, D. A. Mellichamp, and F. Doyle, *Process dynamics and control*. Hoboken, N.J: John Wiley & Sons, Inc, 3rd ed., 2011.

[36] I. Harjunkoski, "Integration of Scheduling and ISA-95," in *Computer Aided Chemical Engineering* (J. J. Klemeš, P. S. Varbanov, and P. Y. Liew, eds.), vol. 33 of *24 European Symposium on Computer Aided Process Engineering*, pp. 427–432, Elsevier, Jan. 2014.

[37] M. Adnan, Y. Lu, A. W. Jones, and F. T. Cheng, "Application of the Fog Computing Paradigm to Additive Manufacturing Process Monitoring and Control," in *Proceedings of the 30th Annual International Solid Freeform Fabrication Symposium*, Aug. 2019.

[38] M. Mani, B. Lane, A. Donmez, S. Feng, S. Moylan, and R. Fesperman, "Measurement Science Needs for Real-time Control of Additive Manufacturing Powder Bed Fusion Processes," Tech. Rep. NIST IR 8036, National Institute of Standards and Technology, Feb. 2015.

[39] E. W. Reutzel and A. R. Nassar, "A survey of sensing and control systems for machine and process monitoring of directed-energy, metal-based additive manufacturing," *Rapid Prototyping Journal*, vol. 21, no. 2, pp. 159–167, 2015.

[40] T. G. Spears and S. A. Gold, "In-process sensing in selective laser melting (SLM) additive manufacturing," *Integrating Materials and Manufacturing Innovation*, vol. 5, pp. 1–25, Dec. 2016.

[41] G. Tapia and A. Elwany, "A review on process monitoring and control in metal-based additive manufacturing," *Journal of Manufacturing Science and Engineering*, vol. 136, no. 6, pp. 060801–1 – 060801–10, 2014.

[42] P. Charalampous, I. Kostavelis, and D. Tzovaras, "Non-destructive quality control methods in additive manufacturing: a survey," *Rapid Prototyping Journal*, vol. 26, pp. 777–790, Mar. 2020.

[43] T. Huang, S. Wang, and K. He, "Quality control for fused deposition modeling based additive manufacturing: Current research and future trends," in *2015 First International Conference on Reliability Systems Engineering (ICRSE)*, pp. 1–6, Oct. 2015.

[44] F. J. Mercado Rivera and A. J. Rojas Arciniegas, "Additive manufacturing methods: techniques, materials, and closed-loop control applications," *The International Journal of Advanced Manufacturing Technology*, vol. 109, pp. 17–31, July 2020.

[45] H. Lhachemi, A. Malik, and R. Shorten, "Augmented Reality, Cyber-Physical Systems, and Feedback Control for Additive Manufacturing: A Review," *IEEE Access*, vol. 7, pp. 50119–50135, 2019.

[46] H. Kim, Y. Lin, and T.-L. B. Tseng, "A review on quality control in additive manufacturing," *Rapid Prototyping Journal*, vol. 24, pp. 645–669, Mar. 2018.

[47] S. Skogestad and I. Postlethwaite, *Multivariable Feedback Control: Analysis and design*. New York: Wiley, 2nd ed., 2005.

[48] B. A. Ogunnaike and W. H. Ray, *Process dynamics, modeling, and control*. Topics in chemical engineering, New York: Oxford University Press, 1994.

[49] M. van de Wal and B. de Jager, "A review of methods for input/output selection," *Automatica*, vol. 37, no. 4, pp. 487–510, 2001.

[50] D. B. Pedersen, S. A. Andersen, and H. N. Hansen, "Measurements in Additive Manufacturing," in *Metrology* (W. Gao, ed.), Precision Manufacturing, pp. 369–397, Singapore: Springer, 2019.

[51] K. Renap and J. Kruth, "Recoating issues in stereolithography," *Rapid Prototyping Journal*, vol. 1, pp. 4–16, Sept. 1995.

[52] T. Hafkamp, G. van Baars, B. de Jager, and P. Etman, "A Classification Scheme for AM Control Strategies: the AM V-model," in *Proceedings of the 2018 ASPE and euspen Summer Topical Meeting - Advancing Precision in Additive Manufacturing*, vol. 69, pp. 161–166, 2018.

[53] T. Hafkamp, G. van Baars, B. de Jager, and P. Etman, "A Trade-off Analysis of Recoating Methods for Vat Photopolymerization of Ceramics," in *Proceedings Solid Freeform Fabrication Symposium*, pp. 687–711, 2017.

[54] T. Hafkamp, G. van Baars, B. de Jager, and P. Etman, "A feasibility study on process monitoring and control in vat photopolymerization of ceramics," *Mechatronics*, vol. 56, pp. 220–241, Dec. 2018.

[55] T. Hafkamp, G. van Baars, B. de Jager, and P. Etman, "Real-time feedback controlled conversion in vat photopolymerization of ceramics: A proof of principle," *Additive Manufacturing*, vol. 30, p. 100775, 2019.

Chapter 2

A classification scheme for AM control strategies: the AM V-model

Abstract
Closed-loop control on the machine level already plays a key role in the industrialization of Additive Manufacturing (AM) technology, but further robustification of product quality calls for closed-loop control on higher levels. This paper facilitates the identification of such higher-level control strategies by presenting a hierarchical classification scheme for AM control strategies. The proposed "AM V-model" scheme decomposes the AM process along the spatial and temporal dimension in analogy to the systems engineering V-model. The scheme defines seven hierarchical control levels analogous to verification and validation in the classical V-model and is based on existing hierarchical control schemes and AM literature examples.

This chapter has been published in *Proceedings of the 2018 ASPE and euspen Summer Topical Meeting - Advancing Precision in Additive Manufacturing*, vol. 69, pp. 161–166, 2018.

2.1 Introduction

The current lack of consistent additive manufacturing (AM) part quality gives rise to the development of novel process monitoring and control strategies [1]. The identification of these strategies can be facilitated by formulating a classification scheme to position development efforts. This work proposes a classification scheme that was developed in the context of vat photopolymerization [2], but is expected to be applicable to a wide range of AM technologies since many commonalities exist in the multi-level control characteristics.

2.2 Existing classification schemes

General control system hierarchies for mechatronic systems [3] and the process industry [4] can be found in literature. Specific classification schemes for AM control strategies can be found in literature as well; most notable are the NIST control organizational structure for metal-based AM [5], the Zero Defects for Additive Manufacturing (ZeDAM) quality control strategy architecture [6] and a hierarchical control method framework for an Exposure Controlled Projection Lithography (ECPL) process [7]. Inspired by these existing schemes and based on examples from literature, a more elaborate classification scheme for AM control strategies is proposed in this work.

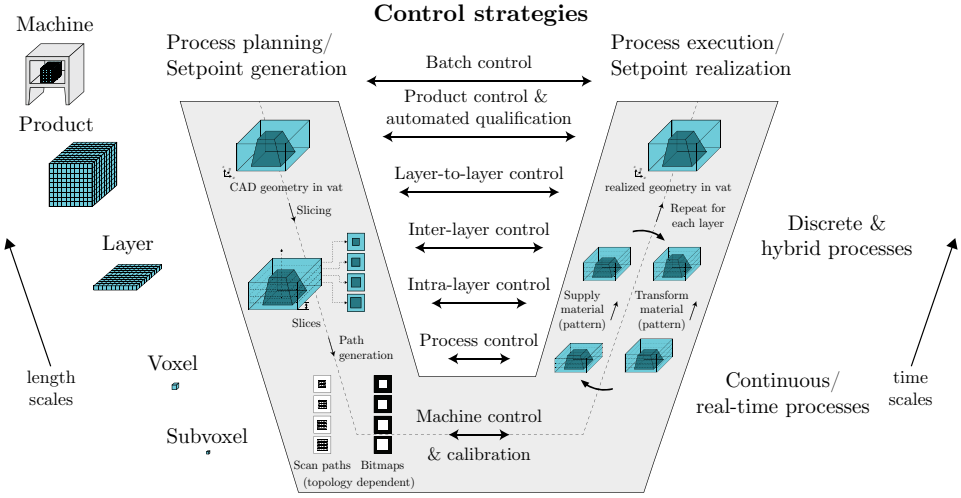

Figure 2.1: The AM V-model hierarchy.

2.3 Proposed scheme: the AM V-model

The planning and realization of a 3D product through an additive manufacturing process can be viewed of as analogous to the following of a V-model, which is a well-known graphical representation of the systems engineering process [8]. Figure 1 shows such a V-model with the type of control strategy indicated in the middle of the V, where the verification and validation arrows are commonly drawn. The left leg of the V concerns process planning or setpoint generation, where a spatial decomposition is made from product geometry via layers into voxels, the elementary building block of the product. The right leg of the V concerns process execution, where the product is built up, usually layer-by-layer, through the patterned supply and transformation of material.

A decomposition of the AM process can be made across both the spatial axis and the time axis as indicated on the left and right sides of the V respectively. Process planning — the complete left leg of the V — can be considered a control strategy in itself. Control strategies for process execution — the complete right leg — can be conceived at each level in the V. Seven such categories can be identified from low- to high-level control: machine control & calibration, process control, intra-layer control, layer control, layer-to-layer control, product control & qualification, and batch control.

2.4 Control strategy categories

2.4.1 Process planning

Process planning in AM primarily consists of placing and orienting the part in the build volume, generating supports, slicing, and path planning [9]. From a control system's perspective, process planning is the offline procedure of generating the reference trajectories or setpoints, or in other words determining the build process parameters and inputs. It can be considered a form of open-loop control, including the generation of feedforward inputs, and is complementary to closed-loop feedback control.

Traditionally the determination of optimal process parameters would proceed via expensive time-consuming trial and error iterations on the actual machine, whereas currently there is a shift towards input parameter optimization through build simulation using high-fidelity physics-based process models [5]. Structural topology design optimization [10] with manufacturability constraints or design for AM can also be noted here. Regardless of the manner obtained, the final result of the process planning procedure is a set of machine instructions stored in a build plan. Figure 2.2 shows the generation of machine instructions from product geometry

during process planning.

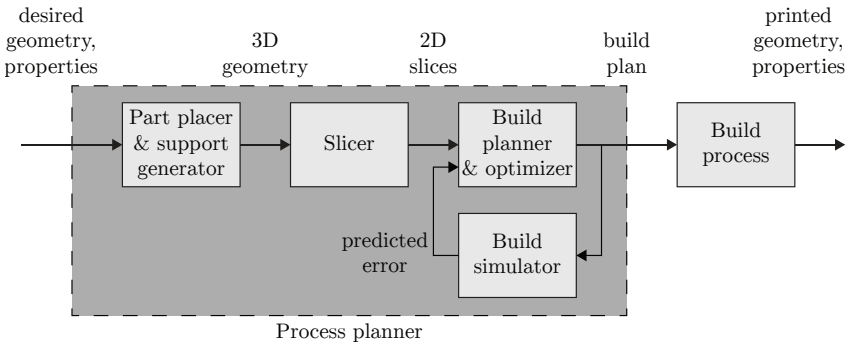

Figure 2.2: Process planning scheme.

Examples of process planning for vat photopolymerization include laser scan trajectory generation, bitmap greyscaling for improved xy- or z-resolution, and inverse geometry compensation for deformations arising during the build.

2.4.2 Machine control & calibration

Low-level *machine control* systems have always been an essential part of any AM machine, since these systems provide basic functionality such as motion control or process parameter control. Machine control systems focus on individual machine functions, which are independent of the process details such as product geometry and material. The goal of these systems is to provide desired process parameter (input) trajectories and to pursue practically constant boundary conditions. Hereby they only *indirectly* influence the actual manufacturing process [11], which consists of a complex coupled material property and geometry transformation.

An example of machine control is motion control for patterning the *supply* of material, patterning the *transformation* of material as shown in Figure 2.3, or elevating the build platform. Positioning errors, owing to the precision and accuracy of the motion stages and scanners, will lead to geometric variations in the part. However, disturbances to these process-independent machine state variables are generally considered small compared to other process variables that do directly affect the quality of the output [12]. Another example is build chamber environment control, which includes temperature, oxygen concentration and pressure control at several locations throughout the machine. Monitoring and control of these machine state variables is typically performed by logging at low sampling frequencies and by warning indicators or independent SISO control loops [13].

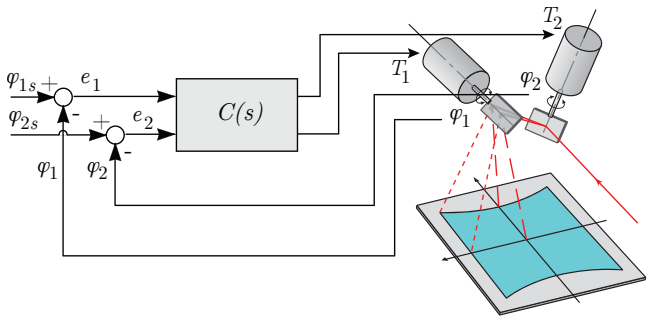

Figure 2.3: Machine control example.

Calibration

A different aspect that can also be gathered under machine control is *calibration* and subsequent adjustment or drift correction. Calibration is the act of comparing measurement values of unknown accuracy to a measurement standard of known accuracy. In AM this means that both the material supply and transformation systems can be calibrated with respect to a calibration standard. For instance, the position of the laser scanning system can be calibrated to a reference plate placed over the build platform [14] or to fiducial markers additionally printed in each layer.

2.4.3 Process control

Contrary to the indirect machine control techniques, *process control* techniques deal directly with the actual manufacturing process, i.e., the production of a desired object through a material transformation process [11]. In AM, this material transformation process is the geometry transformation from feedstock to strands or layers in the recoating process and the material property transformation from, e.g., the liquid to the solid phase in the vat photopolymerization process.

The main idea behind process control strategies is that voxel-level control of material properties [15] can be obtained by real-time, in-situ continuous control [5] of the *material transformation process*. For metal-based processes, examples of process controllers exist in which the temperature or area of the melt pool is controlled [16, 17], see Figure 2.4. For vat photopolymerization this would imply controlling the polymerization reaction [2].

The *geometry transformation process* from feedstock to a layer, i.e., the recoating process, can also be controlled. However, it is arguable whether this is *machine control* or *process control*, since in some AM technologies such as selective laser sintering (SLS) and vat photopolymerization the *requirement* for the quality deposition [13] of a flat layer is independent of the desired part geometry, even though the

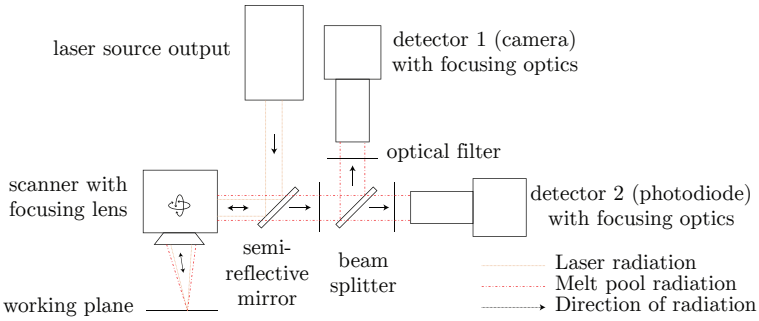

Figure 2.4: Process control example [16].

recoating process dynamics can be product-dependent. In other words, the material deposition is not patterned in SLS whereas it is patterned in, e.g., Fused Deposition Modeling (FDM). In any case, the feed rate of feedstock material can be controlled to ensure a well-defined amount of material at the correct location.

2.4.4 Intra-layer control

Intra-layer control refers to control strategies that take place on the time scale of the processing of a single layer. The idea is to use feedback from the foregoing to improve the process settings for the remainder of the layer. Examples of hypothetical inter-layer control schemes include measuring in the slipstream of the recoater and the scan track behind the laser respectively. These types of control strategies may run at lower control bandwidths than process control strategies and due to their non-colocated nature may lend themselves well to observer-based control schemes that infer the state of the process dynamics at e.g. the laser location from non-colocated measurements. An example of an existing intra-layer control scheme is intra-layer build plan modification of the ordering and timing of hatches [18], see Figure 2.5.

2.4.5 Inter-layer control

The goal of *inter-layer control* schemes is to guarantee - by means of feedback control - the quality of each layer after the layer formation step has been completed. These types of schemes do not operate at the frequencies or time scales of the low-level *continuous* or real-time processes such as machine and process control, but can be rather considered *discrete* or hybrid events. Hence, these schemes are of a supervisory control nature and can be designated as in-situ fault detection and handling controllers [5] that trigger discrete events by interrupting normal control routines and performing a corrective action if necessary.

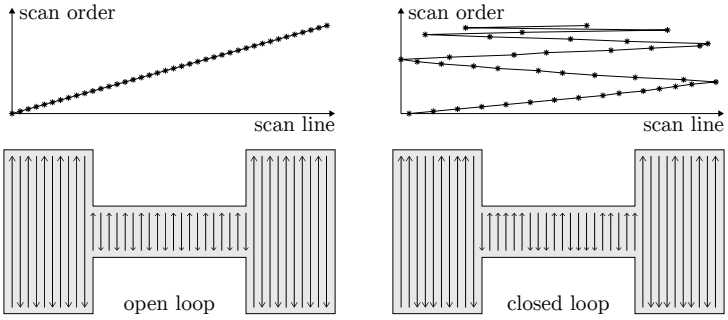

Figure 2.5: Intra-layer control example [18].

Examples of inter-layer control schemes include corrective resweeping in vat photopolymerization [19] depicted in Figure 2.6 or respreading in powder-based systems [17]. The machine state variables such as the chamber environment controlled by machine controllers can also be monitored and controlled by a higher supervisory control scheme that interrupts the process if these variables assume unacceptable values [5].

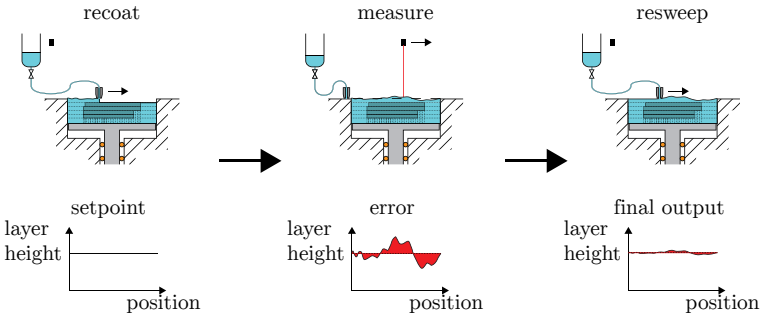

Figure 2.6: Inter-layer control example.

2.4.6 Layer-to-layer control

Layer-to-layer control schemes aim to use information from the current layer N and preceding layers to find better settings for the next layer $N + 1$ as depicted in Figure 2.7. Specifically, these schemes can leverage that subsequent layers are highly similar, i.e., changes from one layer to another are typically gradual. Moreover, if discontinuous changes from layer to layer occur, *a priori* knowledge hereof could be exploited.

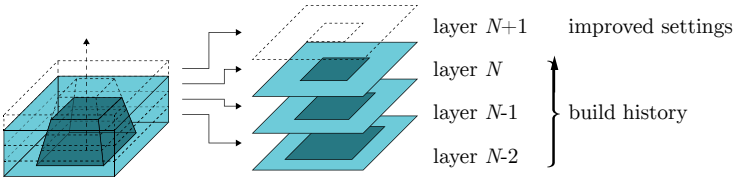

Figure 2.7: Layer-to-layer control.

The formation of a layer can be considered a discrete process where the process inputs - typically depending on the slice cross-section - can be modified ex situ, i.e., in between the formation of each layer. Hence layer-to-layer control can be considered similar to run-to-run control, batch-to-batch control or cycle-to-cycle control [7]. Repetitive and iterative learning control strategies may be applicable since the tasks are repetitive and disturbances are position dependent.

Example layer-to-layer control schemes for ink-jet 3D printing include a model-based feedback control law [20] and an iterative learning control law [21] that use a layer height profile measurement from the last layer to determine the droplet deposition pattern for the following layers. Another example is a layer-to-layer height and temperature controller for laser metal deposition [22].

2.4.7 Product control & automated qualification

The next level of control after layer-to-layer control is *product control*, which is concerned with the control of macroscopic product specifications or properties. The goal of these control strategies is to get the global product properties right and they act on a time scale similar to layer-to-layer controllers where it is still possible to adjust the process before the product is finished. The ultimate controller on the product level would be capable of *automated part qualification* [5] through process monitoring and analysis of product qualities such as dimensional accuracy and material properties.

An apparent example of product control is geometric feedback control, which closes the loop on the overall part geometry level [23]. Another example is closed-loop control of the effective stiffness of a cantilever beam [24]. Future advanced product control schemes would benefit from the tight integration of feedback control with the same multi-physics/finite element simulations and topology optimizations that were used to initially create the build plan [25]. Real-time corrections could be made to machine instructions to meet product specifications [25, 26] as depicted in Figure 2.8. Note that Figure 2.8 is the same as Figure 2.2, but with an additional feedback signal from the build process outputs that represents the digital twin [26] to the build simulator and hence (indirectly) to the build planner & optimizer.

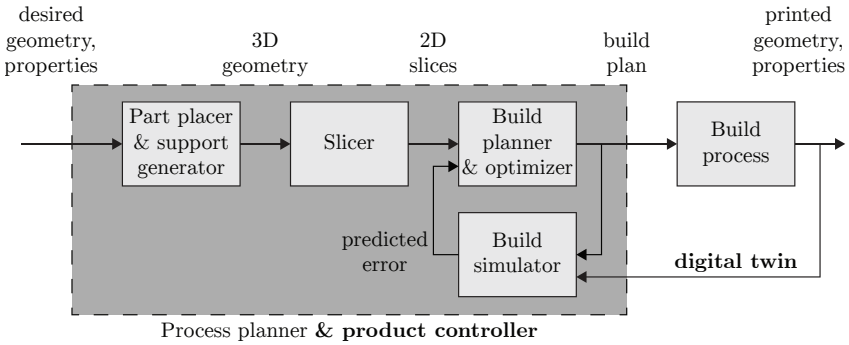

Figure 2.8: Product control scheme.

2.4.8 Batch control

Batch control schemes refer to individual-product-exceeding strategies that apply to the complete build job or batch. It is fairly commonplace in industry to print test specimens such as standardized dog bones oriented in different directions alongside each build to ensure proper material properties of that batch. The printing of additional structures to calibrate the printing process during the build rather than for post-build verification can also be mentioned here.

Batch control typically takes place through *offline* and *ex situ* measurements of printed objects. Non-destructive testing (NDT) and evaluation (NDE) methods are a critical part of quality control and inspection for AM [27]. A straightforward example is dimensional verification through optical or X-ray computed tomography [27]. Feedback loops can be conceived that modify the process inputs between build batches based on pre- and post-process data obtained through aforementioned NDT metrology. One can also envision a (machine) *learning* system that uses long-term learning from errors occurring during the build process to prevent future occurrance [6]. Manufacturability feedback loops [28] fall under the same category, since feeding back information of process (in-)capabilities to the design process can increase the number of successful builds. The digital thread for AM [26] may play a crucial enabling role in this.

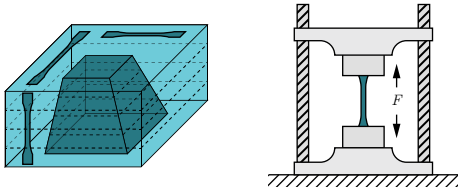

Figure 2.9: Batch control by testing specimens.

2.5 Combining multiple control levels

The foregoing sections describe classes of separate control schemes that can be placed in the respective levels of the control V-model. However, it is thinkable that future AM machines incorporate a multi-level control architecture that combines control strategies from one or more of these levels. Such a hierarchy could be borrowed from the machining industry [29], where machine, process and product controllers are already combined, see Figure 2.10.

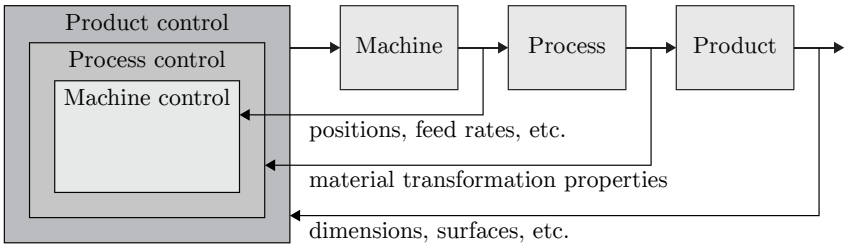

Figure 2.10: Multi-level control hierarchy.

One way to combine multiple controllers, would be to cascade them in series [6]. The main idea behind cascade control is that disturbances can be rejected by a secondary loop before the primary controlled variable deviates from the setpoint [4]. In the case of AM, if overall product quality is the controlled variable, it seems sensible to use cascade control to reject disturbances on the voxel or layer scale.

References

[1] Y. Huang, M. C. Leu, J. Mazumder, and A. Donmez, "Additive manufacturing: Current state, future potential, gaps and needs, and recommendations," *Journal of Manufacturing Science and Engineering*, vol. 137, no. 1, p. 014001, 2015.

[2] T. Hafkamp, G. van Baars, B. de Jager, and P. Etman, "A feasibility study on process monitoring and control in vat photopolymerization of ceramics," *Mechatronics*, 2018. 10.1016/j.mechatronics.2018.02.006.

[3] R. Isermann, *Mechatronic systems: fundamentals*. London: Springer, 2005.

[4] D. E. Seborg, T. F. Edgar, D. A. Mellichamp, and F. Doyle, *Process dynamics and control*. Hoboken, N.J: John Wiley & Sons, Inc, 3rd ed., 2011.

[5] M. L. Vlasea, B. Lane, F. Lopez, S. Mekhontsev, and A. Donmez, "Development of powder bed fusion additive manufacturing test bed for enhanced real-time process control," in *Proceedings Solid Freeform Fabrication Symposium*, pp. 527–539, 2015.

[6] M. Faes, W. Abbeloos, F. Vogeler, H. Valkenaers, K. Coppens, E. Ferraris, and others, "Process Monitoring of Extrusion Based 3d Printing via Laser Scanning," in *PMI 2014 Conference Proceedings*, vol. 6, pp. 363–367, 2014.

[7] X. Zhao, *Process Measurement and Control for Exposure Controlled Projection Lithography*. Phd thesis, Georgia Institute of Technology, 2017.

[8] A. Kossiakoff, ed., *Systems engineering: principles and practice*. Hoboken, N.J: Wiley-Interscience, 2nd ed., 2011.

[9] P. Kulkarni, A. Marsan, and D. Dutta, "A review of process planning techniques in layered manufacturing," *Rapid Prototyping Journal*, vol. 6, pp. 18–35, Mar. 2000.

[10] J. Liu, A. T. Gaynor, S. Chen, Z. Kang, K. Suresh, A. Takezawa, L. Li, J. Kato, J. Tang, C. C. L. Wang, L. Cheng, X. Liang, and A. C. To, "Current and future trends in topology optimization for additive manufacturing," *Structural and Multidisciplinary Optimization*, vol. 57, pp. 2457–2483, June 2018.

[11] D. Hardt, "Modeling and control of manufacturing processes: Getting more involved," *Journal of Dynamic Systems, Measurement, and Control*, vol. 115, pp. 291–300, June 1993.

[12] T. G. Spears and S. A. Gold, "In-process sensing in selective laser melting (SLM) additive manufacturing," *Integrating Materials and Manufacturing Innovation*, vol. 5, pp. 1–25, Dec. 2016.

[13] E. W. Reutzel and A. R. Nassar, "A survey of sensing and control systems for machine and process monitoring of directed-energy, metal-based additive manufacturing," *Rapid Prototyping Journal*, vol. 21, no. 2, pp. 159–167, 2015.

[14] P. Jacobs, *Rapid Prototyping & Manufacturing: Fundamentals of Stereolithography*. Dearborn, MI: Society of Manufacturing Engineers, 1992.

[15] J. Pellegrino, T. Makila, S. McQueen, and E. Taylor, "Measurement science roadmap for polymer-based additive manufacturing," Tech. Rep. NIST AMS 100-5, National Institute of Standards and Technology, Gaithersburg, MD, Dec. 2016.

[16] T. Craeghs, F. Bechmann, S. Berumen, and J.-P. Kruth, "Feedback control of Layerwise Laser Melting using optical sensors," *Physics Procedia*, vol. 5, pp. 505–514, 2010.

[17] M. Mani, B. Lane, A. Donmez, S. Feng, S. Moylan, and R. Fesperman, "Measurement Science Needs for Real-time Control of Additive Manufacturing Powder Bed Fusion Processes," Tech. Rep. NIST IR 8036, National Institute of Standards and Technology, Feb. 2015.

[18] A. R. Nassar, J. S. Keist, E. W. Reutzel, and T. J. Spurgeon, "Intra-layer closed-loop control of build plan during directed energy additive manufacturing of Ti–6al–4v," *Additive Manufacturing*, vol. 6, pp. 39–52, Apr. 2015.

[19] A. Yoshikawa, H. Narahara, and H. Suzuki, "Research on the uneven measurement on the liquid surface of photoresin in the stereolithography," *Journal of the Japan Society for Precision Engineering*, vol. 69, no. 10, pp. 1434–1438, 2003.

[20] L. Lu, J. Zheng, and S. Mishra, "A Layer-To-Layer Model and Feedback Control of Ink-Jet 3-D Printing," *IEEE/ASME Transactions on Mechatronics*, vol. 20, pp. 1056–1068, June 2015.

[21] D. J. Hoelzle and K. L. Barton, "On Spatial Iterative Learning Control via 2-D Convolution: Stability Analysis and Computational Efficiency," *IEEE Transactions on Control Systems Technology*, vol. 24, pp. 1504–1512, July 2016.

[22] L. Tang, *Layer-to-layer control of laser metal deposition processes*. Phd thesis, Missouri University of Science and Technology, 2009.

[23] D. Cohen and H. Lipson, "Geometric feedback control of discrete-deposition SFF systems," *Rapid Prototyping Journal*, vol. 16, no. 5, pp. 377–393, 2010.

[24] K. Garanger, "Introducing the foundations of a general framework for closed-loop control in additive manufacturing via in situ measurements and semantic annotations," Master Thesis, Georgia Institute of Technology, 2018.

[25] I. Wing, R. Gorham, and B. Sniderman, "3D opportunity for quality assurance and parts qualification.pdf," tech. rep., Deloitte University Press, Westlake, TX, 2015.

[26] M. Cotteleer, S. Trouton, and E. Dobner, "3D opportunity and the digital thread: Additive manufacturing ties it all together," tech. rep., Deloitte University Press, Westlake, TX, 2016.

[27] S. K. Everton, M. Hirsch, P. Stravroulakis, R. K. Leach, and A. T. Clare, "Review of in-situ process monitoring and in-situ metrology for metal additive manufacturing," *Materials & Design*, vol. 95, pp. 431–445, Apr. 2016.

[28] G. Ameta, S. Moylan, P. Witherell, and R. Lipman, "Challenges in tolerance transfer for additive manufacturing," in *Proceedings ASPE 2015 Spring Topical Meeting*, pp. 129–135, 2015.

[29] W. S. Levine, ed., *Control system applications*. Boca Raton: CRC Press, 2nd ed., 2011.

Chapter 3

A trade-off analysis of recoating methods for vat-photopolymerization-based ceramic manufacturing

Abstract

Technical ceramic parts can be produced by curing ceramic-filled resins in the vat photopolymerization (stereolithography) process. Scaling up to larger ceramic product sizes and higher product quality calls for the integration of more sensing, actuation and closed-loop control solutions while taking a systems engineering approach. This paper gives a comprehensive overview of methods to deposit a layer of (ceramic-filled) resin, better known as recoating. The aim of this work is to perform a trade-off analysis of recoating methods to enable the selection of the method that best meets the requirements for scaling up the printable object size in the ceramic vat photopolymerization process.

This chapter has been published in *Proceedings Solid Freeform Fabrication Symposium*, pp. 687–711, 2017.

3.1 Introduction

Additive manufacturing (AM) of ceramic parts opens up new possibilities for the high tech industry in comparison to conventional ceramic manufacturing techniques. Particularly, the ability to manufacture near-net 3D shapes in small series with high geometrical flexibility makes the industrial integration of AM into the ceramic processing chain appealing [1–3]. A predominant AM technology for producing ceramics is vat photopolymerization [4], also known as stereolithography [5, 6].

In vat photopolymerization, products are fabricated in a vat through the consecutive deposition of photopolymer resin layers and the subsequent selective irradiation according to the part's cross section. By mixing ceramic powder with the resin and adjusting the process parameters of conventional vat photopolymerization machines, AM can be used to perform the shaping step in the ceramic process chain. The resulting printed product is in the "green" state where the photopolymer acts as a binder to keep the ceramic powder together, highly similar to the state in which ceramic parts remain after injection molding [4]. The green part is then cleaned and put in an oven to pyrolyze the photopolymer in a debinding step and to finally fuse the ceramic particles together in a sintering step.

Although the accuracy of products fabricated by vat photopolymerization is among the highest of AM technologies [7], several challenges are to be solved before the technology can be adopted by the industry for the manufacturing of ceramic parts of substantial size. These challenges include increasing the density of monolithic parts, increasing printable product sizes and wall thicknesses, and avoiding crack and void formation [3], as well as the universal challenge of reducing variability in AM equipment and part quality [8, 9]. The modelling, sensing, actuation and control of the AM process are deemed key enablers to pave the road towards solving the lack of repeatable product quality [8, 10]. Viewing the ceramic 3D printer as a mechatronic system [11] illustrates the importance of each of these components, as shown in Figure 3.1.

This paper gives a comprehensive overview of methods to deposit a layer of photocurable resin, better known as recoating. The aim is to analyze trade-offs between recoating methods to enable the future selection of the recoating method that best meets the requirements for scaling up the printable object size in the ceramic vat photopolymerization process. The scope of the paper encompasses both pure photopolymer resins as well as ceramic-filled resins or slurries, since the vat photopolymerization process for ceramics is closely related to the process for pure photopolymers. Although build platform movement is considered part of the recoating step, it is hardly addressed both in literature and in this paper as it is a matter of proper engineering. Additionally, as literature on the modelling of recoating is scarce, modelling is not treated in this paper.

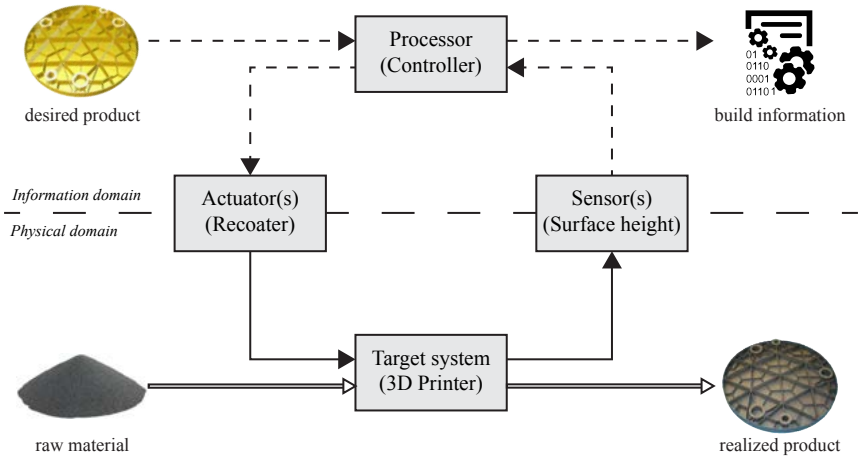

Figure 3.1: Ceramic 3D printer as a mechatronic system.

The outline of this paper is as follows. First, the requirements related to the recoating phase are outlined. Then an overview is given of recoating methods, sensing methods and control strategies respectively. Next, design considerations are discussed from a control systems perspective. Finally, the recoating methods are compared in a concluding discussion.

3.2 Requirements

The first step in trade-off analysis is to define the objective for the trade study itself by identifying the requirements the solution must fulfill [12]. Typical objectives for manufacturing processes in general are the minimization of production variations for product quality, the capability to change target geometries rapidly for flexibility, and the minimization of process times for productivity [13]. The main goal of the recoating phase specifically, is to deposit a layer of (ceramic-filled) resin. The underlying challenge is to obtain an as uniform as possible resin surface as quickly as possible [6]. In the following, the requirements for the recoating step in ceramic vat photopolymerization and their rationale are outlined and categorized according to application properties.

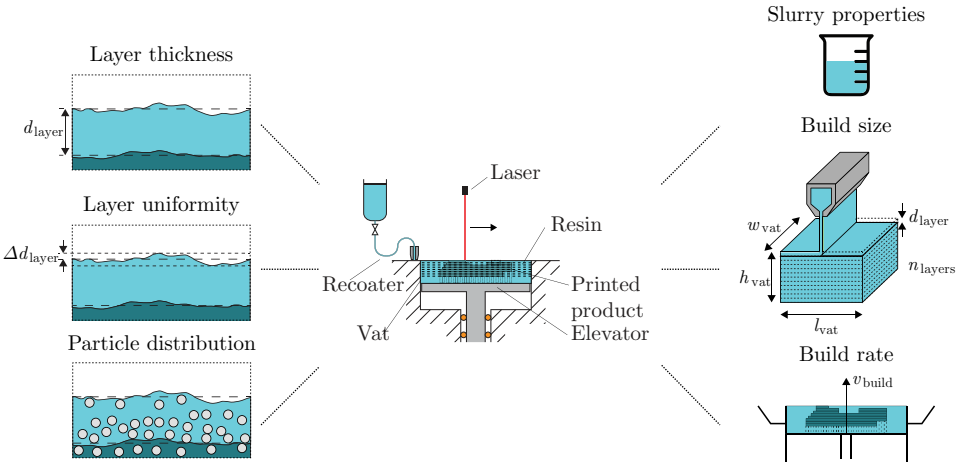

Figure 3.2: Requirements for the recoating step in ceramic vat photopolymerization.

Part geometry requirements

- Build area (size): the build area is defined as the product of vat length l_{vat} with vat width w_{vat} and dictates the maximum allowable part dimensions. Current industrial applications mostly encompass small objects such as medical implants, jewelry and antennas. Examples of high tech industry applications that benefit from the favorable properties of ceramics in their manufacturing equipment are the space, semiconductor and display manufacturing industries. The ever-increasing size of machine components such as substrate carriers motivates us to enable building parts with a cross-sectional area in the order of 1000×1000 [mm^2].

Material requirements

- Rheological resin properties: the recoater should be able to handle highly loaded ceramic suspensions. The mixing of resin with ceramic particles makes the resin highly viscous in comparison to pure non-filled resins. Literature states that the viscosity should be as low as possible and comparable to conventional resins, but not exceed 3 to 5 [Pa·s] for proper flow [14, 15]. Moreover, the recoater should be able to cope with density changes due to volumetric shrinkage upon photopolymerization [6].

- Optical resin properties: the recoater should be able to handle media that exhibit light scattering behaviour due to the presence of ceramic particles alongside the typical light absorbing behaviour in resins. This has consequences for the applicability of optical sensing methods.

Part quality requirements

- Layer thickness: the layer thickness typically determines the z-resolution, i.e., the smallest feature size in the vertical direction, and the surface roughness. For proper photopolymerization, the resin surface should be in the light source's focal plane and at a controlled height from the previous layer [6]. The layer thickness moreover determines the number of layers, the required energy dose or exposure per layer, and the required build time. Since thicker layers require a higher energy dose to bond to the previous layer, thicker layers do not necessarily result in shorter build times [5]. The current typical layer thicknesses of 25 - 100 [μm] are arguably acceptable.

- Layer uniformity: the layer uniformity quantifies the deviation from a flat layer and should be as uniform as possible. Resin surface nonuniformity can result in poor surface quality, undercure with resulting poor layer-to-layer adhesion (delamination), overcure with resulting excessive residual stress and distortion, and part height errors [6, 16]. Hence the deviation from the intended layer thickness Δd_{layer} should not exceed a certain value. To the authors' knowledge no literature is present on acceptable deviations in pure or ceramic-filled resins, but it is thinkable that ceramic-filled resins are more strict due to their lower light penetration depth.

- Layer particle distribution: the distribution of ceramic particles along the deposited layer should be sufficiently homogeneous. An inhomogeneous ceramic particle distribution in the green part influences the isotropy of the green part's properties and can contribute to the formation of defects such as cracks and delamination during post-processing [17–19]. Hence the settling of particles should be avoided both in printing and in storage. For similar reasons, the entrapment of air bubbles should be avoided.

Performance requirements

- Build rate: the build rate is defined as the layer thickness d_{layer} divided by the average time to print a layer t_{layer}, sometimes also multiplied by the build area. However, the recoating step is not the only contribution to the total part production time t_{total} (3.1) that ultimately determines productivity.

$$\begin{aligned} t_{\text{total}} &= t_{\text{pre-processing}} + n_{\text{layers}} \cdot t_{\text{layer}} + t_{\text{post-processing}} \\ t_{\text{layer}} &= t_{\text{recoating}} + t_{\text{photopolymerization}} \end{aligned} \tag{3.1}$$

  The pre-processing and especially the (thermal) post-processing steps including debinding and sintering can take more time than the build process itself. That is, for the current small product sizes post-processing can take several days [3] and will most probably increase when scaling up product sizes. For comparison, printing a 1000 [mm] high part with a layer thickness d_{layer} of 100 [μm] at a

time per layer t_{layer} of 30 seconds, would take 3.5 days. Shorter production times naturally are desirable, but such build times are already an improvement with respect to the total lead time for conventionally produced ceramic parts.

3.3 Recoating (actuation) methods

Many different methods to deposit a layer of liquid are reported in literature [20]. This section attempts to give a comprehensive overview of only those methods that are utilized in the recoating step of vat photopolymerization. Most of the recoating methods developed for vat photopolymerization are derived from the coating industry. A fundamental difference with coating on solid substrates, however, is the flow behaviour when coating a solid substrate as opposed to the flow behaviour when coating a viscous free surface [21]. In vat photopolymerization both situations can occur, depending on the local cross-section of the object to be built.

Recoating methods can be categorized according to several characteristics. In *pre-metered* systems, the amount of liquid applied per unit area is predetermined by an upstream metering pump; in *self-metered* systems the final layer thickness is mostly determined by the fluid flow interactions with the coating applicator [20]. In *constrained surface* systems, the final layer surface is determined by a constraining surface rather than by a free liquid-air interface as is the case for *free surface* systems. In *non-recoating* systems, the light source is immersed in the vat and hence no recoating system is required.

3.3.1 Self-metered, free surface recoating systems

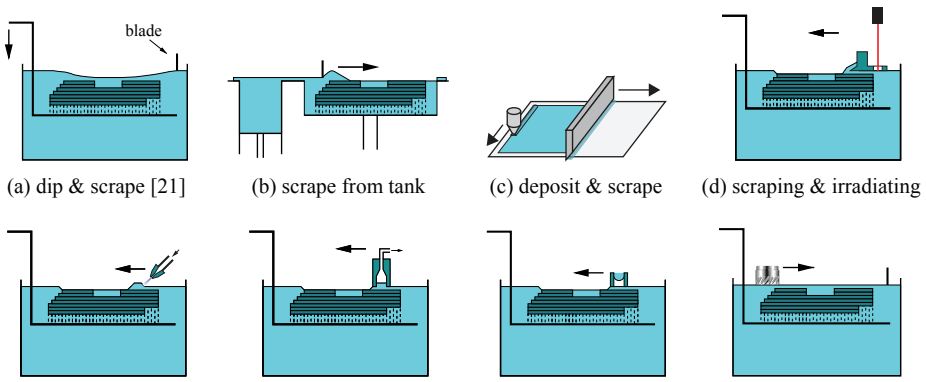

Figure 3.3: Self-metered recoating methods.

Dip & scrape recoating

In the first commercial vat photopolymerization system developed by 3D Systems, the SLA-1, recoating was performed by solely dipping the part in the resin bath, moving up again, and waiting for the resin level to settle [5]. In the successor SLA-250 system a recoater blade was added for sweeping the excess resin from the part and levelling. Figure 3.3 (a) illustrates this dip and scrape recoating method. At the start of the recoating procedure, the last cured layer is at the same height as the resin surface level. The platform is then lowered further than the intended layer height in a so-called "deep dip" step such that the part is fully immersed and resin is allowed to flow over the part [5]. Subsequently the platform is elevated to the position where the top surface of the part is one layer height below the resin level. In the final step a blade is swept across the vat one or more times to scrape away the excess resin and smoothen the resin surface. After sweeping, the resin is allowed to settle for a certain "Z-wait" period to decrease surface nonuniformity [5].

Deposit & scrape recoating

Instead of fully immersing the part by deep dipping in the resin vat, material can be supplied by depositing from an external reservoir. Recoating methods that first deposit material and then scrape the excessive material are designated here as deposit and scrape recoating methods. Both the depositing function and the scraping function can be fulfilled in different ways. One of the ways to deposit material is the scrape from tank technique in which the material is extruded from an adjacent tank by elevating a piston. Figure 3.3 (b) shows this technique, which was applied for vat-photopolymerization-based ceramic manufacturing by Optoform [22]. After lowering the build platform, a blade scrapes the liquid surface one or multiple times to spread the material.

A different way to deposit the material is to dispense the resin onto the previous layer by means of an extrusion head, a syringe or jetting. Cheverton et al. [23] used a syringe on a translation stage to deposit a line of ceramic slurry in one direction and to subsequently spread the material in the orthogonal direction with a doctor blade as depicted in Figure 3.3 (c). Springer et al. [24] developed a similar technique that uses a jet dispensing valve on an xy-stage to selectively dispense droplets of ceramic slurry on the complete build area, a roller to smoothen the material, and a slurry suction unit to actively dispatch surplus material.

Simultaneously scraping & irradiating

In the "semi controlled liquid method" developed by Yamazawa et al. [25, 26], the resin is simultaneously scraped and irradiated directly behind the scraper where the liquid surface is semi controlled. The main idea is to improve accuracy by irradiating at a location where the layer thickness is properly defined and to increase building

speed by eliminating "Z-wait" levelling time. Figure 3.3 (d) shows a constrained surface embodiment of the method, where the resin is irradiated through e.g. a quartz glass coated with a teflon layer [26].

Air knife recoating

The use of an air knife to control liquid film thickness by blowing off excess liquid is commonplace in the coating industry [20]. Dufaud et al. developed an air knife recoating system for vat-photopolymerization-based ceramic manufacturing [14, 27]. Figure 3.3 (e) shows the principle of spreading the resin by means of an air knife recoater, which consists of an injection nozzle through which nitrogen gas is forced; nitrogen is used to prevent oxygen inhibition. Layer thicknesses ranging from 5 to 40 [μm] could be achieved by adjusting the surface-nozzle height, gas pressure, and angle of attack [27].

Inverted U recoating

To eliminate the need for deep dipping and to improve recoating speed, the inverted U recoater was developed [21], also named Zephyr blade [7] or applicator bar [28]. The inverted U is essentially a symmetric hollow blade with a resin reservoir in the centre in which resin is sucked by means of a vacuum pump. Figure 3.3 (f) illustrates the inverted U recoating cycle, which starts with lowering the platform by one layer height and subsequently traversing the vat surface. During the blade sweeping, resin is deposited into regions where no resin is present and the resin reservoir is replenished during and after sweeping from the surrounding resin [29]. Alternatively, resin can be drawn from a separate vat. Inverted U recoaters using capillarity and electrostatic forces to fill the reservoir are reported in [21].

Viscous retention recoating

A recoating technique that utilizes the viscous behaviour of resins called viscous retention was developed by the company Teijin Seiki [30]. The viscous retention recoater consists of a brush or mesh between two doctor blades. As shown in Figure 3.3 (g) the recoater is first submerged into the vat and raised again to take up resin and then the platform is lowered. As the recoater traverses the vat, resin drains out due to gravity at a rate determined by the resin viscosity and the final layer height is determined by the trailing doctor blade [30].

Solid Ground Curing

Solid Ground Curing (SGC) was one of the earliest and now obsolete additive manufacturing techniques [7] in which the final layer height was determined by a face milling operation. SGC is essentially a free surface system, but since the final layer's surface is determined by a milling operation it is categorized here as a

constrained surface system. The manufacturing process commercialized by Cubital essentially consisted out of six steps: deposit layer, develop photomask, expose mask, vacuum uncured resin, deposit wax, mill flat [30]. Figure 3.5 (d) shows the milling step. In a sense, the SGC system was one of the first hybrid AM systems as it integrated both additive and subtractive manufacturing methods into a single machine.

3.3.2 Pre-metered, free surface recoating systems

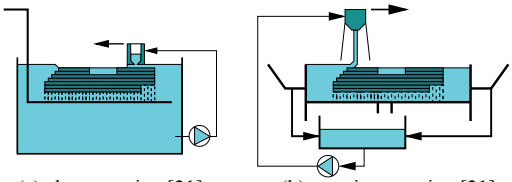

(a) slot recoating [21] (b) curtain recoating [21]

Figure 3.4: Pre-metered recoating methods.

Slot recoating

Slot coating is a layer deposition method derived from the coating industry and has been applied as a recoating method in vat photopolymerization as well. The principle of operation of slot coating is highly similar to that of inverted U recoating, but the essential difference is that slot coating is a pre-metered method. As Figure 3.4 (a) shows, after lowering the platform by one layer height an upstream metering pump regulates the resin outflow as the recoater traverses the vat surface. EOS is the only commercial vat photopolymerization system manufacturer known to have used a slot coater [21]. Haberer et al. developed a slot coater for vat photopolymerization using a highly viscous fiber-photopolymer resin composite liquid [31].

Curtain recoating

Curtain coating is a pre-metered coating technique in which a liquid curtain or sheet of liquid falls onto the surface to be coated [20]. The Catholic University of Leuven developed a curtain recoating system for vat photopolymerization [21], which was commercialized in the large-area Mammoth Stereolithography system by Materialise. Figure 3.4 (b) displays the curtain recoating system, essentially consisting of a recoating die, vat, collecting basin, reservoir and pump. At the start of the recoating cycle the platform is lowered by one layer thickness, the recoating die is accelerated to a constant speed. A liquid curtain is formed and a new layer of liquid is deposited as the recoating die traverses the vat. At the end the recoating die is decelerated. The resin that is impinged onto the collecting basin

at the beginning and end of the recoating cycle is recollected and fed to the central reservoir, with the accompanying risk that air bubbles are formed [21].

3.3.3 Constrained surface recoating systems

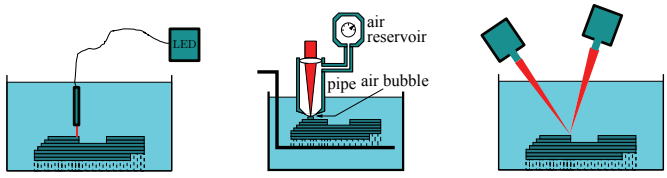

(a) CNC accumulation (b) air bubble [21] (c) two photon

Figure 3.5: Constrained surface recoating methods.

Conventional constrained surface systems

Conventional constrained surface systems have a bottom-up irradiation orientation where the light source is directed vertically upwards and irradiates through a glass substrate. After irradiation, the platform is raised in a separation step to a height above the resin level. In some embodiments a recoater blade is incorporated to spread the resin whereas in other systems gravity is used as the only motive force to let the resin flow underneath the part [32]. In an embodiment by Lithoz GmbH, the vat rotates and a stationary blade spreads out the resin [33]. Finally, the platform is lowered again to a height where the distance between the glass substrate and previous layer is exactly one layer thickness. Figure 3.5 (a) illustrates the constrained surface recoating technique, which eliminates the need for adding extra components to perform the recoating function when only gravity is used.

Continuously irradiating & elevating systems

The separation, recoating, and repositioning steps in constrained surface vat photopolymerization systems can be completely eliminated if the platform is continuously elevated and irradiated simultaneously. The challenge in this configuration is to prevent the resin to adhere to the glass substrate. Recently a technology was invented named continuous liquid interface production (CLIP) that solves this by creating a dead zone or liquid interface where photopolymerization is inhibited [34, 35]. This dead zone is achieved by incorporating an oxygen-permeable window below the image plane. CLIP is a layerless technology owing to the continuous platform elevation and its printing speed is either limited by resin curing or resin flow, depending on the cross-sectional area of the momentary slice [35]. In these continuously elevating systems, resin is constantly flowing underneath the part [36]. According to the inventors, isotropic material properties are obtained

with this technology [36]. Other continuously irradiating and elevating systems are currently under development by major vat photopolymerization system vendors such as 3D Systems, EnvisionTec and Prodways.

Tape casting methods

Tape casting is a manufacturing process for thin sheets of ceramic materials widely used in the production of electronic components [37]. The process involves the deposition of slurry on a moving carrier surface and the scraping of excess material by a doctor blade. Several recoating methods for vat photopolymerization were developed inspired by tape casting. Song et al. [19, 38] developed the bottom-up projection system depicted in in Figure 3.5 (c). In said system, the glass substrate is mounted to a linear stage to enable the depositing and scraping of a ceramic slurry. Separation is realized through a lubricative PDMS film and the linear sliding motion [38]. This is also a constrained surface system, because the dispensed slurry thickness is higher than the layer thickness. 3D Systems developed a similar technique called Film Transfer Imaging, in which a scraper deposits a thin film of resin on top of a stationary transparent material tray. Note also that tape casting methods show a high similarity to Laminated Object Manufacturing (LOM) [7].

Another recoating method closely related to tape casting is the sheet lamination process by Himmer et al. [39] for ceramic vat photopolymerization. In their method, slurry was applied to a plastic sheet and covered by a paper sheet in a lamination preprocess and subsequently pressed onto the previous layer. However, during the photopolymerization step the surface was not constrained. The recoating steps were performed manually, but an automated version was outlined as well in [39]. The method employed in the Admatec Admaflex machines [40, 41] fairly resembles this automated version. Their system consists of a foil handling system, a ceramic slurry depositor including doctor blade and a glass support plate through which the layers are irradiated bottom-up.

3.3.4 Non-recoating systems

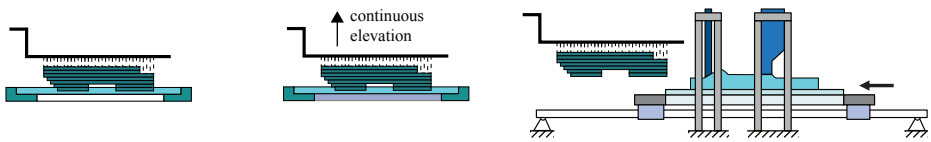

(a) constrained surface [21] (b) continuously irradiating & elevating (c) tape casting [19]

Figure 3.6: Non-recoating methods.

CNC accumulation

CNC accumulation is a non-recoating type of vat photopolymerization technology in which an accumulation tool coupled to a UV light source by a fiber optic cable is immersed in a resin vat [42]. The process is highly similar to CNC machining, as the accumulation tool is mounted to a multi-axis CNC stage. Figure 3.6 (a) shows the basic concept of CNC accumulation. Upon irradiation, the cured resin adheres to the curing tool tip, but due to the small contact area separation is less of an issue than it is with constrained surface systems [42]. The point-based irradiation method in the original CNC accumulation configuration was extended to a line-based irradiation method with still a considerably small contact area [43].

Irradiating through an air bubble

A non-recoating type of vat photopolymerization technology similar to the CNC accumulation process was developed at Osaka Sangyo University [21]. In the method a pipe is submersed into the resin vat and at the lower end an air bubble is formed due to an overpressure. A coaxial laser beam irradiates the resin through the air bubble as shown in Figure 3.6 (b). The difference with the CNC accumulation process is that there is no mechanical bonding between the cured layers and the pipe and thus no accompyanying separation issues [21].

Two-photon vat photopolymerization

In two-photon vat photopolymerization, a photoinitiator molecule requires the simultaneous absorption of two photons in order to form free radicals [7, 14]. In one configuration named beam interference solidification, two lasers are used with potentially different wavelengths. Only at their interference point a photoinitiator molecule can be excited to a high enough state to initiate polymerization as depicted in Figure 3.6 (c). In another configuration, a single laser is used where only near the focal spot of the laser the intensity is high enough to initiate polymerization [7]. As in both configurations polymerization can take place at any depth in the vat, the need for recoating is eliminated. However, the scattering of light in the ceramic particles most probably makes this method unsuited for ceramic vat photopolymerization.

3.3.5 Other recoating methods

For the sake of completeness, it is worthwhile to mention other recoating methods reported in literature. These methods include rolling with a paint roller [27], sweeping with a canvas [27], spraying [44], using counter-rotating rollers [28], material extrusion [45], and establishing a liquid bridge between two plates [46]. Note that the boundaries between different additive manufacturing technologies such as vat photopolymerization and, e.g., material jetting vanish when looking from a conceptual point of view.

3.4 Sensing methods

Few sensing technologies have been applied in the recoating phase in vat photopolymerization, but this section gives a brief overview of those that have been. Two practically the same measurands with different dimensionality are discussed: the bulk resin level, i.e., a single value representing the average resin level, and the layer surface uniformity, i.e., a 2D height map representing the resin level at each point on the layer surface. The techniques listed here are only applicable to free surface systems, as in constrained surface systems the layer height is not determined by recoating.

3.4.1 Bulk resin level sensing

In early vat photopolymerization systems the bulk resin level was measured by means of a mechanical float or a laser beam reflected off the resin surface onto a bi-cell and later onto a linear cell detector [6], see Figure 3.7 (a). However, these systems only measured the level at a single point that could potentially be unrepresentative for the bulk resin level due to local surface undulations. Pham et al. used phototransistors to measure fluctuations of the resin level during recoating at three different vat positions [47]. Renap et al. used a laser distance sensor on a linear motion stage to measure the surface level along the axis of the recoater blade [48], see Figure 3.7 (b).

3.4.2 Confocal laser scanning

Park et al. developed a sensor system for in-process layer surface inspection of stereolithography products [49]. Their goal was to enable the detection of defects such as voids, delaminations and surface undulations. Their sensor system's measuring principle is similar to that of laser scanning confocal microscopy and is based on the fact that the diffused light intensity of a solidified region is higher than that of liquid resin. The realized imaging system consists of a laser source that was scanned over the surface by means of galvanometers, a beam splitter, lenses and a coaxial photodetector; see Figure 3.7 (c).

3.4.3 Fringe projection

Narahara et al. developed a measurement system for liquid surface flatness based on fringe projection techniques [50, 51]. Their goal was to measure the unevenness of the liquid surface to assure flatness of the layers of stereolithography parts. Their systems' measuring principle is based on projecting a stripe pattern by means of a light source and grating plate and capturing an image of the projection that appears distorted if not flat, see Figure 3.7 (d). In an initial implementation [50], the surface height was measured through a phase detection algorithm. In a later implementation [52], a more approximative algorithm was used to measure the

surface height. For small surface angles, i.e., under 0.1 [^{o}], and small angle variations the system is capable of producing a surface height map with a maximum error up to 6 [μm]. In case the surface unevenness exceeded a certain value, a corrective step was performed in the form of an extra recoater sweep.

3.4.4 Machine vision

Cheverton et al. used a surface imaging camera to monitor the quality of each ceramic slurry layer, and a separate camera to monitor the slurry deposition process [23]. The goal was to notify the operator about a problem using machine vision and to make automated decisions in case of anomalies, e.g., re-wiping the layer when necessary.

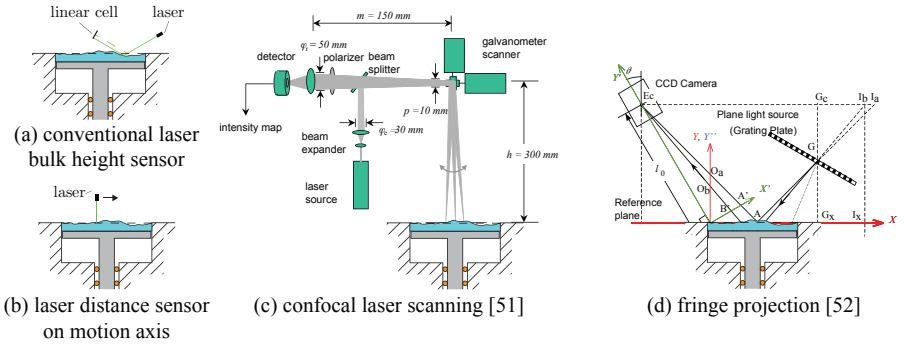

Figure 3.7: Resin surface height sensing methods applied in vat photopolymerization.

3.5 Control strategies

Currently, recoating is typically controlled in open loop, since the deposited layer quality is typically not measured nor used as a feedback signal. Conventional dip and scrape systems had some user-configurable parameters, such as the number of sweeps and sweep speed [5, 6]. Little literature exists on more advanced recoating strategies. Jacobs et al. describe a three-sweep method to move bubbles formed during the recoating process outside the build area [6]. Guangshen et al. [53] developed a dynamically optimized blade speed based on a response surface model to reduce layer thickness deviations with built object height. The following sections describe three closed-loop control schemes relevant to recoating.

3.5.1 Corrective sweeping

In free surface systems, the performance of the recoater can be quantified by the deposited layer surface uniformity. If information of the layer uniformity is available in the form of, e.g., a 2D height map, a decision can be made to perform another scraping or sweeping action. Yoshikawa et al. closed the loop by using layer uniformity information as a feedback signal to decide whether or not to sweep again [51], see Figure 3.8 (a) for the simple control algorithm. Cheverton et al. describe a similar corrective sweeping action, based on a machine vision image [23].

3.5.2 Resin level control

During polymerization the total photopolymer volume and consequently the resin level decrease due to shrinkage. On the other hand, fluid displacement due to elevator immersion and temperature fluctuations can affect the resin level. Resin level feedback control was implemented in early commercial vat photopolymerization systems to reject resin level disturbances [5]. Figure 3.8 (b) schematically shows the resin level control scheme. A laser leveling system measures the resin level and a plunger activated by a precision stepper motor corrects the resin level through simple fluid displacement [6]. In the figure the bulk level and corresponding laser reflection are shown dashed. It holds for both the measurement and the actuation that only one point is considered, although the surface actually has a nonuniform height distribution. Wang et al. developed an improved liquid level detection and control method with a resolution of ± 15 [μm] [54].

3.5.3 Separation force control

In constrained surface systems, a substantial separation force is required to elevate the platform after photopolymerization [55]. This separation process presents a potential threat to part quality, as defects can occur if the stresses in the part exceed a stress limit. Separation force control was developed to achieve efficient separation without breaking the part. Figure 3.8 (c) schematically shows the separation force control system. The pulling force on the platform is measured by means of a load cell and is fed back to the platform motion controller. Based on a predictive model of the force-displacement behavior or a simple force threshold, the separation force or platform motion is limited [55, 56].

3.6 Control system considerations

The inventory of recoating methods, sensing methods, and control strategies conducted in the previous sections, shows that the system designer has a fair amount of design options at hand. This section discusses several considerations from a control systems perspective to enable the system designer to select a recoating method.

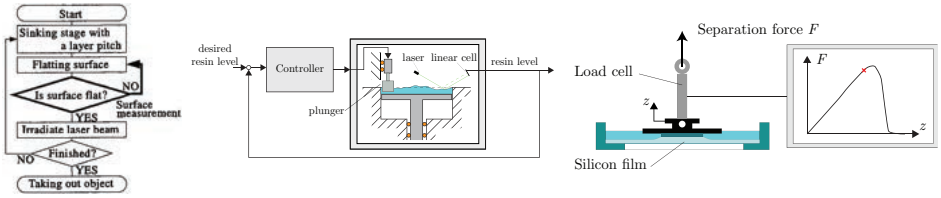

(a) corrective sweeping [53] (b) resin level control (c) separation force control

Figure 3.8: Control schemes.

Ideally, the method should be chosen by conducting a trade-off study in which the characteristics of each candidate are compared in order to determine the method that best balances the assessment criteria [57]. The requirements outlined in the beginning of this paper together with the following considerations constitute said criteria. Design considerations for micro-stereolithography systems are discussed in [32].

3.6.1 Number of actuators

Input-output controllability is the ability of achieving acceptable control performance while using the available inputs and measurements [58]. That is, the outputs need to be within specified bounds from the references. In this case the reference or desired value is a perfectly flat or uniform layer of desired thickness. Controllability is affected by choosing the amount and location of the sensors and actuators. Hence, the number of actuators is a factor in equipment and control design that needs to be considered. Table 3.1 shows a classification scheme that allows for distinguishing recoating methods by the geometry or spatial dimensionality of the recoater and the number of resin deposition actuators. This geometry determines the number of motion degrees of freedom (DOF) in the horizontal plane required to cover a complete area. Hence, the number of deposition actuators and motion actuators together comprise the total number of input variables.

For instance, the recoating method employed by Springer et al. [24] consisting of a single jet dispensing valve, requires two motion DOF to cover the complete area. Most traditional recoating systems, however, have a line geometry that requires a single motion DOF to traverse the surface. Note that a passive doctor blade does not have any actuation capability (represented by a 0 in Table 3.1), while a Zephyr blade does. A 2D array of jets would not require any motion DOF at all if the covered area would be sufficiently large, or could again be augmented with a motion stage to increase the covered area.

The reason as to why multiple actuators along the lateral y-axis can be desirable, is that fluid depth variations can occur along the this axis depending on the product

Recoating method	**Extruding/ jetting**	**Blade/slot/ curtain**	**Extruding/ jetting**	**Tape casting/ lamination**	**Extruding/ jetting**
# Actuators	1	0 or 1	n-point array	1	$n \times m$ point array
Geometry	Point	Line	Line	Area	Area
Schematic illustration	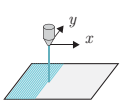	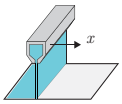	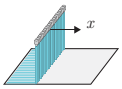	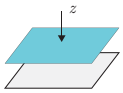	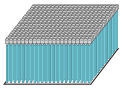
# xy-Motion DOF	2	1	1	0	0

Table 3.1: Recoating methods classification scheme, adapted from [7].

geometry. Hence, the suitability of a recoating method can depend on the desired product geometry. Figure 3.9 illustrates this by means of a block geometry with a pocket, often designated as a *trapped volume* [29]. Increasing the number of actuators can be realized by, e.g., segmenting a blade or extrusion die. A fundamental question remains, however, on what a sensible amount of segments or actuators is.

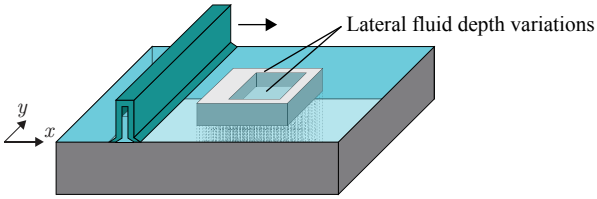

Figure 3.9: Motivation for multiple actuators in the lateral direction.

3.6.2 Resin metering

Another factor that affects controllability is whether the recoating method is able to deposit or withdraw resin. Self-metered systems typically use a surplus of material and withdraw material where it is not needed. On the contrary, pre-metered systems typically only deposit material where it is needed. This implies that pre-metered systems offer the possibility to control or exactly dose the resin outflow, potentially position dependent.

3.6.3 Contact

Closely related to whether the recoating method is self-metered or pre-metered, is whether the recoater is contactless or contactful. Most self-metered systems are

contactful in the sense that a blade or knife is in mechanical contact with the resin and scrapes the excess away. This contact causes shear forces and moments to be exerted on the previously built layers and features, which can cause defects if the shear stress is larger than the mechanical strength of the object [27]. Moreover, the contact can cause fluid dynamic effects such as scoopout and bulges [28] that lead to a poorly controllable layer thickness. In a sense, the only contactless self-metered recoating method is the air knife. Pre-metered systems such as curtain coating are also contactless.

3.6.4 Surface constrainedness

Whether the resin surface is constrained or not during polymerization, impacts the system's design. Figure 3.10 summarizes the design options for the irradiation orientation and surface constrainedness. The main advantage of constraining the surface by means of, e.g., a transparent glass window, is that a well-defined layer thickness can be obtained. Although most constrained surface systems have a bottom-up orientation as in Figure 3.10 (b), alternatives exist that have a side-wise [59] and top-down [60] orientation as in Figure 3.10 (c) and (d) respectively. The main disadvantage of constraining the surface, however, is that in conventional systems the cured layer has to be separated from the window after each layer has been cured as opposed to free surface systems shown in Figure 3.10 (a).

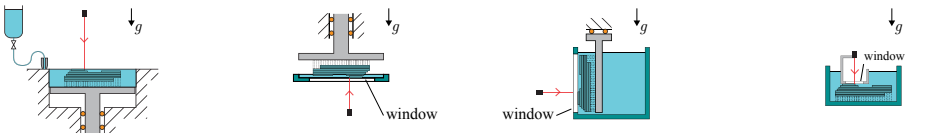

Figure 3.10: Irradiation orientation and surface constrainedness options.

The separation process requires a substantial separation force, which can be reduced by coating the window with a teflon, silicone or PDMS film [56,61,62]. The separation force consists of two components, namely a force due to adhesion of the cured part to the film and a force due to a vacuum state at this interface [63]. An additional fluid drag force is present due to the motion of the cured part in the resin vat. Several methods to improve the separation process have been developed by equipment designers. Gruber et al. developed a tilting mechanism to tilt the complete vat [64]. Pan et al. and Song et al. developed a horizontally translating mechanism to reduce the required separation force [38,65]. Apart from the hardware solutions directed towards minimizing the required separation force, a control system that minimizes separation forces was developed as well.

Next to layer uniformity and whether the cured layer needs to be separated, other considerations are relevant to the choice of surface constrainedness. First of all, in free surface systems the oxygen dissolved in the resin that inhibits polymerization is repleted by oxygen from the oxygen rich build chamber. In constrained surface systems this oxygen repletion can be either prevented or promoted as is the case in CLIP [35]. Second, it is important to realize that the part being built is also mechanically loaded by the separation force and can sustain severe damage or defects when subjected to excessive forces. As the required separation force increases linearly with part cross-sectional area [56], the implication for the scalability to larger product sizes is that the required total force increases. Another mechanical consideration is that during photopolymerization the resin shrinks and this potentially induces flows that can freely flow in free surface systems, but can not in constrained surface systems. A final consideration is that in bottom-up systems the resin volume required in the build vat is independent of part height. Table 3.2 summarizes the considerations pertaining to the choice of surface constrainedness.

Consideration	**Free surface**	**Constrained surface**
Layer uniformity	determined by recoater	determined by substrate
Oxygen inhibition	free oxygen repletion	reduced oxygen repletion
Shrinkage	free	constrained
Separation	not required	force loads part
Build area	freely enlargeable	required force increases
Vat volume	dependent of part height	independent of part height

Table 3.2: Summary of considerations concerning resin surface constrainedness.

3.6.5 Layer nonuniformity compensation

The requirements for a flat and uniform layer of specified thickness might be relaxed in free surface systems if the philosophy of feedback control is adopted. One line of reasoning is that layers should be perfectly flat and that the exposure at each point on the resin surface should equal the predetermined nominal value. Another line of reasoning is that layers may deviate from a flat layer to some extent and that the required exposure should be calculated for each point by virtue of a surface height measurement.

If the irradiance levels or exposure times are allowed to be adapted depending on the local layer thickness, the exposure dose can be chosen such that under- and overcure are prevented. However, light attenuation within the layer limits the amount of layer nonuniformity that can be compensated for. Attenuation of light intensity occurs due to absorption by matter or scattering by irregularities in the medium. Absorption causes the light intensity to exponentially decay with distance travelled into the layer, which can be described by the Beer-Lambert law [5].

Scattering by ceramic particles typically causes the light intensity distribution to broaden and attenuate even further with depth [4].

Thus, the controllability of the exposure dose within the layer is governed by the physical laws of absorption and scattering. This limited controllability poses an upper bound on the permissible layer nonuniformity, since under- and overcure cannot be prevented in too thick layers due to the inhomogeneous exposure distribution. For green ceramic parts the allowable exposure dose inhomogeneity within the part may deviate from that of pure photopolymer parts, since the photopolymer is later pyrolyzed from the green parts.

Layer nonuniformity compensation requires a 2D height map measurement to be available at high spatial resolution, which is not trivial as exemplified by the few sensing methods applied in literature [49, 50]. Another factor that needs to be considered, is the location of the light source's focal plane. Using the same surface height information used for calculation of exposure compensation, the focal plane can be positioned at the resin surface by actuating optical components as is done in the photolithography industry [66]. Obviously the addition of aforementioned sensors and actuators for layer nonuniformity compensation come at the cost of increased system complexity.

3.7 Discussion

The characteristics of the recoating methods outlined in this paper are compared in Table 3.3. The table shows that not all recoating methods have been applied for the deposition of ceramic-filled resins. However, based on the absence of preceding applications one can not directly conclude that those methods are unsuited for ceramics. It does seem unlikely that two-photon systems can be used for ceramics, due to the highly scattering nature of ceramic-filled resins. Viscous retention recoating also seems inapplicable, since the brush or mesh may act as a filter for the ceramic particles. Although preliminary studies show that CLIP technology is compatible with ceramics [35], to the author's knowledge no results have been published yet.

Perhaps one of the most distinguishing aspects is the maximum build area. The inverted U and curtain recoating methods are the only ones reported to have a build area larger than the required 1 [m^2]. However, no hard conclusions can be drawn on the possibility to enlarge the build area of the recoating methods based on reported build areas. For instance, air knives that span 1 [m] are used in the coating industry, while the only application in vat photopolymerization merely spans 8 [mm] [27]. Due to the relationship of cross-sectional area with separation force, it seems unlikely that constrained surface systems are suitable for the required large build areas.

Recoating method	**Resin metering**	**Ceramic application**	**Contact**	**Max. build area [cm²]**	**Min. layer thickness [μm]**	**Max. speed [mm/s]**	**# Deposition actuators**	**# *xy*-Motion DOF**
Dip & scrape recoating	Self-metered	No	Contact-ful	625 [67]	150 [67]	100 [21]	0	1
Scrape from tank	Self-metered	Yes [22, 68]	Contact-ful	3600 [69]	25 [22]	30 [70]	1	1
Deposit & scrape recoating	Self-metered	Yes [23, 24]	Contact-ful	Not reported	10 [24]	3 [23]	1	2
Simultaneously scraping & irradiating	Self-metered	No	Contact-ful	625 [25]	50 [25]	1 [26]	0	1
Air knife recoating	Self-metered	Yes [27]	Contact-less	1 [27]	5 [27]	5 [27]	1	1
Inverted U recoating	Self-metered	No	Contact-ful	11250 [71]	50 [67]	100 [21]	1	1
Viscous retention recoating	Self-metered	No	Contact-ful	2500 [67]	50 [67]	30 [72]	0	1
Solid ground curing	Self-metered	No	Contact-ful	1750 [67]	60 [67]	Not reported		1
Slot recoating	Pre-metered	No, FRP [31]	Contact-ful	86 [73]	300 [31]	10 [73]	1	1
Curtain recoating	Pre-metered	No	Contact-less	14700 [74]	100 [21]	1500 [21]	1	1
Conventional constrained surface systems	Constr. surface	Yes [33]	Contact-ful / -	210 [75]	25 [75]	Not reported	0	0 / 1
Continuously irradiating & elevating systems	Constr. surface	No	-	219 [76]	-	-	0	0
Tape casting methods	Constr. surface	Yes [38–40]	Contact-ful	74 [41]	10 [38]	25 [38]	1	1
CNC accumulation	Non-recoating	No	-	Not reported	-	-	-	-
Irradiating through an air bubble	Non-recoating	No	-	Not reported	-	-	-	-
Two-photon vat photopolymerization	Non-recoating	No	-	Not reported	-	-	-	-

Table 3.3: Recoating methods comparison.

The smallest layer thickness reported is 5 [μm], which is achieved by air knife recoating. This layer thickness is already in the order of the typical ceramic particle size [27], so this represents a practical lower limit. However, the minimum achievable layer thickness is not considered a predominant assessment criterion here. The build rate is expressed in the maximum speed at which the recoater can move over the vat surface, so it is not the flow rate. As Table 3.3 shows, the range of maximum recoating speeds spans three orders and the curtain recoating method outperforms any other method in this respect.

Unfortunately, hardly any data is available on the performance of the respective recoating methods in terms of product quality aspects. That is, layer uniformities and layer particle distributions are not reported in literature, even though the lack of product quality is currently the main challenge in vat-photopolymerization-based ceramic manufacturing. Quantification of the surface height deviations and the length scales over which they occur would serve two purposes. It would allow firstly for comparing the existing recoating methods and secondly for choosing a sensible number of actuators and the achievable performance improvement in, e.g., a segmented blade concept. Hence, the way forward seems to be the quantification of layer uniformities through measurements of actual surface height deviations for the most promising recoating methods.

References

[1] N. Travitzky, A. Bonet, B. Dermeik, T. Fey, I. Filbert-Demut, L. Schlier, T. Schlordt, and P. Greil, "Additive Manufacturing of Ceramic-Based Materials," *Advanced Engineering Materials*, vol. 16, pp. 729–754, June 2014.

[2] J. Deckers, J. Vleugels, and J.-P. Kruth, "Additive Manufacturing of Ceramics: A Review," *Journal of Ceramic Science and Technology*, vol. 5, no. 4, pp. 245–260, 2014.

[3] A. Zocca, P. Colombo, C. M. Gomes, and J. Günster, "Additive Manufacturing of Ceramics: Issues, Potentialities, and Opportunities," *Journal of the American Ceramic Society*, vol. 98, pp. 1983–2001, July 2015.

[4] J. W. Halloran, "Ceramic Stereolithography: Additive Manufacturing for Ceramics by Photopolymerization," *Annual Review of Materials Research*, vol. 46, pp. 10.1–10.22, Aug. 2016.

[5] P. Jacobs, *Rapid Prototyping & Manufacturing: Fundamentals of Stereolithography.* Dearborn, MI: Society of Manufacturing Engineers, 1992.

[6] P. Jacobs, *Stereolithography and other RP&M Technologies: from Rapid Prototyping to Rapid Tooling.* New York: ASME Press, 1996.

[7] I. Gibson, D. Rosen, and B. Stucker, *Additive Manufacturing Technologies*. New York, NY: Springer, 2nd ed., 2015.

[8] M. Mani, B. Lane, A. Donmez, S. Feng, S. Moylan, and R. Fesperman, "Measurement Science Needs for Real-time Control of Additive Manufacturing Powder Bed Fusion Processes," Tech. Rep. NIST IR 8036, National Institute of Standards and Technology, Feb. 2015.

[9] J. Pellegrino, T. Makila, S. McQueen, and E. Taylor, "Measurement science roadmap for polymer-based additive manufacturing," Tech. Rep. NIST AMS 100-5, National Institute of Standards and Technology, Gaithersburg, MD, Dec. 2016.

[10] Y. Huang, M. C. Leu, J. Mazumder, and A. Donmez, "Additive manufacturing: Current state, future potential, gaps and needs, and recommendations," *Journal of Manufacturing Science and Engineering*, vol. 137, no. 1, pp. (014001–1)–(014001–9), 2015.

[11] VDI. 2206, *Design methodology for mechatronic systems*. VDI-Gesellschaft Produkt- und Prozessgestaltung, June 2014.

[12] A. Kossiakoff, ed., *Systems engineering: principles and practice*. No. 67 in Wiley series in systems engineering and management, Hoboken, N.J: Wiley-Interscience, 2nd ed., 2011.

[13] D. Hardt, "Modeling and control of manufacturing processes: Getting more involved," *Journal of Dynamic Systems, Measurement, and Control*, vol. 115, pp. 291–300, June 1993.

[14] P. J. Bartolo, ed., *Stereolithography*. Boston, MA: Springer US, 2011.

[15] M. L. Griffith and J. W. Halloran, "Ultraviolet curing of highly loaded ceramic suspensions for stereolithography of ceramics," in *Proceedings of the Solid Freeform Fabrication Symposium*, pp. 396–403, 1994.

[16] C. Tille, "Process Errors and Aspects for Higher Resolution in Conventional Stereolithography," in *Proceedings of the Solid Freeform Fabrication Symposium*, pp. 281–292, 2004.

[17] C.-J. Bae, *Integrally cored ceramic investment casting mold fabricated by ceramic stereolithography*. PhD thesis, University of Michigan, Ann Arbor, MI, 2008.

[18] S. P. Gentry, *Factors Affecting the Resolution of Photopolymerized Ceramics*. PhD thesis, University of Michigan, Ann Arbor, MI, 2012.

[19] X. Song, *Slurry based Stereolithography: A Solid Freeform Fabrication. Method of Ceramics and Composites*. PhD thesis, University of Southern California, Los Angeles, CA, 2016.

[20] S. F. Kistler and P. M. Schweizer, eds., *Liquid Film Coating*. Dordrecht: Springer Netherlands, 1997.

[21] M. Gilio, *Curtain Recoating for Stereolithography*. PhD thesis, Catholic University of Leuven, Louvain, Belgium, Nov. 2004.

[22] F. Doreau, C. Chaput, and T. Chartier, "Stereolithography for Manufacturing Ceramic Parts," *Advanced Engineering Materials*, vol. 2, no. 8, 2000.

[23] M. Cheverton, P. Singh, L. S. Smith, K. P. Chan, J. A. Brewer, and V. Venkataramani, "Ceramic polymer additive manufacturing system for ultrasound transducer," in *Proceedings of the Solid Freeform Fabrication Symposium*, pp. 863–875, 2012.

[24] P. Springer, E. Schwarzer, O. Refle, and H.-J. Richter, "Equipment, Material and Processes for UV-DLP- Based Additive Manufacturing of Two-Component Ceramic Green Bodies and Dense Structures," in *Proceedings of 3rd Fraunhofer Direct Digital Manufacturing Conference, DDMC 2016.*, 2016.

[25] K. Yamazawa, T. Niino, S. Hayano, and T. Nakagawa, "High Speed UV Laser Beam Scanning by Polygon Mirror," in *Proceedings of the Solid Freeform Fabrication Symposium*, p. 223, 1997.

[26] K. Yamazawa, T. Niino, T. Nakagawa, and S. Hayano, "Apparatus for solidifying and shaping optically cured fluid by carrying out scanning simultaneously with recoating," July 14 1997. U.S. Patent 5780070.

[27] O. Dufaud and S. Corbel, "Dispositif de déposition de couches de suspensions de céramiques appliqué à la stéréolithographie," *The Canadian Journal of Chemical Engineering*, vol. 82, pp. 986–993, Aug. 2004.

[28] T. A. Almquist, "Rapid recoating of three-dimensional objects formed on a cross-sectional basis," May 1999. U.S. Patent 5902537A.

[29] D. T. Pham and C. Ji, "A study of recoating in stereolithography," *Proceedings of the Institution of Mechanical Engineers, Part C: Journal of Mechanical Engineering Science*, vol. 217, pp. 105–117, Jan. 2003.

[30] F. B. Prinz, "JTEC/WTEC panel on rapid prototyping in Europe and Japan: final report," 1997.

[31] M. Haberer, G. Zak, C. B. Park, and B. Benhabib, "Design of a Slot-Coater-Based Layered-Composites Manufacturing System," *Journal of Manufacturing Science and Engineering*, vol. 125, no. 3, pp. 564–576, 2003.

[32] P. M. Lambert, E. A. Campaigne III, and C. B. Williams, "Design Considerations for Mask Projection Microstereolithography Systems," in *Proceedings of the Solid Freeform Fabrication Symposium*, pp. 111–130, 2013.

[33] Schwentenwein, "Lithography-based Ceramic Manufacturing: Layer-by-layer to Dense and Precise Ceramic Parts," in *Proceedings of 3rd Fraunhofer Direct Digital Manufacturing Conference, DDMC 2016*, 2016.

[34] D. Dendukuri, D. C. Pregibon, J. Collins, T. A. Hatton, and P. S. Doyle, "Continuous-flow lithography for high-throughput microparticle synthesis," *Nature Materials*, vol. 5, pp. 365–369, May 2006.

[35] J. R. Tumbleston, D. Shirvanyants, N. Ermoshkin, R. Janusziewicz, A. R. Johnson, D. Kelly, K. Chen, R. Pinschmidt, J. P. Rolland, A. Ermoshkin, E. T. Samulski, and J. M. DeSimone, "Continuous liquid interface production of 3d objects," *Science*, vol. 347, pp. 1349–1352, Mar. 2015.

[36] Carbon3D, "Carbon3d Website." [Online]. Available: http://www.carbon3d.com/. [Accessed: June 20 2017].

[37] R. E. Mistler and E. R. Twiname, *Tape casting: theory and practice*. Westerville, OH: American Ceramic Society, 2000.

[38] X. Song, Y. Chen, T. W. Lee, S. Wu, and L. Cheng, "Ceramic fabrication using Mask-Image-Projection-based Stereolithography integrated with tape-casting," *Journal of Manufacturing Processes*, vol. 20, pp. 456–464, Oct. 2015.

[39] T. Himmer, T. Nakagawa, and H. Noguchi, "Stereolithography of ceramics," in *Proceedings of the Solid Freeform Fabrication Symposium*, pp. 363–369, 1997.

[40] P. A. J. M. Kuijpers, "Additive manufacturing system for manufacturing a three dimensional object," July 23 2015. WO Patent 2015107066 A1.

[41] Admatec, "ADMAFLEX 130." [Online]. Available: http://us10.campaign-archive1.com/?u=d133b148284b0db1a4cb57441&id=30be518c00&e=5ab2ce4df9. [Accessed: June 20 2017].

[42] Y. Chen, C. Zhou, and J. Lao, "A layerless additive manufacturing process based on CNC accumulation," *Rapid Prototyping Journal*, vol. 17, pp. 218–227, Apr. 2011.

[43] H. Mao, C. Zhou, and Y. Chen, "LISA: Linear immersed sweeping accumulation," *Journal of Manufacturing Processes*, vol. 24, pp. 406–415, July 2016.

[44] H. H. Maalderink, "Method and system for layerwise production of a tangible object," June 4 2013. U.S. Patent 8454880.

[45] M. Faes, H. Valkenaers, F. Vogeler, J. Vleugels, and E. Ferraris, "Extrusion-based 3d Printing of Ceramic Components," *Procedia CIRP*, vol. 28, pp. 76–81, 2015.

[46] Y. Lu, *A Study on Liquid Bridge Based Microstereolithography (LBMSL) System*. PhD thesis, University of Akron, Akron, OH, 2016.

[47] D. T. Pham and C. Ji, "Re-coating of SLA parts containing trapped volumes," in *Proceedings of 17th National Conference on Manufacturing Research (NCMR 2001)*, (Cardiff, UK), pp. 199–204, Professional Engineering Publishing, 2001.

[48] K. Renap and J. Kruth, "Recoating issues in stereolithography," *Rapid Prototyping Journal*, vol. 1, pp. 4–16, Sept. 1995.

[49] W. S. Park, M. Y. Kim, H. G. Lee, H. S. Cho, and M.-C. Leu, "In-process layer surface inspection of SLA products," in *Proceedings of Spie–the International Society for Optical Engineering, V. 3517*, International Society for Optical Engineering (SPIE), 1998.

[50] H. Narahara, H. Suzuki, and M. Suga, "Detection of uneven flatness on liquid surface," in *16th IMEKO World Congress, 25–28 September 2000, Vienna, Austria*, 2000.

[51] A. Yoshikawa, H. Narahara, and H. Suzuki, "Research on the uneven measurement on the liquid surface of photoresin in the stereolithography," *Journal of the Japan Society for Precision Engineering*, vol. 69, no. 10, pp. 1434–1438, 2003.

[52] H. Narahara, A. Yoshikawa, and H. Suzuki, "Measurement of Liquid Surface Unevenness in Stereolithography," *JSME International Journal Series C Mechanical Systems, Machine Elements and Manufacturing*, vol. 47, no. 1, pp. 129–135, 2004.

[53] X. Guangshen, M. Xunming, J. Jing, Q. Ronghua, and L. Shen, "Research on Recoating Process in High-Resolution Stereolithography System," in *Proceedings of 2009 Second International Conference on Intelligent Computation Technology and Automation*, pp. 621–624, IEEE, 2009.

[54] Y. Wang, W. Zhao, Y. Ding, Z. He, and B. Lu, "A detection and control method of resin liquid–level of stereolithography apparatus," *Rapid Prototyping Journal*, vol. 15, pp. 333–338, Sept. 2009.

[55] F. Liravi, S. Das, and C. Zhou, "Separation force analysis and prediction based on cohesive element model for constrained-surface Stereolithography processes," *Computer-Aided Design*, vol. 69, pp. 134–142, Dec. 2015.

[56] Y.-M. Huang and C.-P. Jiang, "On-line force monitoring of platform ascending rapid prototyping system," *Journal of Materials Processing Technology*, vol. 159, pp. 257–264, Jan. 2005.

[57] NASA, *NASA Systems Engineering Handbook*. 2007.

[58] S. Skogestad and I. Postlethwaite, *Multivariable Feedback Control: Analysis and design*. New York: Wiley, 2nd ed., 2005.

[59] Z. U. Ihsan, "Projection Microstereolithography Apparatus," Master's thesis, Aalto University, Espoo, Finland, 2016.

[60] K. Ikuta, S. Maruo, and S. Kojima, "New micro stereo lithography for freely movable 3d micro structure-super IH process with submicron resolution," in *Proceedings of the Eleventh Annual International Workshop on Micro Electro Mechanical Systems*, pp. 290–295, IEEE, 1998.

[61] F. Liravi, S. Das, and C. Zhou, "Separation Force Analysis based on Cohesive Delamination Model for Bottom-up Stereolithography Using Finite Element Analysis," in *Proceedings of the Solid Freeform Fabrication Symposium*, pp. 1432–1451, 2014.

[62] Y. Pan, C. Zhou, and Y. Chen, "Rapid manufacturing in minutes: the development of a mask projection stereolithography process for high-speed fabrication," in *ASME 2012 International Manufacturing Science and Engineering Conference*, pp. 405–414, American Society of Mechanical Engineers, 2012.

[63] F. Liravi, "Dynamic force analysis for bottom-up projection-based Additive Manufacturing using finite element analysis," Master's thesis, State University of New York at Buffalo, New York, NY, 2014.

[64] S. Gruber, J. Stampfl, R. Felzmann, and S. Springer, "Lithographiebasierte Fertigung keramischer Bauteile," *RTe Journal*, vol. 8, 2011.

[65] Y. Pan, C. Zhou, and Y. Chen, "Fast Recoating Methods for the Projection-based Stereolithography Process in Micro- and Macro-Scales," in *Proceedings of the Solid Freeform Fabrication Symposium*, 2012.

[66] R.-H. M. Schmidt, "Ultra-precision engineering in lithographic exposure equipment for the semiconductor industry," *Philosophical Transactions of the Royal Society A: Mathematical, Physical and Engineering Sciences*, vol. 370, pp. 3950–3972, Aug. 2012.

[67] C. K. Chua, K. F. Leong, and C. S. Lim, *Rapid prototyping: principles and applications*. New Jersey: World Scientific, 2nd ed., 2003.

[68] R. C. Breneman, *Phase Changes in Silica and Their Impact on Mechanical Properties in 3-D Printed Investment Casting Molds*. PhD thesis, University of Michigan, Ann Arbor, MI, 2014.

[69] Hannover. Messe, "Die machen kurzen Prozess! - DDM Systems CPT6060." [Online]. Available: http://www.hannovermesse.de/de/news/die-machen-kurzen-prozess.xhtml. [Accessed: June 20 2017].

[70] M. Conrad, "Experimental investigations and theoretical modeling of large area maskless photopolymerization with grayscale exposure," Master's thesis, Georgia Institute of Technology, Atlanta, GA, 2011.

[71] 3D. Systems, "ProX 950." [Online]. Available: https://www.3dsystems.com/3d-printers/prox-950. [Accessed: June 20 2017].

[72] B. P. Friedrich, "JTEC/WTEC Panel on rapid prototying in Europe and Japan: final report–site reports," 1996.

[73] M. E. Haberer, *Fibre-resin mixing and layer formation subsystems for the rapid manufacturing of short-fibre-reinforced parts*. PhD thesis, University of Toronto, Toronto, Canada, 2001.

[74] Materialise, "Technical Specifications for Stereolithography." [Online]. Available: http://www.materialise.com/en/manufacturing/3d-printing-technology/stereolithography. [Accessed: June 20 2017].

[75] Formlabs, "Desktop SLA 3d Printing Technical Specifications." [Online]. Available: https://formlabs.com/3d-printers/tech-specs/. [Accessed: June 20 2017].

[76] Carbon, "M2 Printer." [Online]. Available: http://www.carbon3d.com/. [Accessed: June 20 2017].

Chapter 4

A feasibility study on process monitoring and control in vat-photopolymerization-based ceramic manufacturing

Abstract

Vat photopolymerization is a prominent additive manufacturing technology for the fabrication of near-net shape ceramic parts. To serve the high tech industry's needs, additive manufacturing equipment has to scale up to larger product sizes and higher, repeatable product quality. This motivates the integration of more process monitoring and control solutions into the equipment. Hence, this paper reviews the state of the art in process modelling, sensing, actuation and control for ceramic vat photopolymerization. The aim is to analyze the feasibility of real-time control schemes for the vat photopolymerization process. A comparison of time scales related to physical phenomena in vat photopolymerization, sampling rates of sensors, and response times of actuators, shows that feasibility of real-time control is governed by sensor sampling rates. With the current state of sensor technology, real-time control is only feasible in mask projection systems. Alternatively, one can resort to layer-to-layer control schemes.

This chapter has been published in *Mechatronics*, vol. 56, pp. 220–241, Dec. 2018.

4.1 Introduction

Technical ceramics for high-performance applications can be fabricated through at least seventy manufacturing techniques [1]. Most ceramic manufacturing techniques process ceramics in powder form. An alternative for the powder processing route is polymer-derived ceramics [2]. In polymer-derived ceramics, polymers acting as a precursor are transformed into ceramic components upon heat treatment. These so-called preceramic polymers can be shaped using virtually any of the conventional polymer-forming techniques such as injection molding [2]. Recently, additive manufacturing (AM) techniques are increasingly being used to fabricate near-net shape three-dimensional ceramic parts [3–5]. According to ASTM/ISO standards, these AM technologies can be classified into seven categories based on commonality in machine architecture and material transformation physics [6]. All seven AM categories can be used to produce ceramics. One of the most prominent process categories [7] is vat photopolymerization (VP), also widely known as stereolithography [8].

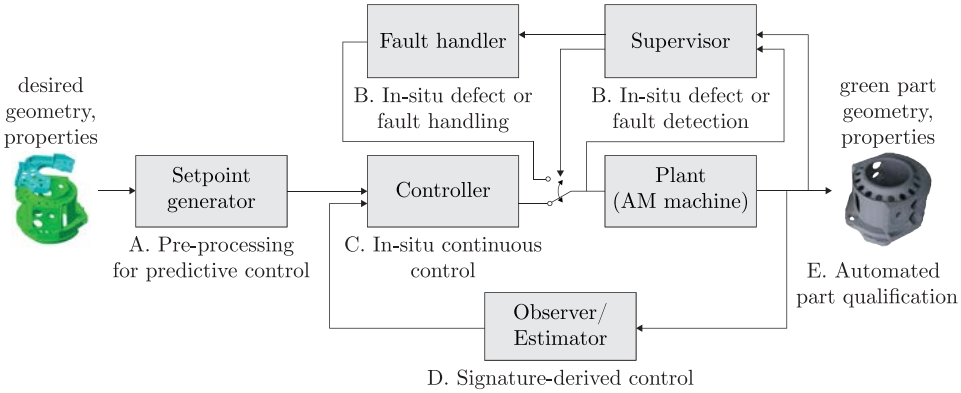

Figure 4.1: Potential AM control strategy classification scheme, based on [9].

Like any manufacturing process, AM processes involve a complex, coupled geometry and material property transformation. The objective of any process is to have a highly repeatable product quality at high flexibility and productivity [10]. AM is a highly flexible manufacturing technology as it poses few restrictions on the geometric complexity. However, the current lack of repeatable product quality, productivity and scalability, hinders the widespread adoption of AM. The advancement of AM technology calls for a systems engineering approach to address these integral challenges in the development of novel equipment concepts. For AM of ceramics specifically, the main challenges are to increase the density of the monolithic part, to increase the ceramic product sizes (large area) and wall thicknesses, and to avoid crack formation [5].

The need for modelling, sensing and control of AM processes is commonly recognized as crucial to the advancement of AM technology [11]. Although control systems have always been a fundamental part of any AM machine, the actual manufacturing process, i.e., the material and geometry transformation, is often still controlled in an open-loop fashion. In most AM equipment closed-loop control is limited to individual machine functions such as motion control or *process parameter control*, which only indirectly influence the actual process output [10]. The disturbances due to these process-independent machine state variables [12] are generally considered small compared to process variables that directly affect the quality of the output [13]. Therefore, this paper focuses on control schemes that close the loop on the actual process output.

This paper reviews the state of the art in process modelling, sensing, actuation and control for vat-photopolymerization-based ceramic manufacturing. The aim of this paper is to identify potential control strategies and analyze their feasibility. The classification scheme for potential AM control strategies by NIST [9] shown in Figure 4.1 allows for positioning novel control approaches in the AM landscape, both for metal-based [14] and polymer-based [15] AM. The intended application area is in AM using ceramic-filled resins, occasionally an excursion to pure (non-ceramic) photopolymer resins is made when this is relevant for the discussion. The paper is based on literature presented in open academic journals and conferences. The paper focuses on real-time (in-situ continuous) control of the vat photopolymerization process for AM of ceramics.

The outline of this paper is as follows. This paper starts with a description of the ceramic vat photopolymerization system in Section 4.2. Subsequently, Section 4.3 gives an overview of relevant process models from literature followed by an overview of actuators and sensors in Section 4.4. Section 4.5 then reviews current control schemes in vat photopolymerization. Finally, Section 4.6 discusses the feasibility of control strategies and the paper offers concluding remarks in Section 4.7.

4.2 System description

Vat photopolymerization is a rather novel technology to perform the shaping step in the complete process chain of polymer-derived ceramics. Hence, the vast expertise on the other process steps in the polymer-to-ceramic conversion from polymer-derived ceramics can be exploited [5]. On the other hand, vat photopolymerization of pure photopolymer resins is a commonly applied process. An extensive knowledge base of the vat photopolymerization process is available. However, given the demanding processing requirements, vat photopolymerization of ceramic materials faces different challenges than of pure polymeric materials.

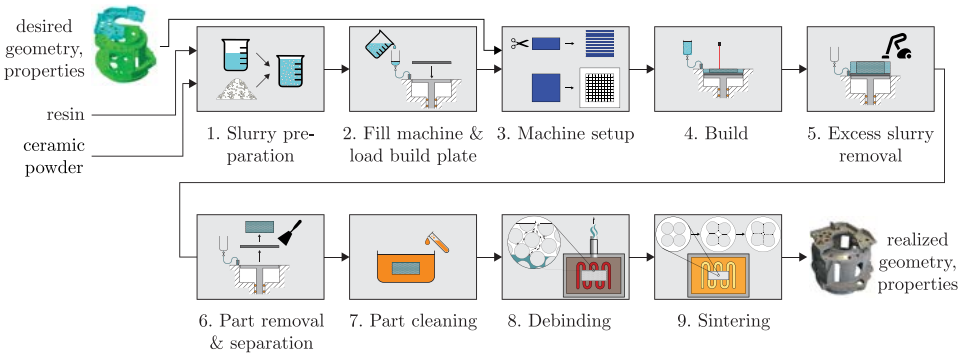

Figure 4.2: Ceramic vat photopolymerization process chain.

4.2.1 Process chain

The ceramic vat photopolymerization process encompasses a complete chain of process steps [16, 17] from product design and raw materials to the final product, as depicted in Figure 4.2. The first step is to prepare the slurry by mixing ceramic powder and photopolymer resin. In the second step, the slurry is fed into the machine. Also the build plate, i.e., the substrate onto which the part will be fabricated, is mounted. Next, the desired product geometry is uploaded to the machine and the build process is set up. In the build step the so-called "green" part is built through vat photopolymerization. The built product is still in a "green" state in which the ceramic powder is held together by cured photopolymer binder [16]. After removing excess slurry from the machine, the green part is separated from the build plate and removed from the machine. The part is cleaned and put into an oven to pyrolize the binder in a debinding step at moderate temperature. Finally, the ceramic particles are sintered at high temperature to obtain the final dense ceramic product, with associated sintering shrinkages up to 20% [18].

4.2.2 Vat photopolymerization system description

Ceramic vat photopolymerization merely replaces conventional unfilled photopolymer resins with ceramic-filled resins. However, as the ceramic filler has a significant influence on the AM build process, purpose-built machines for ceramics have been designed [7]. The main challenges due to the presence of ceramic filler arise from an increased slurry viscosity, decreased resolution due to light scattering, and sensitivity for defects during the thermal post-treatment [19]. Nevertheless, the concept of the vat photopolymerization build process is essentially the same for ceramic-filled and pure photopolymer resins: products are fabricated by selectively irradiating and consequently solidifying layers of liquid photopolymer contained in a vat [6]. Figure 4.3 schematically depicts a typical vat photopolymerization system and its

main subsystems.

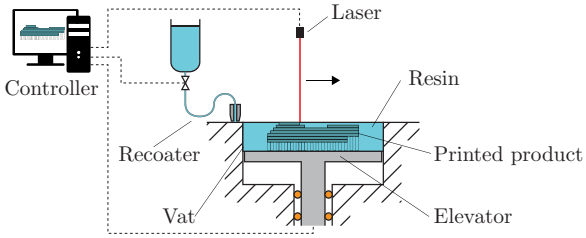

Figure 4.3: Vat photopolymerization system main subsystems.

For the vat photopolymerization system three processing steps can be distinguished [20]: preprocessing, recoating, and irradiation (or photopolymerization). The function of the preprocessing step is to convert the desired part geometry into a sequence of machine instructions stored in a build file, i.e., setpoint or reference generation.

After the build file has been transferred to the machine, the actual build process begins with recoating. The function of the recoating step is to apply a resin layer of specified thickness across the build area. To this end, first an elevator containing the build platform lowers by exactly one layer thickness. Then, a recoater device typically moves one or multiple times over the vat to deposit and recoat photopolymer resin.

Once a fresh layer of photopolymer material has been deposited, irradiation can begin. The function of the irradiation step is to perform the actual material transformation from the liquid to the solid phase through photopolymerization. To this end a light source, typically in the UV range, selectively irradiates only those parts of the vat surface that correspond to the current layer's cross-section of the product. The recoating and photopolymerization steps are repeated for each layer until the product is finished.

Recently, novel photopolymerization processing concepts have been developed, in which recoating and irradiation occur simultaneously [21, 22]. That is, parts are photopolymerized during continuous platform movement. The printing speed is either limited by resin curing or by resin flow, depending on the cross-sectional area of the momentary slice [21]. At the time of writing, such continuous photopolymerization concepts only work for particular polymer resins specifically developed for continuous irradiation, without ceramic fillers.

Current ceramic vat photopolymerization systems lack repeatable part quality, as exemplified by [23–25]. This motivates the integration of more process monitoring

and control solutions into the AM machine. A closed-loop control scheme similar to the one shown in Figure 4.1 can be envisioned for the photopolymerization step. The desired process trajectories, i.e., the references or setpoints, are generated by the preprocessor from the desired product geometry and properties. The process controller computes machine inputs that are sent to the actuator, i.e., the laser. The laser starts to irradiate the photopolymer and consequently the process, photopolymerization, takes place. The actuator and photopolymerization process together form the plant, whose outputs are the realized process trajectories. These realized trajectories may differ from the reference trajectories. To close the loop one or more of the process outputs need to be measured by a sensor. Subtraction of the measured trajectory from the reference trajectory (setpoint) provides for an error signal that can be fed back to the process controller. Such a closed-loop control scheme can be envisioned for both the photopolymerization and the recoating step. The scope of this paper is to survey options to realize closed-loop control of the photopolymerization process.

4.3 Process modelling

In essence, any manufacturing process involves a complex, coupled geometry and material property transformation [10]. Physics-based process models that describe this transformation are crucial to improve understanding of the process and ultimately optimize and control the process for improved part quality [14]. A general overview of photopolymerization process modelling is given in [6, 26]. An overview of (semi-)empirical models rather than of physics-based process models is given in [27, 28].

A fundamental question of any process model is what the purpose of the model is. The purposes of the models reported in literature vary from merely increasing our understanding to planning and controlling the process. For in-situ continuous control of the photopolymerization process, a model is desired that describes the process dynamics under transient conditions. The model should only include those physical phenomena that are considered as relevant to the model purpose [29]. This review aims to give an overview of the phenomena reported in literature and their respective modelling.

An important assumption in most photopolymerization process models is that a perfectly flat layer of photopolymer resin or ceramic slurry has been deposited in the recoating phase. Undoubtedly, the most simple model of recoating is the addition of a perfectly flat layer.

Decomposing the photopolymerization model into two submodels for the actuation or irradiation and for the cure process itself seems a sensible choice for model modularity and was proposed in [30]. Figure 4.4 shows a high level block scheme of

the irradiation and cure process model.

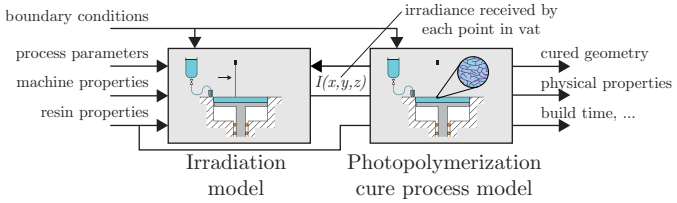

Figure 4.4: Block scheme of irradiation and photopolymerization model.

The model inputs are the process parameters, machine properties, resin properties, and boundary conditions. The cure model outputs can comprise a multitude of outputs depending on the model purpose, but arguably the ideal outputs would be the cured geometry, the physical properties, and performance indicators such as build time. The output of the irradiation model is the irradiance $I(x, y, z, t)$ received by each point in the vat as a function of time; this enables the comparison of different irradiation methods described in Section 4.4. Note however, that a bilateral coupling can exist between the two submodels as indicated by the leftwards arrow in Figure 4.4, which is the case for, e.g., photobleaching resins [31]; see Section 4.3.1. In the following sections, first the modelling of irradiation and optical phenomena is reviewed, followed by the modelling of the photopolymerization cure process.

4.3.1 Irradiation phenomena

Perhaps the most fundamental property of the laser and optics system is the spatial irradiation profile. In the laser and optics system one or more beams are generated, conditioned, shaped, and positioned or steered across the resin surface. Of interest is the resulting incident irradiance at any point in the resin $I(x, y, z)$ (in a fixed reference frame), i.e., the radiant power per unit area [W/m^2]. The resultant irradiance naturally depends on the irradiation method employed, the laser type, the geometry and layout of the optical components, and optical phenomena resulting from the interaction of light with matter.

Irradiation profile

Traditional *vector scanning* vat photopolymerization systems make use of a single Gaussian laser beam [8]. Figure 4.5 (a) shows a Gaussian beam profile, which is characterized by the $1/e^2$ half-width or radius W_0 and the peak intensity I_0 at the beam center. The beam irradiance at a point (x,y) in the focal plane of the beam is given by [6]:

$$I(x, y, 0) = I_0 e^{-\frac{2x^2}{W_0^2}} e^{-\frac{2y^2}{W_0^2}}, \; I_0 = \frac{2P_L}{\pi W_0^2} \tag{4.1}$$

where P_L is the laser output power. An ideal Gaussian beam is assumed here, but in reality the actual irradiation profile deviates from the theoretical one. Through the use of optical elements other irradiation profiles such as a top-hat, a uniform hat shaped profile, can be formed.

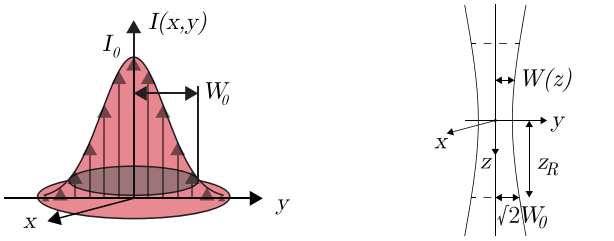

(a) beam profile (b) beam propagation

Figure 4.5: Gaussian beam.

Mask projection vat photopolymerization systems make use of a 2D array of beams. In these systems the irradiation profile of the individual beams (pixels) can be modelled in a similar fashion as in *vector scanning* vat photopolymerization systems [32, 33]. The projection system usually consists of a light source, a Digital Micromirror Device (DMD) and one or more lenses and mirrors. The irradiance profile of a single pixel can be modelled by a Gaussian distribution approximation of a point-spread function [32, 33], i.e., an expression similar to (4.1). Figure 4.6 shows a projection system, a top view of its individual pixels and the irradiation profile of a single pixel [33]. As Figure 4.6 (b) shows, the irradiation profile exceeds the boundaries of a single pixel. Hence, the light beam of a pixel will spread to its neighboring pixels, a phenomenon termed *cross-talk* [32, 34]. The ratio of the Gaussian beam width W_0 and the pixel size gives a quantative measure of the cross-talk between neighboring pixels.

The irradiation profile is an effective metric for the light intensity received by every point on the resin surface. This irradiation profile, however, is the result of light transitting an optical path from the light source via optical components to the photopolymer resin. More detailed models of the optical system can be formulated such as an analytical optics-based model of the individual components that form the light beam. Two approaches exist to modelling the optical system, namely physical optics and geometrical optics [35]. The former treats light as a wave, whereas the latter treats light as a collection of rays. Limaye developed such a geometric irradiance model for mask projection micro-stereolithography systems

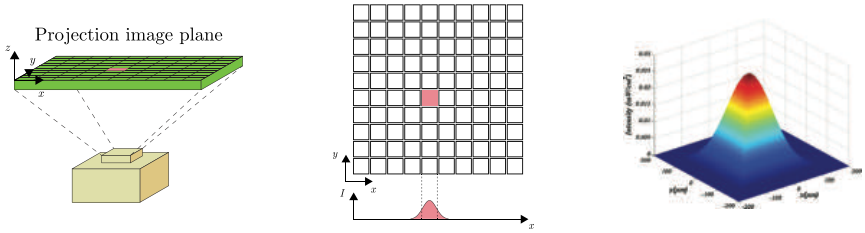

(a) projection system (b) top view (c) single pixel

Figure 4.6: Mask projection system irradiation profile; (a) and (c) adopted from [33].

based on ray tracing [35]. Zyzalo later improved the Limaye model to make it suitable for large parts [36].

Beam propagation

A Gaussian beam always diverges from or converges to a point along the beam propagation axis [37]. Figure 4.5 (b) shows the variation of the Gaussian beam half-width $W(z)$ along the z-axis. The beam intensity decreases along the z-axis and at a distance z_R from the focal point, i.e., the Rayleigh range, the beam half-width equals $\sqrt{2}W_0$ and the maximum intensity equals $\frac{1}{2}I_0$. In traditional vat photopolymerization systems, the machine is designed such that the focal point lies on the resin surface [20]. Although any Gaussian beam exhibits beam propagation, the only work known to the authors to explicitly include the effect in modelling the vat photopolymerization process is the model by Sager [37].

Attenuation & absorption

A fundamental phenomenon and challenge in vat photopolymerization is the attenuation of light travelling through photopolymer resin. Attenuation is the loss of radiant flux intensity due to either absorption or scattering. The result is that the irradiance at the resin surface attenuates with the distance or depth travelled through the resin. Attenuation due to absorption is described by the Beer-Lambert law [38], which states that absorbance A is directly proportional to the path length l and concentration $[c]$ of the attenuating species:

$$A = \varepsilon[c]l = \log_{10}\left(\frac{I_0}{I}\right) \tag{4.2}$$

where I_0 is the ingoing light intensity, I is the exiting light intensity and ε is the extinction coefficient or molar attenuation coefficient. Rearranging the terms in (4.2) and substituting l for z gives an expression for the irradiance as a function of depth z [39]:

$$I(z) = I_0 e^{-\ln(10)\cdot\varepsilon[c]z} \tag{4.3}$$

where the ln(10) term originates from the conversion from base-10 to base-e logarithms. Note that different conventions as to whether absorbance is decadic (base-10) or Napierian (base-e) is used, so the term ln(10) is sometimes omitted. In the remainder of this paper the Napierian extinction coefficient $\varepsilon' = \ln(10) \cdot \varepsilon$ is used.

In vat photopolymerization this expression is often written as a function of the penetration depth D_p, which is defined as the depth z at which the irradiance has decreased to a factor $e^{-1} \approx 0.37$ [6, 8], see Figure 4.7:

$$I(x, y, z) = I_0 e^{-\frac{z}{D_p}} \tag{4.4}$$

The penetration depth is related to the attenuation coefficient and concentration as follows [8]:

$$D_p = \frac{1}{\varepsilon'[c]} = \frac{1}{\ln(10) \cdot \varepsilon[c]} \approx \frac{1}{2.303 \cdot \varepsilon[c]} \tag{4.5}$$

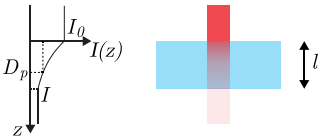

Figure 4.7: Beer-Lambert absorption.

Figure 4.7 illustrates the effect of Beer-Lambert attenuation. For photopolymers, the species of interest is the initiator so the extinction coefficient and (instantaneous) concentration of the photoinitiator is taken. In some resins additives are added such as light absorbers [40]. In this case the material consists of multiple attenuating species and then the absorbance A depends on the concentrations and extinction coefficients of the individual species:

$$A = l \cdot \sum_{i=1}^{N} \varepsilon_i[c_i] \tag{4.6}$$

The preceding expressions for attenuation assume a uniform and constant molar attenuation coefficient and concentration along the path. During photopolymerization however, the absorbance of the photoinitiator can change upon photolysis and diffusion of reactive species can take place [39]. In *photobleaching* resins, the absorbance decreases during photopolymerization and as a result the irradiance is attenuated less as time proceeds [41]. In *non-photobleaching* resins, the Beer-Lambert law for uniform and constant species (4.3) suffices [39]. To model the time-varying absorbance in photobleaching resins, expressions for both the concentration $[c]$ and

intensity I as a function of depth z need to be composed [41, 42]. To this end, the differential form of the Beer-Lambert law is used [43]:

$$\frac{\partial I(z)}{\partial z} = -\varepsilon'[c](z)I(z) \tag{4.7}$$

from which the Beer-Lambert law for uniform and constant absorbance (4.3) can be derived.

Another approach to model the difference in attenuation between cured and uncured resin was proposed by Limaye in a "transient layer cure model" [35]. For the resins used, the penetration depth of the cured part significantly differed from the penetration depth of uncured resin, i.e. the penetration depth of cured resin tended to infinity. Hence a model was developed that takes into account this difference in penetration depths.

Scattering

As described earlier, attenuation of light intensity occurs due to either aborption or scattering [31]. Scattering is an optical phenomenon in which the direction of light (radiation) is changed due to non-uniformities in the medium it is transmitted through as illustrated by Figure 4.8. It is beyond the scope of this work to give a complete overview of all the modelling approaches to light scattering, but several key publications are referred to. Sun & Zhang developed a Monte Carlo ray-tracing technique to compute the spatial irradiance distribution and used this for a bilaterally coupled kinetic photopolymerization model through the photoinitiator concentration distribution [31, 44]. Scattering can ultimately result in a *decrease* in vertical dimensions (cure depth) and an *increase* in lateral dimensions (broadening) [31].

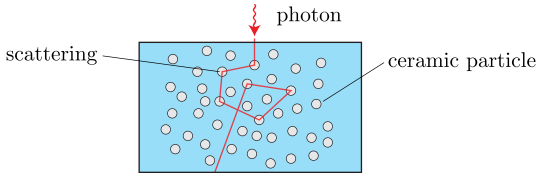

Figure 4.8: Scattering due to ceramic particles, adopted from [31].

Liao gives an overview of modelling techniques of scattering in ceramic slurries for vat photopolymerization [45]. Griffith and Halloran developed an analytical expression for the effective extinction coefficient of ceramic slurries, which is equivalent to penetration depth D_p [46]:

$$D_p = \frac{3\tilde{Q}\Delta n^2}{2\langle d \rangle n_0^2} \tag{4.8}$$

where $\tilde{Q}$ is the scattering efficiency, $\langle d \rangle$ is average particle size, $\Delta n = n_p - n_0$ is the refractive index difference between the ceramic particle n_p and resin n_0, and $\tilde{Q}$ is a scattering efficiency term. A different expression for the penetration depth of ceramic slurries was developed by Tomeckova, Gentry and Halloran [7, 16, 47]

Refraction & optical self-focusing

Refraction is an optical phenomenon in which the direction of light is changed due to a change in the medium it is transmitted through. Refraction can occur for non-zero incident angles at the vat surface, where the medium changes from air to resin, see Figure 4.9 (a). Sager developed a model for vector scanning vat photopolymerization that takes into account non-zero incident angles and resulting refraction, which changes the spatial irradiance distribution $I(x, y, z)$.

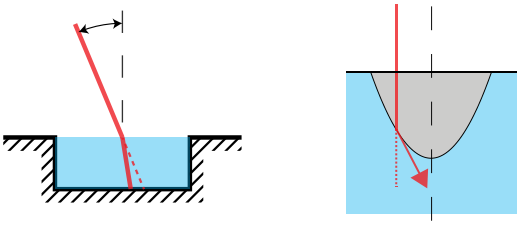

(a) at surface (b) at interface

Figure 4.9: Refraction phenomena.

During photopolymerization the resin shrinks, the density increases and hence the refractive index increases as well [8]. This is the case for refraction at the interface, as shown in Figure 4.9 (b). Brulle et al. developed a Monte-Carlo model to simulate refraction at the solid-liquid interface [48]. Another Monte-Carlo model for the propagation of light in photopolymerization was developed by Schmocker [49].

Another effect known in photopolymerization is the optical self-focusing effect [8, 50]. The non-homogeneous spatial irradiance distribution causes a non-homogenous spatial density and refractive index distribution. So in fact refraction could take place at any portion of the resin that is being photopolymerized and this could lead to an effect called 'self-focusing'. Jariwala developed an optical model of a mask projection system (refer to Figure 4.26) to investigate the effect of optical self-focusing [50]. Jariwala concluded that the optical self-focusing effect was negligible for the shallow incident angles and small refractive index differences for the used system and resin.

Beam positioning

The expression for the irradiance distribution (4.1) is for the situation of a stationary beam. The ability to position the beam is essential to the system functionality and therefore modelling beam movement more closely represents the actual process [51]. To this end, a fixed reference frame (x, y, z) is defined and the original reference frame is named (x', y', z') and is now positioned at $(x, y) = (x_0, y_0)$ as shown in Figure 4.10.

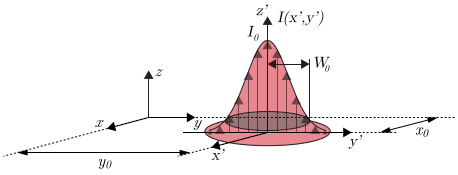

Figure 4.10: Gaussian beam profile in fixed reference frame.

The irradiance $I(x, y, z)$ then becomes:

$$I(x, y, z) = I_0 e^{-\frac{2(x-x_0)^2}{W_0^2}} \cdot e^{-\frac{2(y-y_0)^2}{W_0^2}} \cdot e^{-\frac{z}{D_p}} \tag{4.9}$$

The beam is positioned in the xy-plane by altering the values of the position coordinates x_0 and y_0.

4.3.2 Photopolymerization cure process phenomena

As discussed at the beginning of Section 4.3, the output of the irradiation model is the irradiance $I(x, y, z)$ received by each point in the resin vat. Upon irradiation a photoinitiated polymerization reaction takes place and the liquid resin is locally solidified. The desired outputs of a photopolymerization cure process model would be performance indicators such as the cured geometry, physical properties and build time. Due to the many physical phenomena playing a role in the reaction, models computing all these performance indicators are likely to require a high level of complexity. Before going into detail on these phenomena, a simple and insightful process model is described that enables computation of the cured shape geometry.

Exposure and the exposure threshold model

The extent of resin cure is governed by the amount of energy received rather than the power. The exposure E is the time integral of irradiance I and has the units of energy per unit of area [J/m^2]. Simple integration over time of the spatially distributed irradiance $I(x, y, z)$ gives the exposure $E(x, y, z)$. The most simple cure process model for pure resins is the *exposure threshold model* developed by Jacobs [8, 52]. Central to the exposure threshold model is the assumption that the

resin transition from the liquid to the solid phase occurs at the gel point and that the exposure threshold for the formation of gel is the critical exposure E_c.

The exposure threshold model simply states that every point in the vat for which holds that $E \geq E_c$ is solidified and all other points remain liquid. Assuming a flat layer of resin with constant Beer-Lambert absorption and a laser beam with a Gaussian irradiance distribution, the cured geometry can be easily calculated. This can be done numerically for an arbitrary scan trajectory $(x_0(t), y_0(t))$ by integrating the expression for a moving Gaussian beam (4.9):

$$\begin{aligned} E(x,y,z,t) &= \int_t I(x,y,z,t)dt \\ &= \int_t I_0 e^{-\frac{2(x-x_0(t))^2}{W_0^2} - \frac{2(y-y_0(t))^2}{W_0^2} - \frac{z}{D_p}} dt \end{aligned} \tag{4.10}$$

and subsequently comparing to the exposure threshold E_c. Jacobs however, derived an analytical expression for the cured line shape of a line scan along the x-axis. Figure 4.11 visualizes the exposure threshold model for a line scan with speed V_s along the x-axis. Integration of $x_0(t)$ from $-\infty$ to ∞ gives a very good approximation of the exposure received by every point in the yz-plane at any point along the x-axis [6, 8]:

$$E(x,y,z) = \underbrace{\frac{\sqrt{2}P_L}{\sqrt{\pi}V_s W_0}}_{E_{max}} \cdot \underbrace{e^{-\frac{2y^2}{W_0^2}}}_{\substack{\text{Gaussian} \\ \text{distribution}}} \cdot \underbrace{e^{-\frac{z}{D_p}}}_{\substack{\text{Beer-Lambert} \\ \text{absorption}}} \tag{4.11}$$

where E_{max} is the maximum exposure, which is received on the x-axis at the surface.

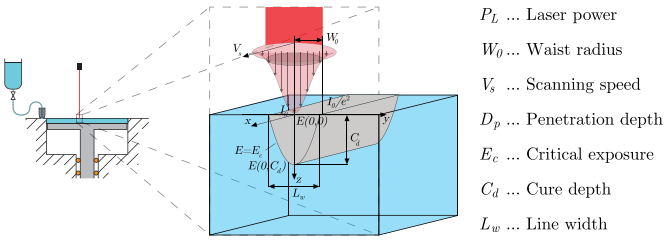

Figure 4.11: Exposure threshold model for a line scan.

As the figure shows, the cured line shape can be obtained by determining the locus of points at which $E = E_c$ from (4.11); this yields a parabolic shape. All the points inside the locus are solidified and all points outside the locus remain liquid. The cured line shape is characterized by two dimensions, namely the cure depth C_d and the linewidth L_w, which are both determined from the locus of points [52]:

$$C_d = D_p \ln\left(\frac{E_{max}}{E_c}\right) = D_p \ln\left(\frac{\sqrt{2}P_L}{\sqrt{\pi}W_0 V_s E_c}\right) \tag{4.12}$$

$$L_w = W_0\sqrt{\frac{2C_d}{D_p}} \tag{4.13}$$

By rewriting the expression (4.12) for laser scanning speed V_s, for a desired cure depth and given resin parameters D_p, E_c and laser power P_L, the required scanning speed can be calculated [52]. Sager extended the exposure threshold model to include the effects of an incident angle, the resulting refraction and the varying beam waist $W(z)$ (see Figure 4.5 (b)), and solved it using numerical simulation [37].

The exposure threshold model only holds for non-ceramic resins. The effects of scattering on the cured part shape can be considerable. Figure 4.12 illustrates the effect of scattering on the cured line shape for a near top-hat irradiation profile [7,53]. Note that the cured linewidth can be several times wider than the incident beam itself. Empirical expressions for the cure depth and linewidth of ceramic suspensions were derived by Gentry, Tomeckova and Halloran [7, 16].

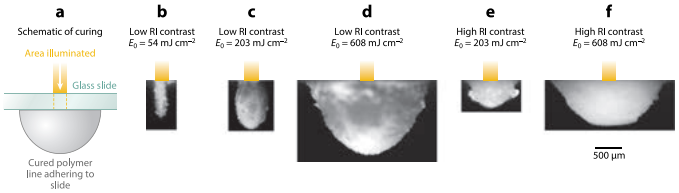

Figure 4.12: Cured line shape for different refractive index (RI) values, adopted from [7].

Although the exposure threshold model is a simple model to determine the geometric shape of the cured part and might prove useful for control purposes, it is arguably an oversimplification of the actual photopolymerization process [54]. Figure 4.13 illustrates the complexity of the photopolymerization reaction and the many physical phenomena that play a role. On the contrary, the simple exposure threshold model assumes that exposure is additive and does not take any of these phenomena into account except the phase transition from liquid to solid at the gel point.

Photopolymerization cure process mechanism

Photopolymerization is a light-initiated chemical reaction in which small molecules termed *monomers* are linked together or combined into larger macromolecules termed *polymers* [55]. The photopolymer resin is generally formulated from monomer and photoinitiator and possibly other fillers or additives, such as reactive diluents,

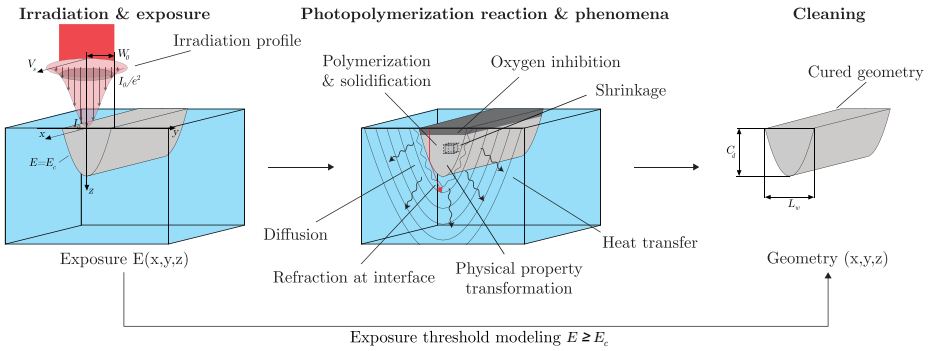

Figure 4.13: Photopolymerization complexity illustrated by the many physical phenomena involved; image inspired by [54].

stabilizers and ceramic particles [6]. Two resin types commercially available are acrylates on the one hand and epoxy and vinylether on the other. The accompanying cure mechanisms are free-radical polymerization and cationic polymerization respectively.

The first resins used in vat photopolymerization were acrylates and therefore free-radical photopolymerization kinetics are characterized the most. Most vat photopolymerization resins are acrylate-epoxy blends, so the cationic photopolymerization kinetics should be characterized as well [54]. The cure mechanism described hereafter is free-radical polymerization, while the cationic polymerization mechanism is similar, but more complex to model [56].

The cure mechanism in *free-radical photopolymerization* consists of a sequence of four steps: radical formation, initiation, propagation and termination [8, 54, 55]. Figure 4.14 shows the cure mechanism in chemical equations. The first step radical formation is often categorized as part of the initiation step. In the radical formation step, the photoinitiator I is dissociated with a rate constant k_d upon absorption of photons having energy hv. In the initiation step, the primary radicals $R\cdot$ react with monomer M to produce the chain initiating radical $P_1\cdot$ with a initiation rate constant k_i. During propagation, the chain initiating radical $P_1\cdot$ grows due to the successive addition of monomer. Each addition of a monomer molecule M increases the polymeric radical P_n by one monomer molecule to P_{n+1}. The rate constant for propagation is denoted by k_p. Finally, the polymer chains stop growing in the termination step with a rate constant k_t due to combination or disproportionation.

The polymerization cure mechanism can be mechanistically modelled by setting up conservation laws for mass and energy, using the kinetic rate constants. More specifically, the species balance can be used to calculate the concentrations of components such as the monomer, photoinitiator and polymeric radical. A number of researchers have developed photopolymerization process models using this approach for vat photopolymerization specifically [31,51,54,57,58] and for photopolymerization

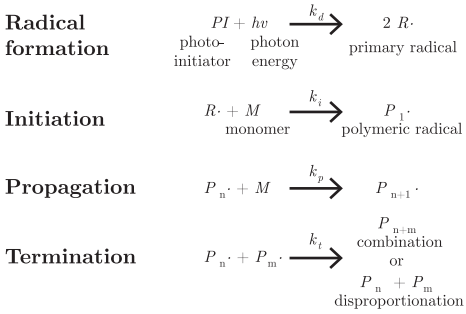

Figure 4.14: Free-radical photopolymerization cure mechanism.

in general [39, 59]. For example, Sun et al. [31] modelled the attenuation of light I, photoinitiation, propagation and termination respectively as follows:

$$\frac{dI}{dz} = -\varepsilon'[PI]I \tag{4.14}$$

$$\frac{d[PI]}{dt} = R_i = -\phi\varepsilon'[PI]I \tag{4.15}$$

$$\frac{d[M]}{dt} = -R_p = -k_p[P\cdot][M] \tag{4.16}$$

$$\frac{d[P\cdot]}{dt} = R_i - R_t = \phi\varepsilon'[PI]I - k_t[P\cdot]^2 \tag{4.17}$$

where ϕ is the quantum yield or efficiency, the terms between brackets represent concentrations, R_i, R_p, R_t are the rates of initiation, propagation and termination respectively, and k_p and k_t are the rate constants for propagation and termination respectively. Similar differential equations are derived by, e.g., Tang [54].

Degree of (monomer) conversion

The extent of polymerization is quantified by the degree of monomer conversion, also known as degree of cure, cure level and fractional conversion. Bartolo et al. describe the relationship between the glass temperature T_g and degree of cure α [26]. A plot of the degree of conversion α as a function of exposure E typically shows a sigmoidal curve [7, 26, 48], as shown in Figure 4.15.

After an induction period due to consumption of radicals by inhibitor such as oxygen present in the resin, the viscosity rapidly increases up to the gel point. The gel point is reached at the critical exposure E_c and represents the point of abrupt transformation from viscous liquid to a gel. As the figure shows, the degree of conversion reaches an asymptote lower than 100%. Rather than using an *exposure threshold* to model whether the gel point has been reached, Tang proposes a *degree*

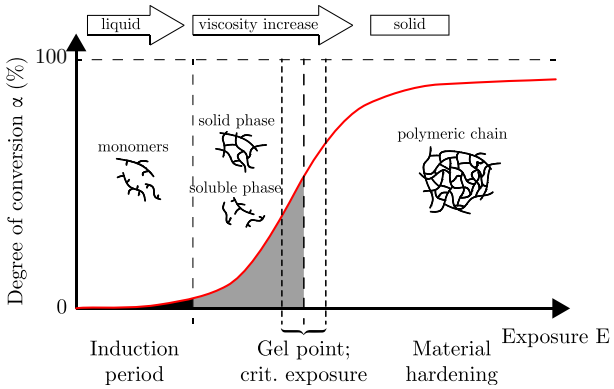

Figure 4.15: Degree of conversion versus exposure; image adapted from [60].

of cure threshold [54]. The main advantage of the latter is that the polymerization reaction and transient intensity effects are taken into account, rather than assuming that conversion simply increases with exposure independently of process dynamics.

Acrylate molecules have carbon-carbon double bonds that are converted into two single bonds, often referred to as double bond conversion in literature [61]. The degree of conversion can be calculated from the monomer concentration $[M]$ by simply taking the fraction of reacted monomer to the initial monomer concentration $[M_0]$ [39, 62]:

$$\alpha = \frac{[M_0] - [M]}{[M_0]} \tag{4.18}$$

Apart from the (semi-)mechanistic models based on species balances, phenomenological models were developed as well that calculate the degree of cure α directly [26, 60]. The phenomenological models are given by the following equation:

$$\frac{d\alpha}{dt} = k_c(T) f(\alpha) \tag{4.19}$$

where $\frac{d\alpha}{dt}$ is the reaction rate, $f(\alpha)$ is a function of conversion and $k_c(T)$ the temperature-dependent rate constant. In its simplest form, the expression for $f(\alpha)$ is:

$$f(\alpha) = (1 - \alpha)^n \tag{4.20}$$

where the constant n corresponds to the reaction order. Moreover, the simplest expression for $k_c(T)$ is given by the Arrhenius law:

$$k_c(T) = k_0 e^{\frac{-E}{RT_{\text{abs}}}} \tag{4.21}$$

where k_0 is a pre-exponential factor, E is the activation energy, R the gas constant, and T_{abs} the absolute temperature. Thus the expression for the reaction rate becomes:

$$\frac{d\alpha}{dt} = k_0 e^{\frac{-E}{RT_{\text{abs}}}} \cdot (1-\alpha)^n \tag{4.22}$$

Variations of $f(\alpha)$ are used in literature to represent so-called autocalytic process, such as in the control-oriented process model by Yebi where $f(\alpha) = \alpha^m(1-\alpha)^n$ [63].

Oxygen inhibition

In free-radical polymerization, a typical degree of conversion plot over time shows an induction period that is accountable to oxygen inhibition [48], see Figure 4.15. In inhibition of the photopolymerization reaction, an inhibitor species such as oxygen or an other intentionally added inhibitor reacts with the growing chain rather than monomer and stops chain growth. The oxygen concentration dissolved in the resin depends on the system configuration; in free-surface systems the resin is irradiated at the resin surface and oxygen particularly inhibits at the surface where it is absorbed from the air [7]. In constrained-surface systems the resin is irradiated from the bottom and oxygen is replenished from the top as shown in Figure 4.16. A method to remove oxygen from the resin is to purge the build chamber with nitrogen [64]. The effect of oxygen inhibition in ceramic suspensions was researched by several researchers [65, 66]

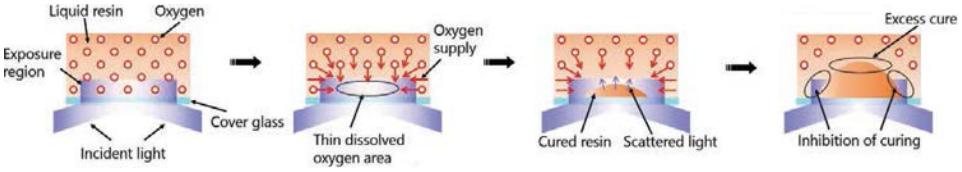

Figure 4.16: Oxygen replenishment in a constrained-surface sytem; adopted from [64].

To model oxygen inhibition, the cure mechanism in Figure 4.14 is expanded with an inhibition reaction and the species balance for oxygen can be set up [39, 58]. To this end, Altun extended the model by Tang [54] with oxygen inhibition [58]. Although oxygen inhibition is generally seen as a negative effect, it is an essential mechanism in constrained surface systems with continuous platform motion [21] to prevent adherence to the window.

Heat transfer

Since the photopolymerization reaction is an exothermic process, heat is generated during photopolymerization [8, 54]. Physical phenomena related to heat transfer

such as heat storage and conduction are usually modelled by the heat equation. The heat equation is derived from the conservation law for energy and is given by [39, 54, 62]:

$$\frac{\partial \rho c_p T}{\partial t} = k\nabla^2 T + \Delta H_p R_p \tag{4.23}$$

where ρ is density, c_p specific heat, T temperature, and k is thermal conductivity. Heat generation is modelled as the source term $\Delta H_p R_p$, which is the product of the heat of polymerization ΔH_p and rate of polymerization R_p (4.16). Some works also include the heat by absorption of laser radiation [39, 63].

The choice of thermal boundary conditions can have a significant influence as exemplified by Yebi's control scheme [63] outlined in Section 4.5.1. Tang included natural heat convection at the free surface boundary [54]. Another important consideration is the change in (material) constants due to temperature changes. Although not explicitly evident from the formulas (4.14) to (4.17), the temperature dependencies of the rate constants are often modelled using the Arrhenius law [39,54] such as in (4.21). Other material "constants" such as density ρ are temperature dependent as well.

Mass transfer

Mass transfer occurs when mass moves from one location to another. Two types of mass transfer occur in vat photopolymerization, namely diffusion and convection of the chemical species. Diffusion of reactive species is modelled by adding diffusion constants to the species balance equations (4.15) to (4.17). The equations then become [39, 40, 54]:

$$\frac{d[PI]}{dt} = D_{PI}\nabla^2[PI] - \phi\varepsilon'[PI]I \tag{4.24}$$

$$\frac{d[M]}{dt} = D_M\nabla^2[M] - k_p[P\cdot][M] \tag{4.25}$$

$$\frac{d[P\cdot]}{dt} = D_{P\cdot}\nabla^2[P\cdot] + \phi\varepsilon'[PI]I - k_t[P\cdot]^2 \tag{4.26}$$

where D_{PI}, D_M, and $D_{P\cdot}$ are the diffusion constants for the photoinitiator, monomer and polymeric radicals respectively. Oxygen diffusion was similarly modelled by Altun [58]:

$$\frac{\partial[O_2]}{\partial t} = D_O\nabla^2[O_2] - R_{in} \tag{4.27}$$

where R_{in} is the inhibition rate. Convection is the bulk motion of fluid and can be caused by shrinkage of the photopolymer; to model this effect it should be included in the mass balance equation [54]. Nakaga et al. studied the flow due to photopolymerization shrinkage [67].

Shrinkage & distortion

Resin shrinkage is the main reason for internal stresses and resulting part distortion such as warpage and curl and defects such as cracks, especially for nonuniform shrinkage [20]. In photopolymerization, shrinkage occurs due to two effects: thermal expansion and specific volumetric shrinkage. Thermal expansion occurs due to temperature fluctuations caused by exothermic heat generation. Specific volumetric shrinkage occurs due to carbon-carbon double bond conversion and the accompanying decrease in average distance between groups; consequently density increases [8]. An important phenomenon is that shrinkage lags exposure [6, 8]. Flach & Chartoff modelled this lag between specific volumetric shrinkage and monomomer conversion for a line scan [68] as an extension to their process model [57]. Narahara et al. argue that the resin first shrinks due to volumetric shrinkage proportional to reaction extent, then expands thermally due to heat generation, and finally shrinks again due to cooling [69].

Several researchers developed models to quantify volumetric shrinkage and/or thermal expansion using finite element method (FEM) models [70–73]. Vatani et al. used classical laminate theory rather than FEM to predict part distortion [74]. These simulation models can be used to limit distortion through process planning optimization. Figure 4.17 shows a comparison by Jiang between FEM distortion results and an actual built part [75].

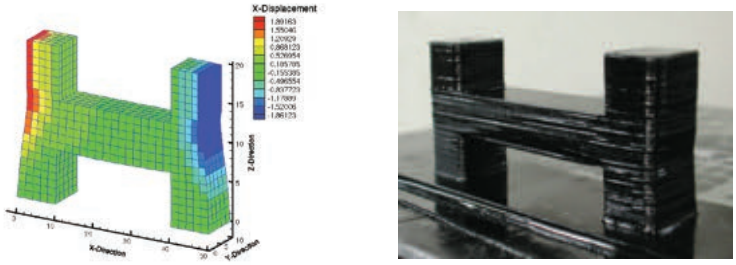

(a) FEM results (b) actual built part

Figure 4.17: Comparison of FEM distortion results with actual built part; adopted from [75].

Although most models are developed for pure photopolymer resins, a noteworthy FEM model is developed in the work of Wu [25] for stress, crack and delamination development in ceramic vat photopolymerization parts.

Mechanical property variation

Although fundamental to the applicability of functional parts, models of the final part's mechanical properties as a function of processing parameters are scarce.

Already in the early days of vat photopolymerization, Jacobs developed an empirical model for the elastic modulus as a function of exposure [8]. The so-called photomodulus is defined as the Young's modulus for parts in the green state and serves as a measure for green part strength. The photomodulus as a function of exposure is described by the following equation [8]:

$$\frac{Y}{Y_{max}} = 1 - e^{-\beta\left(\frac{E}{E_c}-1\right)},\ \beta = \frac{K_p E_c}{Y_{max}} \tag{4.28}$$

where Y_{max} is the maximum achievable modulus and β is a resin constant that is a function of the photomodulus coefficient K_p. Huang & Jiang use a slightly modified version of the photomodulus model to include temperature dependency in their FEM model [73].

To the author's knowledge only two researchers have tried to model the mechanical resin characteristics during photopolymerization with a visco-elastic material model [56, 76]. The obtained material model can be used as an input for FEM models [56] and can be linked to the reaction kinetics [77].

4.3.3 Comparison of existing process models

Models describing the phenomena outlined in the previous sections are compared in Table 4.1. Note that this table is far from complete, since a plethora of other models is available that describe photopolymerization and related phenomena. An important model property is whether or not the model takes the presence of ceramic fillers into account and the irradiation method employed in the system. Concerning the curing mechanism, differences exist between the models that do not become evident from the table due to space limitations. Although all models that contain a cure kinetics model describe a free radical curing mechanism, they do not all explicitly model the four steps comprising the mechanism (radical formation, initiation, propagation, termination). Moreover, it becomes evident from the table that mask projection system models typically do not incorporate a cure kinetics model, probably due to the computational load associated with simulating many pixels at once.

Model #	Process model	Ceramic loaded?	Irradiation method	Irradiation profile	Beam propagation
1	Exposure threshold model	No	Vector scanning	Gaussian	No
2	Analytical irradiance model	No	Vector scanning	Gaussian	Yes
3	Transient layer cure model	No	Mask projection	Exact ray traced pixels	Yes
4	Nonisothermal photopolymerization model	No	Vector scanning	Gaussian	No
5	Stereolithography simulation model	No	Vector scanning	Gaussian	No
6	SLA cure model	No	Vector scanning	Gaussian & top-hat	No
7	Deterministic photopolymerization model	No	Vector scanning	Gaussian	
8	Comprehensive free radical photopolymerization model	No	NA	1D	No
9	1D UV curing process model	No; GFRP	NA	1D	No
10	Ceramic μSL model	Yes	Vector scanning	Gaussian; Monte Carlo ray tracing	Yes
11	Effective Beer's law model	Yes	Vector scanning	Gaussian	No
12	Predictive ceramic photopolymerization model	Yes	Vector scanning	Gaussian	No
13	General photocurable model of resin with microparticles	Yes	Vector scanning	Gaussian	No
14	Space-resolved photopolymerization model	No	Vector scanning	Gaussian with noise	No
15	Mathematical model for photopolymerization	No	Vector scanning	Gaussian	No
16	Photo-thermal-kinetic model	No	Vector scanning	Gaussian	No
17	STLG-FEM	No	Vector scanning	Gaussian	No
18	Semi-empirical material model	No	Mask projection	Exact ray traced pixels	Yes
19	Pixel based solidification model	No	Mask projection	non-axisymmetric Gaussian	No
20	Analytical model for scanning-projection based SL	No	Scanning mask projection	Gaussian	No
21	Diffusion-limited photopolymerization model	No	Vector scanning	Gaussian	No
22	Thermal model of stepless rapid prototyping process	No	NA	1D	No
23	Dynamic FEM model	No	Vector scanning & mask projection	Gaussian	No
24	Phenomenological FEM model	No	Vector scanning	Gaussian	No
25	Thermal deformation model	No	Vector scanning	Gaussian	No

Table 4.1: Comparison of existing photopolymerization process models.

Model #	Attenuation	Scattering	Refraction	Beam motion	Curing mechanism	DOC	Oxygen inhib.
1	Beer-Lambert	No	No	Scanning at constant speed	None	No	No
2	Beer-Lambert	No	At vat surface	Scanning	None	No	No
3	time-varying Beer-Lambert	No	No	No (varying bitmaps)	None	No	Not explicit
4	time-varying Beer-Lambert	No	No	Stationary & scanning	Free radical	Yes	No
5	time-varying Beer-Lambert	No	No	Stationary	Free radical	Yes	No
6	time-varying Beer-Lambert	No	No	Scanning at constant speed	Free radical	Yes	No
7	Beer-Lambert	No	No	Scanning at constant speed	Free radical	Yes	Yes
8	time-varying Beer-Lambert	No	No	Stationary	Free radical	Yes	Yes
9	Beer-Lambert	No	No	Stationary	Free radical	Yes	No
10	time-varying Beer-Lambert	Mie theory	No	Stationary	Free radical	Yes	No
11	Beer-Lambert	Yes	No	Scanning at constant speed	None	No	No
12	Beer-Lambert	Yes	No	Scanning at constant speed	None	No	No
13	Beer-Lambert	Yes	No	Scanning at constant speed	None	No	No
14	time-varying Beer-Lambert	No	At cure front	Stationary	Free radical	No	No
15	Beer-Lambert	No	No	Stationary	None	Yes	No
16	Beer-Lambert	No	No	Stationary	Free radical	Yes	No
17	Beer-Lambert	No	No	Stationary	Free radical + thermal	Yes	No
18	Beer-Lambert	No	No	Stationary	None	No	No
19	Beer-Lambert	No	No	Stationary	None	No	No
20	Beer-Lambert	No	No	Scanning at constant speed	None	No	No
21	time-varying Beer-Lambert	No	No	Stationary	Free radical	Yes	No
22	time-varying Beer-Lambert	No	No	Stationary	Free radical	No	No
23	time-varying Beer-Lambert	No	No	Scanning at constant speed	None	No	No
24	Beer-Lambert	No	No	Scanning at constant speed	None	No	No
25	time-varying Beer-Lambert	No	No	Scanning at constant speed	None	Yes	No

Table 4.1: Comparison of existing photopolymerization process models (cont.).

Model #	Heat transfer	Mass transfer	Shape formation	Shrinkage	Mechanical property variation	Spatial dim.	Ref.
1	No	No	At exposure threshold	No	No	2D	[52]
2	No	No	At exposure threshold	No	No	3D	[37]
3	No	Not explicit	At exposure threshold	No	No	3D	[35]
4	Polymerization heat	No	Yes	Polymerization	No	2D/3D	[51, 57, 68]
5	Polymerization heat	No	No	No	No	3D	[78]
6	Polymerization heat + convection at surface	Monomer & radical diffusion	At conversion threshold	No	No	2D	[54]
7	Polymerization heat	Monomer, radical & oxygen diffusion	At conversion threshold	No	No	2D	[58]
8	Polymerization heat + laser absorption	Diffusion of all species	No	No	No	1D	[39]
9	Polymerization heat	No	No	No	No	1D	[63]
10	No	No	Yes	No	No	2D	[31]
11	No	No	At exposure threshold	No	No	2D	[46]
12	No	No	At exposure threshold	No	No	2D	[47, 53]
13	No	No	At exposure threshold	No	No		[79]
14	No	No	Yes	No	No	2D	[48]
15	No	No	Yes	No	No	2D	[59]
16	Polymerization heat	No	No	No	No	2D	[80]
17	Polymerization heat	No	No	Polymerization	No	2D	[26]
18	No	No	At exposure threshold	No	No	2D	[50]
19	No	No	At exposure threshold	No	No	3D	[33]
20	No	No	At exposure threshold	No	No	2D	[81]
21	Polymerization heat	Initiator & radical diffusion	No	No	No	2D	[40]
22	Polymerization heat + laser absorption	No	No	No	No	1D	[82]
23	Polymerization heat	No	No	Polymerization + thermal	E-modulus	3D	[73, 83]
24	No	No	Element birth	Polymerization	No	3D	[71]
25	Polymerization heat	No	No	No	No	2D	[62, 72]

Table 4.1: Comparison of existing photopolymerization process models (cont.).

4.4 Process sensing & actuation

Sensors and actuators are key components of any control system. Since there is a duality between sensing and actuation, they are often treated as pairs in control system analysis. Hence some sensor properties such as sensor placement must be considered in tandem with actuator properties such as actuator placement (colocation). In vat photopolymerization a similar duality exists as well for instance in the spatial dimensionality of the sensor and the actuator.

4.4.1 Process actuation

The goal of the photopolymerization step is to transform the material from the liquid to the solid phase by irradiating with the actuator, i.e., the light source. In the following section, alternative initiation methods for the polymerization reaction are surveyed. Subsequently, the methods to irradiate the layer are classified.

Initiation method

The way the polymerization reaction is initiated has a major influence on the system architecture. Most polymerization reactions are thermal processes and are often initiated by supplying heat. In photopolymerization, the polymerization reaction is initiated by light exposure. Many other stimuli can be used to initiate the polymerization reaction as well, such as electron beams, X-rays, gamma rays, plasma, microwaves, pressure and addition of a catalyst [84, 85]. Initiation by exposure to light forms a very elegant and powerful excitation approach [84] and is most commonly used in the additive manufacturing context. Figure 4.18 shows the initiation mechanisms for photopolymerization and thermal polymerization.

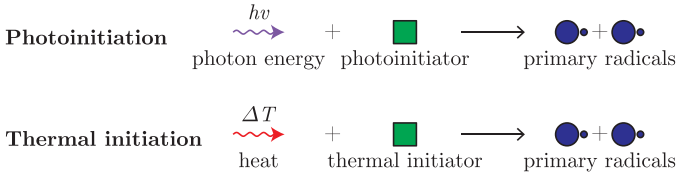

Figure 4.18: Polymerization initiation mechanisms.

Bartolo et al. developed a so-called stereo-thermal-lithography system that uses both UV radiation and IR radiation to initiate a polymerization reaction in a resin that contains both photoinitiators and thermal initiators [26, 86]. More recently, an infrared stereolithography system was developed that uses solely IR radiation to thermally initiate a polymerization reaction [60]. It is important to note that photoinitiators can be thermally initiated as well at a high enough temperature, as demonstrated by Tang [54].

Irradiation method

The method by which the layers are irradiated by the light source, can be classified according to a classification scheme adapted from [6] and shown in Table 4.2. The irradiation methods can be distinguished by the geometry or spatial dimensionalcure kinteics ity of the light source on the part scale and the number of irradiation actuators that comprise this geometry. Furthermore, this geometry determines the amount of motion degrees of freedom (DOF) required to irradiate a complete layer. The total number of actuators and hence total number of input variables is the sum of the number of irradiation actuators and motion actuators.

Irradiation method	**Vector scanning**			**Mask projection**	**Scanning mask projection**
# Actuators	1	2	n-point array	$n \times m$ point array	$n \times m$ point array
Geometry	Point	Points	Line	Area	Area
Schematic illustration	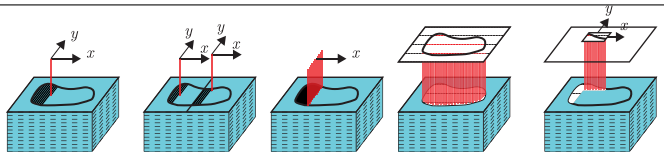				
# Motion DOF	2	2×2	1	0	2

Table 4.2: Irradiation methods classification scheme, adapted from [6].

Traditionally, a single laser point source scanned the resin surface to selectively irradiate the photopolymer, referred to as vector scanning [6]. To this end, the laser beam had to be positioned in two DOF in the horizontal xy-plane as shown in Table 4.2. Hence a total of three variables needed to be controlled and synchronized. To increase productivity, one or more lasers could be added to simultaneously irradiate multiple portions of the resin surface. Continuing to add more beams, one can use a 1D array or a line of n points. If the individual points are touching, then the 1D array only has to be positioned in one DOF, e.g., along the x-axis as illustrated in Table 4.2. Extending this 1D array or line to a 2D array or area of $n \times m$ points, the array does not have to be positioned in the xy-plane at all. In these so-called mask projection systems, an entire surface can be selectively irradiated by, e.g., a Digital Micromirror Device (DMD) [6]. If the 2D array is positioned in one [87] or two [88] DOF in the xy-plane again, as in scanning mask projection, the build area can be increased or the resolution can be improved. Another mechatronic concept to address the inherent trade-off between build area and resolution, is to use a projector whose magnification can be controlled through vertical motion [89]. Many other combinations can be made within the presented classification scheme, such as, e.g., mask projection combined with vector scanning [90] or scanning mask

projection using multiple projectors [34].

4.4.2 Process sensing

In-situ process measurements are a key enabler for the development of process control schemes, improvement of our understanding of the process, and improvement of process efficiency and part quality [14, 15]. The intended process control strategy determines the requirements such as speed and resolution for the sensing technology to be integrated into vat photopolymerization equipment.

The field of monitoring polymerization reactions in general is considerable, as exemplified by [91–93]. Not all the monitoring techniques are relevant for vat photopolymerization, since, e.g., in vat photopolymerization there are no forced flows of polymer as opposed to polymerization reactors. Other polymerization reactions that are more closely related to vat photopolymerization are photolithography, coating and dental composite material reactions [94]. Scrutinizing literature on process sensing and control of these related technologies may prove worthwhile [95].

The approach taken here is to analyze (photo-) polymerization monitoring and characterization techniques and attempting to extract the measuring principles for the development of in-line sensors to be integrated into vat photopolymerization equipment. Even offline, polymer characterization is a complex and challenging field [91]. So although the majority of techniques reviewed here were originally developed to *study* the photopolymerization process rather than to *control* the process, some techniques might be applicable as in-line metrology.

The choice of process variable to be measured by the sensing technology, i.e., the *measurand*, naturally follows from the intended process control scheme. The degree of (monomer) conversion is often considered a highly useful measurand for monitoring and control [63, 93] and hence is the focus of this section. Many different sensing techniques exist to measure the degree of conversion, each with their own advantages and disadvantages. The measuring principles governing these techniques are explained in the following sections, followed by a comparison.

Spectroscopy

Spectroscopy is the field of study concerned with the interaction of electromagnetic radiation and matter [96]. Two spectroscopic measurement techniques have been widely used to monitor the change in concentration of chemical species and consequently the degree of conversion during the photopolymerization reaction, namely infrared (IR) spectroscopy [97] and Raman spectroscopy [98]. Both techniques rely on measuring the vibrational energy of molecules, which consist of atoms bound together by chemical bonds. Other spectroscopic techniques for monitoring photopolymerization reactions include fluorescence spectroscopy [49] and surface plasmon resonance spectroscopy [99]. IR spectroscopy has been used for kinetic analysis of ceramic slurries [61, 100, 101].

Molecules can be considered as consisting of coupled harmonic oscillators where the atoms are point masses and the bonds are springs [102]. Two of these oscillators represent the carbon-carbon double bond, one in a stretching mode and the other in a twisting mode. The vibrational energy of each functional group represented by harmonic oscillators is a function of the concentration of said group and thus spectroscopy can be used to monitor the photopolymerization reaction. As monomer is consumed, double bond conversion takes place, which is perceptible in the spectrum as a decrease of corresponding peaks. The degree of conversion α can be calculated at any time by taking the ratio of the current peak height or area A to the initial peak height or area A_0.

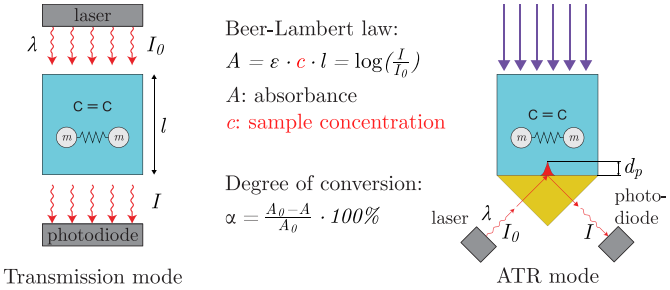

Figure 4.19: IR spectroscopy measuring principle.

The measuring principle governing IR spectroscopy is the absorption of light in a medium, which can be quantified by the Beer-Lambert law [38]. The Beer-Lambert law states that the absorbance A is directly proportional to the wavelength λ and sample concentration $[c]$. As monomer is consumed during the reaction, the monomer concentration decreases and consequently the absorbance decreases. Absorbance can be simply obtained by irradiating the medium with a known intensity and measuring the outgoing intensity, see Figure 4.19. Two common methods to measure absorbance are the transmittance (TR) and attenuated total reflection (ATR) methods. In the transmittance method shown in the left of Figure 4.19, the absorbance is measured by placing the IR source and detector in line, such as in [103]. In the ATR method, a crystal with high index of refraction is used as is shown in in the right of Figure 4.19. As the IR beam reaches the boundary, total internal reflection occurs; a small amount of light penetrates the photopolymer medium in the form of an evanescent wave with penetration depth d_p and is partially absorbed before being measured by the photodiode. Both the TR and ATR methods can be embodied in a fiber optic probe for remote sensing [91].

The goal of IR spectroscopy is to measure the absorption for a range of wavelengths, which can be done in two ways. The first way is to physically split up the radiation in its constituent wavelengths in what is called dispersive spectroscopy and to measure the absorption for each individual wavelength monochromatically [102]. A second way is to radiate the sample with multiple wavelengths simultaneously in

what is called Fourier Transform IR spectroscopy (FTIR). In FTIR, a Michelson interferometer with a stationary and moving mirror is used as a multiplexer to select a set of wavelenghts and the resulting time domain interferogram is Fourier transformed to the frequency domain. Note that Figure 4.19 does not show the interferometer, which can have considerable dimensions with respect to the sample.

Interferometry

Laser interferometric techniques that rely on refractive index changes upon polymerization have been employed by several researchers to monitor the photopolymerization process, using both Michelson [65, 104–108] and Mach-Zehnder [109, 110] configurations. The goals of these systems range from monitoring shrinkage-induced deformations [104, 108] to monitoring the degree of cure [107]. To the author's knowledge, the only work attempting to use interferometry for ceramic vat photopolymerization is [65]. However, the experiments herein were not performed on ceramic suspensions, but on unfilled resins.

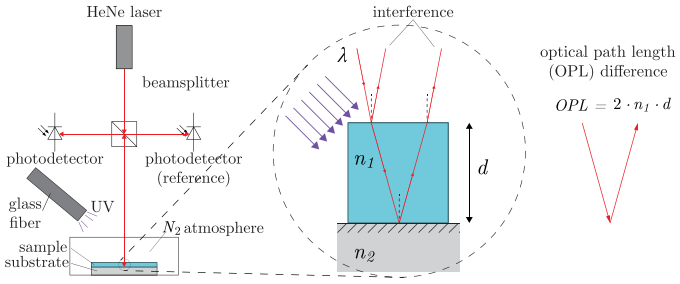

Figure 4.20: Interferometry measuring principle, setup adopted from [105].

The measuring principle is based on detecting differences in optical path lengths (OPL) upon photopolymerization as illustrated in Figure 4.20. The optical path length is the product of the refractive index n and the geometric length d. During photopolymerization, the refractive index of the photopolymer will typically *increase* and the geometric length or thickness will typically *decrease* due to shrinkage. Consequently the total optical path length difference will cause a periodic modulation of the intensity of the reflected laser beam by interference of light as indicated in Figure 4.20.

Jariwala developed an in-situ interferometric cure monitoring (ICM) system based on Mach-Zehnder interferometry for measuring part dimensions in the setup described in Section 4.5.2 and shown in Figure 4.26 [50]. Zhao improved the ICM system by moving from an implicit model relating measured phase angle to cured height empirically to a parameter estimation based method using an elaborated optics model [111]. The ICM system potentially enables real-time, full-field part shape measurements for the layerless process [112].

Calorimetry

Calorimetry is the science of measuring heat transfer associated with chemical reactions or physical changes and is a well-established method for the characterization of polymerization reaction kinetics [91]. Photocalorimetry is simply calorimetry for the study of light-induced processes, such as photopolymerization [113]. As described in Section 4.3, in free radical polymerization reactions, carbon-carbon double bonds (C=C) are converted into two single bonds. The amount of heat Q_r generated during this conversion can be calculated from the difference between the bond energy of the double bond and the two single bonds [113]. Hence, a simple expression for the degree of cure α can be derived for isothermal processes [26, 54, 113]:

$$\alpha = \frac{Q_r}{Q_{tot}} \tag{4.29}$$

where Q_{tot} is the known total reaction heat when all monomers are converted. Thus, the measuring principle governing photocalorimetry for following cure reactions is based on the measurement of generated exothermic heat.

The most widely used method to measure exothermic heat is Differential Scanning Calorimetry (DSC) [113]. "Differential" means that the change of the difference in heat flow rate to the sample and the reference is measured, while "scanning" means that they are subjected to a controlled temperature program [114]. Many researchers have used photo-DSC for kinetic analysis of vat photopolymerization reactions for pure resins [8, 54] and ceramic slurries [115]. Figure 4.21 shows the measuring principle in power compensation DSC.

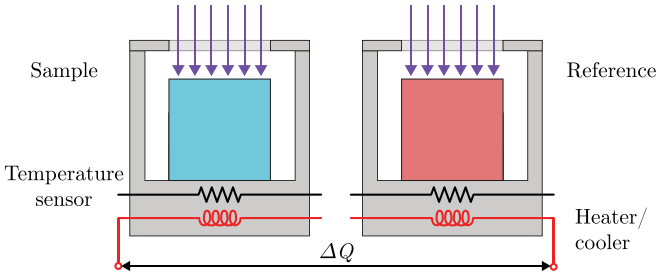

Figure 4.21: Differential scanning calorimetry (DSC) measuring principle.

The measuring principle in heat flux DSC is to measure the difference in temperature ΔT between the sample and reference, whereas in power compensation DSC the measuring principle is to measure the required compensation heat ΔQ, while the temperature is kept (nearly) constant by a control system [114]. Although the extraction of the power compensation DSC measuring principle for use as an in-situ sensor for vat photopolymerization seems non-trivial, the measurement of

released reaction heat by means of temperature measurement (i.e., thermometry) seems more likely.

Thermometry

Photopolymerization is an exothermic process and therefore the usage of temperature measurements, i.e., thermometry, to monitor the cure process seems a viable option. Several researchers have attempted to monitor the cure reaction using a single-point optical pyrometer [116] or an arrayed pyrometer in the form of an IR thermal imaging camera [63, 82, 117]. The measuring principle of pyrometers is based on the detection of infrared radiation from the object to be measured [118]. The usage of thermocouple arrays is also reported in literature [75].

Dielectrometry

Dielectric analysis is an established method [119] to monitor thermoset cure reactions and has been successfully applied to photoinitiated cure reactions [120–122]. The dielectric measuring principle is equivalent to that of an impedance measurement [123] and works as follows. A sinusoidal voltage is applied across two electrodes that are in contact with the photopolymer sample as shown in Figure 4.22. Dipoles will try to orient with the electric field whilst charged ions will move towards the electrode of opposite charge [120]. Two fundamental dielectric properties can be derived from a measurement of the changes in amplitude and the phase shift of the current response, namely the dielectric constant or permittivity ε' and the dielectric loss factor ε''. Since a strong correlation exists between the ionic mobility component of the loss factor, which is described by the ion viscosity, and the mechanical viscosity [120], dielectric analysis can be used as a cure monitoring technique.

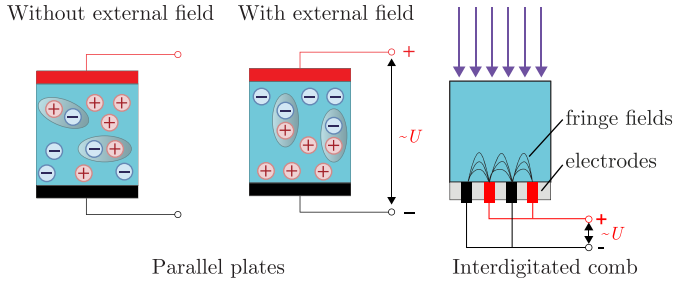

Figure 4.22: Dielectrometry measuring principle, adopted from [123].

A typical implantable sensor geometry consisting of two interdigitated comb electrodes rather than parallel plates is also shown in Figure 4.22. These sensors can be used to irradiate the photopolymer sample on one side and subject the sample to an electric field for measurement on the other as shown in Figure 4.22. The

penetration depth of the fringe field into the sample is controlled by the electrode line width and spacing. Hence spatial variations in the vertical direction can be measured using different penetration depths [124]. The effects of ceramic fillers on the ion viscosity are discussed in [122].

Rheometry

Rheological methods to measure the change in mechanical properties upon curing can be used to monitor photoinduced curing. To this end, traditonal rheometers are typically augmented with a light source [125, 126]. The combination of rheological techniques with spectroscopic techniques allows for the simultaneous measurement of both cure kinetics and mechanical properties [125, 127]. Due to the fast curing of photopolymers, the data acquisition rate for typical rheometers is too low, i.e., in the order of 1 [Hz]. Hence, Schmidt incorporated high-performance data acquisition on a photorheometer, running at 1000 [Hz] [107]. Abstracting such rheological measurement techniques and incorporating them in a vat photopolymerization machine for in-situ cure monitoring seems non-trivial. Rheological techniques using particle tracking velocimetry seem more feasible.

Slopek developed such an in-situ monitoring system for free-radical photopolymerization based on particle tracking microrheology [125]. The measuring principle is based on the tracking of the Brownian motion of micron-sized fluorescent silica particles by video microscopy. The goal of the monitoring system was to monitor the liquid-to-gel transition in real-time and to enable the monitoring of changes in mechanical properties during photopolymerization [125]. Figure 4.23 shows the experimental setup, which incorporated focus knobs to vertically shift the focal plane to enable measurements throughout the sample depth of 120 [μm].

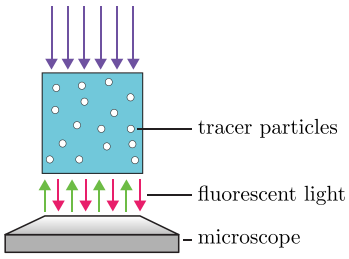

Figure 4.23: Microrheology experimental setup, adapted from [125, 128]

Wave propagation techniques

Wave propagation techniques have been primarily used for cure monitoring of thermosetting polymers [129], but have also been applied in photopolymerization [130]. The measuring principle is based on the change of wave propagation characteristics

due to the change in mechanical properties upon polymerization. For example, in ultrasonic cure monitoring an acoustic wave is transmitted by a transducer through a polymer sample and received by a second transducer [131]. Figure 4.24 schematically shows two acoustic cure monitoring configurations: a contactful configuration and a contactless or air-coupled configuration [132]. The wave propagation velocity, also known as speed of sound, can be obtained by measuring the "time of flight" and is directly related to the resin storage modulus L' and density ρ [132]. During polymerization the wave propagation velocity typically increases. The longitudinal modulus L, consisting of a storage L' and loss L'' component, can be calculated from the wave propagation velocity and these can be subsequently correlated to other elastic moduli and the degree of cure α [132]. Laser ultrasonic sources and sensors have been used as alternative transducers for non-contact ultrasonic measurements [133].

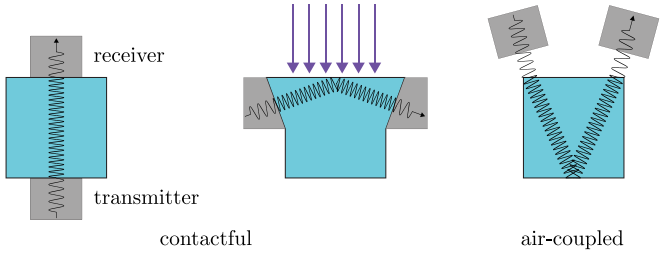

Figure 4.24: Acoustic cure monitoring measuring principle.

Comparison of existing sensing technologies

Table 4.3 compares the sensing methods for measuring the degree of conversion, whose measuring principles are described in the preceding sections. Most sensing methods do not measure conversion directly, but derive it from the actual measurand. The spatial dimensionality of the measured conversion differs among the various sensing methods. Most sensing methods do not measure spatial variations in the xy-plane or along the z-axis, but average over the volume and hence are called point-based methods. Some methods do measure spatial variations in the xy-plane by using an arrayed sensor such as a CCD to capture a full field or area [50, 99, 117, 125]. The only sensing methods reported to be able to measure spatial variations along the z-axis are particle tracking microrheology [125] and dielectrometry [124]. Sensor properties related to the spatial dimensionality not listed in the table are the spatial measurement range and resolution. Another relevant sensor property is whether the measurement is contactful or contactless.

For implementability in vat photopolymerization machines, the space the sensor occupies and the ability to measure and actuate from the same side are relevant properties. Figure 4.19 to 4.24 illustrate that most of the surveyed sensing methods are only capable to measure a single photopolymer layer from one side, while

irradiating it from the other. Note that although interferometric sensing methods irradiate and measure from the same side, they do require a reflective background, which complicates their suitability as a multi-layer sensor.

Both in IR spectroscopy [61, 100, 101] and in calorimetry [115], the effect of ceramic particles on the functioning of the sensor is insignificant. In dielectrometry [122] and (parallel plate) rheometry [65], the ceramic filler has a significant influence on the measured quantities, but does not impair the functioning of the sensor. In interferometry, light scattering is expected to have a significant influence on the functioning of the sensor. The effect of ceramic fillers on thermometers and wave propagation techniques is not reported.

Sensing method	**Measurand**	**Derived property**	**Measuring principle**	**Spatial dimensionality**	**Sampling rate [Hz]**	**Contact**	**Ceramic filler influence**	**Ref.**
Spectroscopy	Aborption spectrum	Conversion	Vibrational energy of molecule measurement	Point	1	Contactful	Insignificant	[97, 98, 102]
Interferometry	Optical path length change	RI change, shrinkage, conversion	Optical path length difference measurement	Point, area	200	Contactless	Significant	[65, 104–110]
Calorimetry	Reaction heat	Conversion	Generated heat measurement	Point	1	Contactful	Insignificant	[113, 114]
Thermometry	Temperature	Conversion	Thermal radiation measurement	Point, area	100	Contactless/ -ful	Not reported	[116–118]
Dielectrometry	Permittivity, loss factor	Ion viscosity, conversion	Impedance measurement	Point	200	Contactful	Insignificant	[119–124]
Rheometry	Viscosity	Gel point	Particle tracking/ shear flow torque	Point, area	1000	Contactless/ -ful	Insignificant	[107, 125–128]
Wave propagation techniques	Speed of sound	Longitudinal modulus, conversion	Time of flight measurement	Point	100	Contactless/ -ful	Not reported	[129–133]

Table 4.3: Comparison of existing sensing technologies.

4.5 Process control

Consistent, repeatable part quality is a key requirement for enabling the application of AM in series production. Variability in part quality can affect both product yield *and* productivity [7], i.e., productivity is determined both by cycle time and product yield. Hence, the objective of a manufacturing process controller is to minimize production variations for a target geometry and properties despite the presence of material and process uncertainties [10]. Rejecting these disturbances is the purpose of feedback control.

Although not the focus of this paper, setpoint generation can be considered a control task as well. In vat photopolymerization, the desired process trajectories are determined by the build style employed. The build style is typically a sequence of scan patterns in vector scanning systems and a sequence of bitmaps in mask projection systems. Many research has been conducted on build styles in non-ceramic resins [6, 8, 20, 34, 35, 134]. The build styles appropriate for pure non-ceramic resins may need to be modified for ceramic slurries [23]. Some research has been conducted on build styles specifically for ceramic vat photopolymerization [24, 135–137].

Yet another type of control loop that is not directly the focus of this paper, is to monitor and control the input variables to ensure that the equipment is actually delivering the commanded inputs [9]. In vat photopolymerization this implies monitoring the irradiance distribution of the light source. Several researchers have employed a camera such as a CCD or CMOS to monitor the irradiance distribution on the vat surface [64, 138–141].

At the time of writing, only three control solutions are reported in literature in which feedback control is applied to a vat photopolymerization cure process or similar. In the first case the control objective is to minimize cure level deviations with layer depth [63] and in the second case the objective is to control the cure height in a bottom-up vat photopolymerization system [142]. In the third case a controller is developed for a system with continuous platform motion [143]. These three control schemes are outlined in the following sections.

4.5.1 Model-based control of a UV curing process

Yebi developed several model-based process control schemes for a layer-by-layer UV curing process of thick resin-infused glass fiber composites [63]. This AM technique is highly similar to vat photopolymerization in the vertical direction, but energy is not patterned in the horizontal plane. A first control scheme for feedback control in curing a single layer has been developed that partially compensates for UV attenuation across layer depth. Since the cure rate is proportional to temperature, the idea is to increase the cure rate by retaining heat at the bottom of the layer where the irradiation intensity is the lowest [39, 63]. Figure 4.25 illustrates this compensation strategy and the feedback control scheme that incorporates a temperature trajectory tracking controller, a temperature distribution observer and

a cure level distribution observer.

A second control scheme for multi-layer parts is also proposed by Yebi termed stepped-concurrent curing (SCC) in which new layers are added before previous ones are completely cured. Robust process control is achieved through an offline optimization of the inter-layer hold times and UV intensity in the presence of parameter uncertainty by minimizing the final cure level deviation. Finally, in a cascaded control scheme, a high level loop generates a reference surface temperature and optimizes the inter-layer hold times, and a low level loop tracks the generated surface temperature trajectory using feedforward and feedback components.

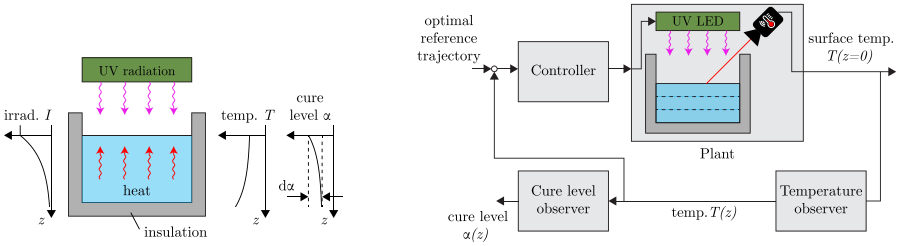

(a) compensation strategy for UV attenuation

(b) feedback control scheme

Figure 4.25: Model-based control strategies for a UV curing process, based on [63].

4.5.2 Evolutionary Cycle to Cycle control

Zhao et al. developed a process control scheme for a layerless micro vat photopolymerization process in which parts are fabricated on a stationary substrate [142, 144]. The cured height of the microparts that are "grown" bottom-up, is controlled in a scheme termed Evolutionary Cycle-to-Cycle (EC2C) control. EC2C is essentially an online parameter estimation algorithm that does not require accurate or detailed models [142]. The controller predicts the remaining exposure dose, calculates the remaining exposure time of the bitmap and switches to the next bitmap if necessary [144]. The actual cured height is measured by an interferometer, filtered using a Kalman filter, and used in the calculation of the remaining exposure time. Figure 4.26 shows the cure height control scheme and the used setup.

4.5.3 3D error based iterative learning control

Türeyen et al. developed a so-called 3D error based learning controller for a vat photopolymerization system with continuous platform movement [143]. In this control scheme, the actual light intensity on the resin surface is obtained by taking an image of the resin surface with a CCD camera and calibrating to the light

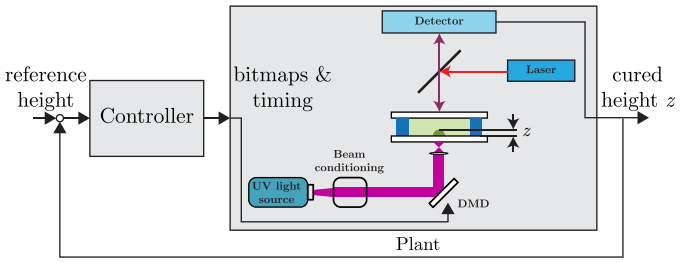

Figure 4.26: Cure height control scheme, based on [142].

intensity obtained from a power meter. The obtained actual light intensity is used as an input to a build simulation using a simple exposure threshold model. The reference image is also used in the build simulation to obtain a reference geometry. The algorithm then calculates the total error between the actual simulated geometry and the reference simulated geometry for each layer by adding the error values of all pixels in a layer. Based on the error, the (continuous) platform speed is then increased when overexposed or decreased when underexposed. After simulating all layers, the build simulation is repeated for several iterations. In essence the algorithm developed by Türeyen et al. merely changes process parameters (platform speed for each layer) through the iterative simulation of the build process and hence the name iterative learning controller is probably not the most appropriate one.

4.5.4 Comparison of existing control schemes

The control schemes described in the previous sections are compared in Table 4.4. Relevant control scheme properties include the control objective, controlled variables, and controller type. Other relevant properties are the type of system that is controlled, the amount of layers the controller addresses, the spatial dimensionality of the controlled variables, and the type of sensor used.

4.6 Discussion on control strategy feasibility

To examine the feasibility of potential control strategies, the following sections consider the first steps in the process of designing a control system.

4.6.1 Control objectives

The first step in control system design is to study the system and the control objectives [145]. Typical control objectives include disturbance rejection and command tracking, which can be expressed by bounds on the error [145]. The existing photopolymerization control schemes in Table 4.4 essentially show two

Control scheme	System type	Layers	Control objective	Controlled variables	Spatial dimensionality	Controller type	Inputs	Sensor	Ref.
Stepped-concurrent layering and curing (SCC)	Layer-by-layer UV curing of polymer composites	Multiple	Minimizing cure level deviations	Temperature distribution	1D in z	Temperature trajectory tracker, state estimator, hybrid controller	Interlayer hold times, LED power	IR camera	[63]
Evolutionary Cycle to Cycle (EC2C)	Mask projection μSL	Single	Minimizing cure height deviations	Cure height	1D in z, 3D capability	State estimator	Bitmap exposure times/ intensity	Interferometer	[142, 144]
3D error based ILC	Mask projection μSL	Continuous platform motion	Minimizing pixel curing errors	Cured geometry	3D	Process planner	Platform speed	DSLR camera	[143]

Table 4.4: Comparison of existing photopolymerization control schemes.

types of control objectives: 1) minimizing spatial variations in degree of conversion, and 2) minimizing dimensional errors. Yebi [63] argues that degree of conversion and thermal gradients compromise the quality and mechanical performance of the end product and hence accordingly formulates a control objective. The degree of conversion is often measured in the characterization of polymerization reactions and hence seems a straightforward variable to control [91, 93].

A different control objective could be to minimize shrinkage strains. This objective is central to several build styles developed for vector scanning systems, which have lead to significant accuracy improvements for pure resins [6, 8, 20]. Mitteramskogler et al. [24] showed that for ceramic-filled resins, minimizing shrinkage strains from photopolymerization can prevent crack formation after debinding. Yet another control objective could be to minimize the fraction of uncured resin, which was also a key aspect in the build styles for vector scanning systems [6, 8, 20]. Bae and Halloran [23] hypothesize that uncured resin in ceramic green parts could be the cause for cracking due to thermally initiated polymerization during debinding. Interestingly, the gaps in the "STAR-WEAVE" scanning pattern [8] intentionally introduced for minimizing shrinkage strains, contradict the objective of minimizing the fraction of uncured resin.

4.6.2 Modelling

The second step in control system design is to model the system and disturbances. Over the years, a significant amount of models have been developed to describe the physical phenomena outlined in Section 4.3. Table 4.1, however, shows that the vast majority of the models describe the photopolymerization of pure resins, rather than of ceramic slurries. Moreover, at the time of writing only one photopolymerization process model has been developed intended for control [63].

The cure mechanism represents the dynamics of the process to be controlled. Both the mechanistic models consisting of a set of coupled differential equations and the phenomenological models consisting of a single equation, show that the photopolymerization process has nonlinear dynamics. Moreover, the process is irreversible as the degree of conversion can not decrease. The attenuation of light with depth introduces a significant spatial distribution of the input. This classification implies that control methods from classical control theory in the frequency domain can not be applied, since they are typically based on sinusoidal steady-state responses.

The currently available process models essentially serve two purposes for control system design. On the one hand, they provide the control engineer with a description of the input-output behaviour of the system for use in model based control system design. On the other hand, they reveal the disturbances acting on the system, which enables the determination of the impact of rejecting these disturbances on the final product.

In modelling for control applications, an analysis of the time scales at which the physical phenomena manifest themselves is relevant. It should be noted from the outset that the photopolymerization process in *vector scanning* systems takes place in different time scales than in *mask projection* systems. Jacobs outlined the time scales relevant for *vector scanning* systems [6, 8]:

- $t_t = \mathcal{O}(10^{-12}$ [s]): photon layer transit time
- $t_k = \mathcal{O}(10^{-6}$ [s]): $1/e$ kinetic reaction time constant
- $t_e = \mathcal{O}(10^{-5}$ - 10^{-3} [s]): characteristic exposure time
- $t_{s,o} = \mathcal{O}(10^{-1}$ - 10^{0} [s]): measurable shrinkage onset
- $t_{s,c} = \mathcal{O}(10^{0}$ - 10^{1} [s]): shrinkage completion
- $t_d = \mathcal{O}(10^{1}$ - 10^{2} [s]): total layer drawing time

The characteristic exposure time t_e, i.e., the time for the laser beam to traverse the "zone of influence" that receives 99.99% of its total exposure, is larger than the characteristic time for the kinetic reaction t_k [8]. The implication for control is that there is a window of opportunity in which the photopolymerization process has already been initiated whilst still being irradiated. Hence, the laser power can

potentially be adjusted according to a feedback control law if sensing, computation and actuation is fast enough. Minimizing shrinkage strains would require a model that - despite the evident time scale separation between polymerization and shrinkage - is capable of accurately predicting shrinkage.

The time scale analysis in [8] did not include the time scales related to oxygen inhibition, heat transfer and diffusion of species. Since these phenomena influence the reaction rates, their respective time scales are of interest as well.

In stationary *mask projection* systems, the characteristic exposure time t_e and total layer drawing time t_d are equal. If mask projection systems would use the same irradiance values to irradiate the entire surface as vector scanning do to irradiate only a small region, the required total power of the light source would be many orders higher. Hence, it can be easily seen that the irradiance values are orders lower in mask projection systems, i.e., milliwatts [33, 146] rather than watts per centimer squared [8]. To reach the same exposure level, the characteristic exposure times t_e are in the order of seconds to tens of seconds in mask projection systems. Consequently, the polymerization reaction in mask projection systems is generally much slower than in vector scanning systems and thus the $1/e$ kinetic time constant t_k is higher. So the $1/e$ kinetic time constant described by Jacobs [8] $\mathcal{O}(10^{-6})$ [s] may be several orders higher in mask projection systems and varies from $\mathcal{O}(10^{-6}$ - $10^{-4})$ [s] in general according to [55].

4.6.3 Input-output selection

The third step in control system design is to select the inputs and outputs, which involves deciding on the number, place and type of the actuators and sensors [147]. The classification scheme presented in Table 4.2 indicates the number and place and hence the spatial dimensionality of the actuators for different irradiation methods. The same classification scheme can be applied to sensing methods. For real-time feedback control, a match between the number of actuators and sensors seems sensible. An example of how colocated actation and measurement can be achieved using the same beam steering hardware in vector scanning systems is given in [148].

The controllability of the degree of conversion is limited due to the irreversible nature of polymerization, that is, the degree of conversion can only increase. The photopolymerization reaction continues after irradiation, a phenomenon termed dark reaction [8, 54]. Nonetheless, it has been shown that the reaction can be terminated by immersing the part in acetone [149]. The observability of the degree of conversion distribution from the temperature distribution was checked by Yebi [63].

Section 4.4.1 outlined several alternative stimuli to initiate the polymerization reaction. The light source's irradiance seems a logical choice for the input. Other variables can be considered as input candidates as well, such as temperature. The coupling between the cure rate and temperature implies that spatial distributions of the degree of conversion can be compensated even further than in Yebi's work by actuating the temperature at the layer boundary. Other input candidates are

the oxygen concentration [66] and the light source wavelength to have control over penetration depth [150].

4.6.4 Potential control strategy feasibility

The fourth step in control system design is to select the control configuration, i.e., specifying the interconnections between the inputs and outputs. Suppose the input is the irradiance and the output is the degree of conversion. In vector scanning systems, a single-input single-output (SISO) control loop could be closed. In mask projection systems, a set of SISO control loops for each pixel could be defined, or a more complicated multiple-input multiple-output (MIMO) control loop that includes interactions between neighboring pixels.

In evaluating the feasibility of real-time feedback control, a key aspect is to check whether sensing, computation and actuation are fast enough to influence the process. Figure 4.27 shows a comparison of the time scales at which the physical phenomena take place, the sampling periods at which the sensing technologies measure, and the time it takes for the actuators to respond.

With respect to vector scanning systems, the figure clearly shows that laser diodes can be modulated fast enough [151] to influence the kinetic reaction, which takes place at least three orders slower. The current sensing technologies, however, are not fast enough for use in real-time feedback control schemes. This implies that either the sampling rates need to be increased, or the process needs to be slowed down by decreasing irradiance values.

With respect to mask projection systems, Figure 4.27 reveals that DMDs can switch fast enough [152] to influence the kinetic reaction, since the polymerization rate is limited by the photon flux [8]. Some sensing technologies are fast enough as well to measure the process. Hence, real-time feedback control seems feasible for mask projection systems.

An alternative to real-time control schemes would be to resort to layer-to-layer control schemes. Rather than adjusting the irradiance *during* photopolymerization, those portions that require a higher degree of conversion can be reirradiated *after* the entire layer has been photopolymerized in a second corrective pass. Referring to Figure 4.1, this type of control strategy can perhaps better be categorized as in-situ defect or fault detection and handling.

4.7 Conclusion

The objective of this paper was to study the feasibility of real-time control strategies for vat-photopolymerization-based ceramic manufacturing. To this end, the state of the art in process control, modelling, actuation, and sensing is reviewed. A considerable amount of process models have been developed, although the majority is not completely applicable to ceramic slurries due to the presence of ceramic particles. In-situ sensors for real-time monitoring and control currently are hardly available,

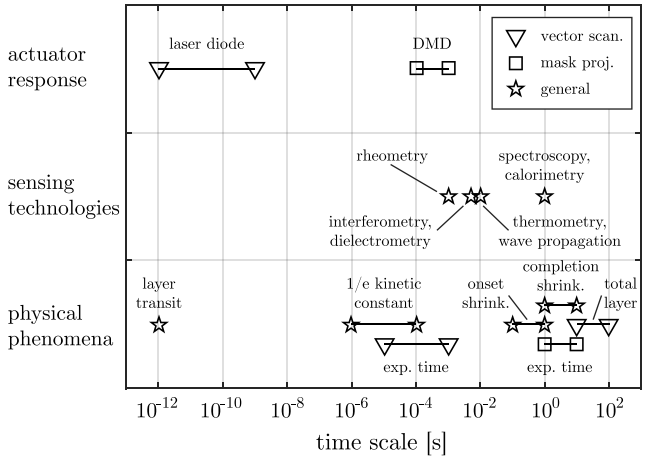

Figure 4.27: Time scale comparison of process dynamics, sensing and actuation.

but the measuring principles known from polymer characterization techniques can potentially be utilized in the development of new sensors. The ceramic particles, however, again complicate the use of some of these measurement techniques. Moreover, the temporal and spatial resolutions at which these measurements currently can be obtained, challenge the suitability for use in control loops. Fortunately, actuator response times do not seem to form a limiting factor in the control loop. Based on the literature review, it can be concluded that the field of closed-loop process control for (ceramic) vat photopolymerization is almost completely open, especially regarding the sensing aspect.

References

[1] J. Evans, "Seventy ways to make ceramics," *Journal of the European Ceramic Society*, vol. 28, pp. 1421–1432, Jan. 2008.

[2] P. Colombo, G. Mera, R. Riedel, and G. D. Sorarù, "Polymer-Derived Ceramics: 40 Years of Research and Innovation in Advanced Ceramics," *Journal of the American Ceramic Society*, vol. 93, pp. 1805–1837, June 2010.

[3] N. Travitzky, A. Bonet, B. Dermeik, T. Fey, I. Filbert-Demut, L. Schlier, T. Schlordt, and P. Greil, "Additive Manufacturing of Ceramic-Based Materials," *Advanced Engineering Materials*, vol. 16, pp. 729–754, June 2014.

[4] J. Deckers, J. Vleugels, and J.-P. Kruth, "Additive Manufacturing of Ceramics: A Review," *Journal of Ceramic Science and Technology*, vol. 5, no. 4, pp. 245–260, 2014.

[5] A. Zocca, P. Colombo, C. M. Gomes, and J. Günster, "Additive Manufacturing of Ceramics: Issues, Potentialities, and Opportunities," *Journal of the American Ceramic Society*, vol. 98, pp. 1983–2001, July 2015.

[6] I. Gibson, D. Rosen, and B. Stucker, *Additive Manufacturing Technologies*. New York, NY: Springer, 2 ed., 2015.

[7] J. W. Halloran, "Ceramic Stereolithography: Additive Manufacturing for Ceramics by Photopolymerization," *Annual Review of Materials Research*, vol. 46, Aug. 2016.

[8] P. Jacobs, *Rapid Prototyping & Manufacturing: Fundamentals of Stereolithography*. Dearborn, MI: Society of Manufacturing Engineers, 1992.

[9] M. L. Vlasea, B. Lane, F. Lopez, S. Mekhontsev, and A. Donmez, "Development of powder bed fusion additive manufacturing test bed for enhanced real-time process control," in *Proceedings Solid Freeform Fabrication Symposium*, pp. 527–539, 2015.

[10] D. Hardt, "Modeling and control of manufacturing processes: Getting more involved," *Journal of Dynamic Systems, Measurement, and Control*, vol. 115, pp. 291–300, June 1993.

[11] Y. Huang, M. C. Leu, J. Mazumder, and A. Donmez, "Additive manufacturing: Current state, future potential, gaps and needs, and recommendations," *Journal of Manufacturing Science and Engineering*, vol. 137, no. 1, p. 014001, 2015.

[12] E. W. Reutzel and A. R. Nassar, "A survey of sensing and control systems for machine and process monitoring of directed-energy, metal-based additive manufacturing," *Rapid Prototyping Journal*, vol. 21, no. 2, pp. 159–167, 2015.

[13] T. G. Spears and S. A. Gold, "In-process sensing in selective laser melting (SLM) additive manufacturing," *Integrating Materials and Manufacturing Innovation*, vol. 5, pp. 1–25, Dec. 2016.

[14] M. Mani, B. Lane, A. Donmez, S. Feng, S. Moylan, and R. Fesperman, "Measurement Science Needs for Real-time Control of Additive Manufacturing Powder Bed Fusion Processes," Tech. Rep. NIST IR 8036, National Institute of Standards and Technology, Feb. 2015.

[15] J. Pellegrino, T. Makila, S. McQueen, and E. Taylor, "Measurement science roadmap for polymer-based additive manufacturing," Tech. Rep. NIST AMS 100-5, National Institute of Standards and Technology, Gaithersburg, MD, Dec. 2016.

[16] S. P. Gentry, *Factors Affecting the Resolution of Photopolymerized Ceramics*. PhD thesis, University of Michigan, Ann Arbor (MI), 2012.

[17] T. Chartier, "Additive Manufacturing to Produce Complex 3d Ceramic Parts," *Journal of Ceramic Science and Technology*, vol. 6, no. 2, pp. 95–104, 2015.

[18] M. Schwentenwein, P. Schneider, and J. Homa, "Lithography-Based Ceramic Manufacturing: A Novel Technique for Additive Manufacturing of High-Performance Ceramics," *Advances in Science and Technology*, vol. 88, pp. 60–64, Oct. 2014.

[19] T. Chartier and A. Badev, "Rapid Prototyping of Ceramics," in *Handbook of Advanced Ceramics*, pp. 489–524, Elsevier, 2013. DOI: 10.1016/B978-0-12-385469-8.00028-9.

[20] P. Jacobs, *Stereolithography and other RP&M Technologies: from Rapid Prototyping to Rapid Tooling*. New York: ASME Press, 1996.

[21] J. R. Tumbleston, D. Shirvanyants, N. Ermoshkin, R. Janusziewicz, A. R. Johnson, D. Kelly, K. Chen, R. Pinschmidt, J. P. Rolland, A. Ermoshkin, E. T. Samulski, and J. M. DeSimone, "Continuous liquid interface production of 3d objects," *Science*, vol. 347, pp. 1349–1352, Mar. 2015.

[22] Z. Ali, E. Türeyen, Y. Karpat, and M. Çakmakcı, "Fabrication of Polymer Micro Needles for Transdermal Drug Delivery System Using DLP Based Projection Stereo-lithography," *Procedia CIRP*, vol. 42, pp. 87–90, 2016.

[23] C.-J. Bae and J. W. Halloran, "Influence of Residual Monomer on Cracking in Ceramics Fabricated by Stereolithography: Influence of Residual Monomer on Cracking," *International Journal of Applied Ceramic Technology*, vol. 8, pp. 1289–1295, Nov. 2011.

[24] G. Mitteramskogler, R. Gmeiner, R. Felzmann, S. Gruber, C. Hofstetter, J. Stampfl, J. Ebert, W. Wachter, and J. Laubersheimer, "Light curing strategies for lithography-based additive manufacturing of customized ceramics," *Additive Manufacturing*, vol. 1-4, pp. 110–118, Oct. 2014.

[25] T. Wu, *Theoretical modeling and experimental characterization of stress and crack development in parts manufactured through large area maskless photopolymerization*. PhD thesis, Georgia Institute of Technology, Atlanta, GA, 2014.

[26] P. J. Bartolo, ed., *Stereolithography*. Boston, MA: Springer US, 2011.

[27] H. Bikas, P. Stavropoulos, and G. Chryssolouris, "Additive manufacturing methods and modelling approaches: a critical review," *The International Journal of Advanced Manufacturing Technology*, vol. 83, pp. 389–405, Mar. 2016.

[28] A. Garg, K. Tai, and M. Savalani, "State-of-the-art in empirical modelling of rapid prototyping processes," *Rapid Prototyping Journal*, vol. 20, pp. 164–178, Mar. 2014.

[29] H. G. Kwatny and V. E. Mablekos, "The modeling of dynamical processes," in *1975 IEEE Conference on Decision and Control including the 14th Symposium on Adaptive Processes*, pp. 271–281, Dec. 1975.

[30] A. Limaye and D. Rosen, "Quantifying dimensional accuracy of a mask projection micro stereolithography system," in *Proceedings of the 15th Solid Freeform Fabrication Symposium, Austin Texas*, pp. 481–492, 2004.

[31] C. Sun and X. Zhang, "Experimental and numerical investigations on microstereolithography of ceramics," *Journal of Applied Physics*, vol. 92, no. 8, pp. 4796–4802, 2002.

[32] C. Sun, N. Fang, D. Wu, and X. Zhang, "Projection micro-stereolithography using digital micro-mirror dynamic mask," *Sensors and Actuators A: Physical*, vol. 121, pp. 113–120, May 2005.

[33] H.-W. Kang, J. H. Park, and D.-W. Cho, "A pixel based solidification model for projection based stereolithography technology," *Sensors and Actuators A: Physical*, vol. 178, pp. 223–229, May 2012.

[34] C. Zhou, *Optimized mask image projection for large-area based additive manufacturing process.* PhD thesis, University of Southern California, Los Angeles, CA, 2011.

[35] A. S. Limaye, *Multi-objective process planning method for Mask Projection Stereolithography.* PhD thesis, Georgia Institute of Technology, Atlanta, GA, 2007.

[36] J. R. Zyzalo, *Masked Projection Stereolithography: Improvement of the Limaye Model for Curing Single Layer Medium Sized Parts.* PhD thesis, Massey University, Albany, New Zealand, 2008.

[37] B. Sager, *SLA characterization for surface finish improvement: inverse design methods for process planning.* PhD thesis, Georgia Institute of Technology, Atlanta, GA, 2006.

[38] J. E. Puskas, T. E. Long, R. F. Storey, S. Shaikh, and C. L. Simmons, eds., *In Situ Spectroscopy of Monomer and Polymer Synthesis.* Boston, MA: Springer US, 2003.

[39] M. D. Goodner and C. N. Bowman, "Development of a comprehensive free radical photopolymerization model incorporating heat and mass transfer effects in thick films," *Chemical Engineering Science*, vol. 57, no. 5, pp. 887–900, 2002.

[40] N. Fang, C. Sun, and X. Zhang, "Diffusion-limited photopolymerization in scanning micro-stereolithography," *Applied Physics A*, vol. 79, Dec. 2004.

[41] A. Bertsch, "Study of the spatial resolution of a new 3d microfabrication process: the microstereophotolithography using a dynamic mask-generator technique," *Journal of Photochemistry and Photobiology A: Chemistry*, vol. 107, pp. 275–281, 1997.

[42] G. A. Miller, L. Gou, V. Narayanan, and A. B. Scranton, "Modeling of photobleaching for the photoinitiation of thick polymerization systems," *Journal of Polymer Science Part A: Polymer Chemistry*, vol. 40, no. 6, pp. 793–808, 2002.

[43] L. H. J. Lajunen and P. Peramaki, *Spectrochemical analysis by atomic absorption and emission*. Cambridge: Royal Society of Chemistry, 2nd ed., 2004. OCLC: ocm57355538.

[44] C. Sun and X. Zhang, "The influences of the material properties on ceramic micro-stereolithography," *Sensors and Actuators A*, vol. 101, no. 3, pp. 364–370, 2002.

[45] H. Liao, *Stereolithography using compositions containing ceramic powders*. PhD thesis, University of Toronto, 1997.

[46] M. L. Griffith and J. W. Halloran, "Scattering of ultraviolet radiation in turbid suspensions," *Journal of Applied Physics*, vol. 81, no. 6, p. 2538, 1997.

[47] V. Tomeckova and J. W. Halloran, "Predictive models for the photopolymerization of ceramic suspensions," *Journal of the European Ceramic Society*, vol. 30, pp. 2833–2840, Oct. 2010.

[48] Y. Brulle, A. Bouchy, B. Valance, and J. C. André, "Industrial photochemistry XXI. Chemical, transport and refractive index effects in space-resolved laser photopolymerization," *Journal of photochemistry and photobiology A: Chemistry*, vol. 83, no. 1, pp. 29–37, 1994.

[49] A. Schmocker, *Surgical probe and implant development for nucleus pulposus replacements*. PhD thesis, École polytechnique fédérale de Lausanne, Lausanne, 2016.

[50] A. S. Jariwala, *Modeling And Process Planning For Exposure Controlled Projection Lithography*. PhD thesis, Georgia Institute of Technology, Atlanta, GA, 2013.

[51] L. Flach and R. P. Chartoff, "A process model for nonisothermal photopolymerization with a laser light source. I: Basic model development," *Polymer Engineering & Science*, vol. 35, no. 6, pp. 483–492, 1995.

[52] P. F. Jacobs, "Fundamentals of stereolithography," in *Solid Freeform Fabrication Symposium Proceedings*, pp. 196–211, 1992.

[53] S. P. Gentry and J. W. Halloran, "Light scattering in absorbing ceramic suspensions: Effect on the width and depth of photopolymerized features," *Journal of the European Ceramic Society*, vol. 35, pp. 1895–1904, June 2015.

[54] Y. Tang, *Stereolithography cure process modeling*. PhD thesis, Georgia Institute of Technology, Atlanta, GA, 2005.

[55] G. G. Odian, *Principles of polymerization*. Hoboken, N.J: Wiley-Interscience, 4th ed., 2004. OCLC: ocm53393894.

[56] C. Koplin, M. Gurr, R. Mülhaupt, and R. Jaeger, "Shape accuracy in stereolithography: a material model for the curing behavior of photo-initiated resins," in *International User's Conference on Rapid Prototyping and Rapid Tooling and Rapid Manufacturing (Euro-uRapid)*, pp. 315–318, 2008.

[57] L. Flach and R. P. Chartoff, "A process model for nonisothermal photopolymerization with a laser light source. II: Behavior in the vicinity of a moving exposed region," *Polymer Engineering & Science*, vol. 35, no. 6, pp. 493–498, 1995.

[58] G. A. Altun-çiftçioğlu, *Mathematical Modeling and Simulation of Photopolymerization Process*. PhD thesis, Istanbul Technical University, Istanbul, 2008.

[59] M. F. Perry and G. W. Young, "A Mathematical Model for Photopolymerization From a Stationary Laser Light Source," *Macromolecular Theory and Simulations*, vol. 14, pp. 26–39, Jan. 2005.

[60] J. M. Matias, *Infrared stereolithography*. PhD thesis, University of Minho, Braga, 2014.

[61] K. Kambly, "Characterization of curing kinetics and polymerization shrinkage in ceramic-loaded photocurable resins for large area maskless photopolymerization (LAMP)," Master's thesis, Georgia Institute of Technology, Atlanta, GA, 2009.

[62] S. S. Hur and J. R. Youn, "Thermal deformation of a photo-cured polymer for the analysis of stereolithography," *Polymer-Plastics Technology and Engineering*, vol. 39, pp. 651–666, Aug. 2000.

[63] A. M. Yebi, *Model-based control of UV curing processes with application to additive manufacturing*. PhD thesis, Clemson University, Clemson, SC, 2015.

[64] Y. Suzuki, H. Tahara, M. Michihata, K. Takamasu, and S. Takahashi, "Evanescent Light Exposing System under Nitrogen Purge for Nano-Stereolithography," *Procedia CIRP*, vol. 42, pp. 77–80, 2016.

[65] C. Provin, *Microstéréolithographie de céramiques*. PhD thesis, Institut National Polytechnique de Lorraine, Nancy, 2002.

[66] O. Dufaud and S. Corbel, "Oxygen diffusion in ceramic suspensions for stereolithography," *Chemical Engineering Journal*, vol. 92, no. 1, pp. 55–62, 2003.

[67] Y. Xu, M. Imamura, and T. Nakagawa, "Microscopic Flow Observation of Photopolymer by UV-Laser Beam Exposure," in *Solid Freeform Fabrication Symposium Proceedings*, p. 177, Center for Materials Science and Engineering, Mechanical Engineering Department and Chemical Engineering Department, the University of Texas at Austin, 1997.

[68] L. Flach and R. P. Chartoff, "A simple polymer shrinkage model applied to stereolithography," in *Proceedings of the Solid Freeform Fabrication Symposium*, pp. 225–233, DTIC Document, 1994.

[69] H. Narahara, F. Tanaka, T. Kishinami, S. Igarashi, and K. Saito, "Reaction heat effects on initial linear shrinkage and deformation in stereolithography," *Rapid Prototyping Journal*, vol. 5, pp. 120–128, Sept. 1999.

[70] G. Bugeda, M. Cervera, G. Lombera, and E. Onate, "Numerical analysis of stereolithography processes using the finite element method," *Rapid Prototyping Journal*, vol. 1, pp. 13–23, June 1995.

[71] R. S. Chambers, T. Guess, and T. Hinnerichs, "A Phenomenological Finite Element Model of Part Building in the Stereolithography Process," in *Proceedings of the Sixth International Conference on Rapid Prototyping*, 1995.

[72] S. S. Hur and J. R. Youn, "Prediction of the Deformation in Stereolithography Products Based on Elastic Thermal Shrinkage," *Polymer-Plastics Technology and Engineering*, vol. 37, pp. 539–563, Nov. 1998.

[73] Y.-M. Huang and C.-P. Jiang, "Curl distortion analysis during photopolymerisation of stereolithography using dynamic finite element method," *The International Journal of Advanced Manufacturing Technology*, vol. 21, no. 8, pp. 586–595, 2003.

[74] M. Vatani, F. Barazandeh, A. Rahimi, and A. Sanati Nezhad, "Distortion modeling of SL parts by classical lamination theory," *Rapid Prototyping Journal*, vol. 18, pp. 188–193, Apr. 2012.

[75] C. P. Jiang, *Development and Curing Analysis of Multi-Optical Source Stereolithography System*. PhD thesis, National Taiwan University of Science and Technology, Taipei, 2003.

[76] J. Eschl, *Die mechanischen Eigenschaften von Stereolithographiematerialien während der Aushärtung*. PhD thesis, University of Stuttgart, Stuttgart, 2002.

[77] C. Koplin, R. Jaeger, and P. Hahn, "Kinetic model for the coupled volumetric and thermal behavior of dental composites," *Dental Materials*, vol. 24, pp. 1017–1024, Aug. 2008.

[78] C. Jelley and C. Thompson, "Rapid Prototyping Simulation: past, present and future," in *Proceedings of the Conference on The Future of Modelmaking*, 1996.

[79] M. Yasui and K. Ikuta, "3d general photocurabel model of resin with various kinds of microparticles," in *Micro Electro Mechanical Systems (MEMS), 2013 IEEE 26th International Conference on*, pp. 453–456, IEEE, 2013.

[80] J. M. Matias, P. J. Bártolo, and A. V. Pontes, "Modeling and simulation of photofabrication processes using unsaturated polyester resins," *Journal of Applied Polymer Science*, vol. 114, pp. 3673–3685, Dec. 2009.

[81] M. M. Emami, F. Barazandeh, and F. Yaghmaie, "An analytical model for scanning-projection based stereolithography," *Journal of Materials Processing Technology*, vol. 219, pp. 17–27, May 2015.

[82] W. Hong, Y. T. Lee, and H. Gong, "Thermal analysis of layer formation in a stepless rapid prototyping process," *Applied Thermal Engineering*, vol. 24, pp. 255–268, Feb. 2004.

[83] Y.-M. Huang, S. Kuriyama, and C.-P. Jiang, "Fundamental study and theoretical analysis in a constrained-surface stereolithography system," *The International Journal of Advanced Manufacturing Technology*, vol. 24, pp. 361–369, Sept. 2004.

[84] J.-P. Fouassier, "Polymerization Under Light and Other External Stimuli," in *Macromolecular engineering: precise synthesis, materials properties, applications*, Weinheim: Wiley-VCH, 2007.

[85] C. B. Williams, F. Mistree, and D. W. Rosen, "A functional classification framework for the conceptual design of additive manufacturing technologies," *Journal of Mechanical Design*, vol. 133, no. 12, p. 121002, 2011.

[86] P. Bartolo and G. Mitchell, "Stereo-thermal-lithography: a new principle for rapid prototyping," *Rapid Prototyping Journal*, vol. 9, pp. 150–156, Aug. 2003.

[87] K. Loose, T. Niino, and T. Nakagawa, "Raster-based exposure through multiple parallel beams in stereolithography," *Rapid Prototyping Journal*, vol. 5, pp. 103–111, Sept. 1999.

[88] M. M. Emami, F. Barazandeh, and F. Yaghmaie, "Scanning-projection based stereolithography: Method and structure," *Sensors and Actuators A: Physical*, vol. 218, pp. 116–124, Oct. 2014.

[89] Y. Pan and C. Dagli, "Dynamic resolution control in a laser projection-based stereolithography system," *Rapid Prototyping Journal*, vol. 23, pp. 190–200, Jan. 2017.

[90] C. Zhou, H. Ye, and F. Zhang, "A Novel Low-Cost Stereolithography Process Based on Vector Scanning and Mask Projection for High-Accuracy, High-Speed, High-Throughput, and Large-Area Fabrication," *Journal of Computing and Information Science in Engineering*, vol. 15, no. 1, p. 011003, 2015.

[91] W. F. Reed and A. M. Alb, eds., *Monitoring polymerization reactions: from fundamentals to applications*. Hoboken, New Jersey: John Wiley & Sons, Inc, 2014.

[92] E. Frauendorfer, A. Wolf, and W.-D. Hergeth, "Polymerization Online Monitoring," *Chemical Engineering & Technology*, vol. 33, pp. 1767–1778, Nov. 2010.

[93] G. E. Fonseca, M. A. Dubé, and A. Penlidis, "A Critical Overview of Sensors for Monitoring Polymerizations," *Macromolecular Reaction Engineering*, vol. 3, pp. 327–373, Sept. 2009.

[94] C. Decker, "Photoinitiated crosslinking polymerisation," *Progress in Polymer Science*, vol. 21, pp. 593–650, 1996.

[95] X. Zhao and D. W. Rosen, "Investigation of Advanced Process Control Methods for Exposure Controlled Projection Lithography," in *Solid Freeform Fabrication Symposium Proceedings*, pp. 143–162, 2014.

[96] I. Pérez-Juste and O. Nieto Faza, "Interaction of Radiation with Matter," in *Structure Elucidation in Organic Chemistry* (r.-M. Cid and J. Bravo, eds.), pp. 1–26, Wiley-VCH Verlag GmbH & Co. KGaA, 2015.

[97] T. Scherzer and U. Decker, "Real-time FTIR–ATR spectroscopy to study the kinetics of ultrafast photopolymerization reactions induced by monochromatic UV light," *Vibrational Spectroscopy*, vol. 19, no. 2, pp. 385–398, 1999.

[98] K. Osaka, A. Kasai, T. Kosaka, and Y. Sawada, "Cure monitoring of UV polymers by Raman spectroscopy," in *16th International Conference on Composite Materials*, 2007.

[99] M. Michihata, K. Takamasu, and S. Takahashi, "Proposal of In-process Measurement for Micro-stereolithography Using Surface Plasmon Resonance," *Physics Procedia*, vol. 83, pp. 964–970, 2016.

[100] K. C. Wu and J. W. Halloran, "Photopolymerization monitoring of ceramic stereolithography resins by FTIR methods," *Journal of materials science*, vol. 40, no. 1, pp. 71–76, 2005.

[101] T. R. Alabi, *Design of photomodifiable material systems for maskless patterning of functional ceramic and metallic materials at multiple length scales*. PhD thesis, Georgia Institute of Technology, Atlanta, GA, 2013.

[102] D. I. Bower and W. F. Maddams, *The vibrational spectroscopy of polymers*. Cambridge solid state science series, Cambridge: Cambridge University Press, 1st ed., 1992.

[103] M. W. M. Cunico and J. D. Carvalho, "Determination of degree of photopolymerization rate by photometric system: application of UV LED and photodiode," in *Proceedings of COBEM 2011*, 2011.

[104] P. Bernhard, M. Hofmann, and M. Hunziker, "(Interferometric) Cure Monitoring As A Useful Tool In The Evaluation Of Resins For Stereolithography," in *Radtech Europe Conference Proceedings*, (Edinburgh), 1991.

[105] J. de Boer, R. J. Visser, and G. P. Melis, "Time-resolved determination of volume shrinkage and refractive index change of thin polymer films during photopolymerization," *Polymer*, vol. 33, no. 6, pp. 1123–1126, 1992.

[106] O. Dudi and W. Grubbs, "Laser Interferometric Technique for Measuring Polymer Cure Kinetics," *Journal of Applied Polymer Science*, vol. 74, pp. 2133–2142, 1999.

[107] L. E. Schmidt, *Low stress acrylated hyperbranched polymers*. PhD thesis, école polytechnique fédérale de Lausanne, Lausanne, 2006.

[108] I. Kostylev, D. Labrie, and R. B. T. Price, "Time-resolved 2d shrinkage field of dental resins using laser interferometry," *Applied Optics*, vol. 54, p. 1852, Mar. 2015.

[109] K. Inoue, S. Komatsu, X.-A. Trinh, T. Norisuye, and Q. Tran-Cong-Miyata, "Local deformation in photo-crosslinked polymer blends monitored by Mach-Zehnder interferometry," *Journal of Polymer Science Part B: Polymer Physics*, vol. 43, pp. 2898–2913, Oct. 2005.

[110] A. S. Jariwala, R. E. Schwerzel, and D. W. Rosen, "Real-Time Interferometric Monitoring System for Exposure Controlled Projection Lithography," in *Proceedings of. Solid Freeform Fabrication Symposium*, pp. 99–110, 2011.

[111] X. Zhao and D. W. Rosen, "Parameter Estimation Based Real-Time Metrology for Exposure Controlled Projection Lithography," in *Solid Freeform Fabrication Symposium Proceedings*, 2015.

[112] X. Zhao and D. W. Rosen, "Real-time interferometric monitoring and measuring of photopolymerization based stereolithographic additive manufacturing process: sensor model and algorithm," *Measurement Science and Technology*, vol. 28, p. 015001, Jan. 2017.

[113] C. E. Hoyle, "Calorimetric analysis of photopolymerization," in *Radiation Curing*, pp. 57–133, Springer, 1992.

[114] G. W. H. Höhne, W. F. Hemminger, and H.-J. Flammersheim, *Differential Scanning Calorimetry*. Berlin, Heidelberg: Springer Berlin Heidelberg, 2003.

[115] G. A. Brady and J. W. Halloran, "Differential photo-calorimetry of photopolymerizable ceramic suspensions," *Journal of materials science*, vol. 33, no. 18, pp. 4551–4560, 1998.

[116] B. Falk, S. M. Vallinas, M. R. J. Zonca, and J. V. Crivello, "Optical Pyrometry: A New Method for Monitoring Photopolymerizations," in *Radtech UV & EB Technical Conference Proceedings*, 2004.

[117] K. Xu, *Deformation control for mask image projection based stereolithography process*. PhD thesis, University of Southern California, Los Angeles, CA, 2016.

[118] J. V. Nicholas and D. R. White, *Traceable temperatures: an introduction to temperature measurement and calibration*. Chichester: Wiley, 2nd ed., 2001.

[119] R. G. May Jr, *Miniature fiber optic viscoelasticity sensor for composite cure monitoring*. PhD thesis, Virginia Polytechnic Institute and State University, Blacksburg (VA), 1998.

[120] K. Zahouily, C. Decker, E. Kaisersberger, and M. Gruener, "Real-time UV cure monitoring," *European coatings journal*, no. 11, pp. 14–34, 2003.

[121] K. Xu, S. Zhou, and L. Wu, "On-line and in-real-time monitoring of UV photopolymerization of nanocomposites with microdielectrometry," *Progress in Organic Coatings*, vol. 65, pp. 237–245, June 2009.

[122] J. Steinhaus, B. Hausnerova, T. Haenel, D. Selig, F. Duvenbeck, and B. Moeginger, "Correlation of shear and dielectric ion viscosity of dental resins – Influence of composition, temperature and filler content," *Dental Materials*, vol. 32, pp. 899–907, July 2016.

[123] N.-G. GmbH, "DEA 288 Epsilon Brochure," June 2016.

[124] Y. Sheiretov and M. Zahn, "Dielectrometry measurements of spatial moisture profiles in oil-impregnated pressboard," in *Proceedings of the 4th International Conference on Properties and Applications of Dielectric Materials*, vol. 2, pp. 701–704, IEEE, 1994.

[125] R. P. Slopek, *In-situ monitoring of the mechanical properties during the photopolymerization of acrylate resins using particle tracking microrheology*. PhD thesis, Georgia Institute of Technology, Atlanta, GA, 2008.

[126] S. S. Lee, A. Luciani, and J.-A. E. Månson, "A rheological characterisation technique for fast UV-curable systems," *Progress in organic coatings*, vol. 38, no. 3, pp. 193–197, 2000.

[127] A. Botella, J. Dupuy, A.-A. Roche, H. Sautereau, and V. Verney, "Photo-Rheometry/NIR Spectrometry: An in situ Technique for Monitoring Conversion and Viscoelastic Properties during Photopolymerization," *Macromolecular Rapid Communications*, vol. 25, pp. 1155–1158, June 2004.

[128] R. P. Slopek, "In-situ monitoring of photopolymerization using microrheology," Master's thesis, Georgia Institute of Technology, Atlanta, GA, 2005.

[129] D. Hunston, W. McDonough, B. Fanconi, F. Mopsik, F. Wang, F. Phelan, and M. Chiang, "Assessment of the State-Of-The-Art for Process Monitoring Sensors for Polymer Composites," Tech. Rep. NISTIR 4514, National Institute of Standards and Technology, June 1991.

[130] I. Alig, D. Lellinger, S. Agarwal, and H. Oehler, "Monitoring of photopolymerization kinetics and network formation by combined real-time near-infrared spectroscopy and ultrasonic reflectometry," *Reactive and Functional Polymers*, vol. 73, pp. 316–322, Feb. 2013.

[131] M. C. Kazilas, *Acquisition and Interpretation of Dielectric Data For Thermoset Cure Monitoring*. PhD thesis, Cranfield University, Cranfield, 2003.

[132] F. Lionetto and A. Maffezzoli, "Monitoring the Cure State of Thermosetting Resins by Ultrasound," *Materials*, vol. 6, pp. 3783–3804, Sept. 2013.

[133] P. A. Fomitchov, Y. K. Kim, A. K. Kromine, and S. Krishnaswamy, "Laser ultrasonic array system for real-time cure monitoring of polymer-matrix composites," *Journal of composite materials*, vol. 36, no. 15, pp. 1889–1901, 2002.

[134] Y. Pan, *Energy control and material deposition methods for fast fabrication with high surface quality in additive manufacturing using photo-polymerization*. PhD thesis, University of Southern California, Los Angeles, CA, 2014.

[135] Z. Chen, D. Li, W. Zhou, and L. Wang, "Curing characteristics of ceramic stereolithography for an aqueous-based silica suspension," *Proceedings of the Institution of Mechanical Engineers, Part B: Journal of Engineering Manufacture*, vol. 224, pp. 641–651, Apr. 2010.

[136] Z. Chen, D. Li, and W. Zhou, "Process parameters appraisal of fabricating ceramic parts based on stereolithography using the Taguchi method," *Proceedings of the Institution of Mechanical Engineers, Part B: Journal of Engineering Manufacture*, vol. 226, pp. 1249–1258, July 2012.

[137] A. V. Rudraraju, *Digital data processing and computational design for large area maskless photopolymerization*. PhD thesis, Georgia Institute of Technology, Atlanta, GA, 2013.

[138] X. Zheng, J. Deotte, M. P. Alonso, G. R. Farquar, T. H. Weisgraber, S. Gemberling, H. Lee, N. Fang, and C. M. Spadaccini, "Design and optimization of a light-emitting diode projection micro-stereolithography three-dimensional manufacturing system," *Review of Scientific Instruments*, vol. 83, no. 12, p. 125001, 2012.

[139] M. Shusteff, "Projection Microstereolithography for Architected Materials," tech. rep., Lawrence Livermore National Laboratory, 2015.

[140] M. P. Alonso, *Optimization of a light emitting diode based projection stereolithography system and its applications*. PhD thesis, University of Illinois at Urbana-Champaign, 2010.

[141] M. P. Lee, G. J. T. Cooper, T. Hinkley, G. M. Gibson, M. J. Padgett, and L. Cronin, "Development of a 3d printer using scanning projection stereolithography," *Scientific Reports*, vol. 5, p. 9875, Apr. 2015.

[142] X. Zhao and D. W. Rosen, "Process modeling and advanced control methods for Exposure Controlled Projection Lithography," in *American Control Conference (ACC)*, pp. 3643–3648, IEEE, 2015.

[143] E. B. Türeyen, Y. Karpat, and M. Çakmakcı, "Development of an iterative learning controller for polymer based micro-stereolithography prototyping systems," in *2016 American Control Conference (ACC)*, pp. 852–857, IEEE, 2016.

[144] X. Zhao and D. W. Rosen, "Simulation Study on Evolutionary Cycle to Cycle Time Control of Exposure Controlled Projection Lithography," *Rapid Prototyping Journal*, vol. 22, no. 3, pp. 456–464, 2016.

[145] S. Skogestad and I. Postlethwaite, *Multivariable Feedback Control: Analysis and design*. New York: Wiley, 2 ed., 2005.

[146] A. S. Limaye, "Design and Analysis of a Mask projection Micro Stereolithography System," Master's thesis, Georgia Institute of Technology, Atlanta, GA, Nov. 2004.

[147] M. van de Wal and B. de Jager, "A review of methods for input/output selection," *Automatica*, vol. 37, no. 4, pp. 487–510, 2001.

[148] T. Craeghs, F. Bechmann, S. Berumen, and J.-P. Kruth, "Feedback control of Layerwise Laser Melting using optical sensors," *Physics Procedia*, vol. 5, pp. 505–514, 2010.

[149] W. Li, M. Bakhtiary Noodeh, N. Delpouve, J.-M. Saiter, L. Tan, and M. Negahban, "Printing continuously graded interpenetrating polymer networks of acrylate/epoxy by manipulating cationic network formation during stereolithography," *Express Polymer Letters*, vol. 10, pp. 1003–1015, Sept. 2016.

[150] P. Lehtinen, S. Laurila, M. Kaivola, and J. Partanen, "Controlling Penetration Depth in Projection Stereolithography by Adjusting the Operation Wavelength," *Key Engineering Materials*, vol. 611-612, pp. 756–762, May 2014.

[151] H. Sun, *A Practical Guide to Handling Laser Diode Beams*. SpringerBriefs in Physics, Dordrecht: Springer Netherlands, 2015.

[152] D. Dudley, W. M. Duncan, and J. Slaughter, "Emerging digital micromirror device (DMD) applications," in *Micromachining and Microfabrication*, pp. 14–25, International Society for Optics and Photonics, 2003.

Chapter 5

Real-time feedback controlled conversion in vat-photopolymerization-based ceramic manufacturing: A proof of principle

Abstract

Technical ceramics for high-performance applications can be additively manufactured using vat photopolymerization technology. This technology faces two main challenges: increasing ceramic product size and improving product quality. The integration of process control strategies into AM equipment is expected to play a key role in tackling these challenges. This work demonstrates the feasibility of real-time and in-situ feedback control of the light-initiated polymerization reaction that lies at the core of vat photopolymerization technology. To prove the principle, a single-layer experimental setup was developed in which the degree of conversion was measured by infrared spectroscopy. Experimental data obtained from this setup was used to develop a control-oriented process model and identify its parameters. A material perturbation was applied by adding an inhibitor and the case with and without feedback control were compared. The results show that the feedback controller successfully compensated for the material perturbation and reached the same final conversion value as the unperturbed case. This result can be considered a fundamental step towards additive manufacturing of defect-free ceramic parts using in-line process control.

This chapter has been published in *Additive Manufacturing*, vol. 30, 100775, 2019.

5.1 Introduction

Additive Manufacturing (AM) opens the door to enhanced product functionality and performance [1], irrespective of the material used. Manufacturing near-net shape parts from high-performance ceramic materials, however, is generally challenging [2]. Current applications of ceramic AM already include bone implants, waveguides, and investment casting cores [3, 4], but these components are relatively small. Future applications in the high-tech industry require build volumes to expand to around one cubic meter. This expansion will enable the fabrication of large structural machine components, such as exposure stages for the semiconductor industry [5].

The machine component designer has several options at hand to additively produce ceramics, one of which is vat photopolymerization [2, 4]. Vat photopolymerization was initially developed to fabricate pure polymers [6] and later to produce green bodies for polymer-derived ceramics [7]. To this end, a mixture of ceramic particles and photopolymer resin is selectively cured in an AM machine, followed by polymer burn-out and ceramic particle fusing in a furnace. From an equipment perspective, nothing changes in the photopolymerization working principle when unfilled photocurable resins are replaced by ceramic-filled slurries. From a rheological or optical perspective, however, adding ceramic materials changes the material properties. This property change makes ceramic slurries more difficult to process than pure polymers. Moreover, the formation of cracks or other defects in the ceramic product can cause inadequate quality or even complete rejection.

Improving product quality and scaling up to large areas calls for advancements in vat photopolymerization equipment and control architecture. To work towards these advancements, one can view the AM machine as a mechatronic system and pursue developments in process modelling, sensing, actuation and control action computation as depicted in Figure 5.1. This approach can be followed for both the major process steps: material supply through recoating [8] and material transformation through photopolymerization [9]. Both process steps need to transition from open-loop to closed-loop control to minimize the sensitivity to equipment, material and process variability [10, 11].

Closed-loop (feedback) control is hardly addressed in literature for both the major process steps in vat photopolymerization. On the contrary, decades of work has been published on photopolymerization or cure *monitoring* [12], which is the process of observing, tracking, and analyzing information about the process to ensure that the process is on-course in meeting performance objectives. Few researchers have attempted to make the transition from using process measurements merely for process *monitoring* to using them for automatic process *control* [13]. Yebi et al. developed a model-based process control scheme for UV curing of glass fiber composites in which a precomputed surface temperature trajectory was tracked [14–16]. Zhao and

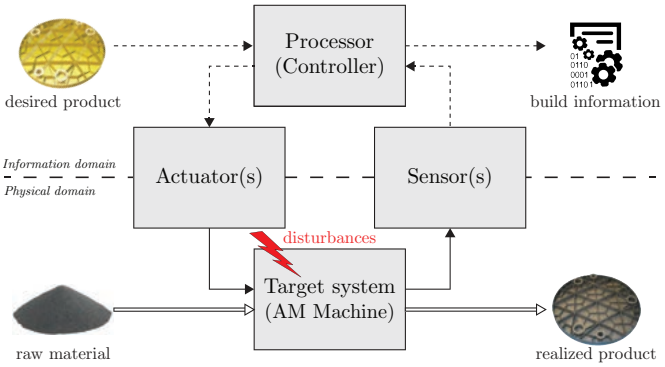

Figure 5.1: Mechatronic system view of an AM machine.

Rosen developed a bang-bang control scheme for a layerless photopolymerization process in which the cured height of microparts was controlled [17, 18].

Building upon these previous works, control strategies can be conceived for both the recoating and the photopolymerization steps at different length and time scales [9]. The applicability of control schemes for the recoating step depends on the specific recoating method, whereas the applicability of photopolymerization control schemes covers a wide area of photopolymerization methods. Since the underlying material transformation principle is the same in all vat photopolymerization systems, this work focuses on the photopolymerization step. Moreover, due to the common working principle, this work is not only relevant for all AM technologies falling into the category of vat photopolymerization, but for virtually any manufacturing technology involving UV curing, including material jetting [1], UV coatings [19], and dental fillings [20].

The works of Yebi et al. and Zhao and Rosen demonstrate that a paradigm shift may be emerging [17] concerning the incorporation of real-time process monitoring and closed-loop control systems into photopolymerization-based AM equipment. The most challenging form of such closed-loop control is arguably real-time in-situ continuous control of the actual material transformation process, i.e., the photopolymerization reaction. Alternatively, ex-situ discrete control strategies can be considered such as cycle-to-cycle [21], layer-to-layer, product, or batch control strategies [22] which were already developed for other AM technologies.

Despite the pioneering works of Yebi et al. and Zhao and Rosen, the implementation of real-time closed-loop control systems in AM machines remains a major challenge. On the one hand, Yebi et al. *indirectly* controlled a one-dimensional (1D) degree of monomer conversion distribution throughout multiple layers by

virtue of an estimate from a surface temperature measurement [14–16]. They argue that minimizing degree of conversion and temperature gradients benefits final part quality [16]. On the other hand, Zhao and Rosen controlled the cured height of single-layer parts using an interferometer [17, 18], thereby essentially controlling a 1D final part dimension instead of monomer conversion. They argue that the next step is to control not only part *geometry*, but also part *properties* [18].

The realization of voxel-level control of material properties is an elemental target [10] towards controlling both part geometry and final part properties. To this end, the measurable and controllable process parameters need to be identified that influence the final part properties [10]. The degree of monomer conversion is commonly accepted as a well-measurable parameter for the progress of the photopolymerization reaction [12, 23] and even can be used to infer material property evolution [24]. Moreover, the degree of conversion is measurable at the sub-voxel scale, so the probing volume is so small that the volume can be considered homogeneous or zero-dimensional (0D) and spatial gradients can be neglected. Contrary to the 1D situations in the works of Yebi et al. and Zhao and Rosen, this 0D situation allows for demonstrating what can be achieved on the microscale by virtue of feedback control when neglecting spatial effects such as light attenuation. The 0D results may serve as a fundamental benchmark for future endeavors to control spatially-distributed photopolymerization. Furthermore, *directly* measuring and controlling the degree of conversion in-situ in an infrared spectrometer eliminates the need for sensor validation, since it is considered a reliable technique to measure conversion [12, 23].

Although monitoring the photopolymerization step is a matured field, the sensing aspect seems to be the most critical for real-time control feasibility, whereas the actuation aspect by light fortunately seems to form no fundamental limitation [9]. Future machine integration poses stringent requirements on the sensing aspect. Specifically, it is desired to measure many voxels spanning a large range at high sampling rates, i.e., at high spatio-temporal resolution. Moreover, it is desired to both actuate and measure multiple layers on the same side.

In this work, these challenging sensing requirements are relaxed and a single-input-single-output (SISO) experimental setup is developed. The setup features a single layer and a practically homogeneous UV irradiation field to represent the process at the (sub-)voxel scale. By conducting proof-of-principle experiments on the lab setup, this work aims to demonstrate the feasibility of real-time and in-situ feedback control of monomer conversion in the photopolymerization reaction.

This paper is organized as follows. First, the experimental setup for photopolymerization control is described in Section 5.2. Sample preparation and the design of the parameter identification and closed-loop control experiments are discussed as

well. Second, a control-oriented process model is derived in Section 5.3. Third, the experimental results are presented in Section 5.4 followed by a discussion on control feasibility in a large-scale machine setting in Section 5.5 and concluding remarks in Section 5.6.

5.2 Methods

The main working principle of vat photopolymerization is that a photocurable resin is selectively cured through a UV light-initiated polymerization reaction [1, 25, 26], see Figure 5.2. In a highly oversimplified form, this polymerization reaction merely converts an amount of liquid monomer M into a solid polymer P:

$$M \rightarrow P. \tag{5.1}$$

Certainly, the actual polymerization reaction is much more involved [27, 28], but this understanding suffices here. The extent to which this polymerization reaction has progressed, can be quantified by a metric termed the *degree of conversion* α:

$$\alpha(t) = \frac{[P](t)}{[M]_0} = \frac{[M]_0 - [M](t)}{[M]_0} = 1 - \frac{[M](t)}{[M]_0}, \tag{5.2}$$

where $[M](t)$ and $[P](t)$ are the instantaneous monomer and polymer concentration respectively and $[M]_0 = [M](0)$ the initial monomer concentration.

A control volume containing monomer or polymer can be considered homogeneous or infinitesimally small if the system boundary is drawn on the sub-voxel or micrometer scale. A simple SISO system is obtained if this notion of a zero-dimensional space is combined with the assumption that the polymerization reaction has only one stationary input and one output, i.e., light intensity and degree of conversion respectively.

5.2.1 Experimental setup layout

Since the degree of conversion is commonly accepted as a good measure for the progress of the reaction [12, 23] and even can be used to infer material property evolution [24], this variable is selected as the measured variable in the control system. A multitude of measuring principles are used to measure conversion in *offline polymer characterization equipment*, including calorimetry, dielectrometry, and spectroscopy [9, 12, 23]. However, measuring the degree of conversion *online* and *in-situ* in the *AM machine* is challenging, let alone at high spatio-temporal resolution.

These challenging requirements were relaxed in this preliminary study, but the requirement for a high spatial resolution was retained to obtain a 0D SISO system.

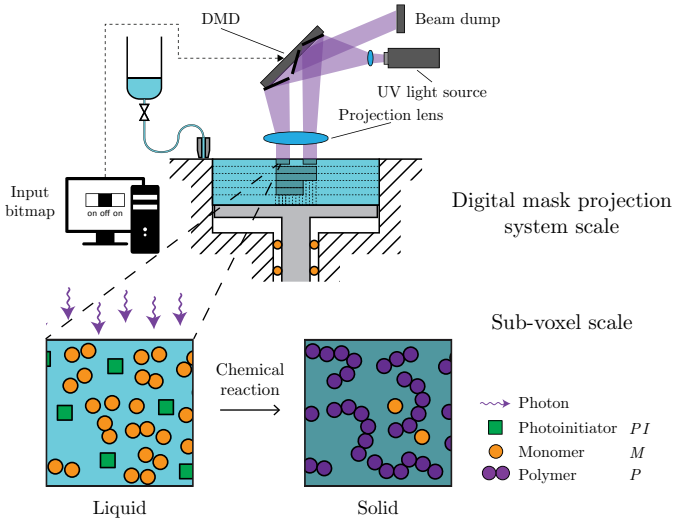

Figure 5.2: Main working principle of a vat photopolymerization system: liquid monomer is converted into solid polymer through a light-initiated polymerization reaction. Contrary to vector scanning systems, mask projection systems have a stationary light source (actuator), which allows for a simple SISO system description.

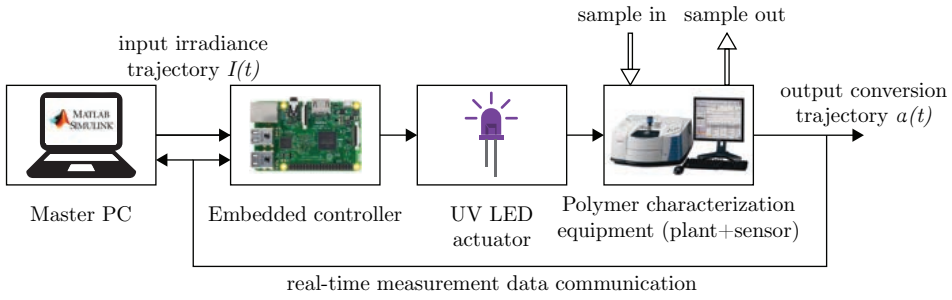

Figure 5.3: Embedded control system layout. The system was obtained by augmenting existing spectrometry equipment with an actuator, an embedded controller, and an interfacing master PC.

Hence, a measuring technology with a small probing volume needed to be selected. Fourier-transform infrared spectroscopy (FTIR) in attenuated total reflection (ATR) mode was selected, due to its micrometer-sized probing volume and its direct relationship between the measured absorbance and monomer concentration. The FTIR spectrometer (Thermo Scientific Nicolet 6700 with Smart Orbit ATR accessory) served both as the *sensor* and as the *plant* in the control system, since samples had

to be applied onto its measuring surface.

To complete the control system, the spectrometer was augmented with a 405 [nm] UV LED *actuator* (Bivar UV5TZ-405-30) and an *embedded controller* (Raspberry Pi 3 Model B) with MATLAB/Simulink support. Control schemes were implemented in MATLAB/Simulink on a master PC and an ethernet connection between the PC and the embedded controller allowed for initiating experiments and logging data. Figure 5.3 schematically shows the layout of the hence obtained embedded control system. Real-time data communication functionality was added to the FTIR spectrometer by self-developed software interfacing with Thermo OMNIC software through the Dynamic Data Exchange (DDE) protocol.

5.2.2 Sample preparation & materials

Samples were prepared by depositing a droplet of material onto the ATR crystal, placing a 300 [μm] thick steel spacer around it, and covering with a 1 [mm] thick quartz window (Thorlabs). The protruding geometry of the ATR crystal makes an impression in the sample as depicted in Figure 5.4. Since the protruding height is 200 [μm], the resulting layer thickness is approximately 100 [μm]. Note that of these 100 [μm] only the bottom few micrometers are probed in the FTIR measurements. Although the UV LED does not yield a homogeneous irradiance field, the irradiance is practically constant in the 3.5 [mm] diameter ATR crystal area and even more so in the smaller (single-bounce) probing area. The UV light intensity was calibrated using a UV power meter (Delta Ohm HD2302.0, LP471 detector). All experiments were performed under lab conditions at 20 [°C] room temperature and purposely performed without nitrogen flushing the sample chamber beforehand, to better match actual 3D printing conditions. Moreover, oxygen replenishment was already reduced due to the covering quartz glass.

The specific choice of materials is insignificant in demonstrating the functionality of feedback controlled photopolymerization. Arguably, even a pure photopolymer resin suffices to prove the principle for ceramic slurries, since the working principle of vat photopolymerization is exactly the same both *with* and *without* ceramic fillers. After initial tests with pure resins, an acrylate-based silica ceramic slurry (Formlabs GmbH, Berlin) was selected for this study.

5.2.3 Identification and application of uncertainties

Uncertainties in AM equipment, input materials, and processes ultimately lead to uncertainty in final parts [10]. Reducing sensitivity to these uncertainties is one of the main drivers behind applying feedback control. According to control theory, two types of uncertainty can be discerned [29]. On the one hand, *signal* uncertainty concerns uncertainty in the value of the input, output or measurement signals. On

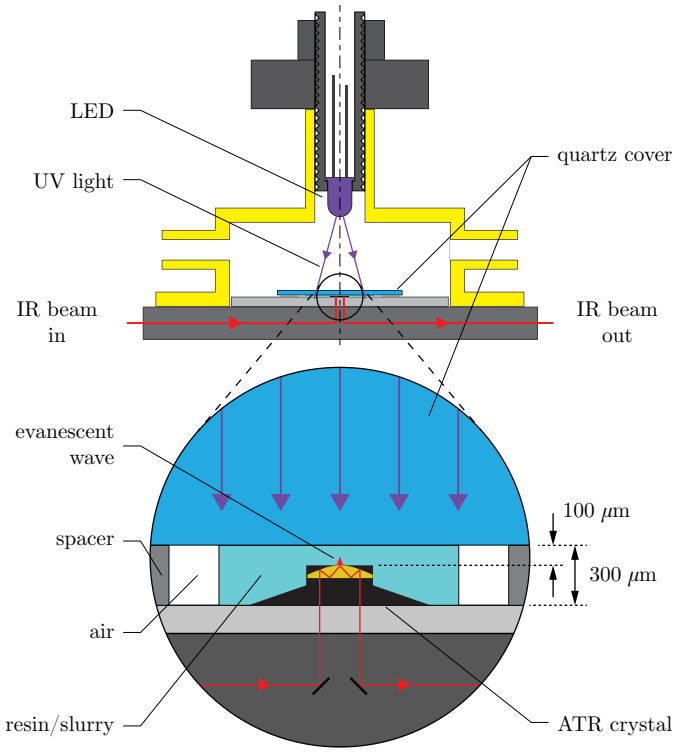

Figure 5.4: Schematic layout of the ATR-FTIR experimental setup.

the other hand, *model* uncertainty concerns neglected or unmodelled dynamics and parametric uncertainty. Figure 5.5 shows each of these different types of uncertainty in a block scheme of the cure process.

In this block scheme, the main *process input* variable evidently is the light intensity. The choice of the *process output* variable(s) to be used for feedback control is less evident, but the most promising output candidate seems to be the degree of conversion. This *measurable* process output can be considered merely a *secondary output*, since on a higher abstraction level the *difficult-to-measure* or *unmeasurable primary output* is product quality and the *primary input* is the product geometry and its properties. In control systems terminology, this problem can be considered an indirect or inferential control problem [13, 29].

Besides input and output disturbances, potential uncertainties could be identified for each parameter and variable by developing and analyzing models of the (vat) photopolymerization process. However, the purpose of this work would be lost if

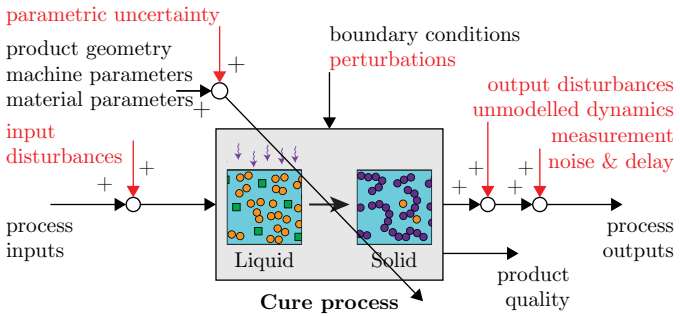

Figure 5.5: Potential uncertainties (in red) in vat photopolymerization.

this approach would be followed. Therefore, a literature screening [18, 25, 26] on possible error sources was performed, resulting in the following shortlist:

- Input uncertainties:
  - light source power/intensity variations;
  - light source intensity profile shape variations;
  - light source positioning errors.
- Exogenous signal uncertainties:
  - layer thickness deviations (poor recoating);
  - oxygen level fluctuations (inhibition);
  - temperature fluctuations.
- Resin parametric uncertainties:
  - deviating resin/slurry properties;
  - spatial composition variations (poor mixing);
- Unmodelled dynamics:
  - non-constant light transmission/photobleaching;
  - oversimplified reaction mechanism kinetics;
  - post-processing (cleaning) steps;
  - scattering due to ceramic particles;
  - shrinkage.

Assessing the potential performance gain that can be obtained by transitioning from open-loop to closed-loop control, would require a model of the magnitude, the occurrence probability, and the dynamics of these uncertainties. Little is known from literature about the significance of these individual uncertainties. However, the system can be subjected to intentionally applied disturbances for proof-of-principle demonstration purposes. From the uncertainties shortlist given above, it was established that it is possible to apply:

1. an artificial input disturbance by adding a signal;

2. a material composition disturbance by:
   adding an inhibitor to the mixture;
   pre-curing to a non-zero initial state;
   purging with nitrogen or oxygen;
   varying the photoinitiator concentration;
3. a thermal disturbance by cooling or heating the sample.

Among these artificial disturbances, the first is a signal uncertainty that was easily digitally applied in the control software. Therefore, initial tests were carried out with a significant input bias disturbance and these already yielded positive results. The second and third disturbances are model uncertainties that needed to be physically applied. The choice was made to add a 4-methoxyphenol inhibitor (MEHQ, Sigma-Aldrich) to the slurry, since this disturbance represents a poorly mixed or deteriorated material, which is presumably more likely to occur in the 3D printer than a significant input bias.

5.2.4 Experimental procedure

Since the main goal of this paper is to demonstrate the feasibility of closed-loop controlled conversion through proof-of-principle experiments, the following three situations are compared:

1. a nominal reference situation (non-disturbed);
2. a disturbed open-loop situation (controller is off);
3. a disturbed closed-loop situation (controller is on).

Figure 5.6 illustrates these three situations with block schemes. First, a series of parameter identification experiments was conducted to obtain a process model relating the input $I(t)$ to the output $\alpha(t)$ under *nominal* conditions. Subsequently, the process model thus obtained was used to generate feedforward input and reference trajectories $I_{FF}(t)$ and $\alpha_{ref}(t)$ for use in the closed-loop control experiments under *disturbed* conditions.

Parameter identification was carried out by performing step-response experiments under *nominal* conditions, in which a step change in the input signal $I(t)$ of 5 [%] = 1.9 $[\frac{\mathrm{W}}{\mathrm{m}^2}]$ was applied for 90 [s] and the change in the output $\alpha(t)$ was recorded [13]. Typically, stationary mask projection photopolymerization systems merely turn on the light source for a certain period, which in fact can be considered a step-response experiment in itself. In Section 5.3 a differential equation model is developed, whose analytical solution is fitted to the experimental data through least squares parameter estimation.

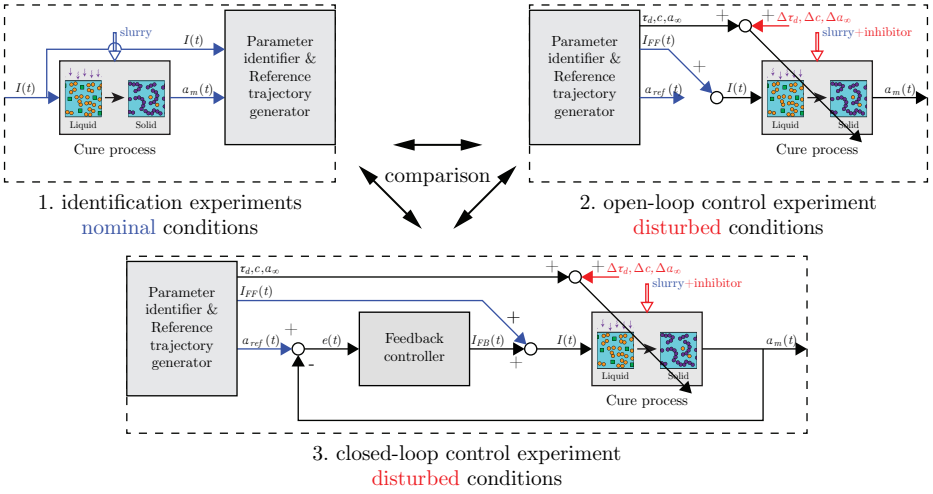

Figure 5.6: Experimental procedure visualized by block schemes of the parameter identification and subsequent open- and closed-loop control experiments. The nominal conditions are indicated in blue; the material composition disturbance and consequent parameteric uncertainty are indicated in red.

Open- and closed-loop control experiments were carried out under *disturbed* conditions by dissolving 0.5 [wt%] of inhibitor into the slurry, applying a feedforward step input $I_{FF}(t)$ of 5 [%] = 1.9 $[\frac{\mathrm{W}}{\mathrm{m}^2}]$ for 60 [s], and turning the controller off or on respectively. To this end, the control schemes shown in Figure 5.6 were implemented in MATLAB/Simulink.

5.3 Control-oriented process modelling

Many models to describe the photopolymerization process have been developed; refer to the books by Bartólo [25] and Odian [27] for a general overview of (vat) photopolymerization process modelling and a previous work by the present authors [9] for an overview of relevant phenomena and process models. However, very few models such as those reported in the works by Yebi [16] and Zhao [18] have been developed with the goal to use them for control purposes. Therefore, a simple, control-oriented model is developed in this section. To obtain the desired SISO model, the assumption is made that light intensity gradients in the vertical direction can be neglected within the probing volume.

5.3.1 Photopolymerization kinetics modelling

Two modelling approaches are typically pursued in photopolymerization kinetic modelling [25]: mechanistic or phenomenological modelling. Mechanistic models are typically set up by determining the reaction mechanisms, formulating species balances and expressions for the reaction rate constants. A typical example is the model for free radical photopolymerization by Odian [27], which is obtained by setting up species balances for the monomer, radical chains and photoinitiator, and applying a steady-state radical concentration assumption to simplify to a single differential equation:

$$\frac{d[M]}{dt} = -k_p[M]\left(\frac{\phi I_a}{k_t}\right)^{1/2}, \tag{5.3}$$

where k_p and k_t are the propagation and termination reaction constants respectively, ϕ the quantum yield for initiation and I_a the absorbed light intensity. The degree of conversion α can be calculated by combining (5.3) with (5.2). In contrast, phenomenological models try to capture the complete polymerization reaction in one differential equation and directly compute the degree of conversion α. A typical example is given by:

$$\frac{d\alpha}{dt} = k(T)I^b(1-\alpha)^n, \tag{5.4}$$

where $k(T)$ is the reaction rate constant as function of temperature, I is the light intensity and n is the reaction order. The exponent b can have a value between 0.5 and 1 [25], so the dependence of the polymerization rate $-\frac{d[M]}{dt}$ on the input light intensity is a square-root dependence, a linear dependence or something in between. Note that for $b = 0.5$ [-] and $n = 1$ [-], combining (5.2) and (5.3) gives (5.4). Mechanistic modelling approaches often lead to models having many parameters [25], whereas phenomenological models generally result in fewer parameters and hence seem more suitable for control.

This work proposes the following control-oriented model based on the notion that photopolymerization is represented by the simple chemical reaction given by (5.1). Chemical kinetics theory [30] says that the rate of reaction v can be given by:

$$v = k[M]^n, \tag{5.5}$$

where k is the rate constant and n the reaction order. If the volume does not change during the reaction, the rate of reaction v can be replaced by the change in concentration $\frac{d[c]}{dt}$ multiplied with the inverse of the stoichiometric coefficient $\frac{1}{\nu_i}$. This gives the following model:

$$\frac{d[M](t)}{dt} = -k(I)[M]^n(t), \tag{5.6}$$

where $k(I)$ is the rate constant as function of light intensity. The rate constant is defined in the same way as in (5.4), but the temperature dependence is neglected:

$$k(I) = cI^b(t), \tag{5.7}$$

where c is a constant representative for the reaction rate. Obviously the term 'rate constant' for k from kinetics theory stricly is not correct in this case, since k is not a constant. Substituting (5.7) in (5.6) and combining with (5.2) gives the proposed model:

$$\frac{d[M](t)}{dt} = -cI^b(t)[M]^n(t), \tag{5.8}$$

$$\alpha(t) = 1 - \frac{[M](t)}{[M]_0}, \tag{5.9}$$

with the initial condition $[M](0) = [M]_0$ and the physical constraint that energy can only be added by irradiation:

$$I(t) \geq 0. \tag{5.10}$$

Equation (5.3) is retrieved for $b = 0.5$ [-] and by taking $k(I) = k_p\sqrt{\frac{\phi I}{k_t}}$. Another physical constraint is that the monomer concentration $[M]$ is nonnegative.

In control systems terminology, the *input* variable $u(t)$ to the system is the light intensity $I(t)$, the internal *state* variable $x(t)$ is the monomer concentration $[M](t)$, and the *output* variable $y(t)$ is the degree of conversion $\alpha(t)$. Using these naming conventions, the model can be rewritten as a state and output equation:

$$\frac{dx(t)}{dt} = -c \cdot u^b(t) \cdot x^n(t), \tag{5.11}$$

$$y(t) = 1 - \frac{x(t)}{x_0}, \tag{5.12}$$

with the initial condition $x(0) = x_0$ and the input constraint:

$$u(t) \geq 0. \tag{5.13}$$

Note that (5.11) and (5.12) can also be combined to a single ordinary differential equation in terms of y by eliminating x. The model (5.3) suggests a first-order reaction, but second-order reactions are reported in literature as well [27], so $n \in \{1, 2\}$ is considered in this paper. Note that the *reaction order* in chemical kinetics is different from the *system order* in control systems theory; the former refers to the sum of the exponents n of the reaction rate, whereas the latter refers to the number of states, i.e., the dimension of the state vector $x(t)$, which in this case is one.

5.3.2 Analytical solutions for parameter estimation

The ordinary differential equations (5.8) and (5.11) have analytical solutions for a constant input light intensity $I(t)$ and a given reaction order n, which can be used to write explicit solutions for the conversion $\alpha(t)$. The existence of these solutions is the reason to use step-response experiments for parameter identification. In these experiments, the following input $u_{FF}(t)$ is applied:

$$u_{FF}(t) = \begin{cases} 0, & t < t_{step} \\ I_{step}, & t_{step} \leq t < t_{end} \\ 0, & t \geq t_{end} \end{cases} \tag{5.14}$$

where t_{step} is the instant the light turns on, t_{end} the instant the light turns off, and I_{step} is the feedforward intensity.

The first step-response experiments showed a noticeable delay between the instant the light was turned on and the instant the process started to respond. This time-delay behaviour is well known for free radical photopolymerization [26, 31] and is attributable to the consumption of inhibitors before the chain reaction can rapidly speed up. This high-order system behaviour can be approximated with a pure time delay in the input [13]. To model this behaviour, the feedforward input (5.14) is delayed by τ_d such that $u_{FF,d}(t) = u_{FF}(t - \tau_d)$ and set to zero once the light is turned off at t_{end}:

$$u_{FF,d}(t) = \begin{cases} 0, & t < t_{step} + \tau_d \\ I_{step}, & t_{step} + \tau_d \leq t < t_{end} \\ 0, & t \geq t_{end}. \end{cases} \tag{5.15}$$

Note that this time-delayed feedforward input $u_{FF,d}(t)$ is only applied in simulations with the model (5.8) or (5.11), whereas the non-delayed input $u_{FF}(t)$ is applied in physical experiments.

The analytical solution to (5.8) with the input (5.15) for a first-order reaction, i.e., $n = 1$ [-], is well known [13] and using this solution with (5.9) gives:

$$\alpha(t) = \begin{cases} 0, & t < t_{step} + \tau_d \\ 1 - e^{-cI_{step}^b(t-(t_{step}+\tau_d))}, & t_{step} + \tau_d \leq t < t_{end} \\ \alpha_{end}, & t \geq t_{end}. \end{cases} \tag{5.16}$$

where τ_d is a time delay and $\alpha_{end} = 1 - e^{-cI_{step}^b(t_{end}-(t_{step}+\tau_d))}$. In control systems terminology, this is the solution for a first-order system with time delay [13].

Similarly, the analytical solution to (5.8) with the input (5.15) for a second-order reaction, i.e., $n = 2$ [-], can be derived and using this solution with (5.9) gives:

$$\alpha(t) = \begin{cases} 0, & t < t_{step} + \tau_d \\ 1 - \frac{1}{1+[M]_0 c I^b_{step}(t-(t_{step}+\tau_d))}, & t_{step} + \tau_d \leq t < t_{end} \\ \alpha_{end}, & t \geq t_{end} \end{cases} \tag{5.17}$$

where $\alpha_{end} = 1 - \frac{1}{1+[M]_0 c I^b_{step}(t_{end}-(t_{step}+\tau_d))}$.

The model (5.8), (5.9) assumes that all monomer M can be converted into polymer, which implies that $\alpha \in [0, 1]$. However, in practice the degree of conversion reaches an asymptote $\alpha_\infty < 1$ [4], so the degree of conversion as defined by (5.9) and the analytical solutions (5.16) and (5.17) should be considered a normalized degree of conversion. The measured absolute degree of conversion α_m can be obtained by introducing a degree of conversion asymptote α_∞:

$$\alpha_m(t) = \alpha_\infty \alpha(t). \tag{5.18}$$

5.3.3 Sensor modelling

The FTIR spectrometer does not directly output the desired degree of conversion $\alpha_m(t)$ sensor signal, so post-processing is required to compute $\alpha_m(t)$ from the absorbance spectra $A(\tilde{\nu}, t_i)$ as function of the wavenumber $\tilde{\nu} \in [400, 4000]$ [cm^{-1}] and time instance t_i. A typical way to do this is to calculate the baseline-corrected areas under the reference peak A_{ref} and the carbon-carbon double bond C=C peak $A_{C=C}$ [32, 33]. This way, the peak area ratio $r_{pA}(t)$ can be calculated:

$$r_{pA}(t) = \frac{A_{C=C}(t)}{A_{ref}(t)}. \tag{5.19}$$

The degree of conversion can be computed from (5.19) by dividing it by the initial peak area ratio $r_{pA,0}$ [33]:

$$\alpha_m(t) = 1 - \frac{r_{pA}(t)}{r_{pA,0}}, \quad t > 20[s], \tag{5.20}$$

where $r_{pA,0}$ was determined by averaging $r_{pA}(t)$ in the range $t \in [0, 20]$ [s]. This initialization time was chosen such that ten samples were used to calculate $r_{pA,0}$, each having a sampling time $T_s = 2.0$ [s]. Note that the degree of conversion was only available online after the 20 [s] initialization period.

IR absorbance spectra of the Formlabs silica material showed that a practically constant peak in the 1750 [cm^{-1}] region could be used as the reference peak, which is associated to C=O stretching [32]. Moreover, the spectra showed that the peak $A_{C=C}$ in the 1635 [cm^{-1}] region could be used to quantify the carbon-carbon double bond (C=C) or monomer concentration $[M]$.

5.3.4 Feedback controller design

A first step in the feedback controller design process is to choose the type of controller to be used. A choice could best be made based on the specific *control problem* at hand. To this end, one could attempt to classify the control problem according to characteristics such as the degree of nonlinearity and the dynamic character of the process behaviour [13]. The control-oriented model given by (5.11) and (5.12) can be classified as a low-order nonlinear SISO system that is either linear ($b = 1$ [-]) or nonlinear ($b \neq 1$ [-]) in the input with input constraints. If the reaction order $n = 1$ [-] and $b = 1$ [-], the system is termed a *bilinear* system [34,35]; if $n = 2$ [-] the system belongs to a class of nonlinear systems that may be feedback linearizable [36]. It can be concluded that the system dynamics at hand are simple, but nonlinear.

The nonlinear system dynamics suggest that a special-purpose controller may be more effective than a classical controller. The control schemes previously developed by Yebi et al. [14–16] can be considered more advanced than classical, but cannot be applied here due to the difference in control objectives and due to the spatially-distributed (1D) and multi-layer nature of their control problem. Moreover, the goal of this work is not to optimize a feedback controller for stability and performance, but to demonstrate disturbance rejection through a proof-of-principle experiment. Thus, a logical starting point is the most commonly used classical feedback controller: the proportional-integral-derivative (PID) controller [13, 37], which was also proposed by Zhao and Rosen as a substitute to their simple binary on-off controller [18, 21]. Moreover, classical control strategies serve as a benchmark for more advanced control strategies. Due to the rather noisy output signal, the choice was made to omit the derivative action and use a proportional-integral (PI) controller to prevent noise amplification.

A PI controller typically has the form [13, 37]:

$$u_{FB}(t) = K_c \left[e(t) + \frac{1}{\tau_I} \int_0^t e(t)dt \right], \tag{5.21}$$

where K_c is the *proportional* gain, $e(t)$ the error, and τ_I the *integral* time. The error signal is defined as the difference between the reference $r(t) = \alpha_{ref}(t)$ and the measured output $y(t) = \alpha_m(t)$:

$$e(t) = \alpha_{ref}(t) - \alpha_m(t). \tag{5.22}$$

Referring to Figure 5.6, the *input* to the PI controller is the error $e(t)$ and the *output* from the controller is the light intensity $u_{FB}(t) = I_{FB}(t)$. Consequently, the total light intensity $I(t)$ applied to the cure process equals the sum of (5.14) and (5.21):

$$I(t) = I_{FF}(t) + I_{FB}(t). \tag{5.23}$$

The working principle of the PI controller can be interpreted as follows. If there is a positive error $e(t)$ between the reference $\alpha_{ref}(t)$ and the actual output conversion $\alpha_m(t)$, i.e., the cure process is not quick enough, then the proportional action of the controller will apply a positive feedback input $u_{FB}(t)$ to increase the reaction rate and vice versa if there is a negative error the proportional action will apply a negative feedback. Additionally, if the time integral of the error $e(t)$ is positive even if the error is momentarily small, the integral action will increase the reaction rate and vice versa decrease if the time integral is negative.

After choosing the PI controller type, the next step was to find suitable controller parameters K_c and τ_I. To this end, a common controller tuning approach based on an approximate model was applied [13]. The approach consists of fitting an approximate model to the process reaction curve $y(t)$ and using the obtained parameters in specific formulas that give recommended controller parameter values. The most commonly applied approximate model is a first-order system with time delay of the form:

$$\tau \frac{dy(t)}{dt} = -y(t) + Ku(t - \tau_d), \tag{5.24}$$

where τ is the effective time constant, K the steady-state gain, and τ_d the effective time delay. The response $y(t)$ of the first-order system (5.24) to a step input $u(t)$ is equal to the response of the first-order reaction (5.16) with $\tau = (cI^b_{step})^{-1}$. Note that although the process responses are equal, the underlying system dynamics differ from each other. Having fit the approximate model to the process response, the controller parameters were obtained from the Integral Time-weighted Absolute Error (ITAE) tuning rule for set-point changes [13]:

$$\begin{aligned} K_c &= \frac{0.586}{K}\left(\frac{\tau}{\tau_d}\right)^{0.916}, \\ \tau_I &= \frac{\tau}{1.03 - 0.165\left(\frac{\tau_d}{\tau}\right)}. \end{aligned} \tag{5.25}$$

5.4 Results

5.4.1 Parameter identification under nominal conditions

Step response experiments were performed by applying a step input, recording the absorbance spectra, and computing the degree of conversion. Figure 5.7 shows the resulting time evolution of the IR absorbance spectrum in the spectral range of interest. As expected, the figure shows that the baseline-corrected area remains practically constant under the reference C=O peak in the 1750 [cm^{-1}] region, whereas the area decreases significantly under the C=C peaks in the 1635 [cm^{-1}] region.

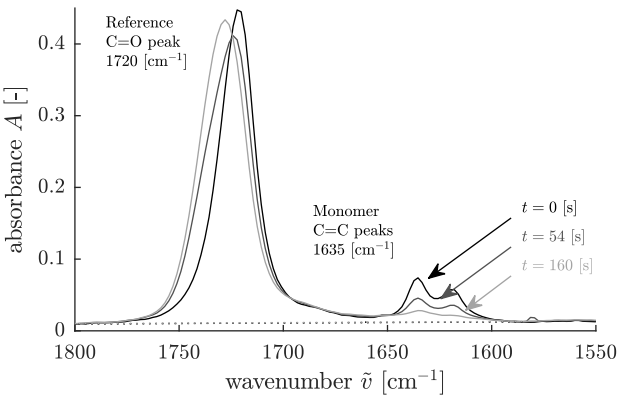

Figure 5.7: IR absorbance spectrum of the Formlabs silica slurry at three different times upon UV curing. The baselines and division line between the peaks are indicated by the dotted lines. Over the course of the cure process, the baseline-corrected reference peak (1750 [cm^{-1}] region) remains constant and the C=C peak (1635 [cm^{-1}] region) decreases.

From these absorbance spectra, the ratio r_{pA} was computed between the double bond and reference peak areas to determine the degree of conversion $\alpha_m(t)$. Figure 5.8 shows the time evolution of the peak area ratio $r_{pA}(t)$ and the estimated initial peak area ratio $r_{pA,0}$. The figure shows a steep decrease in the peak area ratio approximately twelve seconds *after* the light had been turned on. To determine the conversion *online*, the initial peak area ratio was determined *before* the light was turned on. This functionality was implemented in the Simulink control scheme by taking the average of the peak area ratios between $t = 0$ [s] and $t = 20$ [s] and storing in memory for the remainder of the experiment.

Once the initial peak area ratio had been determined, the degree of conversion was computed at each time step and made available for real-time feedback control. A typical resulting degree of conversion measurement is shown in Figure 5.9 along with first- and second-order reaction model fits. Among the two, only the second-order reaction model shows an acceptable fit for the intended purpose, so the model parameter $n = 2$ for this material.

This model fitting procedure was performed for ten equally spaced input levels I_{step} from 10 [%] to 100 [%] and an additional level at 5 [%] with three replications per level in a randomized sequence. Figure 5.10 shows the resulting identified reaction rate k as a function of normalized light intensity I, along with a square root function fit. The experimental data is in accordance with the well-known

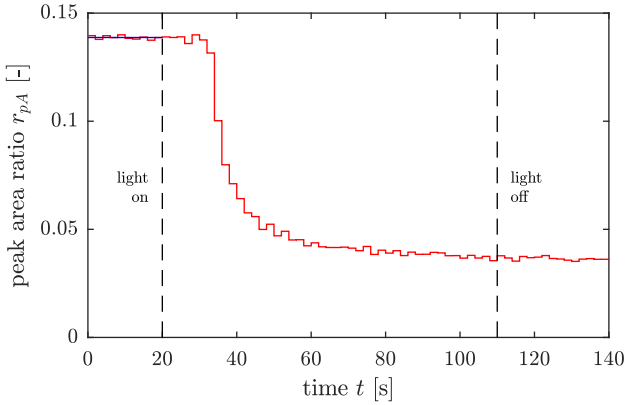

Figure 5.8: Peak area ratio of the Formlabs silica slurry during UV curing. The samples between 0 and 20 [s] are used to determine the initial peak area ratio (blue). Twelve seconds after irradiation starts, the response shows a steep decrease.

Resin	$\boldsymbol{b}$ [-]	$\boldsymbol{n}$ [-]	$\boldsymbol{c}$ [s^{-1}]	$\boldsymbol{\tau_d}$ [s]	$\boldsymbol{\alpha_\infty}$ [-]
Formlabs silica	0.5	2	1.3±0.2	12±0.6	0.77±0.01

Table 5.1: Summary of identified model parameter means ± standard deviations.

square-root dependency [27], so the model parameter $b = 0.5$ [-] for this material. Note that the higher the input, the closer the time constant $\tau = \frac{e-1}{k(I)}$ approaches the temporal resolution or sampling time T_s, which may explain the seemingly inreasing variance with intensity.

To approximate the variance at a single level, a repeatability experiment was performed with ten replications at $I_{step} = 5$ [%]. Table 5.1 shows the parameters identified from this data and their respective standard deviations. The second-order reaction model was fully parameterized at this point and was subsequenlty used to generate a nominal reference trajectory $\alpha_{ref}(t)$ to be followed by the output $\alpha_m(t)$.

5.4.2 Open- & closed-loop control under disturbed conditions

Once the parameter identification procedure under *nominal, non-disturbed* conditions had been completed, the open- and closed-loop control experiments were performed under *disturbed* conditions. Firstly, the controller parameters were obtained by filling in the identified first-order model parameters in the tuning rule (5.25). Table 5.2 gives the resulting model and controller parameters. Secondly, the silica slurry *with* inhibitor was used and the feedback controller was either turned

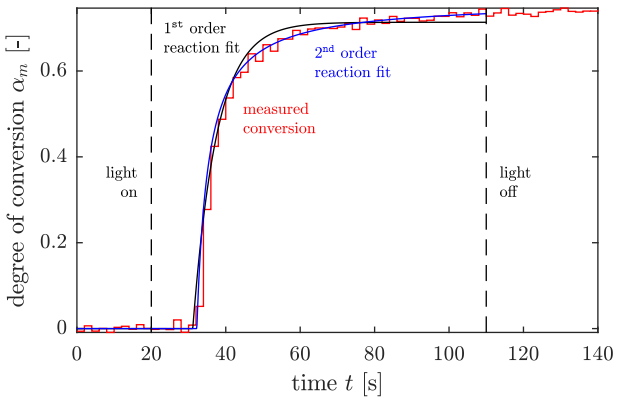

Figure 5.9: Degree of conversion determined from IR absorbance spectra during UV curing. First- and second-order reaction model fits were fitted to the experimental data; the second-order reaction model shows an acceptable goodness of fit.

Parameter	K [-]	τ [s]	τ_d [s]	K_c [-]	τ_I [s]
Value	13.9	3.44	2	0.069	3.68

Table 5.2: First-order approximate model and PI controller parameters.

off or on. Figures 5.11 and 5.12 show the measured degree of conversion $\alpha_m(t)$ and the inputs $u(t)$ respectively for the three different cases: (1) the non-disturbed reference situation, (2) the disturbed open-loop situation, and (3) the disturbed closed-loop situation.

Comparing the open-loop case with the reference case, the open-loop response in Figure 5.11 shows an increasing error over time with respect to the reference. On the contrary, the closed-loop case shows that the feedback controller attempts to minimize this error through significant corrective action as evident from Figure 5.12. If the final reference conversion value is considered a minimal threshold for sufficient curing, then it is *not* met in the open-loop case, but it *is* in the closed-loop case. Hence the material composition disturbance is successfully compensated for and the principle of real-time feedback control is proven in this experimental setting.

5.5 Discussion

The experimental results in Section 5.4 clearly demonstrate that a feedback controller was successful in compensating for an intentionally applied material disturbance in

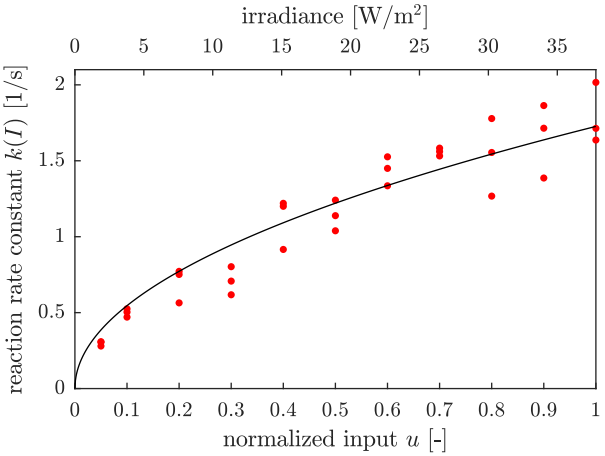

Figure 5.10: Identified reaction rates k as a function of light intensity I. Results conform to the well-known square-root dependency, whose fit to the experimental data is given by the solid line.

a dedicated lab setup. Notwithstanding these promising results, several comments have to be made regarding the experimental results and the limitations of the present experimental setup. The sensing requirements also need to be revisited to draw conclusions on the feasibility of the in-situ real-time control approach in a large-scale machine setting.

5.5.1 Parameter identification experiments

The lab-scale identification experiments in Figure 5.9 show that the second-order reaction model provides a good fit, since the error falls within the measured signal's noise level. Although effective for the majority of the polymerization reaction, the control-oriented model is not capable of accurately describing the reaction kinetics during the initial inhibition period or the final dark polymerization period. Many physical phenomena were excluded from this (over-)simplified model, such as spatial variations due to light absorption, photoinitiator depletion, oxygen inhibition, and heat and mass transfer [9]. Nevertheless, the second-order reaction model is considered acceptable for the purpose of this paper since it is merely used to generate the reference trajectory for the feedback control experiments.

The results also show a rather significant variability in the identified reaction rate constant and time delay. This parameter variability can be considered representative of the total process variability, which is affected by uncertainties in the actuator, the sensor, the data processing and communication, the embedded controller, and the

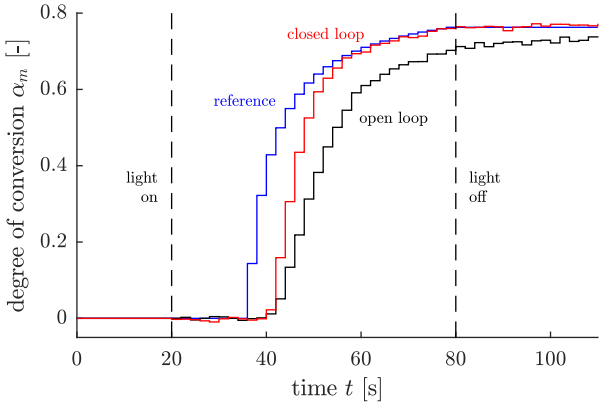

Figure 5.11: Degree of conversion vs. time for the reference, open-, and closed-loop controlled case. The open-loop case shows a reduced level of curing with respect to the reference. On the contrary, the closed-loop case meets the desired final conversion level.

photopolymer itself. However, it is difficult to draw conclusions on how much each source of variability contributes to the total variability and to what extent these uncertainties are encountered in real-life industrial AM machines. In the setup, significant variability may result from the manual deposition of material and the free support of the covering glass on the spacer. These factors may lead to layer thickness deviations and hence to reaction rate variability due to light intensity variations when one assumes Beer-Lambert-like absorption [27].

5.5.2 Control experiments

The ultimate control objective is to reduce variability in final product quality and compensate for disturbances, but product quality is not easily or directly measurable. Firstly, product quality needs to be defined and quantified by metrics [11]. Secondly, the difficulty of measurability implies that product quality needs to be inferred from measurable quantities such as the degree of conversion. Therefore, the question arises what the relationship is between the degree of conversion and the mechanical properties, which ultimately express product quality. Moreover, the question arises what shape the reference conversion trajectory $\alpha_{ref}(t)$ should have such that the desired mechanical properties are obtained. To the author's knowledge, it is still an open research question whether the complete time evolution of the reaction $\alpha_{ref}(t)$ should be closely tracked, or merely the final degree of conversion value $\alpha(t_{end})$ should be met.

Recent literature reports significant sensitivity of mechanical properties to dif-

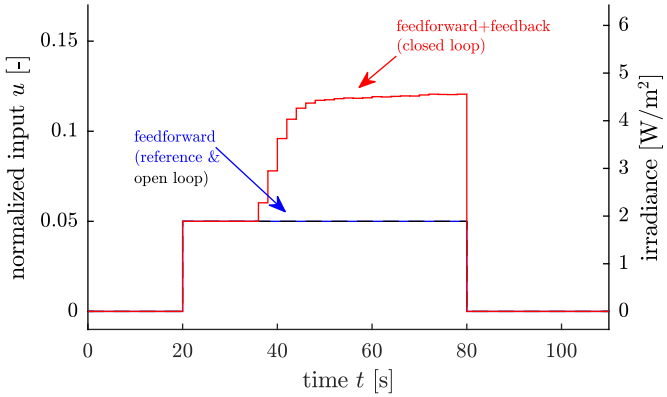

Figure 5.12: Total input vs. time for the reference, open-, and closed-loop controlled case. The closed-loop case shows significant corrective action to compensate for the presence of inhibitor in the slurry.

ferences in conversion levels [24, 38, 39]. This sensitivity implies that if the final reference conversion value is considered a minimal threshold, then the open-loop controlled case in Figure 5.11 would have led to product defects in contrast to the closed-loop case. In other words, the closed-loop case clearly outperforms the open-loop case. However, the opportunities and benefits are yet to be explored in terms of implementing the closed-loop controller in a real AM machine. The material composition disturbance applied in the experiment was for demonstration purposes of the closed-loop control principle, and not intended to be representative for the typical disturbances encountered in an industrial AM setting.

Further performance improvements may be gained by exploiting the potentially fast actuation capabilities of UV light. This work merely applies a constant feedforward step input, which actually is representative for the curing of a single layer in digital mask projection systems. Note that the point of interest at the bottom of the layer receives multiple step inputs of decreasing intensity from successive layers. Different input profiles during the curing of each layer may yield better mechanical properties such as the initially lower intensities in soft-start photopolymerization [40].

5.5.3 Limitations of the experimental setup

A persistent issue faced by researchers is that light intensities need to be reduced to match the reaction and measurement timescales in in-situ photopolymer characterization [41]. Moreover, the achievable control system performance is heavily influenced by the sensor's measurement rate, which is rather limited in the present

setup. Particularly, a key metric for achievable control system performance is the ratio of the process dynamics time constant to the sampling time: $\frac{\tau}{T_s}$. In the system at hand, the reaction time constant is inversely proportional to the nominal light intensity $\tau \propto I_{FF}^{-1}$.

An acceptable ratio $\frac{\tau}{T_s}$ was achieved by choosing a sufficently low nominal input intensity, which is consistent with common practice [41]. The hence achieved measurement time was $T_s = 2.0$ [s]. This rather low value was due to (1) the FTIR spectrometer settings and (2) the overhead in the self-developed software interface between the FTIR spectrometer and MATLAB/Simulink. Note that the spectrometer was not designed for real-time control experiments and hence did not natively support real-time data output.

As a result of the low nominal light intensity, the achieved reaction rate time constant $\tau = 8$ [s] and exposure time of $t_{exp} = 60$ [s] are much larger than in typical mask projection systems, where exposure times range from one to ten seconds per layer. Options to increase the sampling rate are under investigation to allow for increased UV light intensities and, hence, a closer match to actual printing conditions.

5.5.4 Implications of the control approach in a large-scale machine setting

Several steps have to be taken before the present work's real-time control approach can be implemented in real, large-scale AM machines. Figure 5.13 suggests a sequence of steps from 0D sub-voxel control as demonstrated in this work to full 3D product control. Firstly, the vertical dimension needs to be considered to scale up to a single homogeneous layer or 1D voxel. Therefore, a 1D *depth-resolved* degree of conversion measurement $\alpha(z)$ or a *layer-averaged* degree of conversion value $\overline{\alpha}$ needs to be available, as opposed to a 0D point measurement.

Secondly, the lateral dimensions need to be considered to scale up to a 2D array of 1D voxels in the xy-plane. Implementation of the present control approach in a real AM machine is most easily envisioned in stationary digital mask projection systems, where each pixel of the projection system is associated to a surface voxel as depicted in Figure 5.2. Zhao and Rosen have already shown that scaling up laterally in mask projection systems is a matter of using an array detector [17]. In the most simple case, the closed-loop control system presented here can be implemented as multiple parallel SISO systems. Each surface voxel can then be considered a SISO system having its own boundary light intensity input modulated by the projector system, its own layer-averaged degree of conversion measurement, and its own feedback controller. In a more involved case, a multiple-input-multiple-output (MIMO) control strategy could be implemented to address cross-talk between neighbouring pixels.

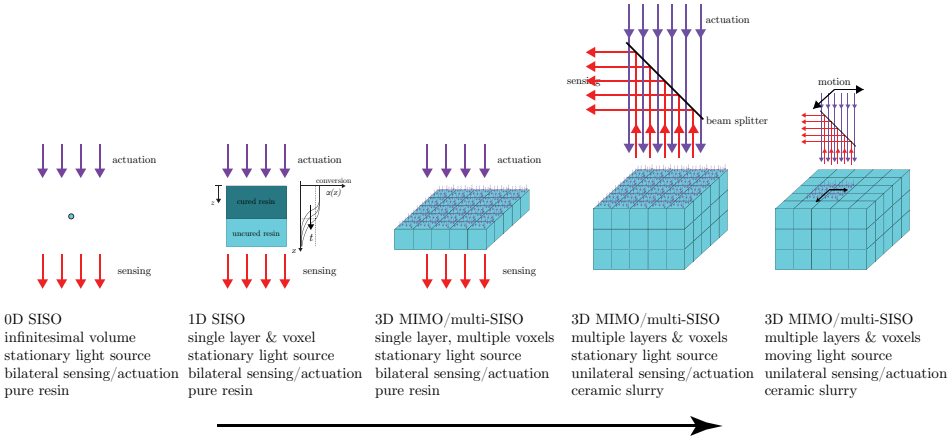

Figure 5.13: Proposed roadmap from single 0D sub-voxel control to full 3D product control.

Thirdly, the single-layer scope needs to be extended to multiple layers. In the most simple case, the single-layer controller in this paper could be reset for each new layer, without considering the effect of UV exposure of the current layer on previously cured layers. Alternatively, the exposure of a layer to subsequent doses can be compensated for in the process planning phase when determining the feedforward step input. More performance may be gained by utilizing a 3D full-field measurement $\alpha(x, y, z)$ of the degree of conversion and applying model-based control techniques such as those by Yebi et al. [14]. Additionally, multi-level control architectures can be envisioned where real-time in-situ continuous control is combined with discrete layer-to-layer or product control [22]. However, even though the control problem can be extended to a full 3D field, the UV light input remains a 2D input field at the boundary (surface) of the layer.

Lastly, light sources moving in the xy-plane need to be addressed to enable implementation of the real-time control approach in vector scanning or scanning mask projection systems [42]. Control strategies for metal-based processes such as melt-pool area or temperature control [11] may be applied to the analogous control problem for photopolymerization-based processes.

The aforementioned scaling-up procedure requires a 3D full-field degree of conversion sensor, having a high spatio-temporal resolution, a range spanning a considerable build volume, and being capable of measuring and actuating on the same side, e.g., in a reflective mode. Such a sensor is not yet available and the feasibility of implementing an FTIR spectrometer into the vat photopolymerization

machine is arguable. Light scattering due to the presence of ceramic particles in the resin [4, 43] may further complicate the applicability of such optical cure monitoring techniques. However, the presented control approach will also work for other measuring technologies, as long as they provide representative sensing signals for the degree of cure. Moreover, plans have been reported of implementing a Raman spectrometer into a vat photopolymerization machine [44]. If real-time degree of cure sensing for continuous control ultimately proves to be impractical in the AM machine, alternative discrete control strategies [22] may be considered. For instance, an in-situ calibration method can be conceived that determines the key material properties offline, but in the machine through parameter identification techniques such as those presented in this work rather than current tedious working curve procedures [26, 45].

5.6 Conclusions

This work demonstrated closed-loop control feasibility of monomer conversion in (ceramic) vat photopolymerization through proof-of-principle experiments. The experiments showed that a feedback controller was successful in compensating for a material perturbation in a small-scale setup. Moreover, a simple control-oriented process model proved to be well capable of describing the photopolymerization system behaviour under lab conditions. These promising results can be considered a fundamental step towards real-time in-situ control of the polymerization reaction that lies at the core of vat photopolymerization technology. Ultimately, such in-line process control strategies are expected to play a key role in the industrialization of vat photopolymerization based AM, as well as in other AM technologies.

References

[1] I. Gibson, D. Rosen, and B. Stucker, *Additive Manufacturing Technologies*. New York, NY: Springer, 2 ed., 2015.

[2] A. Zocca, P. Colombo, C. M. Gomes, and J. Günster, "Additive Manufacturing of Ceramics: Issues, Potentialities, and Opportunities," *Journal of the American Ceramic Society*, vol. 98, pp. 1983–2001, July 2015.

[3] T. Chartier, "Additive Manufacturing to Produce Complex 3d Ceramic Parts," *Journal of Ceramic Science and Technology*, vol. 6, no. 2, pp. 95–104, 2015.

[4] J. W. Halloran, "Ceramic Stereolithography: Additive Manufacturing for Ceramics by Photopolymerization," *Annual Review of Materials Research*, vol. 46, pp. 19–40, Aug. 2016.

[5] T. Ohji, "Additive manufacturing of ceramic components," *Synthesiology*, vol. 11, no. 2, pp. 81–93, 2018.

[6] S. C. Ligon, R. Liska, J. Stampfl, M. Gurr, and R. Mülhaupt, "Polymers for 3d Printing and Customized Additive Manufacturing," *Chemical Reviews*, vol. 117, pp. 10212–10290, Aug. 2017.

[7] P. Colombo, G. Mera, R. Riedel, and G. D. Sorarù, "Polymer-Derived Ceramics: 40 Years of Research and Innovation in Advanced Ceramics," *Journal of the American Ceramic Society*, vol. 93, pp. 1805–1837, June 2010.

[8] T. Hafkamp, G. van Baars, B. de Jager, and P. Etman, "A Trade-off Analysis of Recoating Methods for Vat Photopolymerization of Ceramics," in *Proceedings Solid Freeform Fabrication Symposium*, pp. 687–711, 2017.

[9] T. Hafkamp, G. van Baars, B. de Jager, and P. Etman, "A feasibility study on process monitoring and control in vat photopolymerization of ceramics," *Mechatronics*, vol. 56, pp. 220–241, Dec. 2018.

[10] J. Pellegrino, T. Makila, S. McQueen, and E. Taylor, "Measurement science roadmap for polymer-based additive manufacturing," Tech. Rep. NIST AMS 100-5, National Institute of Standards and Technology, Gaithersburg, MD, Dec. 2016.

[11] M. Mani, B. Lane, A. Donmez, S. Feng, S. Moylan, and R. Fesperman, "Measurement Science Needs for Real-time Control of Additive Manufacturing Powder Bed Fusion Processes," Tech. Rep. NIST IR 8036, National Institute of Standards and Technology, Feb. 2015.

[12] W. F. Reed and A. M. Alb, eds., *Monitoring polymerization reactions: from fundamentals to applications*. Hoboken, New Jersey: John Wiley & Sons, Inc, 2014.

[13] B. A. Ogunnaike and W. H. Ray, *Process dynamics, modeling, and control*. Topics in chemical engineering, New York: Oxford University Press, 1994.

[14] A. Yebi and B. Ayalew, "Hybrid Modeling and Robust Control for Layer-by-Layer Manufacturing Processes," *IEEE Transactions on Control Systems Technology*, vol. 25, pp. 550–562, Mar. 2017.

[15] A. Yebi, B. Ayalew, S. Pilla, and X. Yu, "Model-Based Robust Optimal Control for Layer-By-Layer Ultraviolet Processing of Composite Laminates," *Journal of Dynamic Systems, Measurement, and Control*, vol. 139, pp. 021008–1–021008–11, Nov. 2016.

[16] A. M. Yebi, *Model-based control of UV curing processes with application to additive manufacturing*. PhD thesis, Clemson University, Clemson, SC, 2015.

[17] X. Zhao and D. W. Rosen, "An implementation of real-time feedback control of cured part height in Exposure Controlled Projection Lithography with in-situ interferometric measurement feedback," *Additive Manufacturing*, vol. 23, pp. 253–263, Oct. 2018.

[18] X. Zhao, *Process Measurement and Control for Exposure Controlled Projection Lithography*. PhD thesis, Georgia Institute of Technology, 2017.

[19] R. Schwalm, *UV coatings basics, recent developments and new applications*. Amsterdam; London: Elsevier, 2007.

[20] J. Steinhaus, B. Hausnerova, T. Haenel, M. Großgarten, and B. Möginger, "Curing kinetics of visible light curing dental resin composites investigated by dielectric analysis (DEA)," *Dental Materials*, vol. 30, pp. 372–380, Mar. 2014.

[21] X. Zhao and D. W. Rosen, "Investigation of Advanced Process Control Methods for Exposure Controlled Projection Lithography," in *Solid Freeform Fabrication Symposium Proceedings*, pp. 143–162, 2014.

[22] T. Hafkamp, G. van Baars, B. de Jager, and P. Etman, "A Classification Scheme for AM Control Strategies: the AM V-model," in *Proceedings of the 2018 ASPE and euspen Summer Topical Meeting - Advancing Precision in Additive Manufacturing*, vol. 69, pp. 161–166, 2018.

[23] G. E. Fonseca, M. A. Dubé, and A. Penlidis, "A Critical Overview of Sensors for Monitoring Polymerizations," *Macromolecular Reaction Engineering*, vol. 3, pp. 327–373, Sept. 2009.

[24] J. Wu, Z. Zhao, C. M. Hamel, X. Mu, X. Kuang, Z. Guo, and H. J. Qi, "Evolution of material properties during free radical photopolymerization," *Journal of the Mechanics and Physics of Solids*, vol. 112, pp. 25–49, Mar. 2018.

[25] P. J. Bartolo, ed., *Stereolithography*. Boston, MA: Springer US, 2011.

[26] P. Jacobs, *Rapid Prototyping & Manufacturing: Fundamentals of Stereolithography*. Dearborn, MI: Society of Manufacturing Engineers, 1992.

[27] G. G. Odian, *Principles of polymerization*. Hoboken, N.J: Wiley-Interscience, 4th ed., 2004.

[28] Y. Tang, *Stereolithography cure process modeling*. PhD thesis, Georgia Institute of Technology, Atlanta, GA, 2005.

[29] S. Skogestad and I. Postlethwaite, *Multivariable Feedback Control: Analysis and design*. New York: Wiley, 2 ed., 2005.

[30] K. J. Laidler, *Chemical Kinetics*. New York: HarperCollins, 3 ed., 1987.

[31] Y. Brulle, A. Bouchy, B. Valance, and J. C. André, "Industrial photochemistry XXI. Chemical, transport and refractive index effects in space-resolved laser photopolymerization," *Journal of photochemistry and photobiology A: Chemistry*, vol. 83, no. 1, pp. 29–37, 1994.

[32] K. C. Wu and J. W. Halloran, "Photopolymerization monitoring of ceramic stereolithography resins by FTIR methods," *Journal of Materials Science*, vol. 40, no. 1, pp. 71–76, 2005.

[33] X. Fernàndez-Francos, S. G. Kazarian, X. Ramis, and À. Serra, "Simultaneous Monitoring of Curing Shrinkage and Degree of Cure of Thermosets by Attenuated Total Reflection Fourier Transform Infrared (ATR FT-IR) Spectroscopy," *Applied Spectroscopy*, vol. 67, pp. 1427–1436, Dec. 2013.

[34] R. R. Mohler, *Bilinear control processes: With applications to engineering, ecology, and medicine*. No. 106 in Mathematics in science and engineering, New York: Academic Press, 1973.

[35] D. L. Elliott, *Bilinear control systems: Matrices in action*. No. 169 in Applied mathematical sciences, Dordrecht: Springer, 2009.

[36] H. K. Khalil, *Nonlinear Systems*. New Jersey: Prentice Hall, 3 ed., 2002.

[37] W. S. Levine, *Control system fundamentals*. Boca Raton: CRC press, 2nd ed., 2011.

[38] C. Hofstetter, S. Orman, S. Baudis, and J. Stampfl, "Combining cure depth and cure degree, a new way to fully characterize novel photopolymers," *Additive Manufacturing*, vol. 24, pp. 166–172, Dec. 2018.

[39] Y. Yang, L. Li, and J. Zhao, "Mechanical property modeling of photosensitive liquid resin in stereolithography additive manufacturing: Bridging degree of cure with tensile strength and hardness," *Materials & Design*, vol. 162, pp. 418–428, Jan. 2019.

[40] G. Mitteramskogler, R. Gmeiner, R. Felzmann, S. Gruber, C. Hofstetter, J. Stampfl, J. Ebert, W. Wachter, and J. Laubersheimer, "Light curing strategies for lithography-based additive manufacturing of customized ceramics," *Additive Manufacturing*, vol. 1-4, pp. 110–118, Oct. 2014.

[41] C. I. Fiedler-Higgins, L. M. Cox, F. W. DelRio, and J. P. Killgore, "Monitoring Fast, Voxel-Scale Cure Kinetics via Sample-Coupled-Resonance Photorheology," *Small Methods*, vol. 3, no. 2, p. 1800275, 2019.

[42] M. M. Emami, F. Barazandeh, and F. Yaghmaie, "Scanning-projection based stereolithography: Method and structure," *Sensors and Actuators A: Physical*, vol. 218, pp. 116–124, Oct. 2014.

[43] S. Westbeek, J. A. W. van Dommelen, J. J. C. Remmers, and M. G. D. Geers, "Multiphysical modeling of the photopolymerization process for additive manufacturing of ceramics," *European Journal of Mechanics - A/Solids*, vol. 71, pp. 210–223, Sept. 2018.

[44] T. Chartier, C. Dupas, P.-M. Geffroy, V. Pateloup, M. Colas, J. Cornette, and S. Guillemet-Fritsch, "Influence of irradiation parameters on the polymerization of ceramic reactive suspensions for stereolithography," *Journal of the European Ceramic Society*, vol. 37, pp. 4431–4436, Dec. 2017.

[45] J. Bennett, "Measuring UV curing parameters of commercial photopolymers used in additive manufacturing," *Additive Manufacturing*, vol. 18, pp. 203–212, Dec. 2017.

Chapter 6

Design & realization of an optical measuring instrument for photopolymer conversion

Abstract
Additive Manufacturing offers unique capabilities compared to traditional manufacturing, but faces several challenges that need to be overcome before reaching its full potential. The challenge for product quality can be addressed by developing in-process monitoring and closed-loop control systems aimed at minimizing the sensitivity to uncertainty in equipment, materials, and processes. Therefore, an optical measuring instrument has been developed to determine the degree of conversion of acrylic resins used in vat photopolymerization in real time. This work describes the design, realization and testing of the instrument, and demonstrates its operation in characterizing the cure kinetics of several commercial photopolymers. The instrument's conceptual design is based on the same measuring principle used in general-purpose NIR spectro(photo)meters, but at a specific wavelength range such that a simpler and cost-effective instrument is obtained suitable for high-speed in-line metrology. Although several design modifications were required to make the prototype function properly, the experimental results ultimately provide a proof of concept of in-line photometric metrology for vat photopolymerization.

6.1 Introduction

Additive Manufacturing (AM) is considered a key enabling technology in what may turn out a revolution in the way products are developed and manufactured [1–4]. The reason is that AM offers unique capabilities compared to traditional manufacturing technologies such as high design flexibility, geometric "complexity for free," and customizable material properties [3, 4]. However, AM technologies face several challenges and barriers [3, 5] that need to be overcome in order to fully unlock the unique capabilities envisioned for AM. These challenges include relatively poor dimensional accuracy, low fabrication speeds, and insufficient consistency and repeatability in material properties and part quality [3, 5].

The inconsistencies in part quality originate from uncertainties in AM equipment, input materials, and AM processes, which ultimately lead to uncertainties in final parts [6]. Process monitoring and control systems aim to minimize the sensitivity to these uncertainties [7] and form indispensable tools for manufacturing quality management [8]. Hence, the integration of process monitoring and control technologies in AM systems is considered critical in addressing the major challenges faced by AM [3, 5, 6, 9].

Several types of control strategies have already been reported in generic AM literature [10], but most strategies are still in a research phase [11]. In photopolymer-based AM, the state of the art is that a few researchers have attempted to measure and control the photopolymerization reaction in closed loop [12–15]. Yet, the current open-loop control methods require attention as well, especially the methods used to determine the build process inputs, parameters, and settings. Currently, the photopolymers used in AM are typically characterized by a "working curve" from which two parameters can be derived: the UV light penetration depth D_p and critical exposure E_c [4, 16, 17]. Figure 6.1 shows the so-called WINDOWPANE procedure in which a diagnostic part is built and measured to obtain a working curve. The obtained resin parameters are then used to determine the required UV exposure for a given layer thickness. Although derivatives of this procedure are widely used, the procedure involves several ex-situ steps performed by the operator. Moreover, an ill-defined multiplication factor is used to calculate the required exposure from the critical exposure E_c, approximately ranging from 2 to 50 [16]. As a result, trial and error approaches are frequently encountered in the AM community when attempting to find appropriate build settings [17].

For AM to become a successful manufacturing technology, the production costs, time, and number of defects need to be drastically reduced [5]. These reductions call for technological breakthroughs that are enabled by fundamental research on in-situ diagnostics and real-time process control of AM processes [5]. This demand implies that photopolymer-based AM processes need to develop towards in-line-metrology-based alternatives to working curve procedures and real-time in-situ control of the UV curing reaction, as it lies at the heart of the AM process.

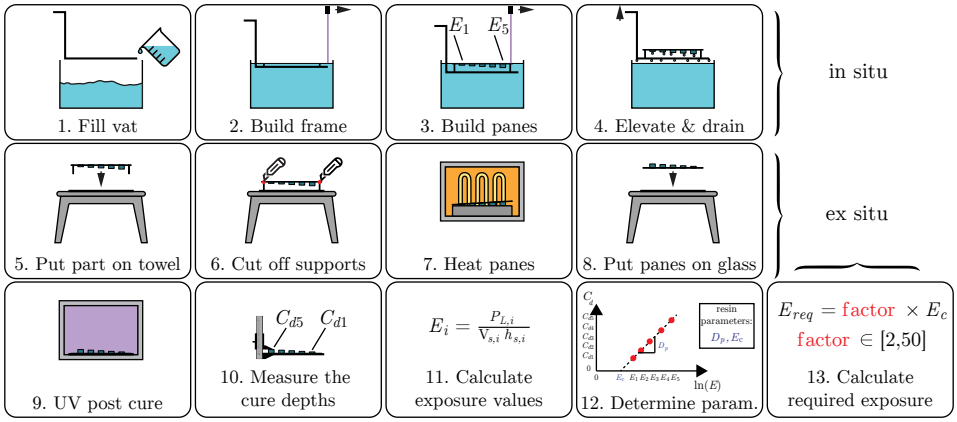

Figure 6.1: Visualization of the WINDOWPANE procedure that was originally developed at 3D Systems [16]. Derivatives of such procedures are still widely used to determine the build settings for photopolymer-based AM processes from the working curve. The required exposure is obtained by multiplying the critical exposure E_c with a rather poorly defined factor, which leaves room for the frequently encountered trial and error approach [17].

Recent work [18] has shown that it is technically feasible to measure and control the UV curing reaction through real-time in-situ feedback control of the photopolymer's degree of conversion [18, 19]. To this end, a general-purpose spectroscopic measuring instrument was used as a sensor. However, such "sensors" are not easily integrated into real AM machines as they are either too slow, occupy too much space, do not provide real-time outputs, or are prohibitively expensive and, hence, less expensive versions of current sensing techniques need to be developed [20].

In an attempt to meet these needs, an optical instrument has been purposely built for measuring the degree of photopolymer conversion based on a measuring principle that was extracted from the previously used general-purpose spectrometer. This work describes the design, realization, and testing of the instrument and demonstrates its use as an in-situ photopolymer characterization device that can be integrated into next generation [20] AM machines. To this end, Sections 6.2 and 6.3 describe the system-level and module-level design by discussing the requirements and design considerations that have led to the final instrument design. Subsequently, Section 6.4 describes several system tests, unanticipated issues and the implementation of several design changes required to make the instrument function properly. Finally, Section 6.5 demonstrates the instrument's operational performance and Section 6.6 provides a discussion and concluding remarks.

6.2 System-level instrument design

The International Vocabulary of Metrology (VIM) [21] defines a *measuring instrument* as a "device used for making measurements, alone or in conjunction with one or more supplementary devices" and a *measuring system* as a "set of one or more measuring instruments and often other devices, including any reagent and supply, assembled and adapted to give information used to generate measured quantity values." A *sensor* is defined as merely an "element of a measuring system that is directly affected by a phenomenon, body, or substance." This work presents the development of a novel measuring instrument or system for in-situ characterization of the degree of conversion, which requires the incorporation of more functionality other than sensing alone.

6.2.1 System-level design requirements

The definition of the desired system functionality and effectiveness is the starting point of the system development process along with the identification of user needs and requirements [22, 23]. A measuring instrument capable of determining the degree of cure of (photo-)polymers with high precision [24] finds many applications, such as polymer characterization, process monitoring, and process control [25]. The present instrument is specifically targeted at process control applications [7, 26] for photopolymerization-based AM processes such as stereolithography [4, 16]. The AM process in itself can be considered to be analogous [11] to the systems development process frequently described by the V-model [22, 23]. In this V-model hierarchy, a control strategy can be conceived at each abstraction level.

Two process control applications are of particular interest to this study. Firstly, the instrument may serve as an experimental setup for the development of real-time control systems for UV curing [18] aimed at future AM machine implementation. Secondly, the instrument may serve as an offline photopolymer characterization tool for in-situ determination of the build settings aimed at substitution of current ex-situ working curve approaches [16, 27] as shown in Figure 6.1. These two applications further determine the requirements for the measuring instrument.

In both applications, the main functional requirement is the ability to measure the degree of conversion, which is a quantity for the extent to which the liquid resin has polymerized to a solid. The reader is referred to Fraden's work [28] for a comprehensive overview of general sensor characteristics that should typically be outlined in the requirements of any sensor application. Similarly, Hergeth's work [29] provides an outline of specific issues that have to be addressed in designing an online polymer cure sensor application. Recent literature on metal [9, 30] and polymer [6] AM provides additional measurement considerations that are specific to in-situ process monitoring and metrology for AM.

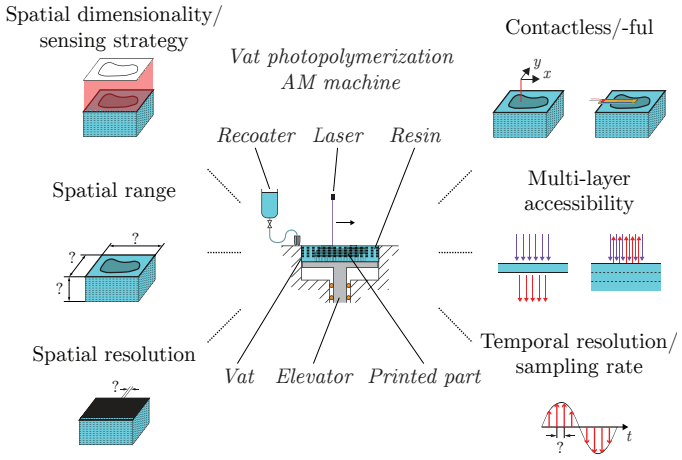

Figure 6.2: The primary system-level requirements for future integration of the measuring instrument into a vat photopolymerization machine.

The first application imposes the most challenging requirements [18, 19] since it needs to be compatible with the AM machine's architecture to be implementable. Figure 6.2 visualizes the primary system-level requirements, which include:

R1. The measuring instrument must be *compatible* with the AM equipment and control system architecture.

R2. The instrument should facilitate *spatially-resolved* measurements in the xy-plane and along the z-axis, i.e., full-field and depth-resolved sensing respectively. The *sensing strategy* to obtain 1D, 2D, or 3D spatial measurements should match the actuation strategy to irradiate layers with UV light.

R3. The *spatial range* should span the complete xy-plane build area in a Eulerian reference frame modality [31] or the smaller zone of influence [16] in a Lagrangian modality, and one or more layers across the z-axis.

R4. The sensor's *spatial resolution* should be greater than or equal to the actuator's resolution.

R5. The sensor should be *contactless* to avoid sensor contamination or fouling and to preclude the need for a separation mechanism [32].

R6. The measuring instrument must have *access* to the current layer without obstructing the UV light path and should facilitate measurement and actuation *from the same side*.

R7. The *temporal resolution* or *sampling rate* should match the photopolymerization reaction timescale [19] under actual AM process conditions [29, 33].

To summarize, the proposed real-time control application requires a 3D full-field measuring instrument, having high spatio-temporal resolution, spanning a considerable build volume, and having access to multiple layers from one side. A prototype measuring instrument has been developed with these requirements in mind, but actual implementation into an AM machine is left for future work.

The second application provides more design freedom because the requirement is relaxed regarding the need to physically implement the measuring instrument into the AM machine. If the instrument is placed oustide the machine, however, special care must be taken to ensure that the photopolymerization conditions during offline characterization are as close as possible to the conditions during actual printing. Figure 6.3 shows a potential embodiment where the measuring instrument stands alone, e.g., directly next to the AM machine. Alternatively, the measuring instrument could be placed inside the machine, e.g., in the corner of the build volume.

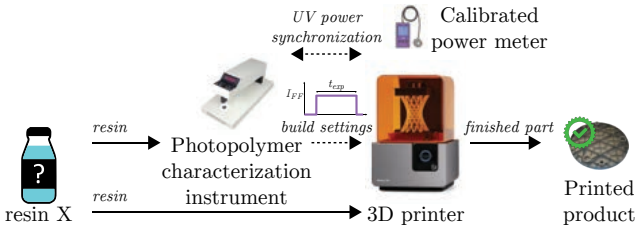

Figure 6.3: A potential embodiment in which the measuring instrument serves as a stand-alone, offline photopolymer characterization device for in-situ first-time-right determination of the build settings.

Depending on the placement in- or outside the machine, the measuring instrument requires the incorporation of additional functionality besides measuring. If placed outside the machine, the additionally required functionality is to supply raw material and to convert or transform the material, which are both important subfunctions of AM in general [34] and vat photopolymerization-based AM [4, 35] in particular. In other words, the measuring instrument requires a means for preparing a photopolymer sample (recoating) and for actuating through UV light. Moreover, the instrument requires a means for adjusting or synchronizing the UV irradiance level to the level in the target AM machine, preferably using a calibrated optical power meter [17]. If placed inside the machine, part of that additional functionality may not be necessary due to the higher level of machine integration. However, the choice was made to develop a stand-alone device favoring system modularity over system integration.

6.2.2 The photometric measuring principle

Having established the system-level requirements, the second phase in the system development process involves identifying, exploring, and synthesizing concepts [23]. This concept exploration phase starts with analyzing predecessor systems and existing technologies meeting the same needs. A vast body of knowledge is available on existing instrumental methods for chemical analysis in general [36] and of cure or polymerization monitoring techniques in particular [25, 29, 37]. These techniques are partly relevant for UV light-initiated reactions [38] and only a subset intends to measure the chemical degree of conversion.

Previous work by the present authors [19] attempted to extract and compare the measuring principles from that subset of photopolymerization monitoring techniques. Among these techniques, the optical ones offer the major advantages that they can have contactless embodiments (R5), can be scaled up from point-wise measurements to full-field measurements (R2&R3), and that optical signals can be easily converted to the electrical domain (R7) [39]. Thus, the optical measurement techniques such as interferometry [40] and spectroscopy [41] meet the majority of the system-level requirements stated in Section 6.2.1. Moreover, optical techniques bring the advantage that the same beam steering hardware can be used for actuation *and* for measurement (R6) as demonstrated by the colocated or coaxial melt pool control modalities in metal AM [42]. Thus, the sensor's spatial resolution can be tailored to the actuator's resolution (R4). In conclusion, optical measurement techniques seemed to best meet the application requirements.

Among the optical measurement techniques, infrared (IR) absorption spectroscopy was found to be the most viable option to base the instrument on for several reasons. Firstly, spectroscopic absorbance measurement results can be directly related to the concentration of the polymer under test according to the Beer-Lambert law [36, 43]. Secondly, the complexity of spectroscopic instruments can be comparatively low and the measurement rate can be inherently high as a result of this direct or short measuring chain. Contrarily, interferometric cure monitoring instruments [40, 44] rely on more complex signal processing techniques that extract phase differences from the measured light intensity, thus leading to a longer measuring chain. Thirdly, spectroscopic methods have been applied to online cure process monitoring for several decades, so it is a well-established technology field [29, 43, 45]. Lastly, the spectroscopic measuring principle lends itself well for developing a purpose-built measuring instrument.

Figure 6.4 shows the measuring principle used in general-purpose molecular absorption spectrometry and how this measuring principle is transferred to the purpose-built measuring instrument developed in this work. General-purpose spectro(photo)meters are based on the measurement of the absorbance A or transmittance T of a sample having a concentration $[c]$ and path length l [36]:

$$A = \log_{10}\left(\frac{1}{T}\right) = \log_{10}\left(\frac{I_0}{I}\right) = \varepsilon \cdot [c] \cdot l, \tag{6.1}$$

where $\varepsilon(\lambda)$ is the wavelength-dependent molar extinction coefficient, and I_0 and I are the in- and outgoing light intensity respectively.

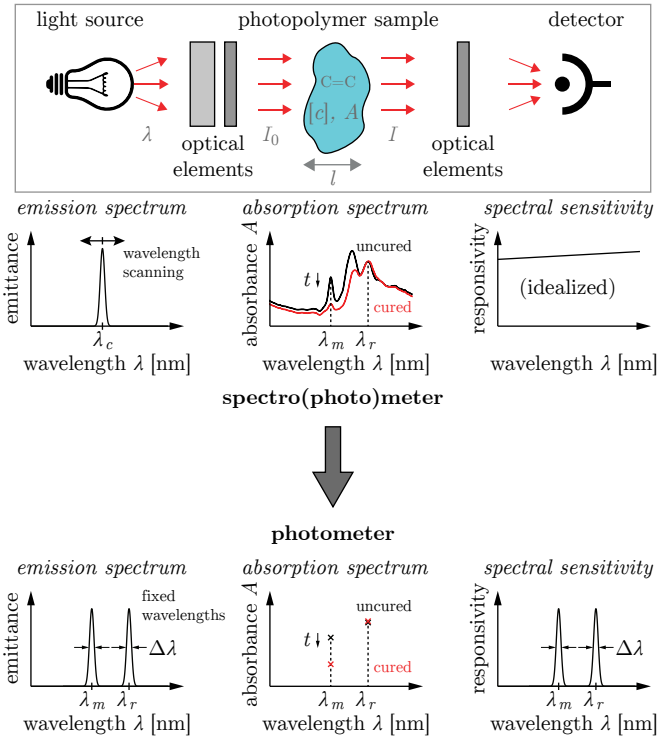

Figure 6.4: The measuring principle used in general-purpose spectro(photo)meters is transferred to a purpose-built photometer. Using two fixed-wavelength light beams circumvents the necessity to spectrally resolve the photopolymer sample's absorbance. Note that the electronics are left out for simplicity. Top part of figure adapted from [46].

In a *spectro(photo)meter*, the sample's absorption spectrum $A(\lambda)$ is obtained by spectrally resolving the absorbance, e.g., through wavelength scanning or through multi-channel measurement using a dispersive element [47]. Peaks in the obtained absorption spectrum can be assigned to functional groups in the sample's chemical structure [43]. Hence, the polymerization reaction can be monitored over time by repeatedly measuring the absorption spectrum and computing the concentration using the Beer-Lambert law (6.1). Finally, the concentration $[c](t)$ can be used to compute the sought-after degree of conversion $\alpha(t)$, which is simply defined as [48]:

$$\alpha(t) = \frac{[c]_0 - [c](t)}{[c]_0} = 1 - \frac{A(\lambda_m, t)}{A_0(\lambda_m)}, \tag{6.2}$$

where $[c]_0$ is the initial concentration and $A_0(\lambda_m)$ and $A(\lambda_m, t)$ are the initial and momentary absorbance respectively at the primary measurement wavelength λ_m. To compensate for losses and improve the instrument's selectivity, a secondary absorbance measurement $A(\lambda_r)$ is typically used at a different reference wavelength λ_r and ratiometrically [28] introduced into (6.2), which gives [48]:

$$\alpha(t) = 1 - \frac{\frac{A(\lambda_m,t)}{A(\lambda_r,t)}}{\frac{A_0(\lambda_m)}{A_0(\lambda_r)}}. \tag{6.3}$$

In a *photometer*, the same measuring principle is used as in a spectrophotometer, but without the need for spectrally resolving the absorbance. Only the relevant parts of the absorption spectrum are measured by using two fixed-wavelength light beams of appropriate wavelength as shown in Figure 6.4. Hence, purpose-built photometers provide a simpler, cost-effective alternative to general-purpose spectro(photo)meters with inherently higher signal-to-noise ratios [36].

Although photometers are commercially available for the process industry [49], no such photometer is suitable for the present target application. Nevertheless, one previous attempt has been reported in which a photometer was developed for a similar cure monitoring application in the context of UV-cured polymer coatings [50, 51]. However, that photometer was not developed in accordance with the system-level design requirements that follow from the real-time control applications as outlined in Section 6.2.1.

6.2.3 Optical sampling configuration

The interaction method with the sample is a high-level design choice that has to be made in all spectroscopic applications. Figure 6.5 shows three common sampling methods or configurations used in spectroscopy [45, 47]. Each sampling method has been embodied into various fiber-optic probes for in-line applications [25, 47].

Among these sampling methods, the transmission configuration gives the highest signal-to-noise ratio for a proper sample thickness and does not distort the spectra [45]. Measuring in transmission also allows for direct quantification of the concentration through the Beer-Lambert equation (6.1) if the absorbance is in the linear domain [45], i.e., the absorbance is small enough to prevent deviations originating from interactions with the absorbing species or from instrumental limitations. The sample cell, container, cuvette or holder [36, 47] determines the path length l in this equation and the transversal sample dimensions. The reflection configuration has several variants, including diffuse reflection, specular reflection and attenuated total internal reflection (ATR) [36, 45] shown in Figure 6.5 (b). The transflection configuration [51] is a compound of transmission and reflection at the sample-substrate interface.

As seen in Figure 6.5, the sample is either sandwiched between two optically transmissive plates, or deposited onto a (non-)transmissive substrate. In the latter

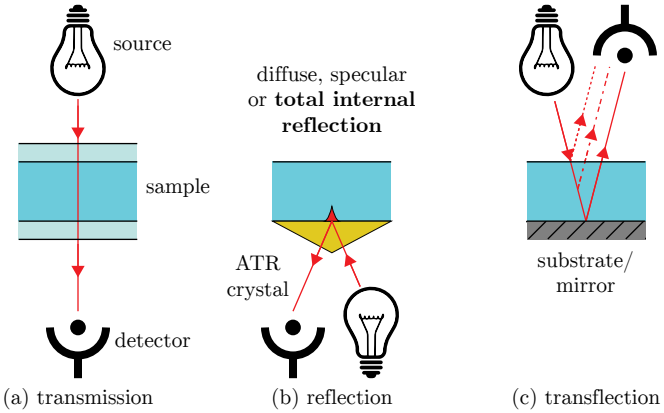

Figure 6.5: Common sampling methods used in spectroscopy [45].

case, the sensor may be contactless and thus appropriate for in-line applications. However, pre-existing results of the transflection concept [51] showed a considerable measurement uncertainty. Moreover, the individual contributions of transmission and reflection are indistinguishable in the transflection configuration, whereas in transmission the absorptive index contribution is known to be major and the refractive index contribution minor [45]. Hence, the transmission configuration was chosen to maximize this absorptive index contribution and to ensure that the information carried by the degree of cure signal can be directly related to a well-defined resin-layer thickness. Furthermore, the transmission configuration can be used in the future as a benchmark for reflection configurations.

6.2.4 Optical measurement system architecture

Based on the anticipated performance and cost characteristics [36], the photometric measuring principle seemed a feasible approach to meet the system-level design requirements. Hence, this approach was selected for the definition of the preferred concept, i.e., the third phase in the system development process [23]. Figure 6.6 schematically shows the system architecture developed in this phase from a functional and physical perspective.

The proposed system architecture embodies the photometric measuring principle shown in the top of Figure 6.4 in threefold. The first light path provides the actuation signal to initiate the photopolymerization reaction, having UV wavelength λ_a. Thus, a detector is not necessarily required in this light path, but it was incorporated to enable the estimation of the UV light penetration depth D_p. The second light path provides the primary measurement signal, having IR wavelength λ_m. The third light path provides the reference measurement signal, having IR wavelength λ_r.

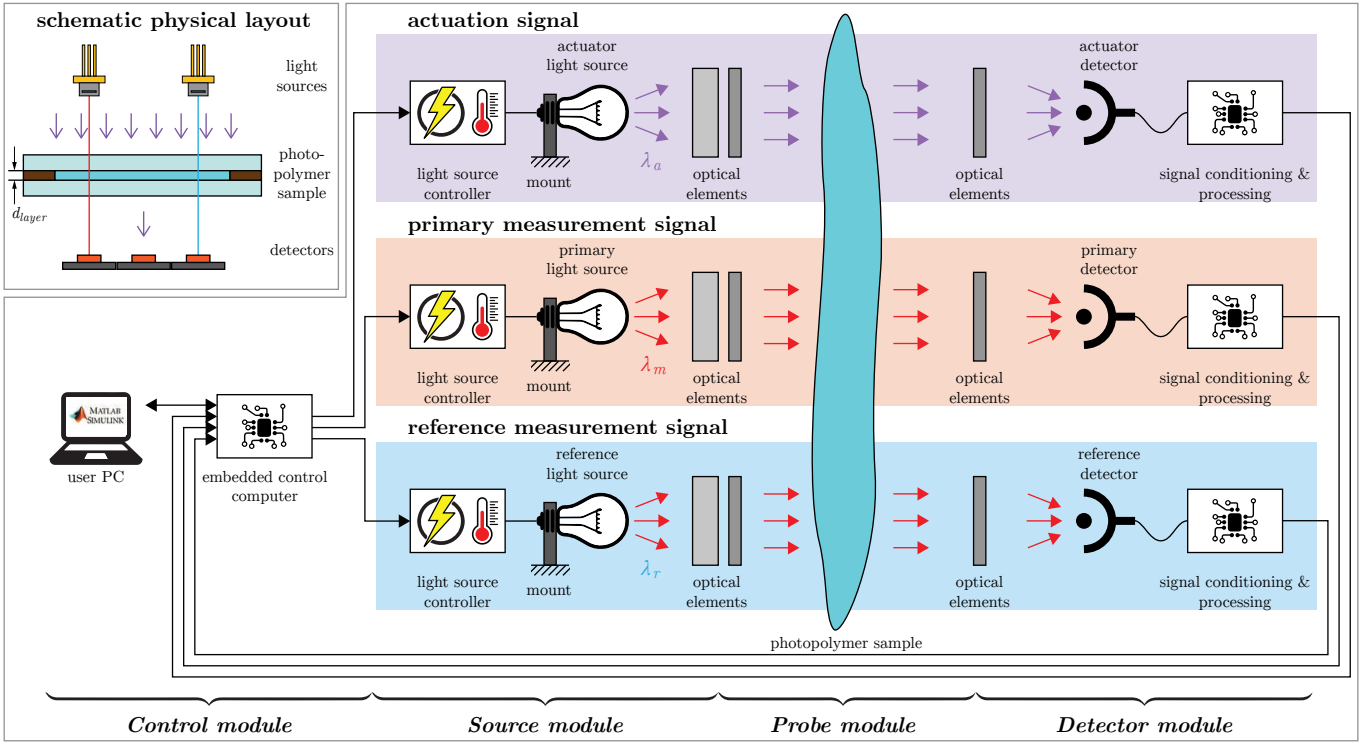

Figure 6.6: Schematic system architecture overview of the photometric measuring instrument consisting of three light paths of different wavelengths.

Each light path consists of a light source, a detector, and a number of optical elements, i.e., the basic components of any optical sensor [46]. The light source and detector fulfill the functions of transducing electrical energy to and from the optical domain respectively. The optical elements fulfill various functions, including directing or guiding the light, manipulating the beam shapes, and limiting or selecting the wavelength ranges [46].

Apart from these optics-specific functions, the system has to incorporate sensor-generic functions. Such functions typically include signal conditioning, signal processing, and communication through interfaces [28, 52]. Moreover, the system has to incorporate functions for data acquisition and manipulation to facilitate implementation of control logic, i.e., the capabilities of an embedded control computer [53].

Based on the aforementioned functions, the system was decomposed into four subsystems or modules as indicated in Figure 6.6. The Control module is connected to the Source module and Detector module through an electrical interface, whereas the Probe module is connected to the same modules through an optical interface. The advantage of this purely optical interface is that flexibility is obtained in terms of the physical probe design to facilitate future machine integration. Fiber optics provide the desired flexibility [54] through optical connector interfaces [55]. Therefore, a fiber-optic approach was pursued in the instrument's optical design.

Figure 6.7 shows the layout of the instrument's fiber-optic design incorporating the three light paths sketched in Figure 6.6. The first light path is generated by an actuator UV laser diode, guided by a single-mode (SM) fiber to an optical enclosure and launched into free space by a UV collimator lens. The UV beam is then reflected by a dichroic mirror, passed through and partially absorbed by the sample to initiate the polymerization reaction, reflected by a second dichroic mirror, filtered by an IR filter, focused by a UV focus lens into a multi-mode (MM) fiber, and directed to a UV detector. The second and third light paths are generated by a main and reference IR laser diode, combined in a wavelength division multiplexer (WDM), guided to the enclosure and launched into free space by an IR collimator lens. The IR beam passes through the first dichroic mirror, interacts with the sample, and passes through the second dichroic mirror and a UV filter. The transmitted IR beam is then coupled into an MM fiber and guided to a 50:50 splitter with two functionally equivalent output arms. In each output arm, the beam is launched into free space through a collimator, filtered by a bandpass filter, and directed onto an IR detector. This optical design is the result of comparing several optical configurations while evaluating several design considerations, which are discussed in the remainder of this section.

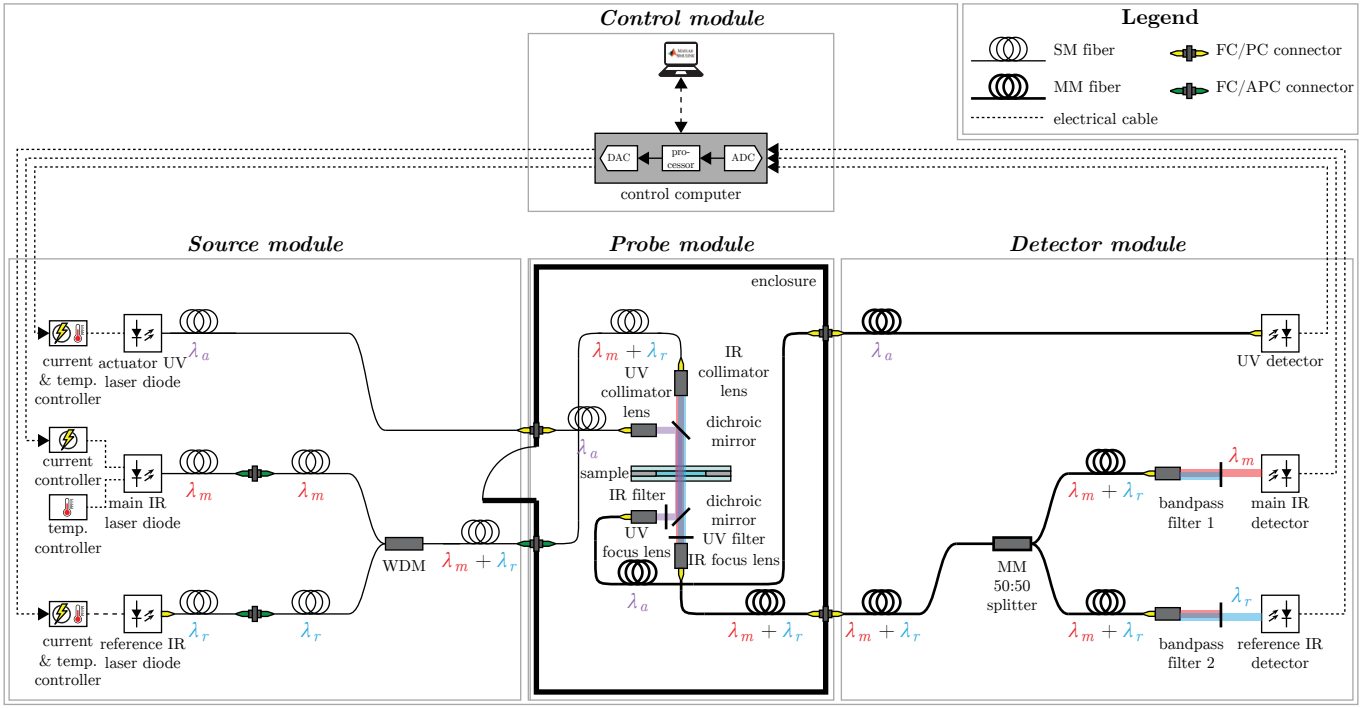

Figure 6.7: Optical layout of the measuring instrument's fiber-optic design. The fiber-optic connectors (FC) provide a flexible interface to the Probe module. The main and reference IR beams are combined to a single beam in a wavelength division multiplexer (WDM) in the Source module, directed through the sample, and separated again using bandpass filters in the Detector module.

6.3 Module-level design

Each module in Figure 6.6 and 6.7 was further detailed in the advanced development and detailed engineering design stages, i.e., the fourth and fifth phase respectively in the system development process [23]. The following sections describe their most important design considerations.

6.3.1 Source module design

The Source module consists of three individual laser sources and supporting hardware. Each source was chosen in accordance with requirements that follow from the UV curing application characteristics. These requirements include the center wavelength and linewidth, the optical power, laser intensity noise level, cost, availability and more [56].

The photopolymer's absorption spectrum determines the requirements on the source's emission spectrum, i.e., the center wavelength λ_c and linewidth $\Delta\lambda$ as illustrated in Figure 6.4. This absorption spectrum depends on the specific polymer chemistry. In vat photopolymerization, the mostly used UV-curable polymers are acrylates or epoxides with acrylate contents [4, 57]. Therefore, the measuring instrument was specifically designed for acrylate-based chemistries, which follow a free-radical polymerization reaction mechanism [4, 58].

UV-curable resin formulations typically consist of monomers, photoinitiators, and additives [57]. Carbon-carbon double bonds (C=C) are common reactive functional groups in vinyl monomers, which is a family of chemistries to which the acrylate monomers belong [16]. These double bonds break open and link with other molecules during the radical polymerization reaction. The double-bond concentration can be determined from the photopolymer's absorption spectrum, which lies at the core of the measuring principle outlined in Section 6.2.2.

Main light source selection

A number of wavelength bands in the IR range are associated to the carbon-carbon double bond, so multiple options exist for the photometer's main center wavelength λ_m. On the one hand, the mid-infrared (MIR) region of the IR spectrum has been assigned to fundamental vibrations [25], such as C=C stretching near the wavenumber $\tilde{\nu} = 1637$ [cm^{-1}] [59–61], which corresponds to the wavelength $\lambda = 6109$ [nm]. On the other hand, the near-infrared (NIR) region has been assigned to overtones and combinations [25], such as the first overtone of CH stretching [60,62,63] near $\tilde{\nu} = 6165$ [cm^{-1}], which corresponds to $\lambda = 1622$ [nm].

In choosing the main wavelength λ_m, the first step was to narrow down the solution space to the MIR or the NIR region. Choosing for the NIR region brings several advantages over the MIR region, including a sufficient sensitivity, signal-to-noise ratio and time resolution for in-line cure monitoring purposes [64, 65]. Moreover, fiber-optic components are widely available for the NIR region [65] and

larger scattering/absorption ratios promote the application of diffuse-reflection techniques [25], which facilitates machine integration and contactless arrangements respectively. However, the NIR optical path lengths need to be larger than MIR path lengths to reach similar absorption levels [25], and band assignment and calibration procedures can be more involved [47,62]. Nonetheless, recent developments in multi-channel InGaAs detectors may provide a viable route towards scaling up to full-field degree of conversion measurements through NIR hyperspectral imaging [66]. Thus, the NIR region was chosen due to a better match to the application requirements.

NIR absorption spectra of acrylates typically show several peaks, offering several options for λ_m. The most prevalent peaks are the peaks near 1620 [nm] and 2100 [nm] [60,62,67]. These peaks are associated to the first overtone of stretching vibrations of C−H groups next to double bonds and combinations of CH vibrations [62]. The 1620 [nm] peak is said to be a combination of two C−H stretch vibrations from the first CH overtone near 1665 [nm] and has overtones at 1109 [nm] and 847 [nm] [62,68]. Since the 1620 [nm] peak it is not a combination of C−H with another type of vibration (like the 2100 [nm] peak), it is termed the first CH overtone. Figure 6.8 shows these four peaks in a typical NIR absorption spectrum of an acrylate-based commercial 3D printing resin (NextDent SG, NextDent, Soesterberg, The Netherlands) before and after UV curing from 800 to 2200 [nm].

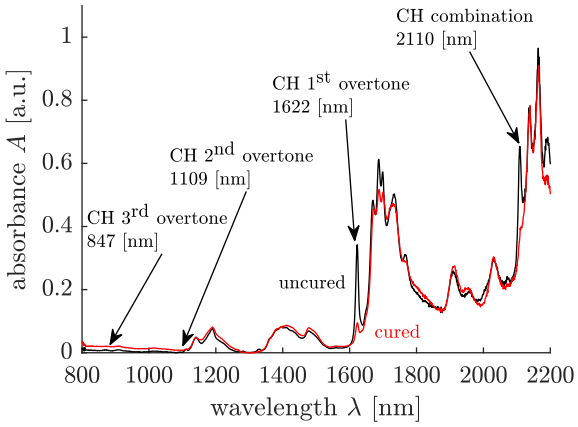

Figure 6.8: NIR absorption spectra of a commercial 3D printing resin (NextDent SG) before and after curing. Spectra were obtained using a UV-VIS-NIR spectrophotometer (UV-3600, Shimadzu, Kyoto, Japan) in transmission mode at 1 [nm] resolution, 1 [mm] path length, and using horizontal baseline correction for comparability.

Thus, at least four options present themselves for λ_m in the wavelength range from 800 to 2200 [nm]. Three criteria were considered in selecting λ_m from these options. Firstly, the absorbance should be as high as possible for a sufficient signal range since the absorbance level is already 10-100 times lower than in

the MIR range [25]. Due to the larger required energy levels for overtones and combinations, it holds that the smaller the wavelength, the lower the absorption level [25]. Secondly, the absorption peak should have little overlap with other peaks to be well distinguishable, i.e., high selectivity [21]. Thirdly, a light source should be available with appropriate optical properties, most importantly wavelength and linewidth.

To evaluate these three criteria, Figure 6.8 shows clearly distinguishable peaks at 1622 [nm] and 2110 [nm] which decrease upon UV curing, but the overtone peaks at 1109 [nm] and 847 [nm] are hardly visible. Moreover, the peak at 2110 [nm] lies in the shoulder of other peaks, so shows too much overlap. In addition, 1622 [nm] lies in or near the L-band in optical communication systems [69], so light sources of appropriate wavelength and linewidth are available. Thus, the 1622 [nm] peak best met the selection criteria, so was the wavelength λ_m of choice.

Apart from the main wavelength λ_m, the choice of linewidth $\Delta\lambda$ determines which part of the polymer's absorption spectrum is probed. Monochromatic emission spectra can be described by a Gaussian function where the linewidth $\Delta\lambda$ is defined as the full width at half maximum (FWHM) [70], as depicted in Figure 6.4. A narrow emission peak can be interpreted as analogous to the peak height processing method in spectroscopy, whereas a broad emission peak can be interpreted as the peak area method.

The choice between a narrow or broad linewidth was made by performing a trade-off analysis between the measurement signal's sensitivity and range on the one hand and the nonlinearity due to peak shifting upon curing on the other. If the source's emission spectrum is broad with respect to the sample's absorption spectrum, a relatively low portion of the energy is absorbed by the sample, which may cause deviations from Beer-Lambert's law [71]. Consequently, the optical power reduction is relatively small, so the measurement signal is insensitive and has a small response range compared to a narrowband source. However, if the spectrum is broad it is practically unaffected by variability in absorption peak locations between materials, which are in the order of 0.3 [nm] [60], or shifts upon curing, which are in the order of 1 [nm] [60] for the materials considered. A narrowband source was favored over a broadband source in the trade-off analysis, because the signal range was already expected to be relatively small for the target path length. That is, the NIR absorption levels are relatively low for path lengths in the order of the layer thicknesses [72] found in photopolymer-based AM, i.e., 10 to 100 [µm].

Distributed Feedback (DFB) laser diodes have particularly narrow linewidths up to 10^{-5} [nm] [70] and a few laser diodes were commercially available in the 1622 [nm] wavelength range. Therefore, a 1622 [nm] laser diode (DFB-1622-003) was acquired (Sacher Lasertechnik GmbH, Marburg, Germany) as the main light source. This laser has a maximum spectral width specification of $\Delta\nu = 10$ [MHz], which corresponds to a linewidth of $\Delta\lambda = 9 \cdot 10^{-5}$ [nm]. To drive this laser diode, a low-noise current controller (LDC201CU), temperature controller (TED200C), and mount (LM14S2) were acquired (Thorlabs GmbH, Bergkirchen, Germany).

Reference light source selection

Contrary to the widely accepted choice of main wavelength $\lambda_m = 1622$ [nm], there is little consensus among acrylate NIR spectroscopists about the choice of reference wavelength λ_r. The question is whether a reference measurement is required in the first place. Some researchers argue that the use of a reference measurement is not an absolute requirement [60], unless the resin layer thickness varies significantly upon curing [73]. The latter can be true for acrylate resins as they can exhibit 5-20 [%] shrinkage [4] depending on their composition. A number of other factors can affect the measurement, including polymer refractive index changes [74], thermal effects, and sample-related optical errors such as back reflection and scattering [75]. These factors may result in random or systematic errors, which both can be compensated for by properly using an internal reference standard [36].

A number of options have been proposed by NIR spectroscopists for the internal reference. Agarwal used the 1725 [nm] peak [76], while Gerasimov and Snavely used the total area under the 1639-1818 [nm] peaks [68]. However, measuring this total area would require a broadband emission spectrum with a steep roll-off near 1639 [nm], which could not be easily created with commercially available optical components. Stansbury and Dickens studied the use of an aromatic peak at 2163 [nm], but found that it cannot be generally recommended [60] and it is not generally present in every acrylate. Rather than using a spectroscopic reference peak, Fong and Rueggeberg both used a thickness measurement to normalize the measurement [77, 78]. However, such a thickness referencing method is only capable of compensating for errors that lead to thickness deviations. Finally, Bach investigated reference wavelengths in the 900-1000 [nm] region, at 1550 [nm], and a referencing method involving a linear extrapolation of the spectrum at two wavelengths 1530 and 1570 [nm] to the point below the peak at 1620 [nm] [51]. Although the latter method may have worked well for resin formulations for UV-cured coatings, the referencing method was found less suitable for 3D printing resins.

On forehand, Bach outlined several requirements for the referencing method [51]: the reference source must have a wavelength λ_r close enough to λ_m to assume a linear spectrum between them, have a similar optical power, be cost-effective and available. However, an important consideration was overlooked in outlining these requirements. That is, internal reference peaks are typically assigned to functional groups that do not participate in the chemical reaction and thus have constant concentration [36]. For example, the C=O peak height or area around 1730 [cm^{-1}] is typically used as the internal reference in MIR spectroscopy [59, 79]. Thus, the measuring instrument's reference wavelength λ_r should ideally coincide with a peak related to such a functional group.

Two approaches were attempted in the search for a suitable reference peak. The first approach entailed searching for overtones or combination peaks that correspond to reference peaks commonly used in MIR spectroscopy. For instance, the commonly used C=O carbonyl group at 1720 [cm^{-1}] has second overtones near

1900 and 1960 [nm] [62]. Moreover, the NH amide peaks near 1537 and 3350 [cm^{-1}] in urethane dimethacrylates [60, 80] have a first overtone near 1470 [nm]. However, this first approach was hampered by severe overlap [62] with other peaks such as water or hydroxyl (OH) groups near 1450 [nm], which generally should be avoided [62].

The second approach involved adding a substance to the sample, rather than using a major constituent of the resin formulation such as C=O. The idea was to add a substance that does not participate in the reaction, determine which peaks remained constant with respect to this susbtance upon curing, and select the most suitable peak as the reference wavelength λ_r. Alternatively, the absorption peak location of that substance itself could be chosen as λ_r and the substance could always be added to the formulation by resin manufacturers if it were economically feasible. To select a reference substance, inspiration was drawn from wavelength calibration standards [81,82], which commonly use rare-earth metals. The rare-earth metals Erbium and Ytterbium were found to be most suitable since they showed the least overlap with acrylate absorption specta and both have also been used for synthesizing luminescent materials [83, 84]. However, this approach was abandoned due to an insufficient solubility of the rare-earth metals in the photopolymer matrix (Erbium(III) acetylacetonate hydrate, Ytterbium(III) acetate tetrahydrate, Ytterbium(III) acetylacetonate; Alfa Aesar and Sigma-Aldrich).

After two unsuccessful attempts of selecting a reference wavelength related to a functional group, the choice was made to select a reference source with a wavelength λ_r close to the main wavelength λ_m. Note that their emission spectra should not overlap to prevent interaction. Choosing λ_r as close to λ_m has several advantages, such as a reduction of chromatic aberrations [56]. A λ_r greater than but close to λ_m would not be a suitable choice, since the complete region from 1639-1818 [nm] is associated to CH stretching [62]. A λ_r smaller than λ_m would be better according to the NIR absorption spectra shown in Figure 6.8. For instance, 1600 [nm] would be a suitable candidate, but due to availability reasons a 1550 [nm] DFB laser diode source (S3FC1550) was acquired (Thorlabs) with integrated current and temperature control and a linewidth of approximately 0.1 [nm]. This wavelength is widely used in optical communication systems [69] and thus fiber-optic components are readily available for 1550 [nm].

Combining the main and reference signals

A major advantage of using fiber-optic components is the ability to combine multiple optical signals into one signal carried by a single fiber, i.e., multiplexing. Figure 6.7 shows the combination of the main λ_m and reference λ_r optical signals into a single signal $\lambda_m + \lambda_r$ by a WDM (WD1525A, Thorlabs). Once the two optical signals are launched into free space by a collimator lens, the resulting light beams have the same shape and size if the respective wavelengths are sufficiently close. As a result, the main and reference beams both probe the same material volume, which

is favored over the case where the two beams are physically separated.

As a consequence of multiplexing, the optical signals need to be demultiplexed or separated again in time or space after interacting with the sample. Separating in time allows for using a single detector as in Figure 6.9 (a), whereas separating in space requires two detectors as in Figure 6.9 (b). In the single-detector case, the main and reference signal are alternately turned on and off electronically in the driver [85] or mechanically using a chopper and demodulated using a dual-phase lock-in amplifier [36, 51, 86].

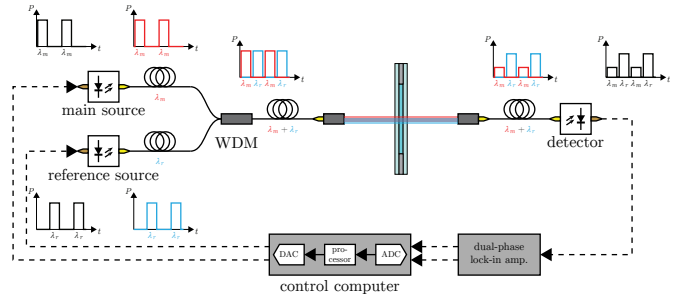

(a) single-detector method

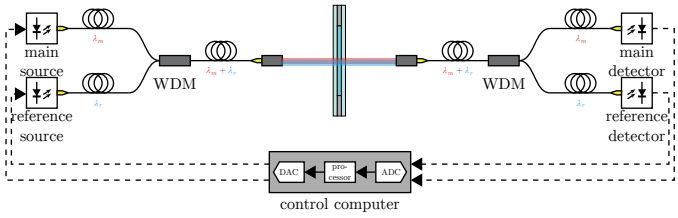

(b) dual-detector method

Figure 6.9: Methods to multiplex and demultiplex the optical signals in time using a single detector, or in space using a dual detector.

In the dual-detector case, both light sources are simply continuously on. Although the single-detector method typically enhances the signal-to-noise ratio [36], the modulation frequency introduces a limit to the sampling frequency and increases system complexity and cost. That is, commercially available optical choppers have maximum modulation frequencies typically in the order of 10 [kHz]. However, the effective measurement bandwidth may be lower because the transmitted intensity has a finite rise and fall time.

To meet requirement (R7), the sampling rate needs to be higher than the reciprocal of the photopolymerization reaction timescale. Exposure times range from 1 to 10 [s] in mask projection [4] actuation topologies, so a sampling rate of at least 10 to 100 [Hz] is required to have 100 samples over the course of the reaction. Though, a higher sampling rate will increase the achievable closed-loop control performance. In vector scanning topologies [4], the exposure times range

from 10^{-5} [s] to 10^{-3} [s], so sampling rates exceeding 1 [MHz] are required. The response times of photodiodes do not prevent a fundamental limit, as they can have response times in the ultrafast [GHz] range if the detector area is made sufficiently small [87]. The caveat is that the frequency-dependent signal-to-noise ratio needs to be taken into account as well. Thus, the dual-detector method was chosen to avoid the 10 [kHz] sampling rate limit such that the instrument can potentially be used at sampling rates suitable for vector scanning topologies.

Actuator light source selection

The center wavelength and linewidth are less critical design parameters for the actuator UV source than for the main and reference IR sources. The reason is that UV curable resin formulations contain photoinitiators that have a rather broad absorption band and typical UV sources for AM have center wavelengths ranging from 355-405 [nm] [57]. On the contrary, the light source response time is a critical design parameter for sufficiently fast actuation in the target control system, but fortunately laser diodes have response times down to 10^{-12} [s] [19]. Moreover, a fiber-optic coupling was desired to interface with the Probe module. These requirements were met by a 405 [nm] laser diode (LP405-SF10, Thorlabs) driven by a current and temperature controller (CLD1011LP, Thorlabs).

6.3.2 Probe module design

The Probe module receives three optical signals from the Source module through two SM fibers, see Figure 6.7. These three signals interact with the photopolymer sample and leave the Probe module again through two MM fibers. The conceptual choice for a transmission configuration largely determines the physical layout of the measuring instrument. A transmission photometer essentially has the same physical layout as radiation densitometers [88] and sensitometers [89], which measure optical density as well. These devices have a form factor in which either the source or detector is mounted to a swing arm such that it can be swung clear of the other for ease of cleaning or placing the sample.

Microvolume spectrophotometers [90, 91] also feature such a swing arm, but hold liquid samples in place by the surface tension between two opposing surfaces [92], forming a liquid bridge [93, 94]. This form factor carried a risk of separation issues once cured [93] and was considered too complex for a first prototype. Instead, it was decided to build the photometer primarily from standard optical cage components for versatility during the prototyping phase. Only the sample holder was custom-made rather than purchased off-the-shelf, because the demountable holders are labour-intensive and the non-demountable holders are inseparable after UV curing such as most cuvettes. The custom design was based on clamping two quartz slides and a spacer, i.e., a known effective method to prepare a photopolymer sample [95].

Figure 6.10 (a) shows a front view of the Probe module realized from 30 [mm] cage components (Thorlabs). The main and reference IR light paths enter the

Probe module in an SM fiber (SMF-28) and are launched into free space by an IR collimator lens (CFC-2X-C). This lens produces a collimated IR beam with an approximate $1/e^2$ beam diameter of 380 [µm], which gives an indication of the measuring instrument's spatial resolution. The IR beam transmits through two identical longpass dichroic mirrors (DMLP1500) having a 1500 [nm] cut-on wavelength and through the sample. Part of the UV beam transmits through the second dichroic mirror and is blocked by a longpass filter (FELH1500), which also has a 1500 [nm] cut-on wavelength and is placed under a small angle to reduce back-reflections. The IR beam is finally coupled into an MM fiber (M42L01) by an IR focus lens (F230FC-1550) mounted to a tip-tilt manipulator (KAD11F). Note that both the IR fibers are mounted to a translator (SPT1T/M) with a lateral offset of 1 [mm] from the center optical axis to compensate for the lateral displacement [96] induced by the dichroic mirrors.

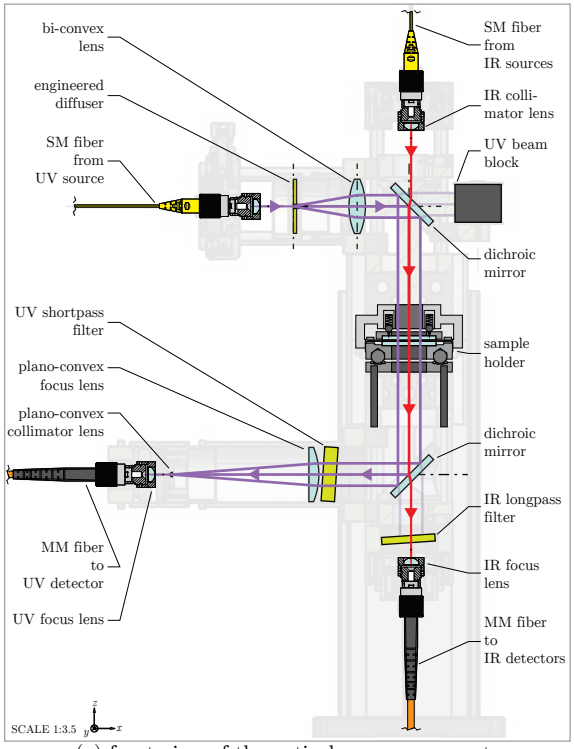

(a) front view of the optical cage components mounted to a U-bracket

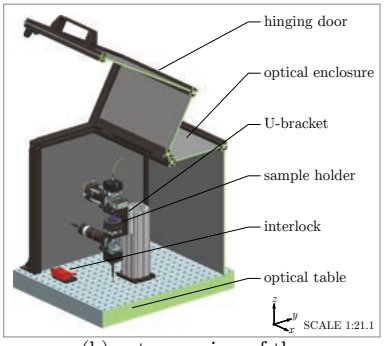

(b) cutaway view of the optical enclosure internals

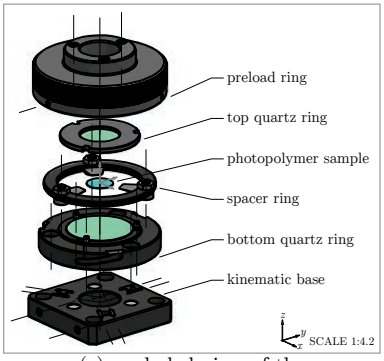

(c) exploded view of the custom-made sample holder

Figure 6.10: CAD drawings of the Probe module's physical layout, which is built primarily from 30 [mm] cage-compatible components.

The UV light path is mostly the same as the IR light path, with the essential difference that the UV beam is expanded and reduced again. After being launched into free space from an SM fiber (SMF28) by a collimator lens (F671FC-405), the UV beam is expanded and shaped into a flat-top beam profile [70] by an engineered diffuser (ED1-C20) and a bi-convex lens (LB1757-A) spaced 30 [mm] apart. This gives an approximately uniform UV irradiation field having a 10 [mm] diameter. The UV beam is reflected by the dichroic mirrors and transmitted through the sample. A UV bandpass filter (FBH405-10) blocks unwanted IR light and a plano-convex focus (LA1134-A) and collimator (LA1024-A) lens act as a Galilean beam reducer [96] in order to couple the UV light into the MM fiber (M42L01) with a focus lens (F671FC-405).

Figure 6.10 (b) shows the placement of the optical components shown in (a) inside an optical enclosure, which has a hinging door for access and is mounted to an optical table. The optical components are mounted to a U-bracket onto which a kinematic base is installed. The kinematic base shown in Figure 6.10 (c) acts as a high-precision mechanical interface between the sample holder and the measuring instrument [97] through three parallel cylinder pairs forming V-grooves [24]. Together with three steel balls and magnets in the bottom quartz ring, it forms a demountable ball-groove quasi-kinematic coupling by virtue of an exact-constraint design [98, 99].

The bottom quartz ring features a 25.4 [mm] diameter quartz window (WG41010-C) glued to an aluminum ring. A spacer ring is placed on top of the bottom quartz ring that has a 100 [µm] steel spacer in the middle. After depositing a droplet onto the bottom quartz window, the top quartz ring is positioned on top of the spacer ring and placed between three retention pins on the bottom quartz ring. Finally, the preload ring is screwed to the bayonet mount on the bottom quartz ring and the resulting axial travel causes three spring plungers to compress and apply a preload force to the top quartz ring. The resin layer thickness is well-defined through this preload force and the spacer design featuring three inward-pointing flaps.

6.3.3 Detector module design

After interacting with the resin sample, the optical signals need to be demultiplexed and converted to the electrical domain by photodetectors as described in Section 6.3.1. Using a second WDM perhaps would have been the most elegant way to demultiplex or separate the main and reference IR signal as shown in Figure 6.9 (b). However, no WDM was commercially available with MM fibers at the desired wavelengths. For the same reason, it was not possible to build a WDM with an optical circulator and a fiber bragg grating (FBG).

A straightforward alternative to this fiber-optic approach was to separate in free space. To this end, the main and reference IR signals are first divided into two nearly identical arms using a MM 50:50 splitter (TM50R5F1B). Both arms launch the light into free space using a fiber-optic collimator (F230FC-1550) and direct the light onto an indium gallium arsenide (InGaAs) photodiode detector (PDA20CS2). The

desired wavelength separation is achieved by the main bandpass filter (FB1620-12) and reference bandpass filter (FB1550-12), each having a bandwidth of 12 [nm] and placed under an angle between the collimator and the detector.

This free-space configuration required a detector active area large enough to cover the complete IR beam, but small enough to obtain an acceptable response time and noise level [46, 100]. The selected InGaAs photodiode meets these requirements, as well as the required optical power and wavelength range. Similar requirements apply to the UV detector, which led to the selection of a silicon-based photodiode detector (PDA36A2) that was directly coupled to the MM fiber output.

6.3.4 Control module design

Once converted to the electrical domain, the detector signals are fed into the Control module. This module consists of an embedded control computer (Baseline Education real-time target machine, Speedgoat GmbH, Köniz, Switzerland), an analog and digital I/O module (IO397, Speedgoat), and electrical wiring. This control computer was selected for its compliance to the application's real-time requirements and its versatility as a development platform for control systems. That is, the maximum sampling rate is 20 [kHz], which is sufficient for mask projection topologies.

Figure 6.11 shows how the control computer is used in an embedded control scheme capable of feedback control. The control computer interfaces with a Master PC on which control schemes are developed in MATLAB/Simulink. The Master PC deploys the control schemes to the real-time target, initiates experiments, and stores experimental data. During experiments, the control computer communicates the control input to the UV laser actuator through an analog voltage. The UV laser initiates the photopolymerization reaction (the plant) and the NIR photometer measures the extent of the reaction (the sensor). Figure 6.12 shows the graphical user interface (GUI) that was developed in MATLAB to provide access to the experimental parameters, initiate experiments, and organize experimental data.

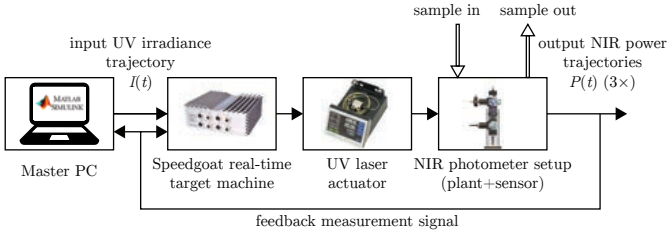

Figure 6.11: Embedded control scheme implemented in the NIR photometer setup.

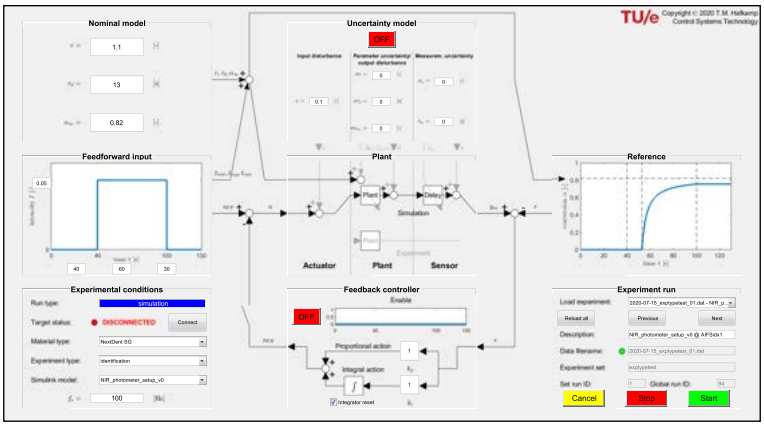

Figure 6.12: MATLAB graphical user interface for the NIR photometer setup.

6.3.5 Summary of design specifications

Table 6.1 gives an overview of the most important design specifications per module.

Module	Description	Parameter	Value	Unit
Source	center wavelength main IR laser	λ_m	1622	[nm]
	center wavelength reference IR laser	λ_r	1550	[nm]
	center wavelength actuator UV laser	λ_a	405	[nm]
	linewidth main IR laser	$\Delta\lambda_m$	$9 \cdot 10^{-5}$	[nm]
	linewidth reference IR laser	$\Delta\lambda_r$	0.1	[nm]
	linewidth actuator UV laser	$\Delta\lambda_a$	0.7	[nm]
	max. optical power main IR laser	P_m	4.75	[mW]
	max. optical power reference IR laser	P_r	2	[mW]
	max. optical power actuator UV laser	P_a	10	[mW]
Probe	beam diameter IR beams	D_{IR}	0.4	[mm]
	beam diameter UV beam	D_{UV}	10	[mm]
	incidence angle IR beams	$\theta_{i,IR}$	0	[°]
	incidence angle UV beam	$\theta_{i,UV}$	0	[°]
	diameter resin sample	D_{resin}	10	[mm]
	layer thickness resin sample	d_{layer}	0.1	[mm]
Detector	center wavelength main bandpass filter	$\lambda_{f,m}$	1550 ± 2.4	[nm]
	center wavelength reference bandpass filter	$\lambda_{f,r}$	1620 ± 2.4	[nm]
	bandwidth main bandpass filter	$\Delta\lambda_{f,m}$	12 ± 2.4	[nm]
	bandwidth reference bandpass filter	$\Delta\lambda_{f,r}$	12 ± 2.4	[nm]
Control	max. sampling frequency	f_s	20	[kHz]
	ADC resolution	n_{bit}	16	[bit]
	full-scale input voltage range	$V_{FS,in}$	± 10.24	[V]
	full-scale output voltage range	$V_{FS,out}$	± 10.8	[V]

Table 6.1: Summary of system design specifications.

6.4 System testing and resulting design changes

The final phase in the system development process is concerned with integrating, testing, and evaluating the total system with the final aim of demonstrating its operational performance [23]. To this end, the NIR photometer was realized according to the initial design, as depicted in Figure 6.13.

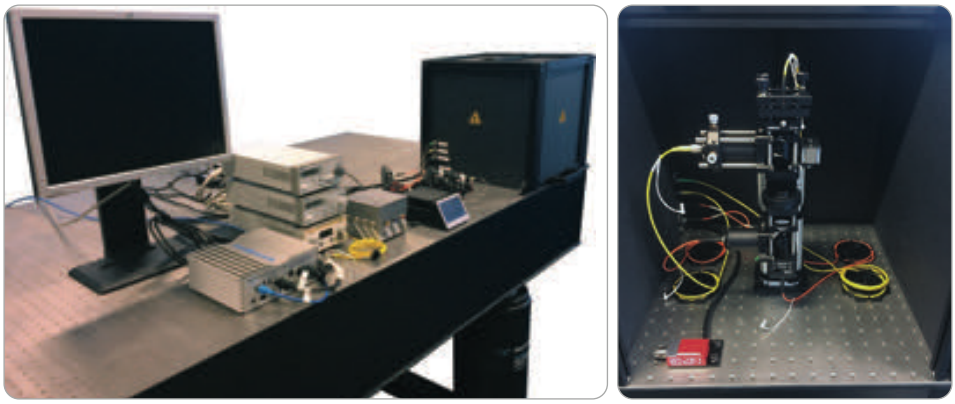

(a) NIR photometer setup on an optical table (b) front view of enclosure internals

Figure 6.13: Photographs of the initially realized NIR photometer setup.

After integrating the modules and components constituting the NIR photometer setup, the individual system functions were tested and verified to work as expected. Subsequently, initial tests were performed to test the instrument's measurement functionality during photopolymerization. Unfortunately, the initial results showed highly unexpected behaviour. Several countermeasures had to be taken to bring the system up to a working state while debugging the system. Regrettably, after solving one problem, another problem surfaced, as is common in debugging and system integration [101]. The following sections describe the testing procedure, several unforeseen problems, and the resulting changes to the instrument's design that were necessary to make the instrument function properly.

6.4.1 Experimental testing procedure

The system test plan consisted of functional component verification and system-level tests. At first, the optical power losses were compared to specifications for each fiber-optic component. The system-level tests simply consisted of turning on the UV light and measuring the photopolymer's response, i.e., a step response experiment. All initial test were performed with a sampling rate $f_s = 100$ [Hz]. Two acrylate-based 3D printing resins were used during testing, i.e., a normal resin (Sparkmaker LCD-T, WOW Innovation Technology Co., LTD., Shenzhen) and a

ceramic-filled resin (Formlabs Ceramic, Formlabs GmbH, Berlin) whose ceramic particles were left to sediment to use only its acrylic resin component.

Photopolymer resin samples were prepared and cleaned according to the procedure depicted in Figure 6.14. A pipette was used to deposit a droplet of resin onto the quartz substrate and the covering quartz window was put on top. This deposition method sometimes led to air bubble entrapment, which was mitigated by holding the sample in a vertical position and tapping it so the bubbles moved to the edges of the sample. After UV curing, the quartz plates were separated and cleaned with acetone.

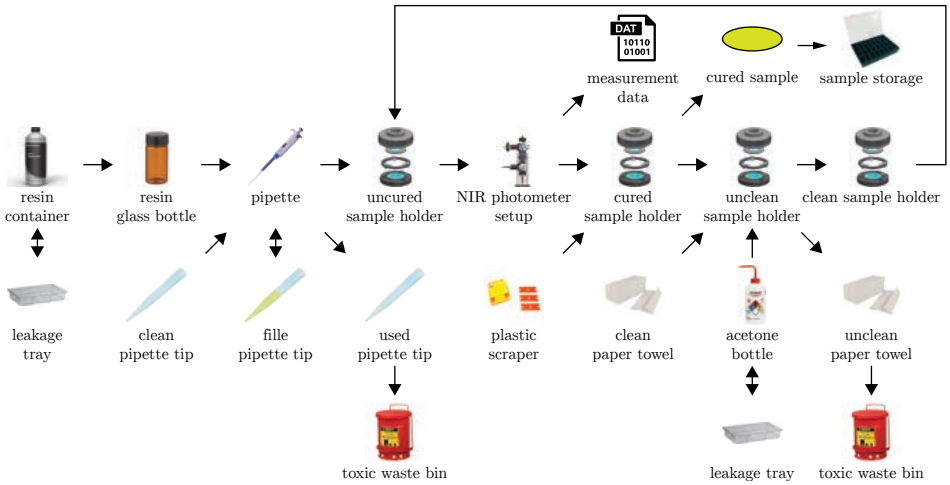

Figure 6.14: Sample preparation and cleaning procedure for the NIR photometer.

6.4.2 Initial test results

Before discussing the initial test results, the reader should have an idea of the expected measurement results. To this end, Figure 6.15 (a) and (b) show simplified absorbance $A(\lambda)$ and transmittance $T(\lambda)$ spectra before and after curing, and the resulting time evolution of optical power $P(t)$ from beginning to end. Recall that the absorbance, transmittance, and optical power in a medium are related through the Beer-Lambert law (6.1), where the irradiances I and I_0 are replaced by the powers P and P_0 respectively [36]:

$$T = \frac{P}{P_0}, \; A = \log_{10}\left(\frac{1}{T}\right) = \log_{10}\left(\frac{P_0}{P}\right). \tag{6.4}$$

Spectro(photo)meters determine the absorbance and transmittance from optical power measurements of the ingoing beam P_0 and the outgoing beam P for each

wavelength in the spectral range, whereas the photometer only measures at two wavelengths. Photopolymer absorbance and transmittance spectra typically show a baseline shift upon curing [45], which manifests itself as an overall increase in absorbance and a reduction in transmittance and optical power as indicated in Figure 6.15.

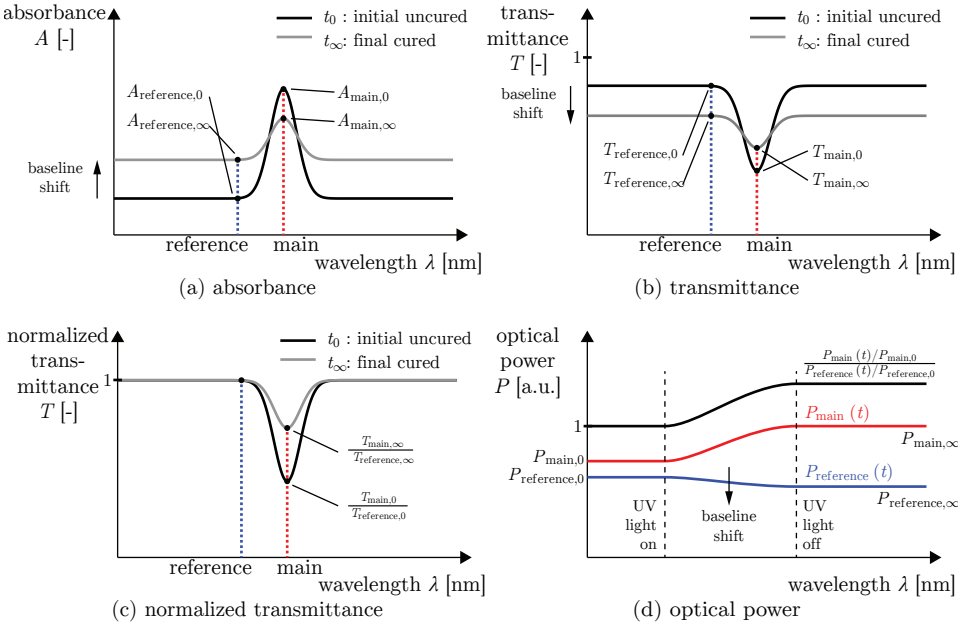

Figure 6.15: Expected spectroscopic measurement results in case of an idealized photocurable material containing a single absorption peak.

By normalizing the transmittance spectrum $T(\lambda)$ to the reference transmittance $T_{reference}$, one can determine the relative peak or valley height as depicted in Figure 6.15 (c) and, in turn, the degree of conversion. Thus, the relative or normalized degree of conversion [18] α_{norm} can be determined from the ratio of the main to the reference optical power $P_{main}/P_{reference}$ and the initial and asymptotic powers [102]:

$$\alpha_{norm}(t) = \frac{\frac{P_{main}(t)}{P_{reference}(t)} - \frac{P_{main,0}}{P_{reference,0}}}{\frac{P_{main,\infty}}{P_{reference,\infty}} - \frac{P_{main,0}}{P_{reference,0}}}, \tag{6.5}$$

where the subscripts 0 and ∞ refer to the initial value and the asymptotic value at $t = 0$ and $t = \infty$ respectively. Note that in practice not all monomer groups are converted into polymer [103], which manifests itself as a degree of conversion asymptote for α (6.2) which is lower than 100 [%] and, thus, α_{norm} (6.5) is a relative

conversion that does range between 0 and 100 [%]. Figure 6.15 (d) schematically shows the expected optical signal time responses upon UV curing. Note that the reference signal is expected to *decrease* and both the main signal and ratio of the two are expected to *increase*.

Figure 6.16 shows the results of an initial test with photopolymer resin in the original configuration. The main and reference IR detector outputs are shown normalized to their initial values, which are proportional to the optical powers P_{main} and $P_{reference}$ respectively. A large dip in both the main and reference signals is clearly visible, in contrast to the expectations. When comparing the expected signals in Figure 6.15 (d) with the actual results in Figure 6.16, it becomes evident that the instrument did not function as expected. However, the main signal is higher than the reference signal after the large dip, as expected. Note that the main signal shows erratic noise probably accountable to unintentional external feedback into the laser [70], which was later reduced by coupling the main laser's output fiber to a Faraday isolator (IO-H-1550APC, Thorlabs).

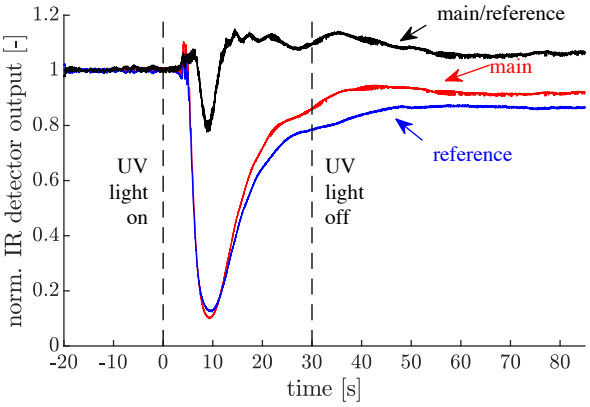

Figure 6.16: Initial test results showing the normalized main and reference IR detector outputs versus time upon UV curing of Formlabs Silica. An unexpected, large dip is evident.

6.4.3 Mitigating UV light field issues

The debugging and troubleshooting process [101, 104] started once the first system tests yielded unexpected results. Unfortunately, debugging of (N)IR optical systems is complicated by the fact that the light is invisible to the human eye and cameras of suitable spectral sensitivity are expensive [101]. A fluorescent disk (VRC2SM1, Thorlabs) was used to visualize the NIR spot alignment, but it was found unsuitable for debugging purposes due to its slow-fading behaviour and low intensity.

Fortunately, the fiber-optic instrument design allowed to easily couple a visible red light source ($\lambda = 635$ [nm], S1FC635, Thorlabs) into the measurement probe instead of the NIR light. The visible red light aided in visualizing the optical phenomenon that caused the large dip in the initial test results. Moreover, the UV detector components were removed from the setup to narrow down the cause and the outgoing optical fiber was connected to the Silicon detector.

Figure 6.17 (a) shows the result of a transmission measurement using the 635 [nm] light source, which again exhibits a large dip. Figure 6.17 (b) shows the modified optical layout at this stage in debugging. As a result of omission of the UV detection path, it was possible to move the receiving fiber upwards. When the receiving fiber was shifted upward and brought closer to the sample, the dip would become less deep. The receiving fiber was ruled out by placing the detector directly under the sample, but was found not to be the cause. To visualize what was happening, a piece of sheet metal was placed above the detector having a white protective film. Figure 6.17 (c)–(e) show snapshots taken from a video of UV curing, which was recorded with a mobile phone.

Initially, three red dots are visible in Figure 6.17 (c), two of which are so-called ghost reflections originating from the dichroic mirror. Note that this effect is much less pronounced at the NIR wavelengths, i.e., the reflectance of the dichroic mirror is 71 [%] at 635 [nm] as opposed to 4 [%] at 1550 [nm]. Shortly after the UV light has turned on, the beam size has severely increased as seen in Figure 6.17 (d). Upon further curing, three red dots are discernable again in Figure 6.17 (e) although their spot sizes are larger than before curing.

These results indicate that the resin layer acts as a lens and severely diverges the measurement beam during curing. However, as the resin cures further, the lens effect is reduced again. This effect may be attributable to an inhomogeneity of an optical property, which reduces once fully cured. As the $1/e^2$ beam diameter [70] of the receiving focus lens is only 0.9 [mm], a large portion of the transmitted light falls outside of the area probed by the fiber. Hence, the measurement beam divergence explains the large dip in the measured signals upon UV curing.

Ultimately, the UV light field was found to be the major cause of the beam divergence. It is suspected that the engineered diffuser was the root cause for the lens effect in the resin layer. Engineered diffusers are known to lead to high-contrast fine-scale granular patterns, but nominally uniform light fields when irradiated by coherent light [105]. This phenomenon is referred to as speckle and is caused by interference of wavefronts at rough interfaces, e.g., on diffusively reflecting surfaces. Interestingly, speckle also leads to so-called modal noise in MM fibers [105]. During initial component tests, it was already noticed that MM fibers introduced a significant amount of noise to the detected signal.

The hypothesis is that the UV speckle pattern caused the polymerization reaction to initiate at one point on the resin surface, and to initially remain unaffected at a point directly next to it. As the polymerization reaction continues, reactive species diffuse from points that are irradiated to points that are not. As a result, it is

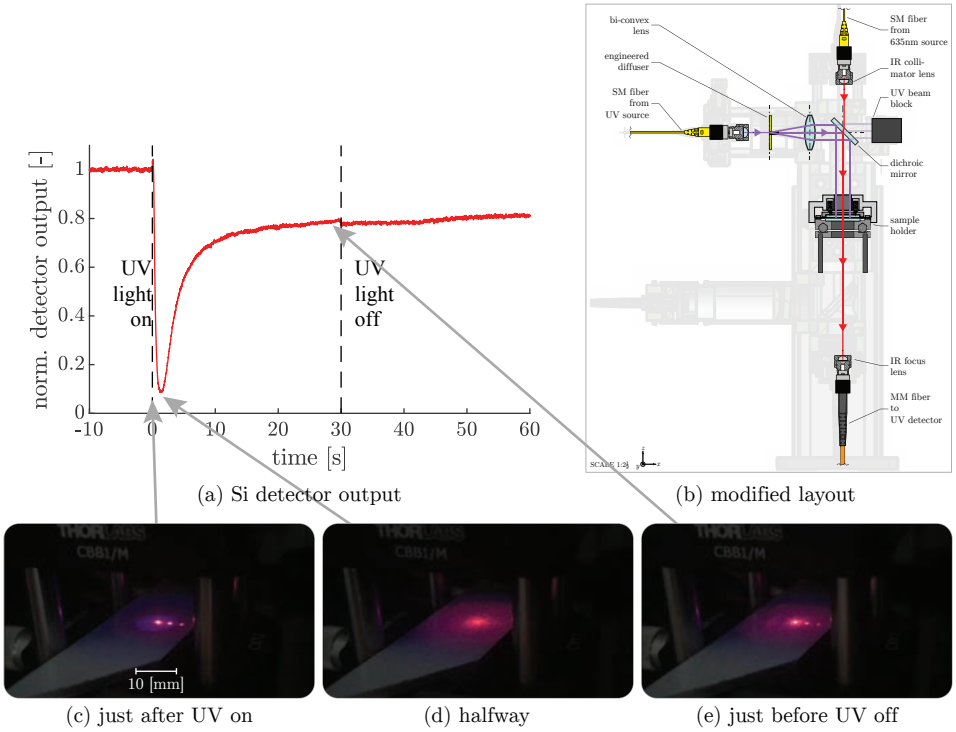

(a) Si detector output (b) modified layout

(c) just after UV on (d) halfway (e) just before UV off

Figure 6.17: Visualization of the beam divergence issue caused by the engineered diffuser in the UV light path. The graph in (a) shows the transmission of a visible red (635 [nm]) beam during UV curing of LCD-T resin. Photographs (c)–(e) show snapshots of the transmitted beam going through phases of collimation, severe divergence and collimation again. More than one red dot is visible as a result of ghost reflections originating from the dichroic mirror.

hypothesized that either the cured part of the resin layer instantaneously takes on the microstructural shape of the engineered diffuser, or the local refractive index changes cause a diverging lens effect. In either case the effect vanishes partly, possibly because the degree of cure distribution becomes more homogeneous due to transport of reactive species. Figure 6.18 illustrates this hypothesis.

Speckle can be suppressed in several ways; a common method is to temporally average by moving the diffuser, e.g., by rotating it [105, 107, 108]. Jariwala and Zhao reported a significant improvement by rotating the diffuser in a similar UV curing setup using an interferometric measuring principle [107, 109]. However, their motivation was not to reduce a beam divergence issue nor did they report such an issue, but they did notice a different irradiance profile at different diffuser rotation angles. The quickest solution to the problem was to use an alternative

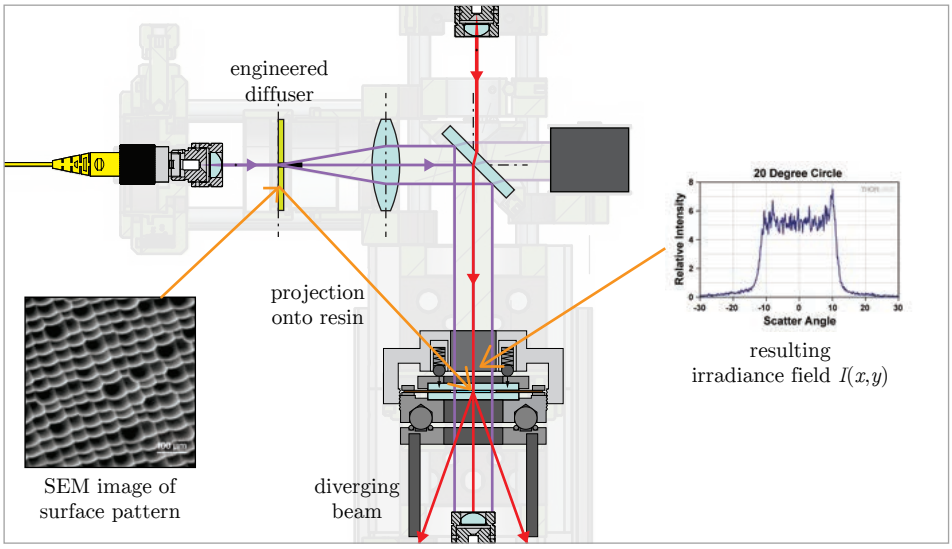

Figure 6.18: Possible explanation for the beam divergence issue. The engineered diffuser's surface structure causes a speckle pattern in the UV irradiance field $I(x, y)$, which causes inhomogeneous cure in the resin layer. As a result, the resin becomes a diverging lens. The SEM image and irradiance plot (as a function of scatter angle instead of position) are courtesy of Thorlabs [106].

UV light source that was readily available in the lab, i.e., a spot UV curing system (CS410-EC, Thorlabs, $\lambda = 365$ [nm]). Fortunately, the beam divergence problem was (temporarily) solved by using this alternative UV light source.

6.4.4 Overcoming optical interference issues

Once the beam divergence problem had been solved, another problem emerged. That is, the measurement results in Figure 6.19 (a) showed a sinusoidal shape with a decreasing frequency over time, also known as a chirp or sweep signal. Upon close examination, a small sinusoidal component can be seen in Figure 6.16 as well, especially visible in the ratio of the main and reference signals. This effect became more pronounced once the beam divergence issue had been eliminated in the modified layout seen in Figure 6.19 (b).

The measured sinusoidal signals highly resemble the signals reported by researchers working on interferometric cure monitoring setups [40, 44, 110, 111]. Therefore, the conclusion was drawn that the signals were the result of an *optical interference* phenomenon [96] and the instrument was now more of an *interferometer* than a *photometer*. Although the interferometric signals looked rather clean, the goal was to build a photometer so it was attempted to eliminate the interference.

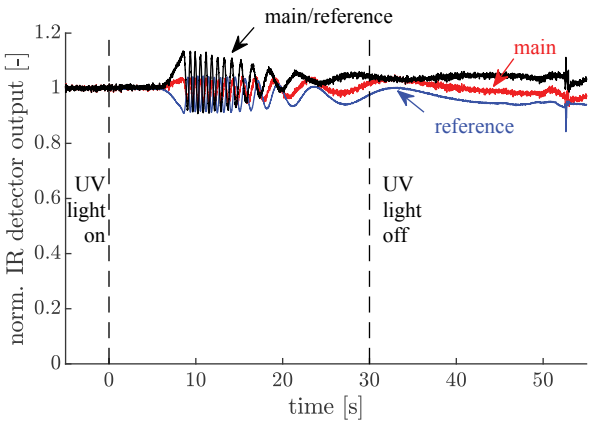

(a) measurement results

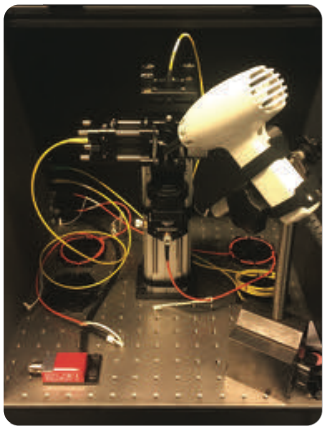

(b) modified layout

Figure 6.19: Test results (a) obtained with the alternative UV light source seen in (b). Optical interference in the resin layer is the cause of the sinusoidally shaped signals whose instantaneous frequency decreases over time.

Optical interference can be described by the wave theory of the electromagnetic nature of light [96]. Interference occurs when two or more light waves or wavefronts overlap in space and results in an irradiance that deviates from the sum of the component irradiances [96]. Suppose two harmonic planar wavefronts E_1 and E_2 of the same frequency overlap and their electric field is described by:

$$E_i(x,t) = E_{0i}\sin[\omega t + \phi_i(x,\varepsilon)],\ \phi_i = -(kx + \varepsilon_i),\ i = 1,2 \tag{6.6}$$

where x is position, t time, ω the angular temporal frequency, ϕ the spatial phase, k the wavenumber or spatial frequency, and ε the initial phase angle. The resultant field E follows from the linear superposition of the waves $E = E_1 + E_2$. The irradiance I is proportional to the square of the electric field:

$$I \propto E_0^2 = E_{01}^2 + E_{02}^2 + \underbrace{2E_{01}E_{02}\cos(\delta)}_{\text{interference term}},\ \delta = \phi_2 - \phi_1, \tag{6.7}$$

where δ is the phase difference. Clearly, the resultant irradiance I is not just the sum of the individual component irradiances I_1 and I_2, but is also dependent on the phase difference δ in the interference term. The phase difference is a function of the wavelength and the difference in optical path lengths:

$$\delta = \frac{2\pi}{\lambda_0}\Lambda,\ \Lambda = n(x_1 - x_2), \tag{6.8}$$

where λ_0 is the wavelength and Λ the optical path difference, which is the product of the refractive index n and difference in the travelled distances x_1 and x_2. The

results in Figure 6.19 (a) can be interpreted as follows. Among other effects, the photopolymer's refractive index typically increases upon UV curing [112], which leads to an increase in optical path length as per (6.8). Reflections in the photopolymer sample lead to multiple waves overlapping and interfering with one another. As a result, the irradiance varies as a function of time since $\delta(n(\alpha(t)))$, which can be modelled [40] as:

$$I(t) = I_o + I_a \sin(\delta(t) + \phi_0), \tag{6.9}$$

where $I_o(\lambda)$ and $I_a(\lambda)$ are the wavelength-dependent offset and interference amplitude irradiances respectively, and $\phi_0(\lambda)$ the wavelength-dependent initial phase. Hence, the main and reference chirp signals show a different instantaneous frequency and initial phase, since the two signals were obtained at different wavelengths $\lambda_0 = \lambda_m$ and $\lambda_0 = \lambda_r$ in (6.8).

Observe that the interference amplitude I_a notably changes as the polymerization reaction progresses in Figure 6.19 (a). Less notably, the offset amplitude I_o changes over time if the photopolymer's absorbance changes, i.e., the desired photometric effect. Thus, if one would want to use the interferometric effect to measure the degree of conversion, it would be advisable to use a wavelength that does not correspond to a peak in the absorption spectrum, such as the reference wavelength λ_r. In this case, the degree of conversion can be determined by extracting the phase difference from the measured irradiance $I(t)$. A seemingly simple method to do so is counting the number of (half) oscillations by determining the local minima and maxima [44, 107]. Moreover, the referencing method would have to be reconsidered.

Having built up a basic understanding of the interference phenomenon, the options were examined to eliminate the phenomenon. Literature suggests the following measures to eliminate or reduce interference [101, 113, 114]:

- applying anti-reflection coatings;
- tilting windows;
- using non-collimated, incoherent beams;
- adding strategic beam dumps;
- roughening at least one face of the sample;
- depositing the sample in a wedge shape;
- placing the sample inside an integrating sphere;
- using polarized light and tilting the sample to Brewster's angle [96];
- modulating the phase or frequency.

Some of these measures had already been taken into account in the instrument's design, such as the use of anti-reflection coatings and tilting planar objects such as filters. A more thorough analysis was needed to select a suitable countermeasure.

Figure 6.20 shines some light on the interference effect in thin films as a result of reflections at interfaces. Figure 6.20 (a) visualizes the interference between the light waves reflected at the top and the bottom of the film in a simplified

representation. Figure 6.20 (b) shows a more realistic representation of single-film interference, by showing the many reflected and transmitted field components E_r and E_t respectively [96]. Note, however, that at each interface the electromagnetic field energy is divided into a reflected part and a transmitted part, governed by the amplitude reflection r and transmission t coefficients in the Fresnel equations [96]. As a result, the intensity of each reflection decreases and becomes insignificant after several reflections. Anti-reflection coatings help to reduce the reflectance, but are typically designed for glass-air interfaces.

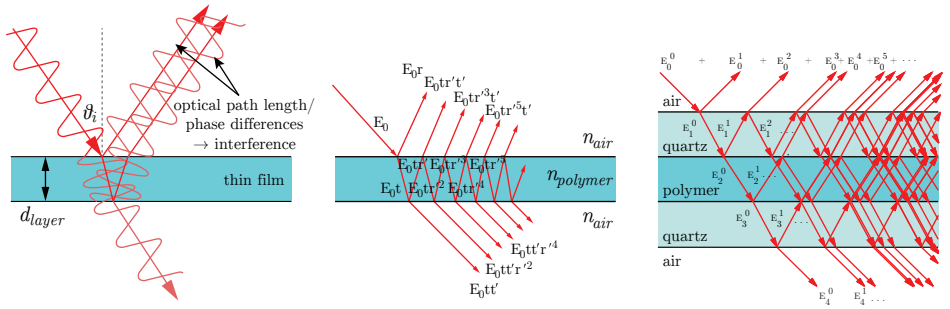

(a) single-film interference at top (b) electrical field components (c) three-layer stack components

Figure 6.20: Light waves in thin-film interference. Images adopted from [96, 101].

Interference may occur both in reflection and in transmission sampling configurations, where the detector is placed at the top or at the bottom of the sample respectively as in Figure 6.5. If the thin films in Figures 6.20 (a) and (b) represent a non-shrinking homogeneous photopolymer layer in air, then the optical path difference varies as the photopolymer cures over time according to:

$$\Lambda(t) = 2d_{layer}\sqrt{n^2_{polymer}(\alpha(t)) - n^2_{air}\sin^2(\theta_i)}, \tag{6.10}$$

where the factor 2 stems from dual layer passage, $n_{polymer}$ is the photopolymer's refractive index as function of the degree of conversion $\alpha(t)$, d_{layer} is the layer thickness, n_{air} the refractive index of air, and θ_i is the incident angle. In reality, the degree of conversion and refractive index are a function of depth z into the layer, so the optical path difference is a function of $2\int_0^{d_{layer}} n_{polymer}(z)dz$. Moreover, in this case the straight ray approximation does not hold anymore and the resin layer acts as a gradient index (GRIN) lens [115, 116]. Note too, that in this case the angle of the transmitted ray with respect to the surface normal may deviate from the incident angle, contrary to the case of a homogeneous plane-parallel plate which is known to laterally displace a beam without changing its direction [96].

In the NIR photometer, the photopolymer sample is sandwiched between two quartz plates and hence represents a three-layer stack as in Figure 6.20 (c). As the figure shows, multiple beams interfere as each beam is split into a reflected

and transmitted part at each interface. Jariwala and Zhao assumed that such a photopolymer sample can be modelled as four-layer stack consisting of two quartz plates, a cured, and an uncured layer [44, 107]. In either case, the quartz plates act as an optical cavity or etalon [96] leading to multiple beam interference.

Having built up a deeper understanding of the interference phenomenon through the foregoing analysis, a solution was conceived to eliminate the interference. To this end, a ray tracing model was developed in MATLAB as depicted in Figure 6.21.

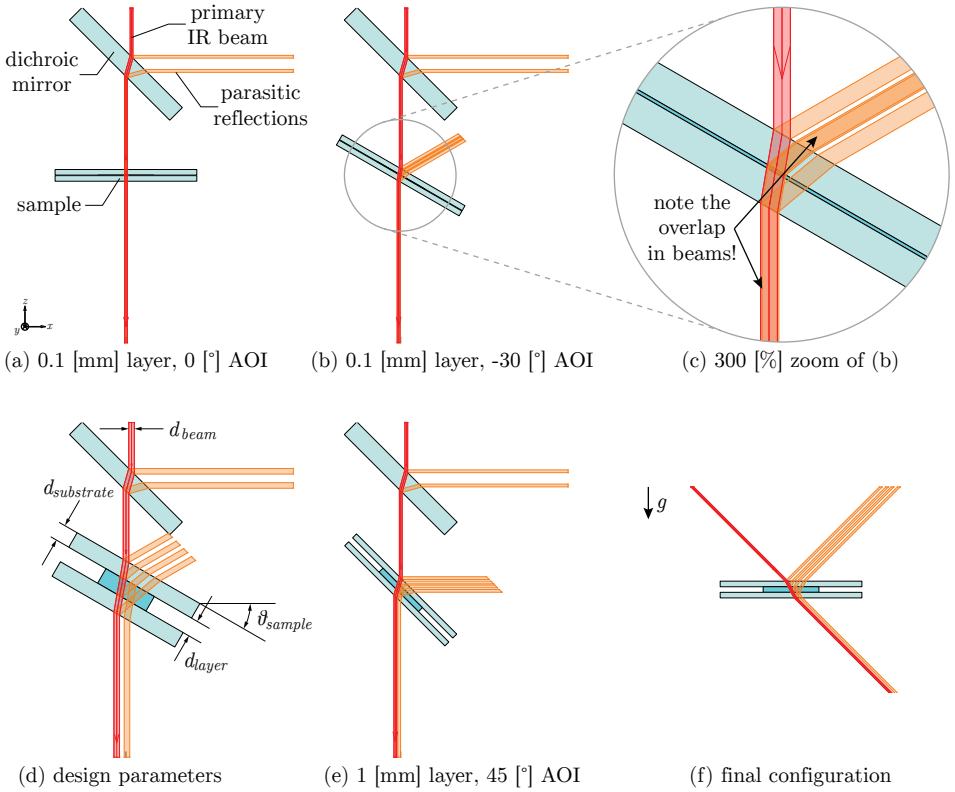

(a) 0.1 [mm] layer, 0 [°] AOI (b) 0.1 [mm] layer, -30 [°] AOI (c) 300 [%] zoom of (b)

(d) design parameters (e) 1 [mm] layer, 45 [°] AOI (f) final configuration

Figure 6.21: Design changes in the optical layout to circumvent interference effects as a result of overlapping reflected beams. Images where generated by a ray tracing model implemented in MATLAB.

The model incorporates the laws of reflection and refraction [96] and uses the geometry, wavelengths and refractive indices representative for those used in the Probe module design. The original design is displayed in Figure 6.21 (a), having a 0.1 [mm] layer and a zero degree angle of incidence (AOI). The primary IR beam is depicted in red; all reflected beams are depicted in orange and considered parasitic such as the dichroic mirror's ghost reflections seen in Figure 6.17. Note that many

higher-order reflections were omitted for clarity and that there is a certain symmetry in the reflected and transmitted parasitic beams at the top and bottom of the sample respectively.

The key to the solution of the interference problem at hand was found in preventing reflected beams from overlapping with the main transmitted beam. If overlap is unavoidable, one of the alternative measures may be used as listed above. To this end, the design parameters included the sample angle θ_{sample}, the sample layer thickness d_{layer}, the substrate thickness $d_{substrate}$, and the beam diameter d_{beam} as indicated in Figure 6.21 (d). Merely rotating the sample was not enough to eliminate interference, as seen in Figure 6.21 (b) and (c). The reason is that no matter the rotation angle θ_{sample}, the beams reflected at the top quartz-resin interface and the bottom resin-quartz interface overlap due to the ratio of the beam diameter d_{beam} to the resin layer thickness d_{layer}. Since d_{beam} is larger than d_{layer}, overlap is insurmountable in the original layout. Thus, in the modified layout, the sample both had to be tilted with respect to the measurement beam and its layer thickness was increased to 1.0 [mm] as seen in Figure 6.21 (e) and (f). Finally, the measurement beam was rotated with respect to the vertical gravity vector $\boldsymbol{g}$ so the resin sample was kept level in order to avoid gravity-driven fluid flows.

The modified Probe module design is shown in Figure 6.22. Unfortunately, the custom-made sample holder's geometry was unsuitable for a 45 [°] angle of incidence, so the sample holder had to be redesigned as in Figure 6.22 (c). A drop-in cage mount with internal threads (QRC1A, Thorlabs) was used for this purpose and an $18 \times 25 \times 1$ [mm] (inner $\times$ outer diameter $\times$ thickness) steel shim was used as the spacer.

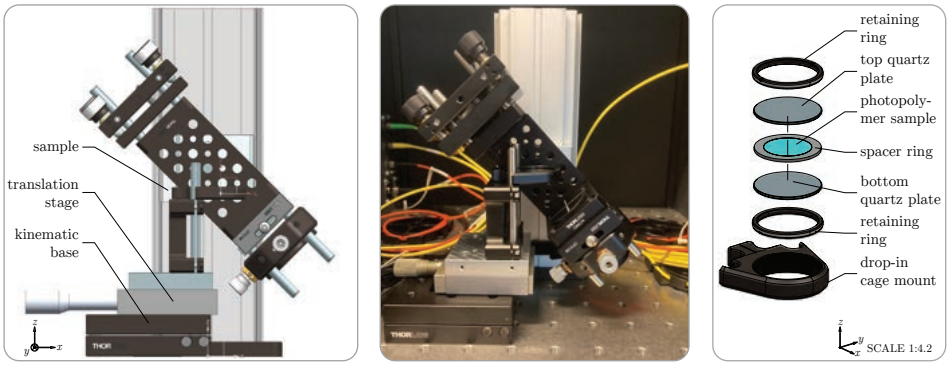

(a) Probe module CAD drawing (b) photograph (c) sample CAD drawing

Figure 6.22: Modifications of the Probe module design to avoid optical interference within the resin layer (optical fibers omitted).

6.4.5 Coping with IR beam divergence issues

The design changes outlined above turned out to be effective in reducing the interference issues. However, a new problem emerged again during tests with the latest modified design. Figure 6.23 shows measurement results obtained in the modified layout. Again, an unexpected reduction of the optical power is observed in both the main and reference signal.

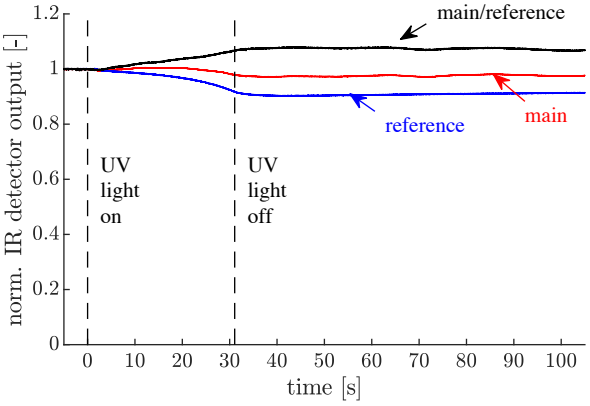

Figure 6.23: Test results obtained with a 1 [mm] thick LCD-T sample and a 45 [°] measurement beam angle of incidence. Both the main and reference signal eventually decline, indicating optical signal loss.

In an attempt to find the source of the problem, the visible red light source was again coupled into the optical fiber instead of the NIR light. Figure 6.24 shows several photographs taken during and after UV curing. A piece of sheet metal with white protective film was placed under and above the sample, normal to the measurement beam and normal to the reflected beam respectively. The measurement beam again showed significant divergence, both in the main transmitted spot and in the reflected spot. At 45 [°] incidence the transmitted beam had the shape of a crescent moon after UV curing, while at normal incidence it was still round as seen in Figure 6.24 (a) and (c) respectively. The transmitted beam divergence half-angle θ_{div} was estimated to be approximately 20 [°] after UV curing.

A speckle pattern can be observed in the normally-incident transmitted beam in Figure 6.24 (c), but is less distinguishable at 45 [°] in (a). Therefore, a CCD camera was placed at the top of the sample, normal to the reflected beams. The top of the captured CCD image in Figure 6.24 (b) shows the first reflection at the air-quartz interface, which still has a round shape as it does not interact with the resin sample. Moreover, the bottom of the image shows a high-contrast, crescent-moon-shaped speckle pattern. The speckle pattern may originate from the relatively rough surface at the bottom of the photopolymer sample. That is, during sample cleaning it was

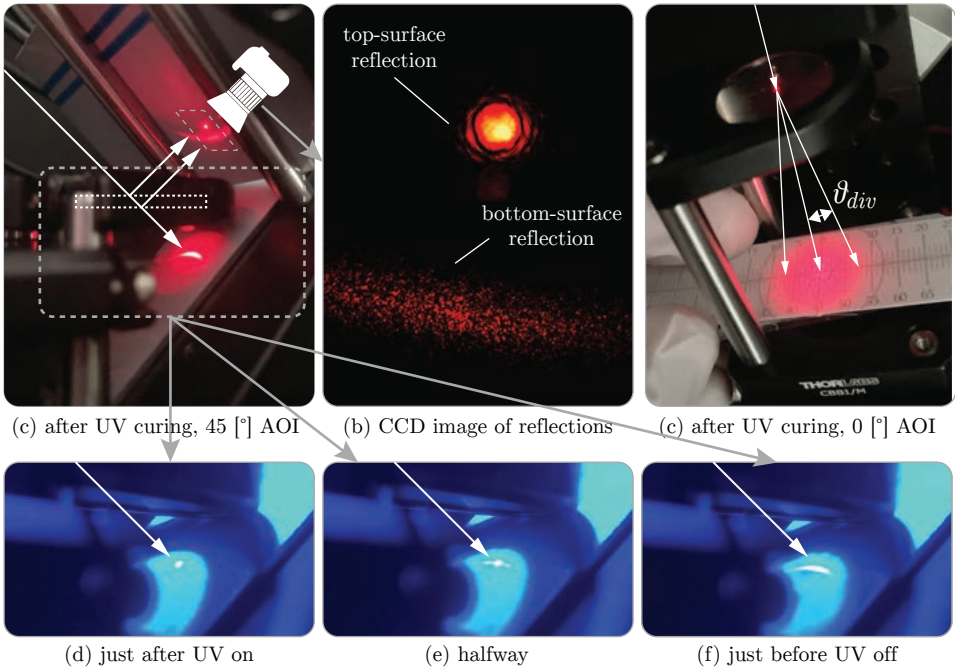

Figure 6.24: Visualization of the divergence of a visible red (635 [nm]) beam upon UV curing at 1.0 [mm] layer thickness and under 45 [°] incidence except for (c). Photographs (d)–(f) show how the transmitted beam shape evolves from a circular spot to a crescent moon shape. The white arrows indicate the beam's direction.

observed that the top surface had a much smoother appearance than the bottom surface, based on observations of ambient light reflections at varying sample tilt angles.

Figure 6.24 (d)–(f) show snapshots from a video of UV curing taken from the same angle as Figure 6.24 (a) and enlarged as indicated by the dashed border. The beam profile is initially round and collimated, but becomes curved and non-collimated as UV curing progresses. Contrary to the previous beam divergence issue in Figure 6.17, the transmitted beam does not return to a collimated state. The cause of the diverging lens effect seen in Figure 6.24 has not been established yet. Nevertheless, it may be attributed to a refractive gradient index throughout the resin layer [115, 116], whose effect is more pronounced in the modified design than the original design due to the tenfold increase in layer thickness.

The choice was made to search for a solution to the beam divergence issue that can cope with it, rather than for the cause(s). This choice was motivated by the desire for robustness of the measuring instrument to sample inhomogeneities. A common solution to divergence issues in spectroscopy is to use a so-called integrating

sphere to collect the transmitted light [71], which is a sphere whose internal surface is covered with a diffuse white reflective coating to spread the incoming light over its entire surface. The integrating sphere is less susceptible to optical power fluctuations as a result of several optical phenomena, including beam deflection, diffraction, refraction, and scattering [71]. Note that this may as well be a solution to the divergent beam issue caused by the diffuser. Thus, an integrating sphere was acquired (IS200, Thorlabs) and incorporated into the setup.

Figure 6.25 shows the final Probe module layout in which the transmitted light is collected by the acquired integrating sphere. It was attempted to maximize the sphere's acceptance cone, by placing the sample as close to the sphere as possible. Nonetheless, the maximum allowable half-beam divergence angle was approximately 20 [°], leaving little to no margin with respect to the previously identified divergence angle. Attempts to directly couple the light into a MM fiber proved unsuccessful due to the relatively low numerical aperture of the used fiber and the relatively low irradiance level as a result of spreading the light over the sphere's entire surface. Therefore, both InGaAs detectors were mounted directly to the ports of the integrating sphere as shown in Figure 6.25.

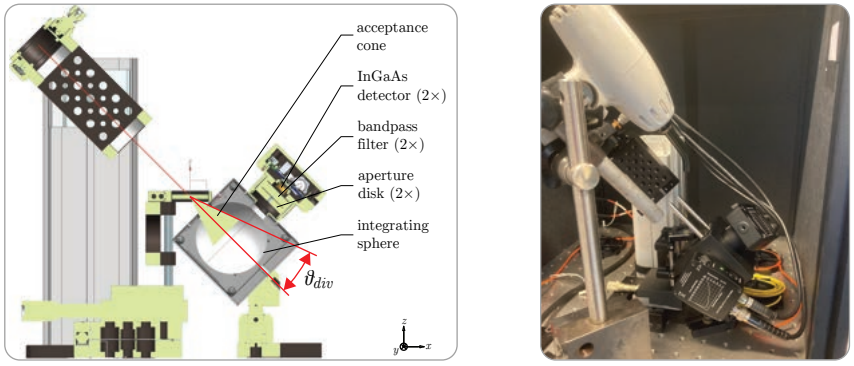

(a) cross-sectional CAD drawing of final Probe module layout

(b) photograph

Figure 6.25: Modifications of the Probe module design to collect the transmitted beam with an integrating sphere instead of a fiber-optic collimator lens.

The bandpass filters were placed directly in front of the detectors. Initial tests in this configuration showed reduced wavelength separation performance, likely due to the wide range of incidence angles of the light irradiating the filters. As the bandpass filters are designed for near-to-normal incidence [47], the shape of the transmission spectrum becomes distorted at large angles of incidence. To improve the wavelength separation performance, a 2 [mm] diameter aperture ring was placed in front of the filters as shown in Figure 6.25 (a). The resulting crosstalk of the main to reference was reduced from 14 [%] to 3 [%] and of the reference to main from 36 [%] to 10 [%]. If the crosstalk is constant for the operating conditions in

UV curing, the pure main and reference signals can be retrieved from the measured signals through a simple transformation matrix.

6.4.6 Summary of design changes

Table 6.2 summarizes the most important changes to the original design.

Module	Description	Parameter	Value	Unit
Source	UV light source	halogen lamp	Thorlabs CS410-EC	-
Probe	beam diameter UV beam	D_{UV}	40 (estimate)	[mm]
	incidence angle IR beams	$\theta_{i,IR}$	45	[°]
	diameter resin sample	D_{resin}	18	[mm]
	layer thickness resin sample	d_{layer}	1.0	[mm]
	IR beam collection optics	integrating sphere	Thorlabs IS200	-
Detector	outgoing fibers	MM fibers/splitter	omitted	-

Table 6.2: Summary of changes to the original design.

6.5 Experimental evaluation of the final design

After addressing the issues described above, the instrument seemed to function properly as the measured signals showed no more signs of optical signal loss. Figure 6.26 shows a comparison of measurement results from the present NIR photometer to literature results from a commercial NIR spectrophotometer [117]. The NIR photometer results were obtained with LCD-T resin at a layer thickness of 1.0 [mm] and 45 [°] incidence, whereas the NIR spectrometer results from literature were obtained with a 2-phenoxyethyl methacrylate resin at 0.5 [mm] and normal incidence [117].

Both the graphs in Figure 6.26 show a distinctive shape in which the slope or polymerization rate increases approximately halfway along the polymerization reaction. This change in polymerization rate is known as autoacceleration and the gel or Trommsdorff effect [58]. The effect may be less pronounced in other resin formulations, which show a degree of conversion time evolution that more closely resembles a first-order system response. Since autoacceleration is considered the normal behaviour for most polymerizations [58], the conclusion can be drawn that the instrument functions properly at least in a qualitative sense based on the results in Figure 6.26. The reference signal in Figure 6.26 (a) shows an increase in contrast to the expected decrease for typical baseline shifts resulting from an overall absorbance spectrum increase. This deviation from expectation is partly attributable to the crosstalk between the main and reference signal. Note that the NIR spectrometer results in Figure 6.26 (b) were obtained from the absorbance peak area at 1622 [nm], without the use of a reference [117].

More experiments were performed to demonstrate that the instrument also works with other acrylic materials. To this end, the following commercially available materials were used in addition to Sparkmaker LCD-T:

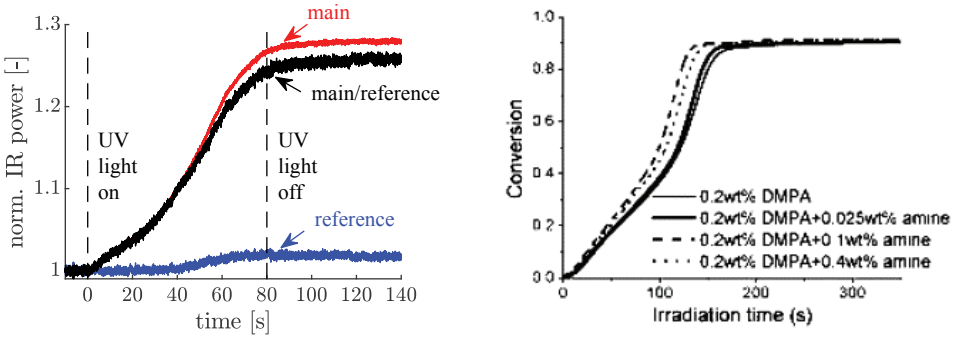

(a) NIR photometric results

(b) NIR spectrophotometric literature results

Figure 6.26: Comparison of UV curing results obtained with the final NIR photometer layout and LCD-T resin (a) to results obtained with an NIR spectrometer and methacrylic resin (b) from literature [117]. The results show a similar shape, which indicates that the cure kinetics are similar and the instrument functions properly.

- FunToDo Industrial Blend (Fun To Do, Alkmaar, The Netherlands);
- NextDent SG (NextDent, Soesterberg, The Netherlands);
- NextDent C&B MFH (NextDent, Soesterberg, The Netherlands);
- NextDent Ortho Rigid (NextDent, Soesterberg, The Netherlands);
- Formlabs Clear (Formlabs GmbH, Berlin).

Although the exact formulations are proprietary [77], each of these materials is based on acrylate monomers according to their respective material safety data sheets. Moreover, it was confirmed that each material contained an absorption peak that reduced in height upon UV curing at 1622 [nm] by measuring NIR absorption spectra before and after curing using a UV-VIS-NIR spectrophotometer (UV-3600, Shimadzu, Kyoto, Japan).

Figure 6.27 shows the measurement results for the variety of commercial photopolymer resins listed above. Due to time constraints only three replications were performed per resin. Nevertheless, the figure clearly shows that the instrument functions properly for each resin. Moreover, the figure shows that the NIR photometer can be used to determine the photopolymerization reaction time scale, as the UV exposure time had to be adjusted for each resin. Among the tested resins, the FunToDo Industrial Blend was the most reactive and the Formlabs Clear was the least reactive. The latter may be explained by the fact that a 365 [nm] light source was used for a resin designed for 405 [nm], i.e., the photoinitiator component of the Formlabs resin may be insensitive to 365 [nm] radiation. Although the final degree of conversion differed per material, the cure state was verified to be past the gel point as each sample was 1.0 [mm] thick after UV curing, which indicates that the cure front had reached the bottom of the sample.

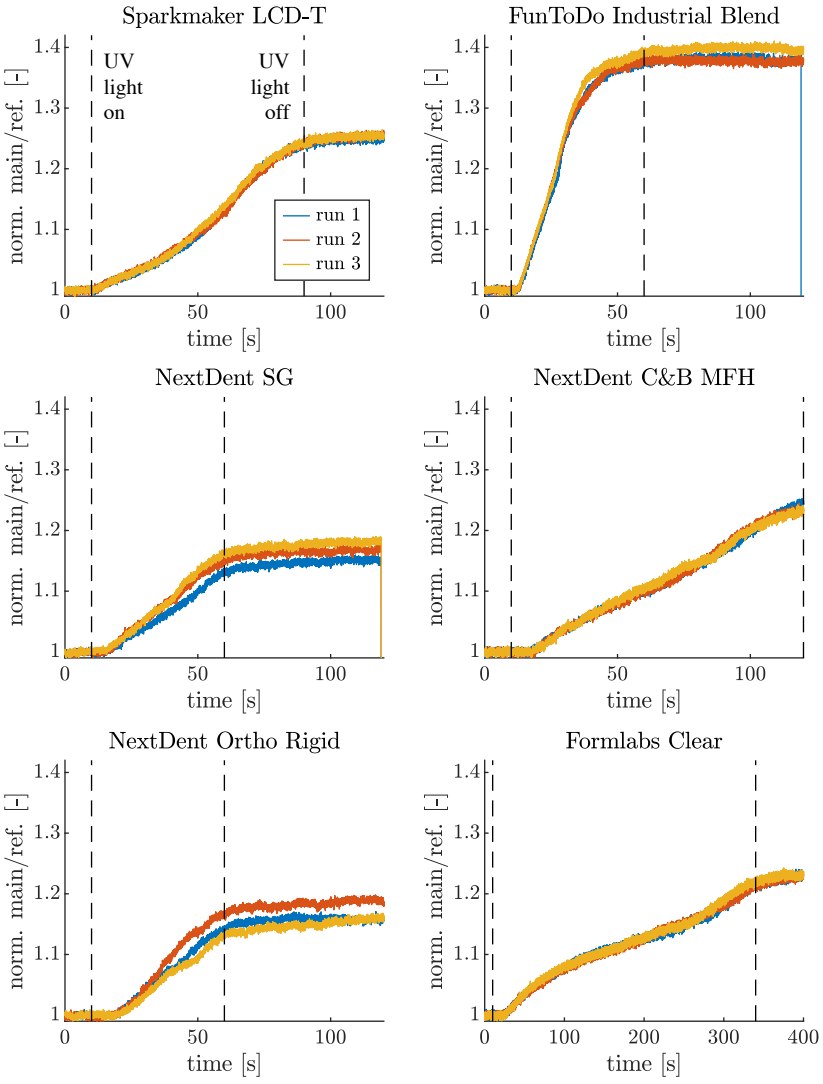

Figure 6.27: NIR photometric UV curing results for a variety of commercially available acrylic photopolymers. The results are indicative of the photopolymer's reactivity; note that the bottom-right graph for Formlabs Clear has a different timescale. Although the results seem to indicate differences between resins in the final conversion level, such a conclusion can not be drawn from these results due to differences in chemical composition and initial monomer concentration. The slope at the end of UV exposure indicates that only the FunToDo resin was fully cured.

6.5.1 High-speed results under high-power UV irradiation

Due to the relatively low UV irradiance level and thick layer, the timescales in Figure 6.27 are rather large in comparison to typical exposure times in photopolymer-based AM. Thus, a high-power UV source was installed in the setup to demonstrate the high-speed measurement capabilities of the NIR photometer. To this end, the maximum power output of a 150 [W] high-pressure mercury lamp (bluepoint 4, Dr Hönle AG, Gräfelfing, Germany) was led to the sample by means of an 8 [mm] diameter light guide placed at a 50 [mm] distance from the sample.

Figure 6.28 shows a measurement result obtained with this high-power UV source, LCD-T resin, and the maximum sampling rate of $f_s = 20$ [kHz]. The figure shows that the resin instantaneously cures and reaches a through-cure at approximately 5 [s]. The figure also shows a good signal-to-noise ratio, even at the highest sampling frequency the control computer allows. A first-order response [7, 18] was fitted to the data using a least-square curve fit algorithm in MATLAB to estimate [7] the reaction timescale $\tau = 2.3$ [s]. The obtained ratio of reaction timescale τ to sampling time $T_s = \frac{1}{f_s} = 5 \cdot 10^{-5}$ [s] was thus $\frac{\tau}{T_s} = 4.6 \cdot 10^4$ [-].

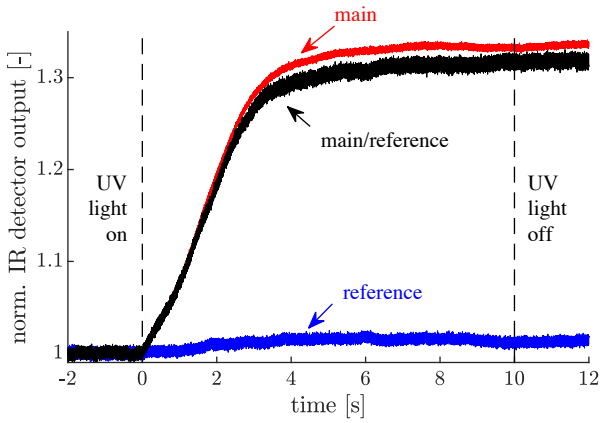

Figure 6.28: High-power UV curing results obtained with the final NIR photometer layout and LCD-T resin. The UV curing reaction shows a first-order reaction timescale of $\tau = 2.3$ [s] and asymptotic behaviour indicating a full through-cure.

The results show that the reaction timescale is in the 1 to 10 [s] exposure time range used in mask projection-based vat photopolymerization, while the measurement speed is more than high enough for real-time control. Thus, the sampling rate limitation found in previous work [18] has been greatly improved and it is no longer needed to reduce the light intensity to match the reaction timescale to the measurement timescale and make unprovable assumptions on the reciprocity between the light intensity and the cure kinetics [33]. Note that the reaction timescale is expected to be shorter for a tenfold smaller layer, which decreases $\frac{\tau}{T_s}$.

The high-speed, high-power experiment was repeated ten times to obtain an indication of the measuring instrument's repeatability. The results in Figure 6.29 show a good match for the first three seconds of the UV curing reaction. From there on, noticeable differences emerge and the final conversion level shows an 8 [%] variation. The maximum final ratio $P_{main,\infty}/P_{reference,\infty}$ among all ten experiments was estimated to equal 1.33 [-] and (6.5) was used to calculate the degree of conversion. Based on this estimation, one could conclude that the resin was not completely cured in the low-power experiment in the top-left of Figure 6.27.

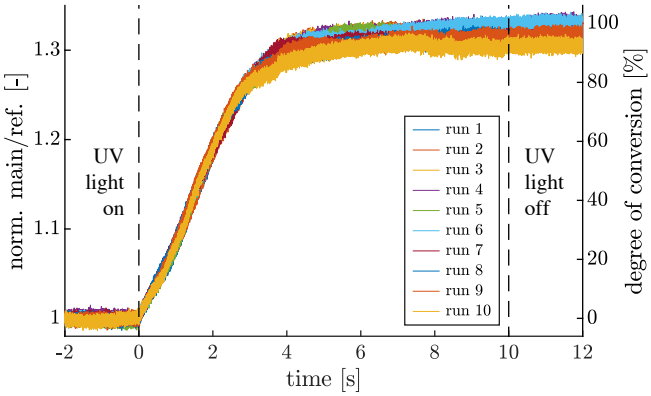

Figure 6.29: Ten replications of the high-power UV curing experiment with the final NIR photometer layout and LCD-T resin. The results give an indication of the measuring instrument's repeatability.

Although the NIR photometer showed well-reproducible results for the LCD-T material, not all low- and high-power experiments were successful. During some measurements, both the main and reference signal showed a sudden drop in intensity, as seen in Figure 6.30 (a) which was obtained with FunToDo resin. After three seconds the intensity suddenly drops and shows an oscillation, perhaps as a result of optical interference. Such sudden drops were visible in nearly all "failed" experiments, but the subsequent behaviour differed from oscillations to smoother behaviour as if the intensity had just experienced a sudden vertical offset.

A visual inspection of the cured sample gave a good indication of whether the experiment was successful or not, since optical impurities were visible in nearly any case in which the measurement results showed remarkable artefacts. Figure 6.30 (b) shows a photograph of a case of sample detachment from the quartz glass plates, which happened quite often at high UV powers. In some of these cases, it was observed that a small amount of uncured resin was still present between bottom quartz plate and the spacer. This small amount of uncured resin may have contributed to the failure mechanism, but it may as well be a result of the combined

effects of chemical shrinkage and thermal expansion due to the exothermic reaction heat and absorption of UV radiation.

Figure 6.30 (c) shows two other failure mechanisms, i.e., sample cracking and air bubble entrapment. Although sample cracking only occurred in FunToDo resin samples, the entrapment of air bubbles occurred quite often as a result of the pipette deposition method. It is detrimental if the air bubble is located in the measurement path, but otherwise it is less of a problem except for the potential influence it has on diffusion of and inhibition by oxygen. Interestingly, after an experiment had finished, it was easier to separate the quartz plates from one another with a razor blade if the samples were fully (over)cured, than if they were cured just beyond the gel point. Since the photopolymer layer acts as an adhesive bond between the quartz plates, it was difficult to separate them in the latter case and often led to a fractured quartz plate. In the former case, especially the FunToDo resin sample became brittle once fully (over)cured. These observations confirm the need for a photopolymer characterization device, as the AM machine operator wants to know when the photopolymer has been underexposed, overexposed or optimally exposed in terms of resulting mechanical properties.

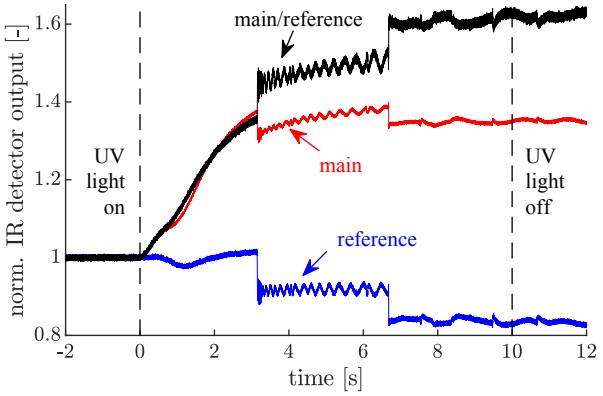

(a) measurement artefacts in case of mechanical sample failure

(b) detached sample

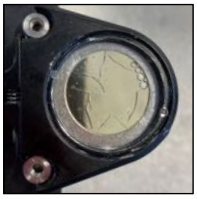

(c) cracked sample & entrapped air bubbles

Figure 6.30: Mechanical sample failures that have occurred with the highly-reactive FunToDo Industrial Blend. The results in (a) show several measurement artefacts of a high-power experiment. Common to nearly all failed experiments is a sudden drop in intensity as seen near $t = 3$ [s]. The photograph in (b) shows a failure mechanism where the sample has become detached from the quartz plates and the photograph in (c) shows a sample that both has cracks and entrapped air bubbles.

6.6 Discussion & conclusion

This work describes the design and realization of a custom-made NIR photometer for acrylic photopolymers. The photometer was realized to ultimately test the generally valid hypothesis [36] that photometers provide a simpler, cost-effective alternative to general-purpose spectrophotometers. To this end, the experimental results in Section 6.5 successfully demonstrate that the NIR photometer functions properly after implementing several design changes. These design changes were required to solve several issues that were primarily related to the sampling optics.

Nevertheless, the results of this work can be considered to provide a proof of concept for a prototype instrument capable of repeatably measuring the degree of photopolymer conversion in situ and in real time at a maximum sampling rate of 20 [kHz], limited by the control computer. In light of the long-term goals, the prototype provides evidence that NIR photometry is a feasible route towards future in-line metrology applications in photopolymer-based AM machines. Still, several development steps have to be taken before the present NIR photometer can be used as a photopolymer characterization device to be implemented into or installed next to the machine as envisioned in Figure 6.3.

Design changes

First of all, the design changes should be reconsidered and the cause of the beam divergence issue should be further investigated. Improving the UV light field uniformity has the highest priority, followed by decreasing the sample thickness. To decrease the sample thickness back to the AM-relevant layer thicknesses of 0.1 [mm] or less, the IR measurement beam diameter has to be reduced in order to prevent reintroduction of interference, e.g., by using a beam reducer [70]. The 45 [°] incidence angle is of no concern to the instrument's conceptual design, except for a design modification in the custom-made sample holder.

Moreover, the sample cell and the preparation and cleaning procedure should be reassessed such that air bubble entrapments, detachments, and cleaning effort can be reduced, possibly through disposable sample cells. A pipette tip comes to mind that has a flat part, such that the already disposable tip becomes the sample cell itself. It is already common to use injection-molded acrylic cuvettes as disposable samples cells in spectroscopy, so it may prove worthwhile to injection mold a cuvette that has a resin inlet tip on one side and an air outlet port on the other for use with a suction device such as a pipette. A disposable sample cell does not have to be cleaned, leading to a reduction of waste, processing time, and variability in layer thickness. Moreover, it is expected that the sample diameter can be significantly reduced, since it is currently much larger than necessary; a single voxel measuring approximately $50 \times 50 \times 50$ [μm^3] is expected to suffice.

Unfortunately, the use of the integrating sphere severely reduced the photometer's signal level and the resulting signal-to-noise ratio, despite the elimination of modal noise from the MM fibers. A considerable amount of light may be lost due

to absorption in the lens tubes that house the detectors and bandpass filters, the input port to the integrating sphere, and the sphere's walls. Other options may be conceived to collect the divergent light and guide it to the InGaAs detectors. If the integrating sphere is retained, either the wavelength separation performance of the bandpass filters should be improved to reduce the crosstalk, or its consistency should be established.

Reference wavelength selection
Secondly, the choice of reference wavelength should be further investigated. Promising results were already obtained in the reference wavelength selection approach where rare-earth metals were added to the photopolymer as a reference standard. The solubility of the rare-earth metals in the polymer matrix may be improved upon further development. Alternatively, a suitable reference peak in the NIR range may be selected through coupled MIR and NIR spectroscopy, e.g., by looking for a consistency between the absorbance of the carbonyl peak at 1720 [cm^{-1}] and the absorbance of peaks in the NIR range.

Interestingly, the measurement results show rather minor changes in the reference signal except for the crosstalk for the specific materials and conditions used; such a near-constant reference signal was already observed by Bach for some resins [51]. Thus, one may draw the conclusion that the reference signal is not required for some materials, which is beneficial to the instrument's cost and complexity. However, if one would want to resolve the degree of conversion in space by performing point IR beam or sample scanning, it may be advisable to maintain the reference signal.

Validation
Thirdly, the measurement results obtained from the NIR photometer have to be validated with respect to NIR spectrophotometer measurements to provide quantitative evidence that both instruments measure the same degree of conversion. The NIR photometry measuring principle was already validated by Bach [51] for a transflection sampling configuration by comparing NIR photometer measurements to NIR spectrophotometer and FTIR-ATR measurements in the MIR range. However, Bach reported [51] a conversion resolution of merely ± 20 [%] to ± 10 [%] so the results had a relatively high uncertainty. Although Bach's transflection configuration has the supposed advantage of being air-coupled at the top side as seen in Figure 6.31, it also has the disadvantage of having a material-dependent probing volume. That is, the so-called information depth depends on the absorption characteristics of the resin as per the Beer-Lambert law [50,51]. An accurate quantitative validation of the present NIR transmission photometer requires a comparison to NIR transmission spectrometer measurements. In this validation, special attention should be paid to the sampling method to ensure that both instruments probe the same volume. Ideally, both instruments would use the same probe.

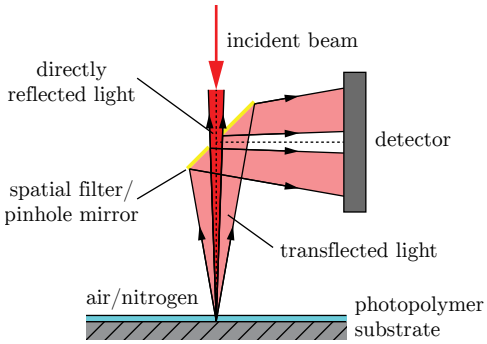

Figure 6.31: Transflection photometer concept developed by Bach [51].

System-level requirements and achieved performance
Fourthly, the achieved measurement performance needs to be established and evaluated against the original system-level requirements. Owing to a lack of time, these invaluable verification and validation activities [23] could not be performed anymore within the project. After optimizing the instrument's settings and validating with an NIR spectrometer, its performance should be identified in terms of generic sensor characteristics such as accuracy and precision, resolution, measurement rate and signal-to-noise ratio [28], as well as specific aspects to the on-line cure sensor application [29]. Moreover, a wider range of acrylic materials should be tested, including dyed resins, opaque resins, and resins with (ceramic) fillers. The signal-to-noise ratio is expected to deteriorate for these opaque resins. Once established, the performance of the NIR photometer can be compared to other measuring instruments for the degree of conversion [19], although this comparison may be complicated by a lack of information on their performance.

Measuring principle and conceptual instrument design
Fifthly, the instrument's measuring principle and conceptual design should be reassessed. To facilitate measurement and actuation from the same side, a reflection or transflection measurement configuration may be investigated. Bach already investigated a transflection concept [51] in which the IR beam is normally incident to the photopolymer layer and whose Lambertian reflectance is measured with a pinhole mirror, see Figure 6.31. As pointed out by Bach, the reflections at the top and the bottom of the photopolymer layer cannot be discriminated in this particular configuration. However, the photopolymer's top-surface reflection can be well discriminated from the bottom-surface reflection in the 45 [°] incidence configuration in the present work, as demonstrated in Figure 6.24.

Therefore, an interesting future direction is to investigate a transflection concept using a non-normally incident measurement beam. After establishing its performance with a highly-reflective metal substrate and with and without a covering glass, the

question is whether the signal intensity remains sufficiently high with a poorly-reflective cured-photopolymer substrate, which emulates the conditions during layer-based AM. If the results are positive, the next question is whether it also works with the films typically used to reduce separation forces in constrained-surface, bottom-up vat photopolymerization systems [118]. Alternatively, an ATR configuration [61] can be investigated where the resin is illuminated through the ATR crystal [119]. If successful, NIR photometry can be successfully applied for in-situ process monitoring and real-time closed-loop control [18] inside actual vat photopolymerization machines. Moreover, sample preparation functionality could be fulfilled by the recoating system, saving time and reducing human error. Otherwise, an automatic sample loader may offer a solution.

Another interesting direction is to further investigate the interferometric measuring principle, embracing the interference phenomenon rather than eliminating it. To the author's knowledge, no reports have been published of interferometric cure monitoring with multiple photopolymer layers, although several works have been published on single-layer UV cure monitoring [40, 44, 110, 111]. Since the interferometric signals in Figure 6.19 look rather clean, interferometry might also work in multi-layer stacks. However, one may expect that the amplitude of the interference contribution I_a in equation (6.9) reduces in the multi-layer case, as the reflectance is lower due to the small refractive index difference between cured and uncured photopolymer in comparison to (un)cured photopolymer and quartz glass. It is reasonable to think that the higher the interference amplitude I_a, the better the phase can be determined from the signal. Nevertheless, the same development steps can be taken as outlined above for the NIR photometer transflection concept.

Coupling cure kinetics to mechanical properties

Sixthly, a relationship has to be established between the layer-scale degree of conversion, which in the future may be measured inside the AM machine by an NIR photometer, and the part-scale material properties [33, 120–122], which are less easily measured inside the AM machine. The NIR photometer may already be used to determine the polymerization kinetics and the characteristic time scale. If one has no information about the required exposure for a given acrylic photopolymer, the NIR photometer may be used to determine at which time the degree of conversion has approximately reached the gel point, i.e., the transition from the liquid to the solid state [16]. To this end, the photopolymer has to be fully cured while measuring the transmitted NIR power. Subsequently, the normalized degree of conversion can be obtained from (6.5). This approach either relies on knowledge of the conversion at the gel point, which may vary at least between 12 and 60 [%] from resin to resin [123], or on a certain threshold for the degree of conversion, e.g., 80 [%] of the final conversion level. Otherwise the gel point might be determined from the NIR photometer's reference signal if a shrinkage effect is present, as the gel point is said to correlate well with the onset of shrinkage [123]. In either case, the resin has to be cured beyond the gel point to build up mechanical strength [16].

In-situ sensor-based alternatives for working curve approaches
Finally, a strategy has to be devised to determine the build settings for the vat photopolymerization-based AM process. Although the NIR photometer may be used to determine the critical exposure E_c at the gel point [16] as outlined above, the UV penetration depth D_p also needs to be determined in order to substitute the current ex-situ caliper-based working curve approaches with an in-situ sensor-based approach. To this end, the UV transmittance could be measured in a similar way as the NIR photometer measures the NIR transmittance by comparing the transmittance of an empty sample cell to a filled one. However, this method only gives one measurement point on the exponentially decaying transmittance versus path length $T(l)$ curve as per the Beer-Lambert law (6.1) and is prone to errors due to differences in reflectances with and without a sample. Although measuring the time-resolved UV-VIS spectrum simultaneous to the NIR spectrum [124] would give even more information, it may be too costly or complex.

Therefore, it may be interesting to use a staircase- or wedge-shaped sample that has different layer thicknesses to provide several path lengths l. In one embodiment, a dual-channel photometer can be used (one for NIR and one for UV) whose measurement beams are scanned over the different stairsteps and whose signals are multiplexed. In another embodiment, both measurement beams can be split into multiple beams and detected by multiple channels, one for each stairstep. To the best of the author's knowledge, such a concept for depth-resolved, simultaneous NIR and UV transmission photometry has not been reported yet.

References

[1] D. Fornea and H. Van Laere, "Living tomorrow. 3D printing — a tool to empower the European economy. Opinion of the European Economic and Social Committee CCMI/131," *Official Journal of the European Union*, pp. C 332/36 – C 332/44, Oct. 2015. 2015/C 332/05.

[2] L. M. Galantucci, M. G. Guerra, M. Dassisti, and F. Lavecchia, "Additive Manufacturing: New Trends in the 4th Industrial Revolution," in *Proceedings of the 4th International Conference on the Industry 4.0 Model for Advanced Manufacturing* (L. Monostori, V. D. Majstorovic, S. J. Hu, and D. Djurdjanovic, eds.), Lecture Notes in Mechanical Engineering, pp. 153–169, Springer International Publishing, 2019.

[3] W. Gao, Y. Zhang, D. Ramanujan, K. Ramani, Y. Chen, C. B. Williams, C. C. Wang, Y. C. Shin, S. Zhang, and P. D. Zavattieri, "The status, challenges, and future of additive manufacturing in engineering," *Computer-Aided Design*, vol. 69, pp. 65–89, Dec. 2015.

[4] I. Gibson, D. Rosen, and B. Stucker, *Additive Manufacturing Technologies*. New York, NY: Springer, 2nd ed., 2015.

[5] Y. Huang, M. C. Leu, J. Mazumder, and A. Donmez, "Additive manufacturing: Current state, future potential, gaps and needs, and recommendations," *Journal of Manufacturing Science and Engineering*, vol. 137, no. 1, pp. 1–10, 2015.

[6] J. Pellegrino, T. Makila, S. McQueen, and E. Taylor, "Measurement science roadmap for polymer-based additive manufacturing," Tech. Rep. NIST AMS 100-5, National Institute of Standards and Technology, Gaithersburg, MD, Dec. 2016.

[7] B. A. Ogunnaike and W. H. Ray, *Process dynamics, modeling, and control*. Topics in chemical engineering, New York: Oxford University Press, 1st ed., 1994.

[8] D. Hardt, "Modeling and control of manufacturing processes: Getting more involved," *Journal of Dynamic Systems, Measurement, and Control*, vol. 115, pp. 291–300, June 1993.

[9] M. Mani, B. Lane, A. Donmez, S. Feng, S. Moylan, and R. Fesperman, "Measurement Science Needs for Real-time Control of Additive Manufacturing Powder Bed Fusion Processes," Tech. Rep. NIST IR 8036, National Institute of Standards and Technology, Feb. 2015.

[10] P. Charalampous, I. Kostavelis, and D. Tzovaras, "Non-destructive quality control methods in additive manufacturing: a survey," *Rapid Prototyping Journal*, vol. 26, pp. 777–790, Jan. 2020. Publisher: Emerald Publishing Limited.

[11] T. Hafkamp, G. van Baars, B. de Jager, and P. Etman, "A Classification Scheme for AM Control Strategies: the AM V-model," in *Proceedings of the 2018 ASPE and euspen Summer Topical Meeting - Advancing Precision in Additive Manufacturing*, vol. 69, pp. 161–166, 2018.

[12] A. M. Yebi, *Model-based control of UV curing processes with application to additive manufacturing*. PhD thesis, Clemson University, Clemson, SC, 2015.

[13] S. D. Beyene, *Optimal Control of UV-Induced Curing Processes for Layer-by-Layer Manufacturing of Composites*. PhD thesis, Clemson University, Clemson, SC, 2019.

[14] X. Zhao and D. W. Rosen, "An implementation of real-time feedback control of cured part height in Exposure Controlled Projection Lithography with in-situ interferometric measurement feedback," *Additive Manufacturing*, vol. 23, pp. 253–263, Oct. 2018.

[15] E. B. Türeyen, Y. Karpat, and M. Çakmakcı, "Development of an iterative learning controller for polymer based micro-stereolithography prototyping systems," in *2016 American Control Conference (ACC)*, pp. 852–857, IEEE, 2016.

[16] P. Jacobs, *Rapid Prototyping & Manufacturing: Fundamentals of Stereolithography*. Dearborn, MI: Society of Manufacturing Engineers, 1st ed., 1992.

[17] J. Bennett, "Measuring UV curing parameters of commercial photopolymers used in additive manufacturing," *Additive Manufacturing*, vol. 18, pp. 203–212, Dec. 2017.

[18] T. Hafkamp, G. van Baars, B. de Jager, and P. Etman, "Real-time feedback controlled conversion in vat photopolymerization of ceramics: A proof of principle," *Additive Manufacturing*, vol. 30, pp. 1–11, 2019.

[19] T. Hafkamp, G. van Baars, B. de Jager, and P. Etman, "A feasibility study on process monitoring and control in vat photopolymerization of ceramics," *Mechatronics*, vol. 56, pp. 220–241, Dec. 2018.

[20] K. Barton, D. Bristow, D. Hoelzle, and S. Mishra, "Mechatronics advances for the next generation of AM process control," *Mechatronics*, vol. 64, pp. 1–5, Dec. 2019.

[21] Bureau International des Poids et Mesures (BIPM), *International vocabulary of metrology – Basic and general concepts and associated terms (VIM)*. 3rd ed., 2012. JCGM 200:2012.

[22] B. S. Blanchard and J. E. Byler, *System Engineering Management*. Hoboken, NJ: John Wiley & Sons, Ltd, 5th ed., 2016.

[23] A. Kossiakoff, ed., *Systems engineering: principles and practice*. No. 67 in Wiley series in systems engineering and management, Hoboken, NJ: Wiley-Interscience, 2nd ed., 2011.

[24] R. K. Leach and S. T. Smith, eds., *Basics of precision engineering*. Boca Raton, FL: CRC Press Taylor & Francis Group, 1st ed., 2018.

[25] W. F. Reed and A. M. Alb, eds., *Monitoring polymerization reactions: from fundamentals to applications*. Hoboken, NJ: John Wiley & Sons, Inc, 1st ed., 2014.

[26] D. E. Seborg, T. F. Edgar, D. A. Mellichamp, and F. Doyle, *Process dynamics and control*. Hoboken, N.J: John Wiley & Sons, Inc, 3rd ed., 2011.

[27] J. Bennett, "Measuring UV curing parameters of commercial photopolymers used in additive manufacturing," *Additive Manufacturing*, vol. 18, pp. 203–212, Dec. 2017.

[28] J. Fraden, *Handbook of modern sensors: physics, designs, and applications*. Cham Heidelberg New York Dordrecht London: Springer, 5th ed., 2016.

[29] W.-D. Hergeth, "On-line Monitoring of Polymerization and Cure," *Sensors Update*, vol. 5, no. 1, pp. 191–242, 1999.

[30] S. K. Everton, M. Hirsch, P. Stravroulakis, R. K. Leach, and A. T. Clare, "Review of in-situ process monitoring and in-situ metrology for metal additive manufacturing," *Materials & Design*, vol. 95, pp. 431–445, Apr. 2016.

[31] T. G. Spears and S. A. Gold, "In-process sensing in selective laser melting (SLM) additive manufacturing," *Integrating Materials and Manufacturing Innovation*, vol. 5, pp. 1–25, Dec. 2016.

[32] H. Ye, A. Venketeswaran, S. Das, and C. Zhou, "Investigation of separation force for constrained-surface stereolithography process from mechanics perspective," *Rapid Prototyping Journal*, vol. 23, pp. 696–710, June 2017.

[33] C. I. Fiedler-Higgins, L. M. Cox, F. W. DelRio, and J. P. Killgore, "Monitoring Fast, Voxel-Scale Cure Kinetics via Sample-Coupled-Resonance Photorheology," *Small Methods*, vol. 3, no. 2, pp. 1–6, 2019.

[34] C. B. Williams, F. Mistree, and D. W. Rosen, "A functional classification framework for the conceptual design of additive manufacturing technologies," *Journal of Mechanical Design*, vol. 133, no. 12, pp. 1–11, 2011.

[35] P. M. Lambert, E. A. Campaigne III, and C. B. Williams, "Design Considerations for Mask Projection Microstereolithography Systems," in *Proceedings of the Solid Freeform Fabrication Symposium*, pp. 111–130, 2013.

[36] D. A. Skoog, F. J. Holler, and S. R. Crouch, *Principles of instrumental analysis*. Boston, MA: Cengage Learning, 7th ed., 2017.

[37] G. E. Fonseca, M. A. Dubé, and A. Penlidis, "A Critical Overview of Sensors for Monitoring Polymerizations," *Macromolecular Reaction Engineering*, vol. 3, pp. 327–373, Sept. 2009.

[38] R. Schwalm, *UV coatings basics, recent developments and new applications*. Amsterdam; London: Elsevier, 1st ed., 2006.

[39] T. Yoshizawa, *Handbook of Optical Metrology*. Boca Raton, FL: CRC Press Taylor & Francis Group, 2nd ed., 2015.

[40] J. de Boer, R. J. Visser, and G. P. Melis, "Time-resolved determination of volume shrinkage and refractive index change of thin polymer films during photopolymerization," *Polymer*, vol. 33, no. 6, pp. 1123–1126, 1992.

[41] T. Scherzer and U. Decker, "Real-time FTIR–ATR spectroscopy to study the kinetics of ultrafast photopolymerization reactions induced by monochromatic UV light," *Vibrational Spectroscopy*, vol. 19, no. 2, pp. 385–398, 1999.

[42] T. Craeghs, F. Bechmann, S. Berumen, and J.-P. Kruth, "Feedback control of Layerwise Laser Melting using optical sensors," *Physics Procedia*, vol. 5, pp. 505–514, 2010.

[43] J. E. Puskas, T. E. Long, R. F. Storey, S. Shaikh, and C. L. Simmons, eds., *In Situ Spectroscopy of Monomer and Polymer Synthesis*. Boston, MA: Springer US, 1st ed., 2003.

[44] X. Zhao, *Process Measurement and Control for Exposure Controlled Projection Lithography*. PhD thesis, Georgia Institute of Technology, Atlanta, GA, 2017.

[45] J. L. Koenig, *Spectroscopy of polymers*. New York, NY: Elsevier, 1st ed., 1999.

[46] J. Haus, *Optical Sensors: Basics and Applications*. Weinheim: WILEY-VCH Verlag GmbH & Co. KGaA, 1st ed., 2010.

[47] H. W. Siesler, Y. Ozaki, S. Kawata, and H. M. Heise, *Near-Infrared Spectroscopy: Principles, Instruments, Applications*. Weinheim: WILEY-VCH Verlag GmbH, 1st ed., 2002.

[48] X. Fernàndez-Francos, S. G. Kazarian, X. Ramis, and n. Serra, "Simultaneous Monitoring of Curing Shrinkage and Degree of Cure of Thermosets by Attenuated Total Reflection Fourier Transform Infrared (ATR FT-IR) Spectroscopy," *Applied Spectroscopy*, vol. 67, pp. 1427–1436, Dec. 2013.

[49] H. Danigel, "Fiber optical process measurement technique," *Optical Engineering*, vol. 34, pp. 2665–2669, Sept. 1995.

[50] M. Bach and W. Heering, "NIR-laser based detection of the photopolymerization state of acrylate coatings suitable for in situ measurements," *Journal of Applied Polymer Science*, vol. 124, no. 4, pp. 3494–3500, 2012.

[51] M. Bach, *Near infrared laser sensor system for in-line detection of conversion in UV-cured polymer coatings*. PhD thesis, KIT Scientific Publishing, Karlsruhe, Baden, 2012.

[52] R. M. Schmidt, G. Schitter, A. Rankers, and J. v. Eijk, *The design of high performance mechatronics: high-tech functionality by multidisciplinary system integration*. Amsterdam: Delft University Press, 1st ed., 2011.

[53] T. Noergaard, *Embedded systems architecture: a comprehensive guide for engineers and programmers*. Embedded technology series, Amsterdam; Boston: Elsevier/Newnes, 1st ed., 2005.

[54] U. Utzinger and R. R. Richards-Kortum, "Fiber optic probes for biomedical optical spectroscopy," *Journal of Biomedical Optics*, vol. 8, no. 1, pp. 121–147, 2003.

[55] E. Udd, ed., *Fiber optic sensors: an introduction for engineers and scientists*. Wiley series in pure and applied optics, Hoboken, NJ: Wiley-Interscience, 2nd ed., 2006.

[56] R. E. Fischer, B. Tadic-Galeb, and P. R. Yoder, *Optical system design*. New York: McGraw-Hill, 2nd ed., 2008.

[57] S. C. Ligon, R. Liska, J. Stampfl, M. Gurr, and R. Mülhaupt, "Polymers for 3D Printing and Customized Additive Manufacturing," *Chemical Reviews*, vol. 117, pp. 10212–10290, Aug. 2017.

[58] G. G. Odian, *Principles of polymerization*. Hoboken, N.J: Wiley-Interscience, 4th ed., 2004.

[59] G. Socrates, *Infrared and Raman characteristic group frequencies: tables and charts*. Chichester; New York: Wiley, 3rd ed., 2001.

[60] J. Stansbury and S. Dickens, "Determination of double bond conversion in dental resins by near infrared spectroscopy," *Dental Materials*, vol. 17, pp. 71–79, Jan. 2001.

[61] H. A. Boonen, J. A. Koskamp, W. Theiss, P. D. Iedema, and R. X. Willemse, "Simultaneous Real-Time Analysis of Bulk and Bottom Cure of Ultraviolet-Curable Inks Using Fourier Transform Infrared Spectroscopy," *Applied Spectroscopy*, vol. 71, pp. 2699–2706, July 2017.

[62] J. Workman Jr. and L. Weyer, *Practical Guide and Spectral Atlas for Interpretive Near-Infrared Spectroscopy*. Boca Raton, FL: CRC Press Taylor & Francis Group, 2nd ed., 2012.

[63] O. Daikos, K. Heymann, and T. Scherzer, "Development of a PLS approach for the determination of the conversion in UV-cured white-pigmented coatings by NIR chemical imaging and its transfer to other substrates," *Progress in Organic Coatings*, vol. 132, pp. 116–124, July 2019.

[64] T. Scherzer, R. Mehnert, and H. D. Lucht, "Process Control of UV and EB Curing of Acrylates by In-line NIR Reflection Spectroscopy," in *RadTech e|5 2004 Technical Proceedings*, RadTech USA, 2004.

[65] T. Scherzer, S. Müller, R. Mehnert, A. Volland, and H. Lucht, "In-line monitoring of the conversion in photopolymerized acrylate coatings on polymer foils using NIR spectroscopy," *Polymer*, vol. 46, pp. 7072–7081, Aug. 2005.

[66] O. Daikos, K. Heymann, and T. Scherzer, "Monitoring of thickness and conversion of thick pigmented UV-cured coatings by NIR hyperspectral imaging," *Progress in Organic Coatings*, vol. 125, pp. 8–14, Dec. 2018.

[67] L. G. Weyer, "Near-Infrared Spectroscopy of Organic Substances," *Applied Spectroscopy Reviews*, vol. 21, pp. 1–43, Mar. 1985.

[68] T. G. Gerasimov and D. L. Snavely, "Vibrational Overtone Spectroscopy of Ethylene Glycol Diacrylate and Ethylene Glycol Dimethacrylate, Monomer and Polymer," *Applied Spectroscopy*, vol. 56, pp. 212–216, Feb. 2002.

[69] G. P. Agrawal, *Fiber-optic communication systems*. New York, NY: John Wiley & Sons, Inc., 2nd ed., 2002.

[70] H. Sun, *A Practical Guide to Handling Laser Diode Beams*. SpringerBriefs in Physics, Dordrecht: Springer Netherlands, 1st ed., 2015.

[71] D. A. Burns and E. W. Ciurczak, *Handbook of Near Infrared Analysis*. No. 35 in Practical Spectroscopy Series, Boca Raton, FL: CRC Press, 3 ed., Sept. 2007.

[72] T. Hafkamp, G. van Baars, B. de Jager, and P. Etman, "A Trade-off Analysis of Recoating Methods for Vat Photopolymerization of Ceramics," in *Proceedings Solid Freeform Fabrication Symposium*, pp. 687–711, 2017.

[73] T. Scherzer, S. Mueller, R. Mehnert, A. Volland, and H. Lucht, "Process control in UV curing: In-line monitoring of the acrylate conversion by near-infrared spectroscopy," *JCT CoatingsTech*, vol. 3, pp. 30–37, Aug. 2006.

[74] K. C. Cole, "Vibrational Spectroscopy of Polymer Composites," in *Handbook of Vibrational Spectroscopy*, vol. 3, Wiley Online Library, 2002.

[75] J. Coates, "Classical Methods of Quantitative Analysis," in *Handbook of Vibrational Spectroscopy*, vol. 3, Wiley Online Library, 2002.

[76] S. Agarwal, *In Situ Monitoring of UV-Curing Kinetics of Acrylate Coatings by Combined Ultrasound Reflectometry and Near-Infrared Spectroscopy*. PhD thesis, TU Darmstadt, Darmstadt, 2011.

[77] F. A. Rueggeberg, "Determination of resin cure using infrared analysis without an internal standard," *Dental Materials*, vol. 10, pp. 282–286, July 1994.

[78] H. Fong, "Effects of water contents and postcuring conditions on Bis-GMA/TEGDMA dental restorative composite resins," *Journal of Applied Polymer Science*, vol. 94, no. 2, pp. 492–502, 2004.

[79] A. Oueslati, S. Kamoun, F. Hlel, M. Gargouri, and A. Fort, "Real-time FTIR monitoring of the photopolymerization of a pentaerythritol triacrylate-based resin," *Akademeia*, vol. 1, no. 1, pp. 1–6, 2011.

[80] R. M. Guerra, I. Durán, and P. Ortiz, "FTIR monomer conversion analysis of UDMA-based dental resins," *Journal of Oral Rehabilitation*, vol. 23, no. 9, pp. 632–637, 1996.

[81] S. J. Choquette, D. L. Duewer, L. M. Hanssen, and E. A. Early, "Standard Reference Material 2036 Near-Infrared Reflection Wavelength Standard," *Applied Spectroscopy*, vol. 59, pp. 496–504, Apr. 2005.

[82] C. Burgess and J. Hammond, "Wavelength Standards for the Near-Infrared Spectral Region," *Spectroscopy*, vol. 22, no. 4, pp. 40–48, 2007.

[83] I. Y. Denisyuk, Y. . Burunkova, N. O. Sobeshchuk, V. V. Zakharov, and A. V. Veniaminov, "Synthesizing erbium and ytterbium oxide nanoparticles and obtaining luminescent polymeric composites based on them," *Journal of Optical Technology*, vol. 81, p. 681, Nov. 2014.

[84] P. S. May, A. Baride, M. Y. Hossan, and M. Berry, "Measuring the internal quantum yield of upconversion luminescence for ytterbium-sensitized upconversion phosphors using the ytterbium(iii) emission as an internal standard," *Nanoscale*, vol. 10, no. 36, pp. 17212–17226, 2018.

[85] S. Stueflotten, T. Christenser, S. Iversen, J. O. Hellvik, K. Almas, T. Wien, and A. Graav, "An Infrared Fibre Optic Gas Detection System," in *Conference proceedings, OFS '84: 2nd International Conference on Optical Fiber Sensors* (R. T. Kersten and R. Kist, eds.), (Stuttgart, Germany), pp. 87–90, Nov. 1984.

[86] H. Gross, ed., *Handbook of Optical Systems. Volume 5: Metrology of Optical Components and Systems*. No. ed. by Herbert Gross; Volume 5 in Handbook of optical systems, Weinheim: Wiley-VCH Verlag GmbH & Co. KGaA., 1st ed., 2005.

[87] S. Gateva, *Photodetectors*. Rijeka, Croatia: InTechOpen, 1st ed., 2012.

[88] B. G. Lipták and K. Venczel, eds., *Instrument and automation engineers' handbook Volume I*. Research Triangle Park, NC: Boca Raton: International Society of Automation; CRC Press/Taylor & Francis Group, 5th ed., 2017.

[89] R. M. Hardesty, "Development of sensitometric techniques for the characterization of stereolithographic resins," Master's thesis, Rochester Institute of Technology, Rochester, NY, July 1994.

[90] C. W. Robertson, "Liquid photometer using surface tension to contain sample," U.S. Patent US6628382B2, Sep. 30, 2003.

[91] P. Desjardins, J. B. Hansen, and M. Allen, "Microvolume Spectrophotometric and Fluorometric Determination of Protein Concentration," *Current Protocols in Protein Science*, vol. 55, no. 1, pp. 3.10.1–3.10.16, 2009.

[92] C. W. Robertson, "Liquid photometer using surface tension to contain sample," Sept. 2003. US Patent US6628382B2.

[93] Y. Lu, *A Study on Liquid Bridge Based Microstereolithography (LBMSL) System*. PhD thesis, University of Akron, Akron, OH, 2016.

[94] K.-H. Jo, S.-H. Lee, and J.-W. Choi, "Liquid Bridge Stereolithography: A Proof of Concept," *International Journal of Precision Engineering and Manufacturing*, vol. 19, pp. 1253–1259, Aug. 2018.

[95] J. Wu, Z. Zhao, C. M. Hamel, X. Mu, X. Kuang, Z. Guo, and H. J. Qi, "Evolution of material properties during free radical photopolymerization," *Journal of the Mechanics and Physics of Solids*, vol. 112, pp. 25–49, Mar. 2018.

[96] E. Hecht, *Optics*. Boston: Pearson Education, Inc, 5th ed., 2017.

[97] D. L. Blanding, *Exact Constraint Machine Design Using Kinematic Principles*. New York, NY: The American Society of Mechanical Engineers, 1st ed., 1999.

[98] M. L. Culpepper, *Design and Application of Compliant Quasi-Kinematic Couplings*. PhD thesis, Massachusetts Institute of Technology, Cambridge, MA, Jan. 2000.

[99] H. Soemers, *Design Principles for Precision Mechanisms*. Enschede, NL: T-Point Print, 1st ed., 2010.

[100] J. G. Graeme, *Photodiode amplifiers: op amp solutions*. New York, NY: McGraw-Hill, 1st ed., 1996.

[101] P. C. D. Hobbs, *Building electro-optical systems: making it all work*. Wiley series in pure and applied optics, New York: Wiley, 2nd ed., 2009.

[102] A. Cusano, G. Breglio, M. Giordano, A. Calabrò, A. Cutolo, and L. Nicolais, "An optoelectronic sensor for cure monitoring in thermoset-based composites," *Sensors and Actuators A: Physical*, vol. 84, pp. 270–275, Sept. 2000.

[103] A. Maffezzoli and R. Terzi, "Effect of irradiation intensity on the isothermal photopolymerization kinetics of acrylic resins for stereolithography," *Thermochimica Acta*, vol. 321, no. 1, pp. 111–121, 1998.

[104] H. P. Bloch and F. K. Geitner, *Machinery failure analysis and troubleshooting*, vol. 2 of *Practical machinery management for process plants*. Oxford: Butterworth-Heinemann Elsevier, 4th ed., 2012.

[105] J. W. Goodman, *Speckle Phenomena in Optics: Theory and Applications*. Greenwood Village, CO: Roberts and Company Publishers, 1st ed., 2010.

[106] Thorlabs, "Engineered Diffusers ™," 2020. Accessed on: Jun. 4 2020. [Online]. Available: https://www.thorlabs.com/newgrouppage9.cfm?objectgroup_id=1660.

[107] A. S. Jariwala, *Modeling And Process Planning For Exposure Controlled Projection Lithography*. PhD thesis, Georgia Institute of Technology, Atlanta, GA, 2013.

[108] F. Shevlin, "Phase randomization for spatiotemporal averaging of unwanted interference effects arising from coherence," *Applied Optics*, vol. 57, p. E6, Aug. 2018.

[109] X. Zhao, "Process Planning for thick-film mask projection micro stereolithography," Master's thesis, Georgia Institute of Technology, Atlanta, GA, 2009.

[110] A. Jariwala, H. Jones, A. Kwatra, and D. W. Rosen, "Process Planning Method for Exposure Controlled Projection Lithography," in *Proc. 24th Solid Free. Fabcrication Symp*, pp. 95–110, 2013.

[111] I. Kostylev, D. Labrie, and R. B. T. Price, "Time-resolved 2D shrinkage field of dental resins using laser interferometry," *Applied Optics*, vol. 54, pp. 1852–1860, Mar. 2015.

[112] F. Aloui, L. Lecamp, P. Lebaudy, and F. Burel, "Refractive index evolution of various commercial acrylic resins during photopolymerization," *Express Polymer Letters*, vol. 12, no. 11, pp. 966–971, 2018.

[113] G. Owen, "Suppression of interference effects in spectroscopy using an integrating sphere," *Review of Scientific Instruments*, vol. 68, pp. 1369–1371, Mar. 1997. Publisher: American Institute of Physics.

[114] N. L. Alpert, W. E. Keiser, and H. A. Szymanski, *IR - Theory and Practice of Infrared Spectroscopy*. Boston, MA: Springer US, 1970.

[115] C. Ye, *Three-dimensional Gradient Index Optics Fabricated in Diffusive Photopolymers*. PhD thesis, University of Colorado, Boulder, CA, 2012.

[116] C. Gomez-Reino, M. V. Perez, and C. Bao, *Gradient-Index Optics*. Berlin, Heidelberg: Springer Berlin Heidelberg, 1st ed., 2002.

[117] Y. Lin and J. W. Stansbury, "Kinetics studies of hybrid structure formation by controlled photopolymerization," *Polymer*, vol. 44, pp. 4781–4789, Aug. 2003.

[118] Y. Pan, H. He, J. Xu, and A. Feinerman, "Study of separation force in constrained surface projection stereolithography," *Rapid Prototyping Journal*, vol. 23, no. 2, pp. 353–361, 2017.

[119] M. Michihata, K. Takamasu, and S. Takahashi, "Proposal of In-process Measurement for Micro-stereolithography Using Surface Plasmon Resonance," *Physics Procedia*, vol. 83, pp. 964–970, 2016.

[120] Y. Yang, L. Li, and J. Zhao, "Mechanical property modeling of photosensitive liquid resin in stereolithography additive manufacturing: Bridging degree of cure with tensile strength and hardness," *Materials & Design*, vol. 162, pp. 418–428, Jan. 2019.

[121] S. Westbeek, J. A. W. van Dommelen, J. J. C. Remmers, and M. G. D. Geers, "Multiphysical modeling of the photopolymerization process for additive manufacturing of ceramics," *European Journal of Mechanics - A/Solids*, vol. 71, pp. 210–223, Sept. 2018.

[122] R. Anastasio, *UV-cured polymer networks*. PhD thesis, Eindhoven University of Technology, Eindhoven, The Netherlands, 2019.

[123] C. Gorsche, R. Harikrishna, S. Baudis, P. Knaack, B. Husar, J. Laeuger, H. Hoffmann, and R. Liska, "Real Time-NIR/MIR-Photorheology: A Versatile Tool for the *in Situ* Characterization of Photopolymerization Reactions," *Analytical Chemistry*, vol. 89, pp. 4958–4968, May 2017.

[124] A. Aguirre-Soto, A. T. Hwang, D. Glugla, J. W. Wydra, R. R. McLeod, C. N. Bowman, and J. W. Stansbury, "Coupled UV–Vis/FT–NIR Spectroscopy for Kinetic Analysis of Multiple Reaction Steps in Polymerizations," *Macromolecules*, vol. 48, pp. 6781–6790, Oct. 2015.

Chapter 7

Conclusions and future research directions

As Additive Manufacturing (AM) technologies are maturing, the underlying control systems are becoming increasingly important in safeguarding product quality and enabling the realization of their full potential. In light of these developments, this thesis presents advancements in closed-loop control systems for photopolymer-based AM by addressing the necessary steps in the control system development cycle. In following this cycle for both major process steps, i.e., recoating and photopolymerization, it is hypothesized that final product quality may improve as a result of integrating closed-loop control systems into AM machine architectures. Several research objectives were defined to investigate the hypothesis; this chapter outlines the main conclusions regarding these objectives and provides directions for future research.

7.1 Conclusions

The main conclusions are outlined below in accordance with the research objectives (i) to (v) and the main research objective, as formulated in Chapter 1.

(i) Formulation of a classification scheme for AM control strategies
A tool is proposed in Chapter 2 for identifying potential control strategies by drawing inspiration from literature examples of AM control strategies. The result is an "AM V-model" classification scheme that decomposes the AM process both spatially and temporally into seven hierarchical levels ranging from low-level machine control to high-level product or batch control. Despite the wide use of low-level machine controllers, higher-level process and product controllers have not found industrial application yet, let alone researched by academia. Moreover, no unified hierarchical

framework has been proposed yet to control final product quality by combining multiple control levels, for instance by cascading machine, process, and product controllers.

(ii) Trade-off analysis between recoating actuation methods
A categorization of recoating methods is presented in Chapter 3, along with several sensing and control methods. It was found that most recoating methods are controlled in open loop on the process level in the AM V-model, which may be attributed to the unavailability of feedback signals that are representative of deposited layer quality. The system designer was found to have at least sixteen options to fulfill the recoating function and these options were compared in terms of, among others, maximum build area, minimum layer thickness, and maximum recoater speed. Based on these reported specifications, the system designer may choose a recoating method. However, this choice is complicated by the fact that hardly any data is available on the actual performance of the recoating methods in terms of layer uniformity or final product quality.

(iii) Feasibility analysis of real-time controlled photopolymerization
A vast body of literature is reviewed in Chapter 4 in terms of (1) process models, (2) actuators, (3) sensors, and (4) controllers in order to assess (5) the feasibility of real-time photopolymerization control schemes.

Firstly, a comparison is made among process models to show which models take which physical phenomena into account. It was found that only one out of many models had been developed for control purposes and that there is a need to develop other control-oriented models for implementation in real-time control systems.

Secondly, several mechatronic concepts are identified from existing VP equipment to actuate the polymerization reaction with UV light. Fortunately, their response times do not seem to form a limiting factor for control and the characteristic exposure times were found to range from $\mathcal{O}(10^{-5})$ [s] for vector scanning systems to $\mathcal{O}(10)$ [s] for digital mask projection systems. A scanning mask projection concept is expected to be capable of combining large-area, high-throughput UV exposure with a characteristic exposure time suitable for control.

Thirdly, several measuring principles are evaluated for suitability as real-time in-line metrology for the degree of conversion. Unfortunately, suitable sensors are hardly available for in-situ photopolymer characterization, which reveals the need for developing new sensor modalities that meet the application's spatial and temporal resolution requirements. Due to the duality in sensing and actuation, the optical measuring principles are of special interest.

Fourthly, only three closed-loop control strategies were found for photopolymerization, which aimed at either minimizing spatial conversion variations or dimensional errors. Therefore, it was established that the literature lacked both experimental and theoretical proof that the photopolymerization process may benefit from real-time control of conversion.

Finally, the feasibility of real-time photopolymerization control is evaluated by checking whether sensor sampling rates and actuator response times are fast enough compared to the time constants of relevant physical process phenomena. The conclusions are that real-time control seems feasible only for mask projection systems and that feasibility is currently governed by sensor sampling rates and AM machine compatibility.

(iv) Proof of principle of real-time controlled photopolymerization
Experimental proof is provided in Chapter 5 to demonstrate that real-time feedback control of conversion is actually feasible for mask projection systems. After relaxing several sensing requirements, an existing spectroscopic measuring instrument was selected and augmented with a UV-LED-based actuator, an embedded controller, and interfacing software to obtain an experimental setup capable of closed-loop control. A single-input-single-output (SISO) system was obtained by actuating a single resin layer at the top and measuring the surface conversion at the bottom.

The setup was used to develop a simple control-oriented model, which was found to be capable of describing the photopolymerization process to an acceptable extent. Moreover, a real-time feedback controller demonstrated to be capable of rejecting a material disturbance and of reaching the same final cure level as with the undisturbed material. Thus, the conclusion is that real-time and in-situ feedback control of photopolymer conversion is principally feasible under small-scale lab conditions.

Chapter 5 finally proposes a roadmap to translate the small-scale lab conditions under relaxed requirements to large-scale AM machine factory conditions. Particularly, the requirements for machine implementability and a sufficiently high sampling rate were relaxed to provide the small-scale proof of principle. The UV light intensity had to be reduced to obtain an acceptable ratio of the sampling rate to the reaction time constant resulting in exposure times of 60 [s], which is a factor of ten higher than the typical exposure times in mask-projection-based vat photopolymerization. The achieved sampling rate was only 0.5 [Hz] and was mainly limited by overhead in the instrument's software, as it did not natively support real-time outputs.

(v) Instrumentation development for photopolymer conversion
A proof of concept is presented in Chapter 6 for a new optical measuring instrument. The instrument is capable of determining the degree of conversion in acrylic photopolymers and is expected to overcome several limitations of existing instrumentation. The purpose-built instrument is based on molecular absorption photometry in a narrow NIR wavelength range and is hypothesized to provide a simpler, cost-effective alternative to general-purpose, wide-range spectro(photo)meters as the one used in Chapter 5. Experimental results demonstrate that the realized instrument functions properly after adapting its design to solve several unforeseen issues related to the optical probe and the sample cell. Based on these issues, one can conclude

that attention should be paid to the details of the sample and probe design to accommodate the interactions of the multiphysical UV curing process.

Nonetheless, the NIR photometer was expected to outperform NIR *spectro*-photometers due to its reduced complexity. Although further research is required to establish its actual performance, the conclusion can be drawn that NIR transmission photometry is a viable concept to measure the degree of conversion of acrylate-based resins in a repeatable manner and at high measurement speeds. This conclusion is supported by NIR photometric results obtained with a variety of commercial resins, which indicates its potential for implementing the instrument into, or installing it next to, photopolymer-based AM equipment. Owing to the simple and direct measuring principle, the required signal processing is kept to a minimum and, thus, implementation into an embedded control system should be rather straightforward.

The NIR photometer demonstrated to be capable of measuring at a 20 [kHz] sampling rate while maintaining a proper signal-to-noise ratio. Hence, the sampling rate was $4 \cdot 10^4$ times higher than the 0.5 [Hz] sampling rate achieved in Chapter 5. Its sampling rate was limited by the control computer and it is expected that it can be increased to the [MHz] range if measurement noise remains manageable, since ultrafast photodetectors are available with bandwidths in the [GHz] range [1]. Hence, it seems that the main barriers for AM machine implementation can be overcome, especially the sampling rate limitation.

However, machine implementation remains a challenge if one wants to measure and control the photopolymer reaction in situ and in real time inside the AM machine. The transmission measuring principle is not expected to work for AM applications where tens of thousands of layers are stacked, but a transflection sampling configuration may provide a means to measure and actuate from the same side. Nevertheless, the transmission configuration is expected to work in an offline application where the sensor is placed in the corner of the machine to determine the build settings from a cure kinetics measurement. The transmission configuration is also expected to work for a stack of at least ten 0.1 [mm] layers, as the NIR photometer demonstrated to be well capable of measuring a single 1.0 [mm] thick layer and the additional losses due to interfacial reflections are relatively small due to the small refractive index difference between cured and uncured polymer. In conclusion, NIR photometry is expected to be suitable for future machine implementation upon further development, operating at high speeds and providing in-situ measurements for control of the UV curing process that lies at the core of photopolymer-based AM.

(Main objective) Improving product quality through closed-loop control
Each research outcome above contributes to the main objective of investigating closed-loop control system architectures for photopolymer-based AM. Generally speaking, it was found difficult to assess their potential to improve final product quality, since little is known in the literature about the magnitude and impact of the uncertainties in the AM equipment, material and process. This conclusion holds both for recoating and for photopolymerization. Nonetheless, several po-

tential uncertainties have been identified in Chapter 5 that may adversely affect photopolymerization and, hence, the final product quality.

The lifetime definition of UV LED sources gives an idea of the magnitude of input disturbances that can be expected in UV curing practice. According to the IESNA LM-80-20 standard [2], their end-of-life is defined as the operating time at which their light intensity has reduced to 80 [%] of the original value. Moreover, a case has been reported [3] where an aircraft coating was insufficiently cured due to an estimated 20 [%] reduction in UV energy as a result of a too long extension cord. Thus, a 20 [%] UV power reduction seems a realistic estimate of the magnitude of static input disturbances encountered in UV curing practice and apparently leads to quality issues.

Since a chain is as strong as its weakest link, insufficient curing of just one out of thousands of layers may lead to AM part failure. Experimental results (not reported in this thesis) have demonstrated [4] that a resin layer can be sufficiently cured even in the presence of a 50 [%] static input disturbance by virtue of the feedback control scheme presented in Chapter 5. Thus, the main conclusion is that performance indeed can be gained by using closed-loop control on the individual-layer scale as opposed to the open-loop control. Although quantification of the actually achievable performance gain is left for future work, closed-loop control of UV curing may prove indispensable to the long-term goal of zero-defect AM.

7.2 Directions for future research

Based on the research results presented in this thesis, one could say that Technology Readiness Level (TRL) 1 to 4 have been covered [5] regarding closed-loop photopolymerization control. That is, fundamental research has been carried out to formulate the basic technology concept (TRL 1 & 2) [6] and research has been conducted to prove feasibility in a lab environment (TRL 3 & 4) [5]. Evidently, several steps have to be taken before the technology reaches the highest TRL level 9, such that it is ready for implementation into AM machines on the shop floor. The remainder of this chapter gives several recommendations and suggestions for future research on closed-loop control for AM.

Closing the feedback loop in recoating

This thesis focused primarily on the photopolymerization step, as the underlying material transformation principle is the same, no matter the actuation strategy. In the recoating step, the actuation strategy principally differs between the recoating methods outlined in Chapter 3. As a result, it is less straightforward to develop closed-loop control strategies that are applicable to more than one recoating method. Moreover, the control problem may differ from one machine architecture to another in the sense of the conceptual machine design choices seen in Figure 1.2. Although not explicitly mentioned in this figure, the light engine type, irradiation orientation, and surface constrainedness are in principle three independent choices.

These conceptual design choices may have implications for the control requirements, e.g., the mechanics in constrained-surface systems call for a separation force control scheme that is irrelevant for free-surface systems. Although at the time of writing there seems to be a shift among AM equipment manufacturers towards constrained-surface machine architectures in which the build platform continuously moves, the build areas of these continuous systems have not reached those of conventional systems in which recoating and UV curing are alternated and which tend to have a free surface. Therefore, it is suggested to go through the control system development cycle and close the feedback loop for blade-based recoating systems, using recently developed CFD models [7, 8]. In continuous systems, separation force control [9] may be combined with platform speed and UV power control.

Exploring how the wealth of control theory can be applied to AM
AM presents a practically unexplored but interesting control problem to the well-established field of control systems technology. By definition, any 3D printing process is a distributed parameter or infinite-dimensional system [10], i.e., a system having spatial dependency. In this framework, laser-based AM is a boundary input control problem at the top or bottom of the layer [11, 12]. Thus, the AM control problem can be considered a multiple-input-infinite-dimensional-output (MI∞O) problem, i.e., one of the most challenging control problems. When considering multiple layer stacks, it can be formulated as a hybrid control problem switching between continuous dynamics at each discrete layer addition event [11, 12].

To make the control problem even more challenging, AM processes are multi-physical [13, 14], with widespread length and time scales and high spatio-temporal resolution. The AM V-model classification scheme may provide guidance in managing this complexity through hierarchical control, but it is still an open research question how to best combine low-, mid-, and high-level control schemes. Based on current insight, it is the author's opinion that future development efforts should first focus on an in-situ sensor-based alternative to ex-situ working curve approaches and subsequently on real-time closed-loop control.

Repeating the control system development cycle for single-layer curing
Several steps in the control system development cycle require further research, as this work has only gone through it once. First of all, it is recommended to reperform the closed-loop experiments with the MIR spectrometer from Chapter 5, but using the NIR photometer setup from Chapter 6. An important difference between the two setups is the sampling method. The former setup only probes a few micrometers at the bottom of the layer and is considered 0D, whereas the latter probes the complete layer and is considered 1D. The question is whether the simple feedback controller used on the 0D micrometer scale can also be used on the 1D layer scale as the photopolymerization dynamics may become more complex as a result of spatial variations. The roadmap proposed in Chapter 5 may serve as a guideline in progressing from the 0D point scale to the full 3D product scale.

Investigating other feedback control strategies on the single-layer scale
Secondly, the feedback control strategy requires reconsideration. To this end, the control objectives need to be formulated and translated into specifications of the required performance in terms of the degree of conversion trajectory, preferably in discussion with experts in photopolymer chemistry. If it is merely desired to reach a degree of conversion target *at the end* of the UV curing period, one could consider using a simple bang-bang or on/off controller [15]. If it is desired to track a degree of conversion trajectory as close as possible *throughout* UV curing, a PID type or model-based controller may be used. If it is desired to reach a certain degree of conversion level *after* UV exposures and during the dark polymerization period, a model-predictive controller may prove useful [11, 12]. In these control strategies, the unmeasurable material properties are only indirectly controlled, so the coupling to the measurable degree of conversion needs to be established to safeguard product quality.

Exploiting the UV actuation capabilities in feedforward control
Thirdly, the UV actuation capabilities may provide a means to improve the cured material properties. Most vat photopolymerization systems only turn the light on and off, or scan the resin's surface once or more with a UV laser. In essence, this is just a simple step input, while the equipment is typically capable of modulating the UV light intensity over time. Literature already provides evidence that soft-start [16] and pulsed [17] irradiation strategies can improve the material properties, so the feedforward UV input requires further research.

Considering closed-loop control in other UV curing applications
UV curing finds many other industrial applications than AM, such as adhesives, coatings [18–20], composite panels [11], and dental fillings [21]. Thus, the closed-loop control strategy may be applied in these application areas as well. Recent developments in NIR cameras and array detectors indicate that it is feasible to use NIR hyperspectral imaging for in-line monitoring of UV-cured coatings [22]. Such sensors may provide the measurement signals required for feedback control, although in some cases the UV light is not patterned as in AM, which presents an actuation challenge.

Material jetting is an example photopolymer-based AM process in which the UV light is not patterned. Although the scope of the present thesis is limited to the vat photopolymerization AM process category, the presented control approaches may be applied in material jetting as well. Vat photopolymerization and material jetting processes differentiate themselves in the patterning of energy or material respectively. In this respect, material jetting processes may provide *more* spatial actuation freedom in recoating, but *less* in UV curing. On the one hand, the increased actuation freedom in recoating may allow for closed-loop control of the deposited layer's flatness as already demonstrated by Guo et al. [23] for ink-jet-based AM.

On the other hand, the reduced actuation freedom in UV curing may make it less effective to use the presented closed-loop photopolymerization control approaches.

Developing a testbed for integrated modelling, metrology and control
An intermediate step towards TRL level 9 may be the development of a photopolymer-based version of the Additive Manufacturing Metrology Testbed (AMMT) for metal-based AM developed at the National Institute of Standards and Technology (NIST) [24,25]. Such a testbed allows to assess in-situ process metrology such as NIR photometry and relate in-process measurements to pre-process measurements of resin properties and post-process measurements of final product quality [26]. The integral approach of process modelling, metrology, and control may prove the principle of first-time right printing for photopolymer-based AM, as was recently demonstrated for metal-based AM [27]. Moreover, it may enable the automated qualification of part quality [24], also known as the "certify-as-you-build" paradigm [6]. A metrology testbed provides the open control architecture required for these developments and may cause a shift towards opening up the black-box, closed control architectures frequently found in commercial AM equipment [28, 29].

References

[1] S. Gateva, *Photodetectors*. Rijeka, Croatia: InTechOpen, 1st ed., 2012.

[2] ANSI, *Measuring Luminous Flux and Color Maintenance of LED Packages, Arrays, and Modules*. 2020. ANSI/IES LM-80-20.

[3] M. J. Dvorchak, M. L. Clouser, and A. D. Harbourne, "AEROSPACE UV CURED Coatings; Yesterday, Today & Tomorrow," in *RadTech 2020 UV & EB Technical Conference Proceedings*, (Orlando, FL), 2020.

[4] T. Hafkamp, G. van Baars, B. de Jager, and P. Etman, "Real-time feedback controlled monomer conversion: a new paradigm for UV curing process control," in *RadTech 2020 UV & EB Technical Conference Proceedings*, (Orlando, FL), 2020.

[5] S. R. Hirshorn, L. D. Voss, and L. K. Bromley, *NASA Systems Engineering Handbook*. 2017. SP-2016-6105, Rev 2.

[6] Y. Huang, M. C. Leu, J. Mazumder, and A. Donmez, "Additive manufacturing: Current state, future potential, gaps and needs, and recommendations," *Journal of Manufacturing Science and Engineering*, vol. 137, no. 1, pp. 1–10, 2015.

[7] A. Kozhevnikov, R. Kunnen, G. van Baars, and H. Clercx, "Investigation of the fluid flow during the recoating process in additive manufacturing," *Rapid Prototyping Journal*, vol. 26, pp. 605–613, Jan. 2019.

[8] A. Kozhevnikov, R. Kunnen, G. van Baars, and H. Clercx, "Influence of the recoating parameters on resin topography in stereolithography," *Additive Manufacturing*, vol. 34, p. 101376, Aug. 2020.

[9] F. Liravi, S. Das, and C. Zhou, "Separation force analysis and prediction based on cohesive element model for constrained-surface Stereolithography processes," *Computer-Aided Design*, vol. 69, pp. 134–142, Dec. 2015.

[10] R. F. Curtain and H. J. Zwart, *An Introduction to Infinite-Dimensional Linear Systems Theory*. New York, NY: Springer-Verlag, 1st ed., 1995.

[11] A. M. Yebi, *Model-based control of UV curing processes with application to additive manufacturing*. PhD thesis, Clemson University, Clemson, SC, 2015.

[12] S. D. Beyene, *Optimal Control of UV-Induced Curing Processes for Layer-by-Layer Manufacturing of Composites*. PhD thesis, Clemson University, Clemson, SC, 2019.

[13] S. Westbeek, J. A. W. van Dommelen, J. J. C. Remmers, and M. G. D. Geers, "Multiphysical modeling of the photopolymerization process for additive manufacturing of ceramics," *European Journal of Mechanics - A/Solids*, vol. 71, pp. 210–223, Sept. 2018.

[14] K. Classens, T. Hafkamp, S. Westbeek, J. Remmers, and S. Weiland, "Multi-physical modeling and optimal control of material properties for photopolymerization processes," *Additive Manufacturing*, pp. 101520–1 – 101520–16, Aug. 2020. Journal Pre-proof.

[15] X. Zhao and D. W. Rosen, "An implementation of real-time feedback control of cured part height in Exposure Controlled Projection Lithography with in-situ interferometric measurement feedback," *Additive Manufacturing*, Aug. 2018.

[16] D. C. Watts and A. Al Hindi, "Intrinsic 'soft-start' polymerisation shrinkage-kinetics in an acrylate-based resin-composite," *Dental Materials*, vol. 15, no. 1, pp. 39–45, 1999.

[17] R. Anastasio, *UV-cured polymer networks*. PhD thesis, Eindhoven University of Technology, Eindhoven, The Netherlands, 2019.

[18] F. Zeng, *Estimation and Control of Robotic Radiation-Based Processes*. PhD thesis, Clemson University, Clemson, SC, 2010.

[19] M. Bach, *Near infrared laser sensor system for in-line detection of conversion in UV-cured polymer coatings*. PhD thesis, KIT Scientific Publishing, Karlsruhe, Baden, 2012.

[20] R. Schwalm, *UV coatings basics, recent developments and new applications*. Amsterdam; London: Elsevier, 1st ed., 2006.

[21] J. Steinhaus, B. Hausnerova, T. Haenel, M. Großgarten, and B. Möginger, "Curing kinetics of visible light curing dental resin composites investigated by dielectric analysis (DEA)," *Dental Materials*, vol. 30, pp. 372–380, Mar. 2014.

[22] O. Daikos, K. Heymann, and T. Scherzer, "Monitoring of thickness and conversion of thick pigmented UV-cured coatings by NIR hyperspectral imaging," *Progress in Organic Coatings*, vol. 125, pp. 8–14, Dec. 2018.

[23] Y. Guo, J. Peters, T. Oomen, and S. Mishra, "Distributed model predictive control for ink-jet 3D printing," in *2017 IEEE International Conference on Advanced Intelligent Mechatronics (AIM)*, pp. 436–441, July 2017.

[24] M. L. Vlasea, B. Lane, F. Lopez, S. Mekhontsev, and A. Donmez, "Development of powder bed fusion additive manufacturing test bed for enhanced real-time process control," in *Proceedings Solid Freeform Fabrication Symposium*, pp. 527–539, 2015.

[25] B. Lane, S. Mekhontsev, S. Grantham, M. L. Vlasea, J. Whiting, H. Yeung, J. Fox, C. Zrobila, J. Neira, M. McGlauflin, J. Hanssen, S. Moylan, A. Donmez, and J. Rice, "Design, Developments, and Results from the NIST Additive Manufacturing Metrology Testbed (AMMT)," in *Proceedings of the 26th Annual International Solid Freeform Fabrication Symposium*, pp. 1145–1160, 2016.

[26] J. Pellegrino, T. Makila, S. McQueen, and E. Taylor, "Measurement science roadmap for polymer-based additive manufacturing," Tech. Rep. NIST AMS 100-5, National Institute of Standards and Technology, Gaithersburg, MD, Dec. 2016.

[27] M. Megahed, H.-W. Mindt, J. Willems, P. Dionne, L. Jacquemetton, J. Craig, P. Ranade, and A. Peralta, "LPBF Right the First Time—the Right Mix Between Modeling and Experiments," *Integrating Materials and Manufacturing Innovation*, pp. 1–23, Apr. 2019.

[28] D. Fornea and H. Van Laere, "Living tomorrow. 3D printing — a tool to empower the European economy. Opinion of the European Economic and Social Committee CCMI/131," *Official Journal of the European Union*, pp. C 332/36 – C 332/44, Oct. 2015. 2015/C 332/05.

[29] S. A. Andersen, S. D. Rio, D. B. Pedersen, and H. N. Hansen, "A Beam Modulator and Galvanometer Controller for Metal Powder Bed Fusion," in *Proceedings - 2018 ASPE and euspen Summer Topical Meeting: Advancing Precision in Additive Manufacturing*, pp. 172–177, American Society for Precision Engineering, 2018.

Acknowledgements

In one of our first meetings, my supervisors told me that I would be embarking on a thrilling academic research journey, as if I would be wading through the jungle with a machete like a true explorer. Today, I must say that this journey has been thrilling indeed and far exceeded my expectations. Although at times a true explorer has a serious chance of finding himself washed ashore on a lonely island, making it back to the inhabited world is a matter that lies in his own hands. As Thomas H. Huxley said, "Perhaps the most valuable result of all education is the ability to make yourself do the thing you have to do, when it ought to be done, whether you like it or not."

This lesson is perhaps one of the most valuable things that I have learned during the course of my PhD journey. This is not to say that you should do everything by yourself though. On the contrary, the developing PhD researcher should stand on the shoulders of his fellow researchers to see further into the sea, in an attempt to get off the island and actually do what he or she is supposed to do – pushing the boundaries of our knowledge. All in all, I am deeply grateful to have been standing on the shoulders of giants for my whole life and, even more so, for the past four years. Although words cannot express how thankful I am to each and every one who has contributed to this thesis in any way, I would like to express my gratitude to certain persons in particular.

Firstly, I would like to thank my daily supervisors and promotors Bram, Gregor, and Pascal. I experienced our meetings and discussions as very pleasant, since it always felt as if we were going through the jungle as a team. Pascal, it is my honor to be the first one to be promoted under your authority. Your seemingly infinite patience and charitable attitude towards students is highly admirable. Bram, your broad and in-depth knowledge of control systems and critical attitude has definitely lifted this thesis to a higher level. Gregor, your excellent way of posing industrially relevant research questions has stimulated me from the start and your guidance along the way has really helped me to keep the morale up even when things got hard. I would also like to thank the other committee members, prof.dr. Ian Gibson, prof.dr.ir. Maarten Steinbuch, prof.dr.ir. Patrick Anderson, and prof.dr.ir. Fred van Keulen, for taking part in my PhD defense and reviewing this thesis.

Secondly, my thanks go out to all the people affiliated to the AMSYSTEMS

Center, both from the TNO Equipment for Additive Manufacturing (EfAM) department and from the TU/e's High Tech Systems Center (HTSC). Special thanks go out to fellow PhD candidates Andrei, Steyn, and Rosaria, their supervisors, and all others involved in our fruitful quarterly meetings. Moreover, I would like to thank PDEng graduates Jordy, Remco, and Tim and TNO's stereolithography equipment experts Fabien and Hessel for the many interesting discussions we had that were geared towards implementation into TNO's Lepus Next Gen machine. I feel like the collaboration between TNO and TU/e really has been quite unique and I would like to acknowledge HTSC directors Katja and Maarten and EfAM managers Erwin and Pieter for doing a great job in establishing the AMSYSTEMS Center, which was certainly promoted by colocation and an open door policy. The AM research topics did not only appeal to me, but also to all the talented students with whom I had the pleasure to work with in the form of Bachelor End Projects (Bart, Ben, David, Joost, Kevin, and Stijn), internships (Bart, Martin and Tushar), and MSc graduation projects (Koen, Nourdin, Yu-Jen, and Zhihao) – thank you all.

Thirdly, I would like to express my gratitude to all staff members at TNO and TU/e who have supported me during my PhD project. Fidel, Henk, Javier, Jonathan, Jorgen, Raymond, Tessa, and all the others at TNO Materials Solutions, thank you for supporting me in the lab and facilitating my FTIR spectroscopy experiments. Erwin, you have been an outstanding sparring partner from the TNO Optomechatronics department and I think that I would have never been able to finish the design and realization of the NIR photometer without your invaluable help. Erik, Irene, and Jaap, thank you for granting me access to the facilities at TU/e's well-organized Microfab/Lab and for housing my experimental setup. Hans, many thanks for offering me a spot in the Mechanical Design Lab during the final months of my project after COVID-19 disrupted "normal" everyday life and forced us all into a(n) (inter)national lockdown. Prakhyat, Gerrit, and Patrick from the Polymer Technology Group and Erwin, Gerrit, Rob, and others from TU/e's EPC, thank you for the interesting discussions we had on the SLS printer development project. Nancy, Roos, Petra, and Geertje, thank you for providing excellent administrative support and for a chat every now and then.

Fourthly, my thanks go out to all my colleagues from the CST and D&C departments. I really enjoyed our coffee breaks, lunch seminars, outings, and the Benelux meetings. I wouldn't be surprised if I held some sort of record for having had the highest number of officemates, since I must have had at least seventeen of them over the years. Aida, Chyannie, Daniel, Enzo, Ferdie, Jeroen, Joshua, Karlijn, Lars, Lennart, Martijn, Nick, Roy, Sander, Sjoerd, Stijn, and Tim, it was my honor to share a room with you in the Systems Engineering lab. Despite the rather large number of people in that room, there always seemed to be a good balance between hard work and a casual chat.

Finally, my deepest gratitude goes to those who are dearest to me: my family, my friends, and my partner. I owe my life to your unconditional love and support and I would like to dedicate this thesis to you. Big thanks to my parents Ans and Peter,

my brother Maurits, my sister Florianne, their partners, and my future in-laws for showing interest throughout my study career. I would also like to give a shout-out to my friends for helping me escaping my PhD island and providing me with very welcome distractions every now and then. The final person I would like to thank is my dear partner Merel. I reckon you were most impacted by my commitment to this thesis, especially during the last half year. I am eternally grateful that you love me, support me, patiently give me space and, most importantly, stimulate me to make the most out of life together with you!

Thomas Hafkamp
Eindhoven, September 2020

Curriculum Vitae

Thomas Hafkamp was born on March 28, 1991 in Dieren, The Netherlands. He completed his secondary education in 2009 at the Stedelijk Gymnasium Arnhem, The Netherlands. He went on to study Mechanical Engineering at Eindhoven University of Technology and obtained his Master of Science degree (cum laude) in 2015 with a specialization in mechanical design principles for high-precision constructions and mechanisms.

Directly following his studies, Thomas was granted the opportunity to pursue a PhD degree within the Control Systems Technology group at the same university. He conducted his PhD research project in collaboration with TNO and under the supervision of dr.ir. Pascal Etman, dr.ir. Bram de Jager, and ir. Gregor van Baars (TNO Optomechatronics), the results of which are presented in this dissertation.